The Design and Development towards a Biosensor for the Detection of Bovine Tuberculosis

by

Ronja Hess

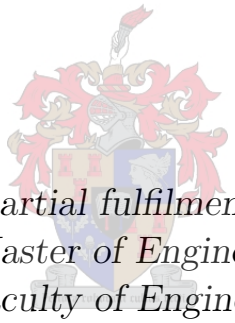

Thesis presented in partial fulfilment of the requirements for the degree of Master of Engineering in Electronic Engineering in the Faculty of Engineering at Stellenbosch University

Supervisor: Prof. WJ Perold

Co-supervisor: Prof. MA Miller,
Dr L Kleynhans, and
Dr W Goosen

December 2021

The support of the DSI-NRF Centre of Excellence for Biomedical TB Research towards this research is hereby acknowledged. Opinions expressed and conclusions arrived at, are those of the author and are not necessarily to be attributed to the CBTBR.

Declaration

By submitting this thesis electronically, I declare that the entirety of the work contained therein is my own, original work, that I am the sole author thereof (save to the extent explicitly otherwise stated), that reproduction and publication thereof by Stellenbosch University will not infringe any third party rights and that I have not previously in its entirety or in part submitted it for obtaining any qualification.

Date: December 2021

Acknowledgements

I would like to thank the NRF and the CBTBR for their financial support.

The support of the DSI-NRF Centre of Excellence for Biomedical TB Research towards this research is hereby acknowledged. Opinions expressed and conclusions arrived at, are those of the author and are not necessarily to be attributed to the CBTBR.

The financial assistance of the National Research Foundation (NRF) is hereby acknowledged. Opinions expressed and conclusions arrived at, are those of the author and are not necessarily to be attributed to the NRF

I would like to thank my supervisor Professor Perold as well as all my co-supervisors Professor Miller, Dr Kleynhans, and Dr Goosen for their continuous support throughout this project. I would also like to thank the members of the animal TB research group, that have assisted me.

The SAND research team has been invaluable to me throughout the course of this project. I would like to thank my seniors for their advice and assistance and all my colleagues for their support. Special thanks to Taskeen, Daniel, Annemie and Wesley who kept me going even in the roughest times.

My gratitude is also directed to the administrative and technical staff from the engineering faculty. Especially; Wessel Croukamp and Gift Lecholo.

Additional thanks to Dr Bosman and Professor Tame from the Department of Physics, for allowing me to make use of your expertise, as well as the department's space and equipment.

A huge thank you to Professor Pretorius, Dr du Toit, Dr Venter and everyone else at the Department of Physiology that assisted me with the biological component of my project. Also, thank you for allowing me to use your laboratory space and equipment.

I would herewith also like to thank Mr Malcomb from Organic Chemistry as well as Dr Botes from CAF who assisted me in the creation of my SPR chips.

Last, but not least, I would like to thank my family and friends, who have endlessly supported me.

Abstract

The Design and Development towards a Biosensor for the Detection of Bovine Tuberculosis

R. Hess

Department of Electrical and Electronic Engineering,
University of Stellenbosch,
Private Bag X1, Matieland 7602, South Africa.

Thesis: MEng (Electronic)

December 2021

Bovine Tuberculosis (bTB) is a contagious disease often found in buffaloes and cattle. The disease can affect various mammals and poses a huge socioeconomic risk. Current diagnostic methods require highly skilled personnel and cannot be done in the field. Hence, the development of a biosensor to detect bTB is proposed. This thesis details the design of a system towards the development of a biosensor to detect bTB in buffalo. A literature study to investigate biosensors was conducted and Surface Plasmon Resonance (SPR) was selected as the biosensor type. SPR is an optical phenomenon that can be implemented to monitor binding and unbinding of biological components.

For this project various parts of an SPR system were designed, manufactured and tested. SPR chips with a 50 nm thick gold substrate were manufactured. Various optical setup configurations were tested and prism types were investigated. The Infiniter VLM-635/650-03 laser was selected and a power supply system was designed and produced. The SPR phenomenon was observed using these components. The microfluidic system that was developed allowed for the introduction of the sample to the gold layer at low velocity. The prototype was flexible, to allow for adjustments during development and testing phase. Two different immobilisation methods were attempted and various verification methods were implemented, but the results were inconclusive. Software to plot the intensity profiles of the SPR system was developed. The prototype was tested with bovine serum albumin and at a concentration of 10 $\text{mg}\cdot\text{ml}^{-1}$ a change in the intensity minimum of the signal could be observed with the naked eye.

Even though the system needs refinement and further development, it is concluded that an SPR based biosensor is a viable solution for the in the field detection of bTB.

Uittreksel

In die rigting van die Ontwerp en Ontwikkeling van 'n Biosensor vir die Opsporing van Beestuberkulose

R. Hess

Departement Elektries en Elektroniese Ingenieurswese,
Universiteit van Stellenbosch,
Privaatsak X1, Matieland 7602, Suid Afrika.

Tesis: MIng (Elektronies)

Desember 2021

Beestuberkulose (bTB) is 'n aansteeklike siekte wat dikwels by buffels en beeste voorkom. Die siekte kan verskillende soogdiere aantas en hou 'n groot sosio-ekonomiese risiko in. Huidige diagnostiese metodes benodig hoogs bekwame personeel en kan nie in die veld gedoen word nie. Daarom word die ontwikkeling van 'n biosensor vir die opsporing van bTB voorgestel. Hierdie tesis beskryf die ontwerp van 'n stelsel vir die ontwikkeling van 'n biosensor om tuberkulose by beeste op te spoor. 'n Literatuurstudie om biosensors te ondersoek is uitgevoer en 'n oppervlak plasmon resonansie biosensor is gekies vir die projek. Oppervlak Plasmon Resonansie (OPR) is 'n optiese verskynsel wat geïmplementeer kan word om binding en ontbinding van biologiese komponente te monitor.

Vir hierdie projek is verskillende dele van 'n OPR-stelsel ontwerp, vervaardig en getoets. OPR -skyfies met 'n 50 nm dik goue substraat is vervaardig. Verskeie optiese opstellings is getoets en prisma-soorte is ondersoek. Die Infiniter VLM-635/650-03 laser is gekies en 'n kragtoevoerstelsel is ontwerp en vervaardig. Die OPR-verskynsel is waargeneem deur die gebruik van hierdie komponente. Die mikrofluïdiese stelsel wat ontwikkel is, het toegelaat dat die monster teen 'n lae snelheid met die goue laag kontak maak. Die prototipe was verstelbaar om aanpassings tydens die ontwikkelings- en toetsfase moontlik te maak. Daar is twee verskillende immobilisasie-metodes getoets en verskillende verifikasiemetodes is geïmplementeer, maar die resultate was onduidelik. Sagteware om die intensiteitsprofiele van die OPR-stelsel grafies voor te stel, is ontwikkel. Die prototipe is met beesserumalbumien getoets en by 'n konsentrasie van 10 $\text{mg}\cdot\text{ml}^{-1}$ kon 'n verandering in die intensiteit minimum in die sein met die blote oog waargeneem word.

Alhoewel die stelsel verfyning en verdere ontwikkeling nodig het word dit afgelei dat 'n OPR-gebaseerde biosensor vir die opsporing van bTB in die veld 'n uitvoerbare oplossing is.

Contents

List of Figures

List of Tables

Nomenclature

Abbreviations

3MPA	3 Mercaptopropionic acid
AFM	Atomic Force Microscope
BJT	Bipolar Junction Transistor
BSA	Bovine Serum Albumin
bTB	Bovine Tuberculosis
CAD	Computer Aided Design
CAF	Central Analytical Facilities
CCD	Charge-Coupled Device
CMIR	Cell-Mediated Immune Response
DI	Deionised
DNA	Deoxyribonucleic acid
DPV	Differential Pulse Voltammetry
EBL	Electron Beam Lithography
EDC	1-Ethyl-3-(3-dimethylaminopropyl)carbodiimide
EDX	Energy Dispersive X-Ray
EIS	Electrochemical impedance spectroscopy
ELISA	Enzyme-linked immunosorbent assay
FET	Field Effect Transistor
FITC	Fluorescein isothiocyanate
FLIM	Fluorescent Lifetime Imaging Microscopy

FRET	Fluorescent Resonance Energy Transfer
FWHM	Full Width Half Maximum
He-Ne	Helium-Neon
hCG	Human Chorionic Gonadotropin
HDMI	High-Definition Multimedia Interface
HRP	Horseradish peroxide
IDE	Interdigitated electrode / Integrated development environment
IFN-γ	Interferon Gamma
IP-10	Interferon Gamma-Induced Protein 10
IR	Infrared
LIF	Laser Induced Fluorescence
M. bovis	*Mycobacterium bovis*
MOSFET	Metal–Oxide–Semiconductor Field-Effect Transistor
MES	2-(N-morpholino)ethanesulfonic acid
NHS	N-Hydroxysuccinimide
NP	Nanoparticle
OD	Optical Density
PBS	Phosphate-Buffered Saline
PCA	Principal Component Analysis
PCB	Printed Circuit Board
PEG	Poly(ethylene glycol)
PPD	Purified Protein Derivative
QCM	Quartz Crystal Microbalance
RAM	Random Access Memory
RGB	Red, Blue, Green
SAM	Self-Assembled Monolayer

SAND	Sensor Application and Nano Devices
SAW	Surface Acoustic Wave
SD	Secure Digital
SEM	Scanning Electron Microscope
SERS	Surface-Enhanced Raman Spectroscopy
std	Standard
SWCNT	Single-Wall Carbon Nanotubes
SPR	Surface Plasmon Resonance
TIRF	Total Internal Reflection Fluorescence
TMB	Tetramethylbenzidine
USB	Universal Serial Bus

Chapter 1

Introduction

This project aims to establish if a biosensor can be implemented as a diagnostic test for bovine Tuberculosis (bTB) in African buffaloes.

1.1 Background and Motivation

Bovine tuberculosis is a contagious disease caused by the pathogen *Mycobacterium bovis (M. bovis)* and affects a wide range of both wild and domestic animals as well as humans. Signs of infection vary by species and duration, leading to chronic disease and potentially death. The disease is a serious problem in developing countries and, due to its broad host range, has a negative effect on numerous commercial operations and food safety. According to Hassan *et al*, it affects "public health, international trade, tourism, animal mortality, and milk production" [1]. Therefore, this disease poses a huge socioeconomic risk.

Veterinarians, animal managers, and animal health agencies across the world aim to control the geographic spread and transmission of the disease, because if left uncontrolled, it poses a consequential zoonotic risk [2]. The understanding and controlling of the disease spread can assist in the limiting of disease expansion from animals to human hosts. Surveillance of the disease helps in the prediction of outbreaks so that biological disasters can be approached at their source [3]. Disease surveillance, along with quarantine, slaughter, and potentially vaccination, may lead to the eradication of the disease [3]. Hence, surveillance does not only enhance animal well-being and food security, but also benefits human health [3]. Therefore, it is important to detect infected animals as efficiently as possible.

Bovine tuberculosis is a chronic and progressive disease. This means that it is a long-lasting disease that continuously worsens over time. Since animals can carry this disease for a long time period before lesions develop, early detection of the disease is often done by detecting the Cell-Mediated Immune Response (CMIR) to the *M. bovis* pathogen, often using blood samples to perform tests. Examples of biomarkers of CMIR are IP-10 and IFN-γ which are produced when the host animals' blood is stimulated with antigens from the bacteria [2]. These antigens are biomarkers for bTB.

Current diagnostic methods implemented for the detection of bTB include detection of immune mediators (by ELISA), tuberculin skin tests, and mycobacterial culture [4]. However, these methods have drawbacks such as high costs, long time to produce results (in

the case of culture) and they require trained personnel. ELISA and culture tests also cannot be done in the field. This is an issue as wildlife, such as African buffaloes (*Syncerus caffer*) are often found in remote areas and samples must be transported to centralised laboratories for processing.

An engineering approach may aid in the solution of the problem. The implementation of a qualitative biosensor to detect proteins which serve as biomarkers for bTB is proposed. A functional biosensor that allows for accurate in-field biomarker detection will help in overcoming some of the logistical problems and therefore aid in controlling the transmission of the disease by detection of infected animals within a herd. This information will further aid in managing the spread of the disease and thereby mitigate the effects of the disease on human society as well as on the economy.

1.2 Objectives and Goals

- Investigate bTB to establish a basic understanding of the disease and its effects on society
- Review existing biosensor techniques in literature
- Determine an applicable sensor type using information obtained in literature
- Design a biosensor system for the detection of bTB based on the chosen transducer type
- Develop various parts of the biosensor system
- Evaluate the functionality of the various sub systems
- Construct a Prototype
- Evaluate functionality of the prototype
- Recommend improvements to the system

1.3 Thesis Overview

This chapter serves as an introduction to the project. Chapter 2 is a literature review that covers a brief overview of the disease bTB and existing diagnostic methods. It further gives an overview of basic biosensor terminology and continues to discuss several existing biosensor types, briefly touching on their basic working principles and finally discusses immobilisation methods. This is followed by a more detailed study on the selected sensor type, SPR, in Chapter 3. Chapter 4 briefly discusses the planned methodology to solve the problem, while Chapter 5 goes into more detail with regards to the implementation of the methodology, the design and manufacturing of the prototype, as well as testing. Recommendations for future projects are discussed in Chapter 6. The final chapter, Chapter 7, concludes this report. Any additional information can be found in the appendices.

Chapter 2

Literature Review

This chapter presents and analytically discusses findings in the literature. As mentioned in Chapter 1, bovine TB is a threat to both society and the economy. In order to approach a solution to the problem, a better understanding of various aspects needs to be acquired. The literature review establishes a basic understanding of bTB and discusses existing methods of disease detection. It moves on to a discussion of transducer types, touching on existing biosensors and the technology currently implemented. Finally, various immobilisation methods are described.

2.1 Bovine Tuberculosis

Bovine TB is caused by the bacterial pathogen *M. bovis*. Although buffalo and other bovine species are the maintenance host of the disease, the *M. bovis* pathogen can affect a variety of mammals including domestic animals, such as cattle, sheep and dogs [5]. Even humans can be affected by this disease. Although air is the primary disease vector and inhalation is the main cause of infection, *M. bovis* can spread through the ingestion of infected meat and unpasteurised milk. Granulomatous nodules, known as tubercles, are a pathological feature of the infection. These granulomas can be found in the lungs and other areas of the respiratory tract, as shown in Figure 2.1, which depicts the lung of an infected cow. *M. bovis* bacteria can propagate through the body via the lymphatic vessels and infect other organs as well. [6]

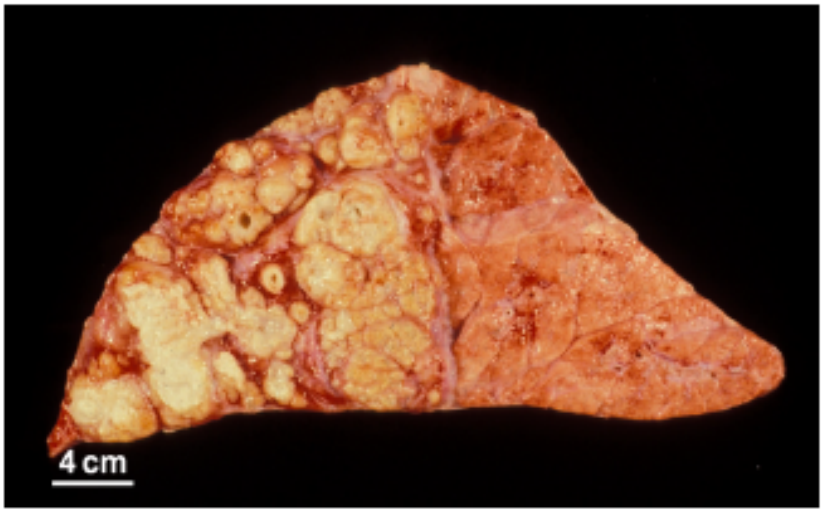

Figure 2.1: Lung of a cow with chronic tuberculosis (from [6])

The signs of the disease include coughing, weight loss and fever. In buffaloes, the infection can be detected by monitoring the production of the cytokines, interferon gamma (IFN-γ) and interferon gamma-induced protein (IP-10) [2]. Cytokines are proteins produced by the immune system to respond to infection. When the immune cells in blood from infected animals are stimulated with *M. bovis* antigens, these cytokines are produced.

2.1.1 Diagnostic Methods

Current methods implemented for the detection of bTB include tuberculin skin tests, Enzyme-Linked Immunosorbent Assays (ELISAs) and mycobacterial culture techniques [7].

Tuberculin skin tests require that wild animals, such as African buffaloes, are chemically immobilised to be handled in the field. Two areas on the animal's neck are shaved and injected with bovine Purified Protein Derivative (PPD) and avium PPD to stimulate an immune response in infected animals. The animals are then released and immobilised again 3 days later [7]. The skin thicknesses at the injection spots are then measured and compared to each other, where infected animals would have an increased skin swelling at the bovine PPD site. This method of testing is both time consuming and expensive. It requires highly trained personnel and is subjected to human error, making it sub-optimal [7].

A cytokine release assay, ELISA, involves the drawing of blood from selected animals. The blood is stimulated with mycobacterial peptide to induce a memory response. After incubation in the laboratory, the blood is centrifuged and the plasma is subjected to ELISA testing [7]. These tests are done in vitro. The QIAGEN cattletype IFN-γ assay is a sandwich ELISA, as is the bovine IP-10 in-house ELISA [7]. A sandwich assay consists of a primary, the capture, and a secondary, the detection, antibody. The antigen is 'sandwiched' between these two antibodies [8].

A detailed protocol for the Kingfisher bovine IP-10 in-house ELISA can be found in Appendix 1 [9]. Figure 2.2 is a visual representation of the IP-10 ELISA at a molecular

level. The testing is usually performed in 96-well plates. The black in figure 2.2 indicates the well wall. The green antibody is known as the capture antibody and is bound directly to the wall of the well [7]. The capture antibody acts as the binding site for the biomarker, in this case IP-10. A capture antibody is designed so that only one specific antigen binds to it, which provides specificity of the test [7]. In a further step, Bovine Serum Albumin (BSA) is then added (orange circles). The purpose of this agent is to ensure that no other materials bind to the areas that are not covered with the capture antibody i.e. to avoid non-specific absorption. This is known as blocking. A sample (plasma from incubated blood) is then introduced to the wells of the ELISA. The protein that is being detected, also known as the target protein, (depicted in red), which is found in the plasma sample, will then bind to the capture antibody. A detection protein (purple) is a biotin-conjugated antibody that, similar to the capture antibody, binds specifically to the target protein (biotin in blue). Between the various steps, the wells are thoroughly cleaned with wash buffers and the plates incubated over specified time periods with each step, as described in the protocol. Streptavidin-horseradish peroxidase (magenta) and tetramethylbenzidine (TMB) are added, respectively. The adding of tags to aid the detection is known as labelling. In this case, a colour change is induced when the TMB is added to the wells. Lastly, sulphuric acid is added to stop the enzymatic reaction from continuing. The wells, in which the sandwich ELISA was formed, are then placed into an ELISA plate reader and an optical density of the colour reaction is determined. The optical densities (OD) of the samples are determined at two different wavelengths. The values obtained are used to determine a final optical density by subtraction. A standard curve is used to calculate the concentration of the protein measured [7], [9]. The threshold for the identification of a positive bTB result is 66 pg·ml^{-1} for IFN-γ and 1500 pg·ml^{-1} for IP-10 [7].

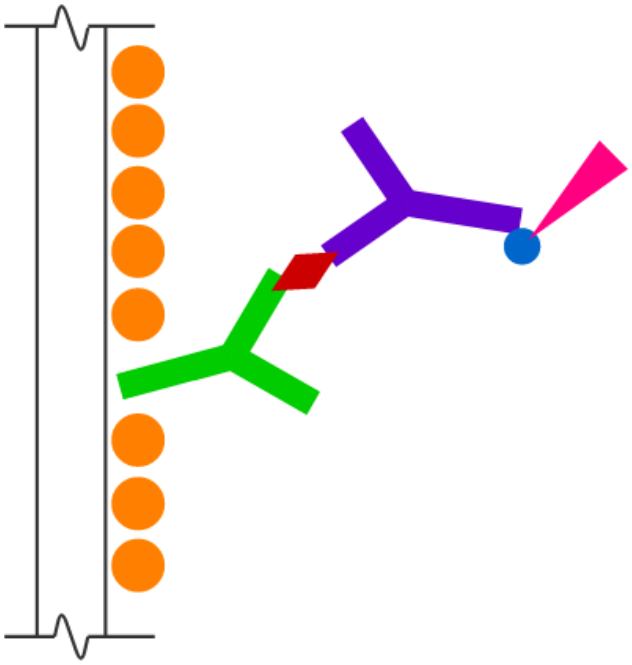

Figure 2.2: Schematic representation of a Sandwich ELISA

However, it is important to note that IP-10 and IFN-γ are not exclusively associated

with bTB and may be indicators of other diseases as well. To overcome this problem, current testing methods stimulate the samples with mycobacterial peptides to induce an antigen-specific memory immune response [7].

Another method that is used to detect the disease are mycobacterial culture tests. Culture tests can be done both ante-mortem as well as post-mortem. During the ante-mortem test, nasal swabs of the animals are taken. However, the majority of the animals sampled (roughly 80 %) have environmental non-pathogenic mycobacteria making it challenging to identify the *M. bovis* bacteria. For the post-mortem culture tests tissue samples of the deceased animal are cultured in a lab. If the bacteria grows, the infection with *M. bovis* is confirmed. Culture tests are often done in conjunction with skin tests and ELISAs to confirm results. [7]

2.2 Biosensors and Transducer Methods

A biosensor is a device that is used to analyse the presence of specific biological elements within a sample. For the creation of biosensors a number of components need to be looked at. Figure 2.3 shows an overview of these elements.

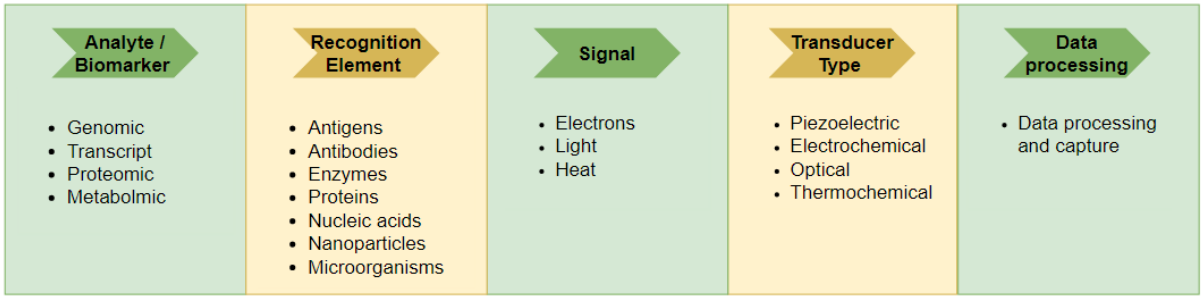

Figure 2.3: Critical elements of a biosensor

The first element of the biosensor that needs to be determined is the biomarker that the sensor aims to detect. The choice of the biomarker must be informed by the biological activities and properties of the disease that will be diagnosed [10]. Once the applicable biomarker has been determined the recognition element, as well as the immobilisation method, need to be considered. Immobilisation, in the context of this project, is the process of 'linking' the recognition element to the transducer. The interaction between the analyte and the recognition element results in a signal [10]. This signal can vary in nature and will need to be converted into a signal that can be processed and analysed. This is done by the most important component of the sensor, the transducer. Currently, a number of different transducing methods exist, as can be seen in Figure 2.4. This section aims to discuss and assess some of the viable methods, briefly discussing their operation principles and highlighting their advantages and disadvantages.

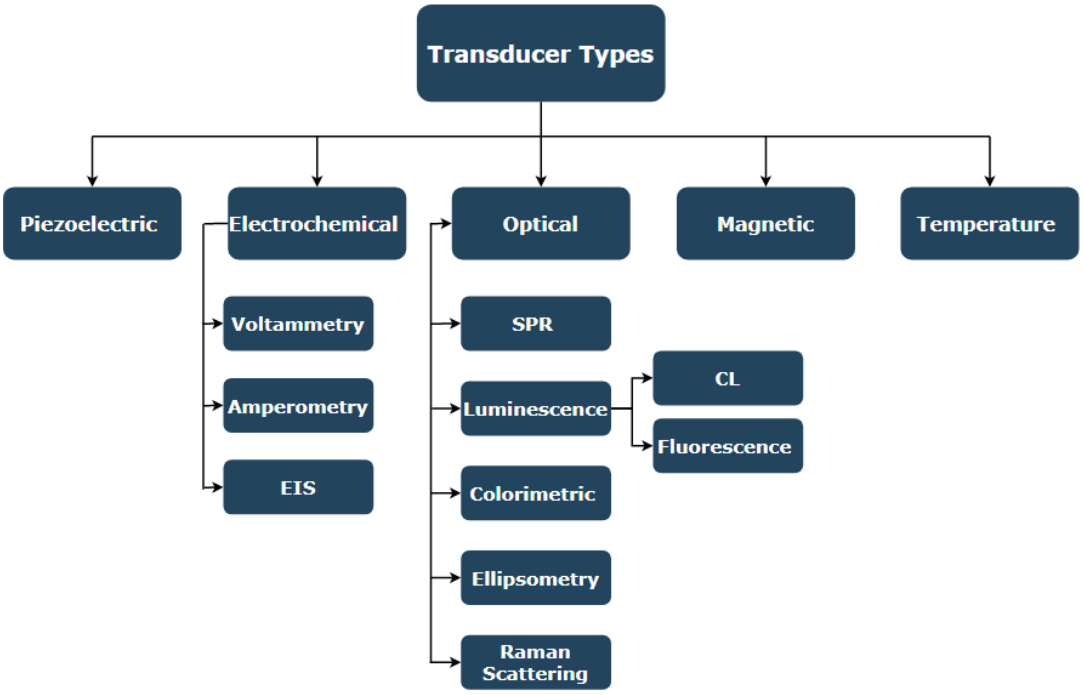

Figure 2.4: Summary of transducer types

2.2.1 Piezoelectric Biosensors

Piezoelectric biosensors use mass changes on the piezoelectric crystal, that result in a change in the resonance frequency, as the method of detection. The mass change is brought about by the chemical binding of the biomarker to the crystal. There are two types of piezoelectric sensor methods, namely Quartz Crystal Microbalance (QCM) and Surface Acoustic Wave (SAW) [11]. SAW crystals oscillate at higher frequencies than piezoelectric crystals [12]. Both these methods make use of a quartz disk with electrodes on it [13]. The crystal surface is covered with a thin layer of immobilised antigens [12]. Relevant antibodies are added, which bind to the antigen on the crystal surface. [12]. The antibodies have a higher affinity for the antigens in the sample, than for the antigens on the crystal surface. Therefore, when the sample is introduced to the crystal the antibodies, that were bound to the crystal surface now bind to the antigens in the sample, which leads to the displacement of the mass [12]. The mass on the crystal decreases, since the antibodies are no longer bound, and the measured frequency decreases [12].

A reference as well as an indicator crystal are used. Initially the ratio between the resonant frequency waves of the two crystals is determined when both are immersed in a blank solution [12]. The two crystals are then subjected to the sample one after the other. After the binding has taken place the new resonant frequencies are documented and a new ratio is established [12].

Advantages of QCM include label-free detection and low cost. In the past, QCM has been shown to be successful at detecting dioxins [14], bacteria [12], viruses [12] and various other markers.

2.2.2 Electrochemical Biosensors

Electrochemical transduction methods are one of the largest groups, they are commonly implemented in biosensors and have various methods of application. These transducers, like piezoelectric sensors, are based on the principle of the binding of the target biomarker (analyte) to the biological sensing element [10]. This binding causes an electrochemical reaction that produces electronic signals that can be measured by numerous methods, including voltammetry, amperometry, Electrochemical Impedance Spectroscopy (EIS), conductometry, potentiometry, resistivity and capacitance measurements [10], [15].

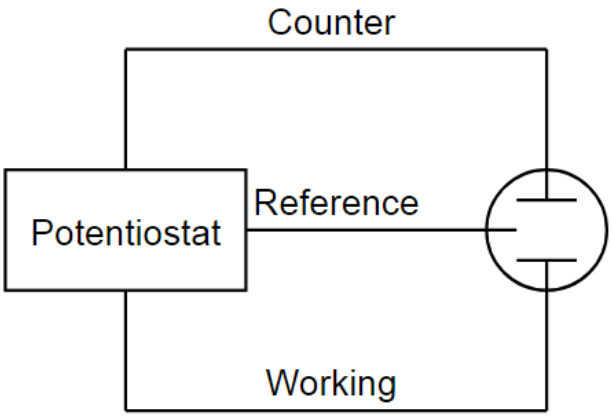

Figure 2.5: Schematic representation of an electrochemical sensor (from [16])

Electrochemical biosensors usually consist of 3 electrodes, namely, a working, a reference and a counter electrode, as shown in Figure 2.5. The biological sensing element is immobilised onto the working electrode. The electrodes are submerged into an electrolytic liquid [10]. The biological binding reaction or chemical reactions result in the transfer of ions or electrons, which in turn effect the electrical properties of the solution [15]. This setup can be modified so that more than one working electrode is integrated into the system, hence more than one biomarker can be detected at the same time, by the same sensor.

Due to their desirable mechanical, chemical and electrical properties, metals (such as silver, gold, platinum and stainless steel) and carbons (graphite and carbon fibers) are commonly used for the fabrication of the electrodes [17]. The chemically inert nature of these materials as well as their low residual currents make them well suited for these applications [17].

Advantages of electrochemical detection methods include their adaptability. A variation in the electrode shape, size and material used is possible. Additionally, there are a number of different measurement methods available. Another aspect that sets electrochemical transduction methods apart, is the potential for minimisation of the transducer components and the ability to sense more than one analyte at once.

2.2.2.1 Voltammetry

One of the methods used to analyse the signals from an electrochemical reactions is voltammetry. There are different types of voltammetry, the most common ones are linear, cyclic and square wave voltammetry [10]. In its simplest description voltammetry is the sampling of current at different voltages. The voltage is applied between the counter and working electrode, and specific voltage ranges are swept depending on the type of voltammetry. The results of these sweeps are plotted on voltammograms. Generally, the current is directly proportional to the concentration of the target [10].

Wang and team developed a label-free electrochemical sensor for the detection of telomerase activity [18]. The team made use of gassy carbon electrodes (working electrode), telomerase, capture DNA and gold nanorods to detect concentrations of Human cervix adenocarcinoma (HeLa) cells [18]. The telomerase activity was linked to the electrochemical signal. The team made use of Differential Pulse Voltammetry (DPV) to measure the electrochemical response signals to different concentrations of HeLa cells. The sensor achieved a good linear relationship for concentrations between 1×10^2 and 1.04×10^7 HeLa cells per ml and a limit of detection of 52.81 HeLa cells per ml [18].

2.2.2.2 Amperometry

The electron transfer or ion transfer brings about a change in the current of the system. Amperometry is the direct measurement of this current change, while the voltage at the working electrode is kept constant to the reference electrode [10]. The potential at the working electrode is forced to be the desired value and the current is then measured [10]. Once again, the current value is directly proportional to the concentration of the target. However, it is important to note that the current measurements in amperometry are substantially smaller than the readings obtained from voltammetry.

2.2.2.3 Electrochemical Impedance Spectroscopy

Electrochemical impedance spectroscopy consists of the measurement of both the resistive and capacitive properties of a system. To attain these measurements an alternating current in the form of a low amplitude sinusoid with a varying frequency is applied to the system. This is done to acquire an impedance spectrum. The resistance and capacitance can then be obtained from the in-phase and out-of-phase current responses [10].

Janssen *et al.* made use of Single Walled Carbon Nanotubes (SWCNT) coated discs integrated on a PCB electrode to detect BSA [19]. The anti-BSA was immobilised on the nanotube disc. The team used an Arduino Uno to determine the electrical resistance of the circuit. The change in the resistance was correlated to the concentration of the BSA. The team showed that when BSA is present, the current flowing through the biosensor is reduced and therefore the resistance is increased. The sensor's limit of detection was 2.89 $ng{\cdot}ml^{-1}$ [19].

2.2.2.4 Field Effect Transistors (FETs)

Immo-FETs or bio-FETs are electrochemical transducers that function on the principle of FETs. FETs are designed with a "channel" between the source and the drain [20]. This channel's conductivity can be altered by changing the surface charge density at the gate. This can be done by immobilising capture antibodies on the gate. The binding of

the antigen alters the charge density. The conductivity of the channel can be determined from the source-drain voltage-current characteristics [20].

Kim *et al.* describe a silicon-nanowire FET biosensor that was successful at the real-time detection of a sample with a concentration of approximately 330 pmol·l^{-1} of thrombin [21].

2.2.2.5 Interdigitated Electrodes

Electrochemical sensors can take the shape of interdigitated electrodes (IDE's) as shown in Figure 2.6, these electrodes act as working electrodes [10]. This setup increases the surface area for the binding of antibodies. The micro-sized electrodes have high manufacturing complexity and can be made by photolithography[22]. Singh *et al.* developed a 3D nanogap gold interdigitated electrode that was made with standard silicon photolithography and consists of 39 fingers [22]. The sensor was used for the label-free detection of the C-reactive protein (CRP), a cardiovascular disease risk indicator. The anti-CRP was done via a Self-Assembled Monolayer (SAM). The binding of the marker resulted in a change to the physical attributes of the metal, which was measured with EIS. The team found that the resistance parameter was the most sensitive to the CRP concentration levels. The sensor gave a linear response in the 0.1 ng·ml^{-1} to 1 µg·ml^{-1} range [22].

Figure 2.6: Typical layout of an IDE

2.2.3 Optical Biosensors

Like electrochemical sensors, optical transducers have a large variety of operating principles. Some of these methods are colorimetry, fluorescence, ellipsometry, interferometry, and surface plasmon resonance [23].These sensors offer advantages, such as direct, label-free and real-time detection. In this section, a few of the existing optical methods are discussed.

2.2.3.1 Surface Plasmon Resonance

One optical method often implemented in bio-sensing is known as Surface Plasmon Resonance (SPR). SPR can be observed on the surface of a thin metal that is between two dielectrics. When the metal is excited by light at the resonance angle, the energy of the light causes surface plasmons to propagate, transferring the light energy [24]. The energy conversion can be observed by analysing the reflected light. The energy lost by the light reflects as a dark band in the reflected spectrum. When antibody binding at the surface of the metal takes place, there is a shift in the position of the dark band. Figure 2.7 shows SPR in the Kretschmann configuration. Advantages of SPR are label-free and real-time detection [25].

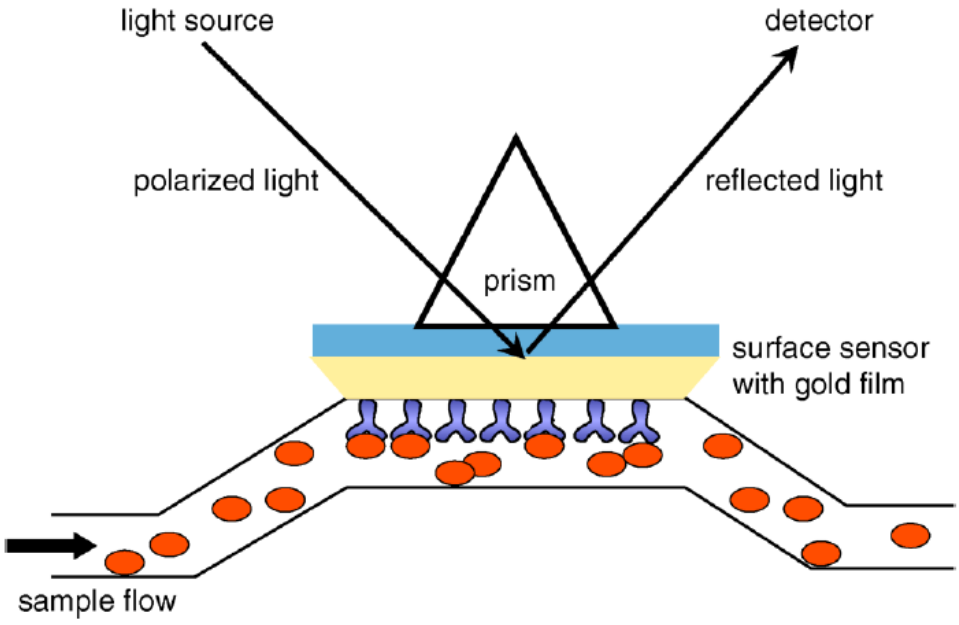

Figure 2.7: The working principle of SPR (from **B**)

Localised Surface Plasmon Resonance(LSPR) is a form of SPR in which nanostructures are implemented instead of a solid substrate. The diameter of the nanostructure is less than the wavelength of the light that is used to excite the system [26]. Ertürk and team was able to detect Prostate Specific Antigen (PSA, a cancer biomarker) in the concentration range of 0.1 – 50 $ng{\cdot}ml^{-1}$. The team used microcontact imprinting to imprint the PSA onto the sensor chip surface [27].

2.2.3.2 Chemiluminescence

Chemiluminescence (CL) is an optical effect that may result from chemical reactions. Qu *et al.* showed, that by using Horseradish Peroxidase (HRP) labelled detection antibodies in combination with a luminescence substrate solution, a chemiluminescent effect was created [28]. Chemiluminescent effects generate optical signals which can be measured with luminometers. The aim of the sensor was to determine the amount of carcinoembryonic antigens (CEA), a lung cancer marker. The team used streptavidin coated magnetic beads to capture anti-CEA. The sample with the biomarker was then introduced and finally, HRP labelled anti-CEA was allowed to bind. This resulted in a sandwich scheme assay.

A chemiluminescent substrate solution was added. The mixture was analysed with a home-made luminometer. The signals formed by these devices were directly proportional to the concentration of the biomarker within the sample. The team was able to detect concentrations of CEA as low as 5.0 pg·ml^{-1} [28].

2.2.3.3 Fluorescence

Another form of luminescence is known as fluorescence. Fluorescence is when a molecule is excited with a light source, and then emits light of a different wavelength (usually a longer wavelength) back [29]. These molecules are called fluorophores. Fluorescent biosensors usually require the labelling of the biomarker with a fluorophore. This can be done using fluorescently tagged antibodies [30]. Autofluorescence is a phenomenon observed in some molecules and in these cases fluorophores are not required. The bound fluorescent tags are proportional to the amount of biomarker present. The fluorescent signals are then analysed by confocal or Total Internal Reflection Fluorescence (TIRF) microscopy [30]. Laser Induced Fluorescence (LIF) is often implemented, where a laser is used to excite the fluorophores. Yao and Wolfe paired a LIF sensor with an ellipsoidal reflector, which increased the signal significantly. The team was able to achieve a detection limit of a 5 nmol concentration of fluorescent dye in a 2.4 µl sample volume [29].

Another commonly applied method of fluorescence is Fluorescent Resonance Energy Transfer (FRET). Fluorescent Lifetime Imaging Microscopy (FLIM) is implemented to measure FRET [31]. To analyse the interaction between two proteins, FRET requires two fluorescent tags, namely a donor and an acceptor. The emission wavelength of the donor must overlap with the excitation wavelength of the acceptor [32]. One protein is tagged with the donor and the other with the acceptor. When the two proteins bind or come into close proximity of one another, intra-molecular FRET takes place [32]. The sample is excited with a light source that emits the excitation wavelength of the donor. The emission light wave of the donor then, in turn, excites the acceptor. A FLIM is then used to analyse all the light signals. The intensities of the donor and acceptor waves is measured. FRET is an intricate process that relies on a vast number of variables, such as the distance between, orientation of and the fluorescent lifetime of the fluorophores [32].

2.2.3.4 Colorimetric

There are various different types of colorimetric biosensors [33]. Many of these sensors involve the use of dye or labelling with nanoparticles. These colour changes are then detected by the human eye or intensity based optical detectors [33].

The most well-known colorimetric biosensor is likely the pregnancy test. Pregnancy tests are often colorimetric Lateral Flow Assays (LFA). The sensor brings about a visible change that can be analysed with the bare eye. Pregnancy tests aim to determine the presence of the hormone human Chorionic Gonadotropin (hCG) in a urine sample [34]. LFAs are often paper-based sensors that move the sample though the sensor sections via mechanisms such as capillary action [34]. A schematic representation of an LFA can be seen in Figure 2.8. The flow assay consists of three sections, namely a reaction, detection and control section. The sample is deposited onto the sample pad, then flows through to the reaction pad. In this section the dye tagged antibodies specific to the target analyte bind to the target [35]. This section also contains the dye marked control molecules. The sample then moves to the detection section, often referred to as the test line/zone [35]. Target specific antibodies

are immobilised on the test line, where the target and the dye labelled antibody bind, forming a sandwich [34]. If binding takes place, a visible line will appear. The sample moves further through to the control section. This section works in the same way as the test section, the dye marked molecules bind to the control line capture antibodies, creating a visible line [35]. The function of this section is to verify that the sample moved through the various sections of the sensor. LFA can be used for qualitative as well as quantitative detection. The more intense the colour signal, the more binding took place. LFAs require 5-30 min to complete and can be implemented with various sample types including urine, plasma and whole blood. Advantages of these types of sensors are that they are cheap to produce and do not require trained personnel [34].

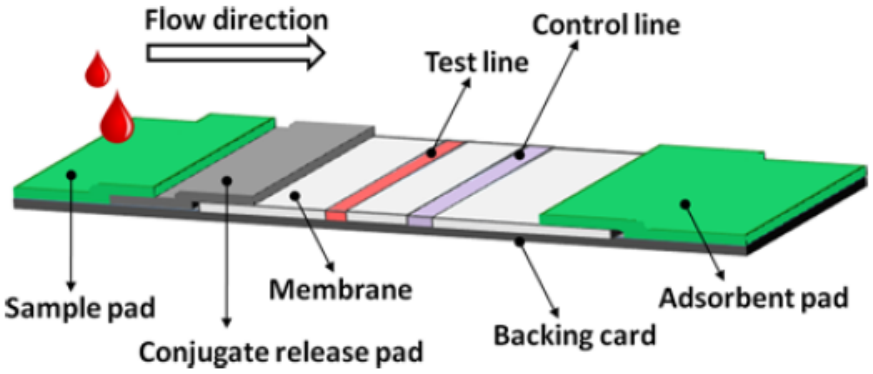

Figure 2.8: The working principle of a lateral flow cell (from [34])

However, colorimetric sensors are not limited of LFAs.

2.2.3.5 Ellipsometry

Ellipsometry is based on the changes in the phase and amplitude of polarised light when it reflects off a surface [36]. The changes in the aforementioned parameters can be used to determine the thickness of deposits on the surface of reflection. If, for example, a thin protein layer were to be deposited on the reflection surface, a change in the phase and amplitude can be noted [36]. In 1999, Van Noort and Mandenius showed that when a porous gold surface is used as opposed to a planar one, the ellipsometric response is significantly greater [36]. The porous gold layer was deposited by electrochemical deposition in a solution of tetrachloroaurate and lead acetate [36]. The basic setup of ellipsometry sensors is depicted in Figure 2.9. In 2010, Jin *et al.* discussed a biosensor based on the imaging ellipsometry [37]. The setup described consists of a Xenon lamp, three lenses, optical fibre, a polariser, a compensator, an analyser, an alignment telescope, and a Charge-Coupled Device (CCD) camera. The team further discussed the various biomedical applications in which the ellipsometry biosensor showed promising results. Their sensor was able to detect CD146 with the majority of the results from the sensor being in agreement with the ELISAs [37]. Ellipsometry based biosensors have been used to detect numerous other markers, toxins and viruses . In 2013 Stehle and team reported on the development of a multi-pass spectroscopic ellipsometry setup. In this setup the light beam reflects on the sample multiple times [38].

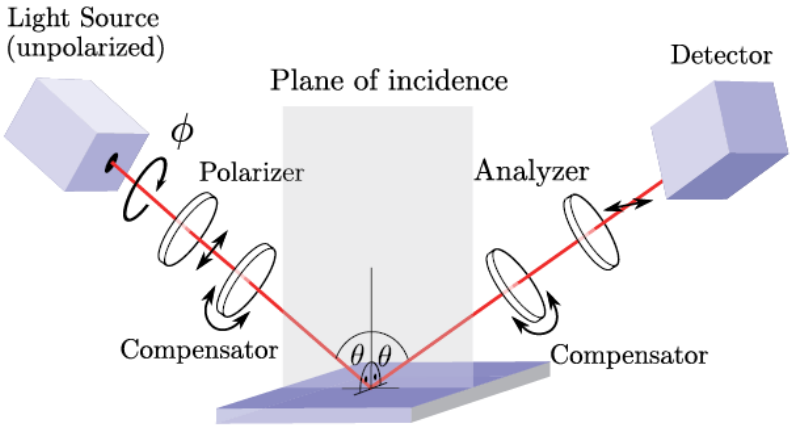

Figure 2.9: Schematic representation of ellipsometry (from [39])

2.2.3.6 Interferometers

Interferometers are analytical devices that combine various light sources to form interference patterns that are then analysed. Interferometers have various configurations. One of these configurations is the Mach-Zehnder Interferometer (MZI) configuration, depicted in Figure 2.10 (a). The Mach-Zehnder configuration requires a single frequency, single polarization laser. The light from the laser enters the device, where it is split equally into the reference arm and the sensing arm. The light of the sensing arm is allowed to interact with the sample via a window [40]. The reference arm is left untouched. At the end of the sensor the two arms, i.e., light beams, recombine, which results in interference. A photodetector is used to measure the intensity of the light at the output of the device [40]. In their paper, Hsu and Huang incorporated dual Anti-Resonant Reflecting Optical Waveguides (ARROWs) into the MZI setup [41]. ARROWs can accomplish low-loss single-mode propagation. Young's interferometer works similarly to MZI except that the light in the reference and sensing arms do not recombine, but instead form interference patterns on a detector [40]. Young's interferometer can be seen in Figure 2.10 (b). The Hartman interferometer is based on the same principle as the MZI and Young's interferometer. However, this setup is more intricate and involves optical gratings and integrated optics [40].

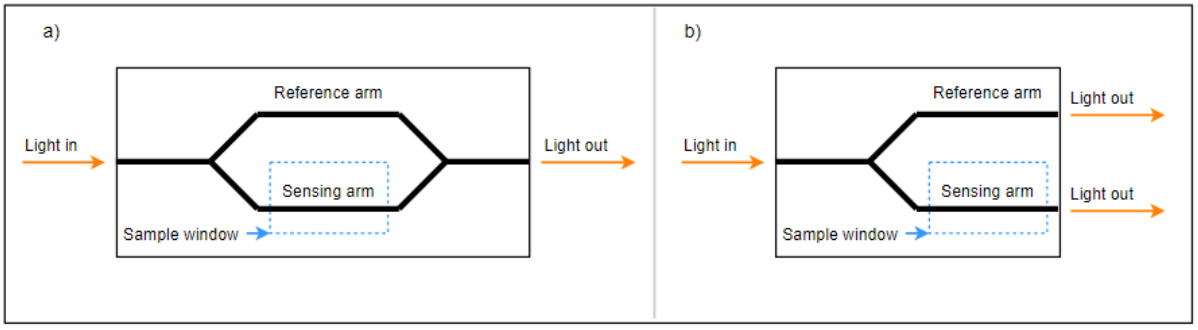

Figure 2.10: Schematic representation of (a) Mach-Zehnder Interferometer and (b) Young's interferometer

2.2.3.7 Raman Scattering

When incident light photons interact with a material, the vast majority of the photons experience Rayleigh/elastic scattering, and the minority experience Raman/inelastic [42]. The photons of the monochromatic light source interact with the sample, during this process the photons either transfer or gain energy from the molecules in the sample [43]. If the frequency of the scattered photon is less than the incident photon then the electrons absorb energy (stokes) or if the frequency of the scattered photon is more then the electrons emit energy [42]. This change in vibrational frequency can be used to analyse samples. Raman signals are smaller than the emission signals, hence enhancement of the Raman scattering is required. Surface Enhanced Raman Scattering (SERS) is one method to do this [43]. Raman spectroscopy gives information about the vibrational energy levels of molecules that are excited with the light. The vibrational energy of a sample is dependent on its chemical composition [43], hence the vibrational energy 'fingerprint' of a sample can indicate if binding took place. The setup of these sensors usually includes a laser, a diffraction grating and a CCD detector. SERS is most often implemented in the study of live cells [43].

2.2.4 Magnetic Sensors

Magnetic sensors work by introducing magnetic nanobeads into the system and exposing the sample to a magnetic field. There are various magnetic sensing techniques available, namely Anisotropic Magnetoresistance (AMR) rings, planar Hall effect sensors, giant magnetoresistance, spin valves, nuclear magnetic resonance, and magnetic tunnel junctions [44]. However, magnetic beads and nanoparticles can also be implemented in other transducer types, such as electrochemical, optical, and piezoelectric to increase the magnitude of measured signals. The magnets can be used as labels or to assist in sample separation and flow assays. Magnetic labels are stable over time and the beads can be made fluorescent by using quantum dots or dyes. Additionally, the magnetic beads are widely available [45]. In this section the Giant magnetoresistive method is briefly discussed.

2.2.4.1 Giant Magnetoresistive Sensor

When a small magnetic field is applied to these sensors the particles obtain a magnetic moment, which can induce a change in the resistance [44]. Giant Magnetoresistive Sensor (GMR) devices are constructed with alternating multiple ferromagnetic and non-magnetic layers. In the absence of an external magnetic field the device's state is known as a high resistance state. When an external magnetic field is applied, the behaviour of the electron spins is altered and the state is then known as a low resistance state [46]. A higher number of Magnetic Nanoparticles (MNPs) bound to GMR sensors, leads to a larger detection signal [47].

2.2.5 Thermochemical Transistors

Thermochemical transistors are based on the heat generated or absorbed during a binding reaction [48]. In a biochemical reaction the change in temperature is based on the enthalpy changes [48]. A thermistor is a thermal resistor that can be implemented to measure small changes in temperature. A change in temperature results in a change in resistance [48]. The resistor is usually connected to a Wheatstone bridge [48]. Numerous studies have

successfully implemented a thermochemical resistor for the monitoring of enzyme activity [48]. Thermometric sensing has been shown to successfully measure glucose.

2.2.6 Existing biosensors for the detection of bTB

Currently there are not many point-of-care (POC) devices for the detection of bTB. However, Studies on various LFA have been done in the past to determine the aptness of these tests as point-of-care devices in diagnostics for bTB.

ALERE Determine LAM TB urine antigen test is a lateral flow assay that has been designed for human TB diagnosis [49]. The test is a qualitative method that detects lipoarabinomannan (LAM) antigen of Mycobacteria in urine samples [50]. The test typically takes 25 min [49]. LIONEX is also a lateral flow test analysis blood, serum, or plasma to detect M. Tuberculosis complex antigens [51].

Kelley *et al.* set out to determine if these two LFA devices could potentially assist in the infield detection of bTB, using urine and milk samples from cattle in the USA [51]. The team found that the results from the ALERE determine LAM TB urine antigen test and United States Department of Agriculture USDA standard diagnostic tests yielded poor agreement. The team further tested LIONEX Animal TB Rapid Blood Test using milk samples and positive trends were seen [51].

Zewude *et al.* tested 175 Ethiopian cattle, each animal was tested with single intradermal comparative tuberculin test (skin test), IFN-γ, TB LAM Ag test and LIONEX Animal TB rapid test [50]. These results were then compared to each other. The team found a high similarity between the single intradermal comparative tuberculin test and the TB LAM Ag test. The similarity between the IFN-γ and TB LAM Ag test was substantial. The sensitivity of the TB LAM test was 72% and specificity was 98.8%. The results of the LIONEX compared to the skin test was substantial. The sensitivity was 54% and the specificity was 98.8%. The team concluded that the TB LAM test performed better in the detection of btb than the LIONEX test, and that it could maybe be employed as an auxiliary test in the diagnosis of bTB [50].

Bermàdez *et al.* used a commercially available multi-antigen lateral flow assay and PCR for detection of antibodies to Mycobacterium bovis in dairy cattle [52]. These results were compared to culture tests results and it was found that the false negative rate for the PCR was 34.6% and 54.2% for the LFA. Since these false positive rates were so high the team concluded that the LFA cannot be a useful test for detecting btb, even in combination with PCR [52].

A qualitative Nitrocellulose membrane flow assay with a control strip was developed. The test strip is based on MPB83, which is an m. Bovis antigen [53]. Fresco-Taboada *et al.* tested the LFA and the results were compared to 3 different ELISA tests results. The LFA showed substantial similarity to the ELISA results and the team concluded that the LFA is a suitable first assay for the diagnosis of btb in adult wild boars[53].

Dual Path Platform (DPP) is a rapid test that measure antibody binding in various species [54]. The device has two nitrocellulose test strips, which are connected in a T-shape inside the device, which allows independent delivery of the test sample and the antibody-detecting reagent (protein A/G hybrid conjugated to colloidal gold particles)

[55]. Test line 1 (antigen MBP83) and/ or test line 2 (antigen CFP-10/ESAT-6) [56], [54]. The results are determined using an optical reader and reported in relative light units (RLU) [56]. The manufacturer's recommended visual cut-off value (RLU = 5) was considered test positive [55]. The device further has a control line to validate the results [56]. Results are typically obtained within 15 [54] to 20 [55] min.

Boadella textitet al. did ELISA and DPP tests on Eurasian wild boar. The DPP had a sensitivity of 89.6% and a specificity of 90.4% [55]. Further, Lyashchenko *et al.* did ELISA and DPP tests on deer. The DPP tests resulted in an estimated test sensitivity of 65.1% and a specificity of 97.8% [54].

Table 2.1 shows a summary of diagnostic methods for the detection of bTB.

Table 2.1: Summary of the current detection methods used for bTB

Method		**Biorecognition agents**	**Biomarker**	**Sample type**	**bTB/ TB**	**Test time**	**In the field**
Skin test		N/A	N/A	N/A	bTB	3 days	Yes
ELISA		Anti-IP-10/ Anti-IFN-γ	IP-10/ IFN-γ	Plasma	bTB	2 days	No
Culture test		N/A	N/A	Mucus/ sediment	bTB	6-8 weeks	No
LFA	LAM	Unknown	Lipoarabinomannan	Urine	TB	20 min	Yes
	LIONEX	Recombinant antigens	Antibodies against active tuberculosis	Serum/ plasma	bTB	20 min	Yes
DPP	T1	Antigen MBP83	Antibody	Serum	bTB	20 min	Yes
	T2	Antigen CFP-10/ ESAT-6					

2.2.7 Transducer Discussion

There is a large variety of transducer types available and even more working principles. All the transducers have their own advantages and disadvantages. In order to decide which transducer type to implement for a in-field bTB sensor, criteria needs to be established.

The in-field biosensor needs to be robust and able to run on low power supply, such as a battery or 12V car port. The mechanical, electronic and manufacturing complexity should be kept as simple as possible. The sensitivity needs to be high and the test time short, ideally less than 20 min. The sample type will be blood or plasma and the sample size needs to be as small as possible. Ideally the process would not require the labelling, as this requires an extra step and affects the test duration. The sensor should be able to determine the concentration of the biomarker within the sample, this means a quantitative measurement is required. The device should be easy to use and the results need to clear and easy to interpret.

Many of the aforementioned transducer types, such as piezoelectric, electrochemical and optical are able to function using various sample types such as urine, serum, plasma and saliva. Many of these methods are also able quantitative and not just qualitative measurements. Furthermore, piezoelectric, electrochemical and SPR transducer types do not require labelling hence, less steps during immobilisation are required.

Electrochemical and piezoelectric sensors often require complex and expensive electronic support equipment, such as potentiostats and impedance analysers. Often, when using electrochemical and piezoelectric sensors, the sample requires an incubation period before measurements can be taken this affects the duration of the tests.

Temperature sensors are potentially sensitive to environmental temperature changes, making them problematic for in-field use. Magnetic based sensors require an additional labelling step.

SPR has the advantage of real-time monitoring and the analysis of the kinetic interactions of the biomolecules. This leads to a deeper understanding of the reactions taking place, which may in turn help with the identification of the sample. Another advantage of SPR is that the chips are re-usable, this lowers production cost and reduces waste. It also has the potential to use blood samples directly without purification processes being required [57].

Therefore an SPR sensor for the detection of bTB is proposed.

2.3 Immobilisation

It can be seen from the previous section that most transducers rely on the process of the biomarker binding to a material (crystal, electrodes, gold, etc.) and in this way change and/or affect the properties of the material, bringing about a quantifiable signal. This is done by immobilising biorecognition elements to the sensor surface. These recognition elements can be enzymes, antibodies, proteins, nucleic acids or cells [25]. In the case of cytokines such as INF-γ and IP-10, this can be done using antibodies as in the ELISAs. This binding is usually done with the help of capture antibodies. Capture antibodies are usually made by goats, rabbits and other suitable animals or synthesised in labs, and fit uniquely to their biomarker counter parts. Immobilisation is the process of 'linking' the capture antibody to a solid material, which will be the transducer medium. This solid material is often referred to as the substrate. In order to aid the immobilisation process the substrate often undergoes some form of surface modification, either to ensure that capture antibody binding takes place or to increase the surface area to allow for more antibodies to immobilise. An example of such a substrate surface modification method is oxidative electrografting [58]. The following section will discuss some of the immobilisation methods as well as the surface modification for these methods.

2.3.1 Antibodies

To better understand the mechanism of immobilisation, a basic understanding of antibodies, their structure and composition is required. An immunoglobulin G (IgG) antibody consists of four chains that are bound to each other by disulphide bonds. Two of these chains are known as light chains and the other two are heavy chains [59]. The active

binding site of the antibody is the part that binds to its complementary antigen. The active binding site is found at the top of the Y-shaped protein [60]. Figure 2.11, shows the basic structure of an IgG protein, which is the most abundant form of antibodies. Figure 2.11 further indicates the Fab (numbered 1) and Fc (numbered 2) regions of the antibodies, which will be referred to in later parts of this chapter. When referring to orientated immobilisation, it is meant that the antibodies are bound in such a way that the antigen binding site is facing upwards and open towards where the sample will be and the bottom of the Fc region is connected to the substrate or linker [61].

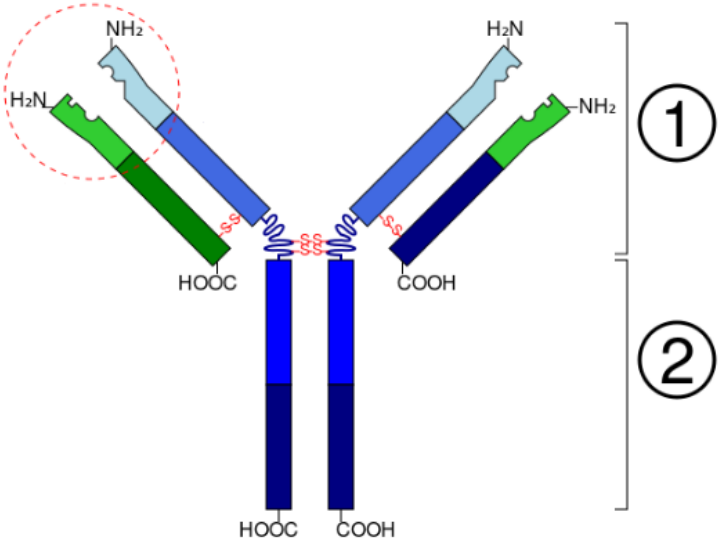

Figure 2.11: Schematic representation of the immunoglobulin G (adapted from [60])

2.3.2 Methods of Immobilisation

There exist two main types of immobilisation methods: covalent and non-covalent [62]. Covalent coupling is the formation of a permanent (irreversible) chemical bond. Non-covalent coupling is often referred to as capture coupling or reversible immobilisation [63]. Reversible immobilisation simply means that the biomolecule, in this case the capture antibody, can be detached from the substrate without destroying it and thus maintains its biological activity [62]. This section will continue to discuss these methods in more detail.

2.3.2.1 Reversible Immobilisation

One of the simplest forms of reversible immobilisation is known as physical adsorption and results in the random orientation of the antibodies on the substrate. Physical adsorption requires no antibody alteration or surface modification. However, this method requires large amounts of the capturing antibody and is pH sensitive [63]. The bond is usually formed by ionic bonds, electrostatic hydrogen bonds, van der Waal's forces or hydrophobic interactions [62]. However, it is important to note that these forces are weak [62].

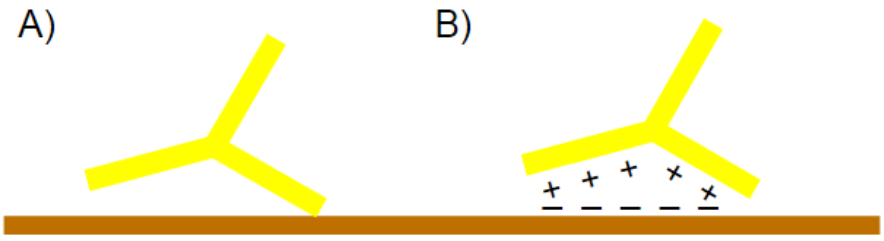

Figure 2.12: a) hydrophobic interaction and b) ionic interaction

Bioaffinity, disulphide bonds and metal linking immobilisation methods are also types of reversible immobilisation [62]. Bioaffinity-based immobilisation is commonly achieved with the biotin-avidin reaction or by protein mediation [61]. Proteins A or G are often implemented. Bioaffinity binding between streptavidin and biotin has been widely used and results in a stable surface. Advantages of bioaffinity antibody capturing is that the biotinylated antibodies bind to the streptavidin in an orientated manner; the biotinylated capture antibody is bound specifically to the streptavidin. The biotin-avidin bond is one of the strongest non-covalent biocompatible bonds [64]. The disadvantage of this method is that it requires an additional step of immobilisation and/or labelling [63].

Metal linking based on metallic bonds is also a form of non-covalent linking. Entrapment is a method of immobilisation implemented for enzymes, for which various types exist. However, these methods will not be discussed in more detail as they do not involve antibodies.

2.3.2.2 Irreversible Immobilisation

The most commonly applied method is covalent immobilisation. Covalent immobilisation results in stable irreversible bonds [62]. A covalent bond forms when two atoms share electrons. These types of binding methods result in high surface coverage [61]. There are various chemical reactive functional groups that can be utilised for covalent immobilisation, such as thiol, carboxyl and amine groups. Often, many of these mentioned functional groups can be found on the surface of antibodies.

Covalent immobilisation via the amine groups results in random orientation [65], as the amines on the antibody are found in various places and not just at the Fc region of the antibody. Amine groups are usually linked with the addition of N-hydroxysuccinimide (NHS) esters, sulfonyl chlorides, isocyanates and isothiocyanates [66]. Carboxyl groups are found on the Fc region on the bottom of the antibody, and immobilisation using this group leads to better orientation, as opposed to amine groups, as the binding site is facing towards the sample.

Disulphide bonds are covalent and often found between thiol groups (disulphide bonds can be broken). Thiol groups are found in the cysteine residues, which may be found on the antibody. However, cysteine residues are less abundant than lysines, which contain the amine groups [61]. Thiol forms a strong bond with gold through chemisorption [67].

As described earlier, covalent bonding is the sharing of electrons. Dative binding is the bond that takes place when one atom supplies both of the shared electrons. This bond usually forms between a metal and the sulfhydryl (Thiol) groups on the antibody [68]. Further antibodies can be thiolated with the addition of 2-Iminothiolane hydrochloride [69]. Immobilisation via the thiol group results in better orientation of the antibody as opposed to the immobilisation via amine groups [61]. However, this method may lead to the partial loss of antibody activity [61].

The molecules that are used to combine (link) two or more functional groups are known as cross-linkers. Cross-linkers have at least two reactive points that can chemically attach to the previously mentioned functional groups found on the antibodies [70]. It is important to note that cross-linking involves either covalent or ionic binding. Cross-linkers have many functions ranging from surface modifications to labelling [62]. N-Hydroxysuccinimide (NHS) is an example of a cross-linker, along with (3-Aminopropyl)triethoxysilane, 1-Ethyl-3-(3-dimethylaminopropyl)carbodiimide and others. The ThermoFisher Scientific website has a cross-linker selection tool that allows the user to enter the functional groups to be linked, and then recommends a cross-linker [71].

Another commonly implemented method of immobilisation is the use of Self-Assembled Monolayers (SAMs). Some SAMs are based on the thiol-gold bond that was described earlier. SAMs require a metal substrate, and alkanethiol solutions are deposited on the substrate [72]. The alkanethiol forms an extra layer between the substrate and the linker to the antibody. The thiol end of the alkanethiol binds to the metal (usually gold) and the other end of the molecule can be one of various functional groups, depending on the chosen alkanethiol, which then can be linked to the antibody via cross-linkers as previously mentioned. In this way SAMs provide a layer that accommodates many immobilisation methods, such as physical interactions as well as chemical binding [73]. SAMs can prevent direct contact between the substrate and the antibody, and this reduces non-specific adsorption [72].

Further studies have been done on dendrimers. Dendrimers are 3- dimensional branched macromolecules, which consist of 3 layers [74]. Figure 2.13 shows the structure of a dendrimer. The innermost layer is referred to as the central core. The middle layer is the dendritic structure (branches) and the exterior layer consists of functional groups. The functional groups are then covalently bound to the antibodies, as described previously [75]. Dendrimers can be synthesised out of Poly(amidoamine) and are grown one generation at a time. A generation refers to the number of branch layers the dendrimers have. Dendrimers have many advantages including high density surface coverage and a versatile design and modifications of the functional groups [74]. Furthermore, they increase the surface area for binding to take place. However, dendrimers are expensive and add an extra step to the immobilisation process.

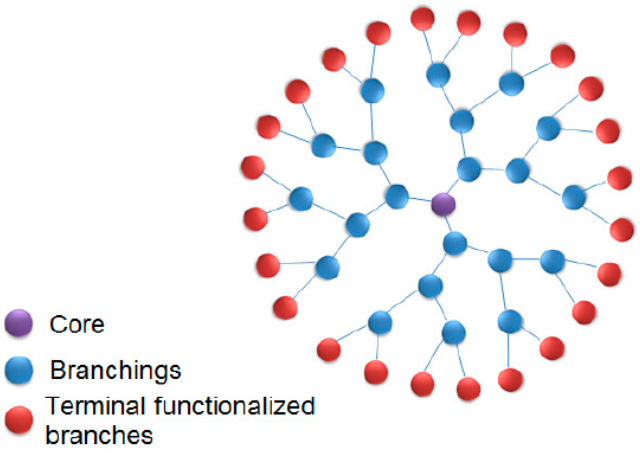

Figure 2.13: Schematic representation of a dendrimer (from [76])

When immobilising antibodies, there are a number of points one needs to keep in consideration. It is important to ensure operational stability of proteins and their ability to maintain biological activity. This can be done by confirming that immobilisation takes place in a non-denaturing environment [77]. Factors that affect the denaturing of antibodies are high temperatures, as well as incorrect pH values in the buffer solution. Also, the immobilisation of the antibody in its native form is beneficial, as it is most stable in this form. If antibodies are bound directly to the substrate, they lose some of their mobility, and this can affect the binding interaction between the antibody and antigen. This problem can be solved by implementing a long flexible linker, such as poly(ethylene glycol) (PEG) [65].

In addition, consideration needs to be given to the incubation periods; special attention needs to be given to the time, as well as the required temperatures. Further, attention needs to be given to the concentration of capture antibodies being immobilised in order to achieve a high surface coverage without resulting in antibody overlapping [61]. After immobilisation it is beneficial to block the remaining active sites on the substrate, to ensure that no non-specific binding takes place; this can be done with bovine serum albumin (BSA) [65]. Cleaning steps should also be implemented to ensure that the binding sites on the antibody are open, and this can be done with Tween 20 [73].

Methods implemented to improve surface coverage during immobilisation include antibody modification. Often, antibodies are broken up into smaller pieces by processes known as antibody fragmentation. Cleaving is the process of splitting the antibody into two pieces, by breaking the disulphide bridges between the two heavy chains. This can be done by enzymatic digestion and chemical reduction [65]. The fragments can be immobilised using thiol-specific cross-linkers. This method may result in better surface coverage of the antibody on the substrate, as well as better orientation [65]. However, during this process the protein may become unstable, and therefore its behaviour could become unpredictable.

Another aspect that needs to be considered during the immobilisation process is the verification of the steps in the process. Since the molecules in this process are all at a nanoscale, it is impossible to tell if the processes take place as expected without making

use of verification methods. One of the most common verification methods is the use of fluorescent markers that bind to the primary antibody and can then be seen under a confocal microscope or a wide field microscope. Other verification methods include Atomic Force Microscope (AFM) analysis and scanning electron microscope (SEM) [27], as well as X-ray photoelectron spectroscopy (XPS) analysis [78]. It is also necessary to determine the reproducibility of the immobilisation method, because the more antibodies bind, the more antigens can bind and, therefore, the higher the sensor's signal. Inconsistent immobilisation will lead to incorrect signal interpretation.

2.4 Conclusion

In this literature study bTB and biosensors were investigated. The aim was to give context to the choices made in the design and implementation of the chosen biosensor.

The first section of the review described the threat of bTB to African wildlife, as well as the course of the disease. From this section, it was concluded that the biomarkers for this project will be IP-10 and IFN-γ in buffalo plasma. These antibodies bodies are readily available in ELISA kits, which are the standard test for IP-10 and IFN-γ. The threshold to detect will be 66 pg·ml^{-1} for IFN-γ and 1500 pg·ml^{-1} for IP-10.

This chapter considered various transduction techniques, briefly described their working principles and reviewed their advantages. After this initial look at existing transducer types, it was decided to focus on Surface Plasmon Resonance (SPR). As previously mentioned, the advantages of SPR include real-time and label-free detection. Additionally past research has shown promising results.

There is potential in the development of a cheap robust sensor that can be easily used in the field. Optical transducers of the SPR type have not been studied in the Sensor Application and Nano Devices (SAND) research group. However, they are considered to be a promising option and investigation of this may result in a successful introduction of them to the group.

Another aspect to consider when selecting the biosensor components is manufacturability; the device needs to be designed, built and tested in the laboratories available on Stellenbosch campus. Close attention should thus be paid to the required manufacturing processes. Another aspect that needs to be considered is the availability of materials and how safe it is to work with them. It further seems possible that a functional SPR sensor can be manufactured at Stellenbosch University.

In summary, the device that will be designed aims to be a qualitative affinity biosensor based on the SPR sensing technique. The antibodies will be immobilised by means of SAMs, since these are commonly implanted in SPR sensors. This is because they have short chains, strong bonds and little non-specific binding occurs. The following chapter is a more detailed review of these chosen methods.

Chapter 3

Surface Plasmon Resonance

As previously mentioned, SPR technology has the advantages of label-free and real-time detection. It further only requires relatively small sample sizes. This chapter is a detailed literature study on SPR theory and sensor setup. Additionally, existing devices are considered. Self-Assembled Monolayers are discussed as a possible immobilisation method. It will further discuss how the data acquired from the sensor is interpreted.

3.1 Surface Plasmon Resonance Phenomenon

In the early 1900s Wood first described Surface Plasmon Resonance. In his paper *On a Remarkable Case of Uneven Distribution of Light in a Diffraction Grating Spectrum*, published in 1902, he describes the phenomenon as: "If the spectra of an incandescent lamp are viewed directly in the grating without any other optical appliance, at certain angles of incidence perfectly sharp monochromatic images of the filament appear in different parts of the first order spectra. Sometimes these images are nearly black, and sometimes they are far brighter than the rest of the spectrum." [79]

Today, the Surface Plasmon Resonance phenomenon is often described as the energy transfer between a light source and plasmons [77]. In simple terms, the energy of a light source excites the free electrons on the metal film, causing them to oscillate [80]. This generates electron charge density waves called plasmons [81]. These waves propagate along the surface of a noble metal and a dielectric material [82], in a direction parallel to the plane of incidence. Figure 3.1 shows the incident light exciting the gold surface, inducing the plasmon wave. This energy conversion can be observed in the reflected light. Later sections will detail the results and their interpretation.

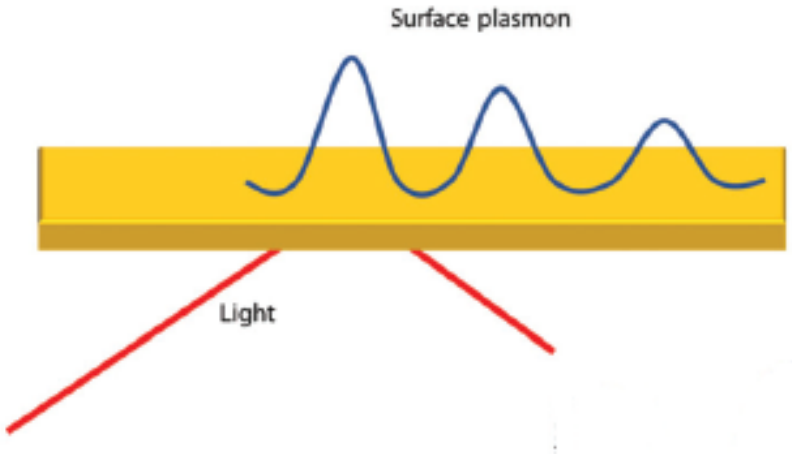

Figure 3.1: Schematic representation of the propagation of a surface plasmon wave (adapted from [82])

In the 1960s, Kretschmann and Otto studied the phenomenon [23]. In the Kretschmann configuration, light is used to excite the plasmon wave on a thin metallic film at the resonance angle through a prism. The reflected light is then analysed either with a camera or a CCD sensor. The Kretschmann configuration is one of the most commonly used configurations for SPR sensors. It is important to note that in the Kretschmann configuration, both the reflectivity and phase of the reflected light are different to that of the light source, i.e. the SPR affects both the reflectivity and the phase of the light [77].

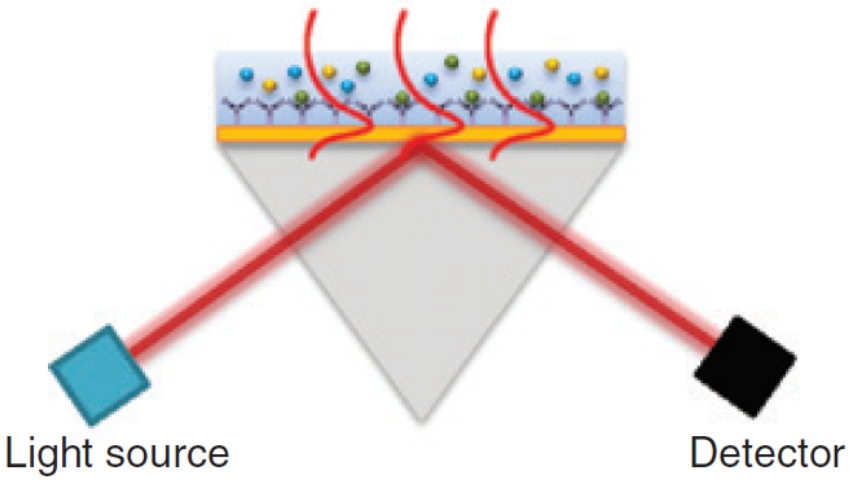

Figure 3.2: Schematic representation of Kretschmann configuration (from [83])

Light waves are electromagnetic waves that vibrate in all directions. Light is polarised when the electric field only oscillates in one plane [84]. P-polarised light is light that is polarised parallel to the plane of incidence [85]. The polarisation of light can be easily achieved by using a polarisation lens. To obtain a clear dip in the intensity results, the

light source should be p-polarised and monochromatic. Any other light will only cause noise and contribute to background signals [81].

In Figure 3.2, p-polarised light with a specific wavelength is used to excite a thin metal surface at an angle known as the resonance angle, hence the phenomena of Surface Plasmon Resonance can be observed [86].

Mathematically, the SPR phenomenon in the Kretschmann configuration can be explained by

$$k_{in} = \frac{2\pi}{\lambda} \sin\Theta\sqrt{\varepsilon_p} \tag{3.1}$$

where k_{in} is the wave vector of the excitation light, λ is the wave length of the excitation light, Θ is the incident angle and ε_p is the dielectric constant of the prism material, and by

$$k_{sp} = \frac{\omega_{sp}}{c}\sqrt{\frac{\varepsilon_m\varepsilon_s}{\varepsilon_m + \varepsilon_s}} \tag{3.2}$$

where k_{sp} is the wave vector of the surface plasmon, ω_{sp} the angular frequency of the surface plasmon, C is the speed of light, ε_m is the dielectric constant of the metal and ε_s is the dielectric constant of the dielectric medium. The Surface Plasmon Resonance phenomenon is observed when the wave vector of the excitation light and that of the surface plasmon are equal. Therefore 3.1 and 3.2 can be combined into

$$\frac{2\pi}{\lambda} \sin\Theta\sqrt{\varepsilon_p} = \frac{\omega_{sp}}{c}\sqrt{\frac{\varepsilon_m\varepsilon_s}{\varepsilon_m + \varepsilon_s}} \tag{3.3}$$

The derivations and details of these formulas are described by, Pockrand in 1978 [87] and Kurihara *et al.* in 2002 [88].

There are many different prism materials and shapes available. Mukhtar *et al.* investigated different prism shapes and materials and compared the SPR performance of these [24]. The team compared the performance of 2 sets of triangular, conical, hemispherical and semicircular prisms. The one set of prisms was made of BK7 glass and the other of SF11 glass. 50 nm of gold was deposited directly onto the prisms and the experiment was setup in the Kretschmann configuration [24]. All of these tests obtained clear SPR intensity dips. The SPR dips with the SF11 material prisms occurred at smaller resonance angles than the dips with the BK7 material. Further, in both sets the dip was deeper in the semicircular and hemispherical prism tests that with the triangular and conical prisms [24].

It is important to consider the behaviour of light in the respective prism shapes. Figure 3.3 shows how the collimated laser light behaves in different prism types. In a triangular prism only one point of light is reflected, i.e. the light remains collimated, this setup would require either the laser or the prism to rotate in order to plot an intensity curve. In a semicircular prism the light diverges, creating a larger signal.

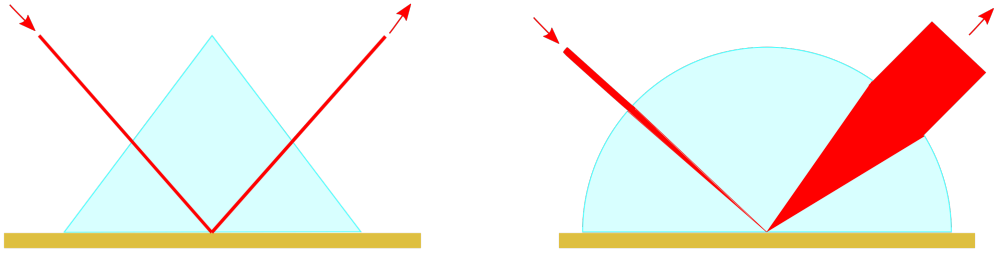

(a) Triangular prism **(b)** Semicircular prism

Figure 3.3: Schematic representation of light in different prisms

Further, the diffraction of light inside these prisms is important. When light does not enter a prism at a 90° angle to the prism surface diffraction occurs, this makes it harder to predict where and how the laser light travels in a triangular prism.

However, there exist a number of other configurations as well. One of these configurations uses an approximately 400 mm thick multimode fibre [81]. This fibre is used to guide the light, making use of the total internal reflection phenomenon [89]. The fibre can be modified as follows: at some point of the fibre a small section, roughly 10 mm, of the coating is removed and this open section is then coated with 40 nm silver or gold. The immobilisation of the bioelement takes place on this metallic surface. In this configuration, the light source is an evanescent wave and is placed at the input end of the fibre, and light at the output end is recorded [89]. Often, a spectrophotometer is used for analysing the light signal at the output of the fibre [90].

Grating-coupled sensors make use of the diffraction of light on a diffraction grating [91]. The grooves of the diffraction grating are usually made of gold, which when viewed from the top, make a pattern of evenly distributed parallel straight lines. These lines are orientated perpendicular to the light source [92]. Viewed from the side, the pattern is a sinusoid [90]. The pattern is often made by etching or lithography [91]. The formula for this configuration is given by

$$\varepsilon_s \sin\Theta + m\frac{\lambda}{\Lambda} = \pm\sqrt{\frac{\varepsilon_m \varepsilon_s}{\varepsilon_m + \varepsilon_s}} \tag{3.4}$$

where m is an integer and Λ is the pitch of the grating [92]. As with the Kretschmann configuration, the intensity minima from the reflected light is recorded [92]. This grating method is, in simple terms, a method of replacing the prism [90].

Another configuration makes use of optical waveguide systems [90]. Waveguides can be thought of like the optical fibre, the light enters at one end and the exiting light is measured and analysed. These are a number of different waveguides that can be categorised depending on geometry, mode structure or material. Waveguide configurations are also implemented in other optical sensor setups and are not by definition linked to SPR [93]. Suzukia *et al.* describe a planar waveguide made of 10 mm × 60 mm × 0.4 mm glass covered in a 50 mm thick gold film in their paper [94]. In their setup, two monochromatic light sources are used. One is a reference and the other is used to excite the plasmon

wave. The light is shone through a prism sheet and a polariser into the glass plate. In this plate, the light is internally reflected and, finally, the output light is measured with a photodiode [94]. Often grating couples are integrated in the planar waveguide. Waveguide interferometers are often implemented to measure the outputs of waveguide systems [95].

In addition to SPR, there is LSPR (Localised Surface Plasmon Resonance). LSPR makes use of metallic nanoparticles. When the light waves from the source reach the nanoparticles, the plasmon oscillations are induced locally on the nanoparticle [25]. In these systems, white light is used to excite the plasmons. Optical spectroscopy can be implemented to detect LSPR [96]. These sensors can be coupled in either a transmission or reflection arrangement [97]. Figure 3.4 shows LSPR in the transmission configuration. LSPR does not require a prism and is not dependant on the incident angle. This makes the sensor's physical setup less complex than that of SPR.

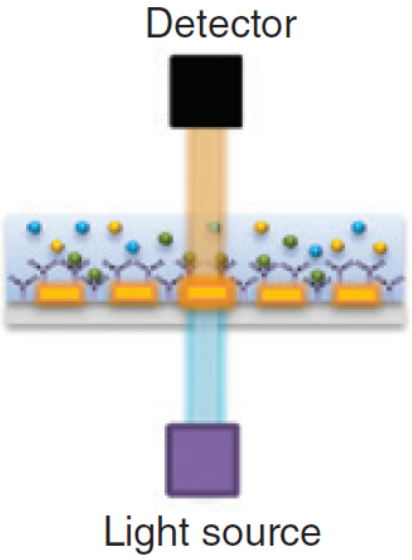

Figure 3.4: Schematic representation of the LSPR configuration (from [83])

3.2 SPR Technology in Biosensors

This section discusses how the SPR phenomenon is used in a sensor. It briefly touches on the areas where SPR sensors are implemented and lastly, reviews some existing SPR devices that have been commercialised.

The resonance angle and the plasmon behaviour depends on the properties of the dielectric medium through which the plasmon wave propagates. Properties of the output light signal are dependent on the properties of the dielectric properties [77]. If the properties of the dielectric are altered, the output light signal will change too [77]. This is where the biological binding of biomolecules to capture molecules comes into play. Capture molecules, such as antibodies, are immobilised to the noble metal surface and the output light signal is analysed. Once the sample is added, the output light signal is analysed once again. If binding took place, there will be a change in the signal and if no change is

recorded, no binding took place. In the case of a Kretschmann configuration the change observed is a shift in the intensity minimum. Figure 3.5 shows the setup of a Kretschmann configuration sensor. The shift of the SPR band is directly proportional to the mass of the analyte that bound to the sensor surface [25]. Often, SPR systems are combined with microfluidic flow channels through which the sample flows with the help of a syringe pump [25]. This allows for the kinetic analysis of the binding and unbinding taking place between the analyte and the capture element.

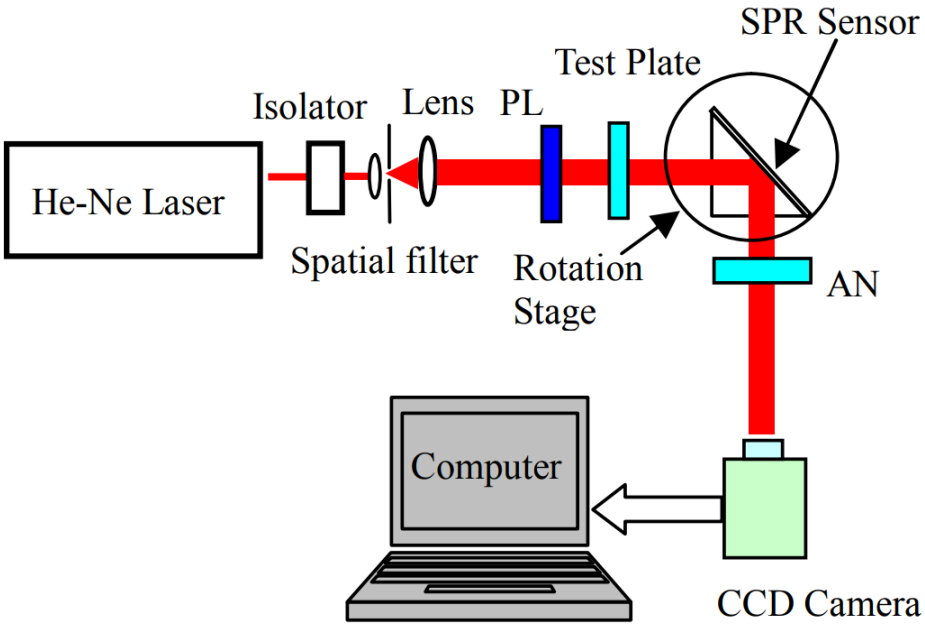

Figure 3.5: Schematic representation of SPR sensor setup (from [98])

As described in the literature, there are various versions of this setup. However, most include a laser as the excitation source, polarisation lenses, a glass prism and a camera. The light source wavelength is usually in the near infrared range of the spectrum.

Both SPR and LSPR systems are often paired with a microfluidic system. This allows the sample to flow through the system, enabling kinetic analysis of the samples binding and unbinding properties [25]. One of the advantages of microfluidic is that it reduces the amount of reagent needed [99]. Poly(dimethylsiloxane) (PDMS) is commonly used for the fabrication of the flow channels. There are various methods used to manufacture flow channels, including: laser micromachining, soft lithography and replica molding [99] [100]. The selected flow rate for the system is dependent on the binding and unbinding properties of the protein.

Zhou and team developed an SPR sensor that was able to detect tropomyosin, an allergen found in shellfish [101]. The team implemented a gold biochip in a home-built SPR sensor. The design of the sensor is based on the Kretschmann configuration. The sensor chip is placed on a right-angled glass prism and a polarized HeNe laser with a wavelength centered at 650 nm is used to excite the system. The light goes through a p-polariser and is reflected on the gold film of the biochip. The reflected beam is collimated by a cylindrical convex lens. The light beam then travels through a quarter-wave plate and

a polariser. Lastly, the light moves through a cylindrical concave lens to diffract the beam on the horizontal plane. This is done to enhance the angular resolution of the system. A CCD camera and a personal computer are then used to analyse the results. Anti-tropomyosin monoclonal antibody was used to capture the analyte. The team's SPR sensor made use of a microfluidic flow system, where 200 µl of each sample was allowed to flow onto the gold chips at a rate of 20 µg·ml^{-1} at 37°C. After the incubation period, the SPR signals were recorded. The sensor achieved a limit of detection (LOD) of 1.0 µg·ml^{-1} [101].

The setup of an LSPR sensor can be seen in Figure 3.6. In this specific setup, the light is transmitted through the sensor chip; this is known as T-LSPR [102]. As with SPR in the Kretschmann configuration, when the target binds, there is a change in the properties of the light. In LSPR a spectrometer is used to analyse this. There are two types of LSPR sensors, aggregation type and refractive index type [96]. In aggregation based LSPR, both the complementary biomolecules are attached to metal nanoparticles and when the biomolecules then bind to one another, the respective nanoparticles come into close proximity. This causes aggregates to form due to near-field electromagnetic coupling. This induces a colour change that can be inspected with a spectrometer. Refractive based LSPR depends on the change in the refractive index around the metal nanostructures. When biomolecular interactions take place, a shift in the red peak can be observed [96].

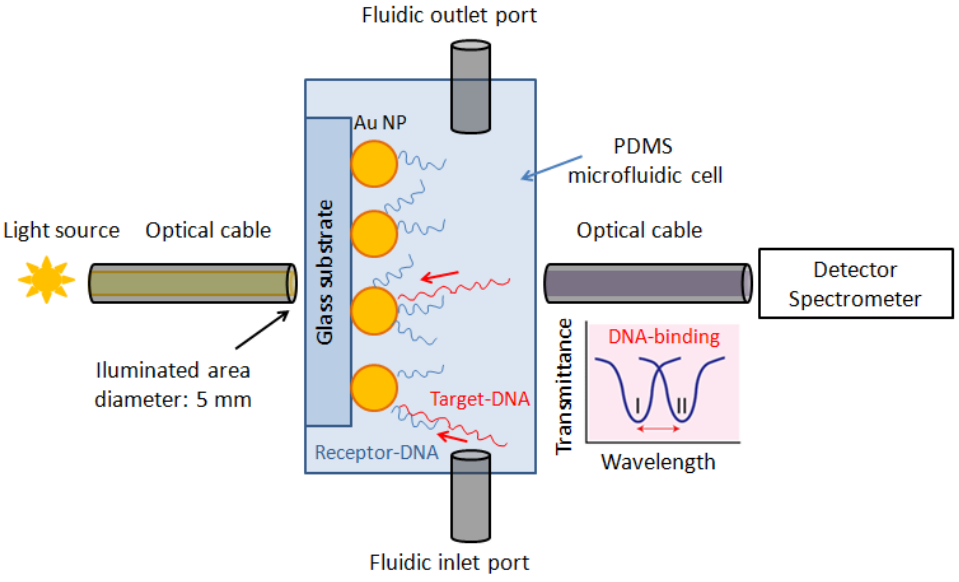

Figure 3.6: Schematic representation of LSPR sensor setup (from [102])

Cappi *et al.* demonstrated an LSPR device that was able to detect concentrations of 0.5 µmol tobramycin [100]. The team built a T-LSPR device that was able to detect concentrations of tobramycin label-free and in-real time. Gold nanoislands were implemented on the glass for the creation of the biochips. The team also implemented a flow system to allow the sample to flow onto the chip. Non-polarized white light was implemented as the excitation source and the light was transmitted through the biochips. A complementary metal oxide semiconductor (CMOS) image sensor was employed as a light detector [100].

3.2.1 SPR Chips

The chip implemented depends on the chosen configuration. This sub-chapter will concentrate on the chips needed for the Kretschmann configuration as well as LSPR.

SPR sensor chips are often glass chips coated with a noble metal on top. Gold is usually chosen, as it is the most practical option, for the application. Gold is an inert metal [103] and thus does not react with other materials. Copper and aluminium are often not chosen as they have a too wide SPR response while aluminium and silver oxidise, making them impractical as well [81]. The thickness of the metal layer is in a range of 40-50 nm [103]. Mukhtar *et al.* tested the sensitivity of SPR with gold and silver metal films with thicknesses ranging from 25 nm to 95 nm in 10 nm increments [104]. The team used q-factor and Full Width Half Maximum (FWHM) analysis to compare the SPR curves to each other and found that 55 nm of silver yielded the best results. However, due to the previously mentioned oxidation problem when working with silver, the analysis of the gold films from this study were considered. The best q-factor and FWHM for the gold films were attained between 45 nm and 55 nm. [104]. The glass used has a refractive index ranging from 1.26 to 1.52 depending on their applications. The glass chip is often coated with a thin layer of titanium or chromium, roughly 2-4 nm, before the gold is deposited onto the glass. This is done to increase the adhesion between the gold and the glass [86]. There are various methods to deposit a thin film of gold, which include sputter coating [102] or thermal evaporation [80]. In some cases, the gold is patterned on the chip surface, as this can increase the surface area and may result in denser biomolecule immobilisation. Existing commercial SPR chips range in size, Sofchip offers chips from 9×9 mm to 20×20 mm [105]. In the Kretschmann configuration it is important to ensure optical coupling between the prism and the chip, which can be done by using optical glue or matching oil. Thiodiglycol (bis 2-hydroxyethyl sulfide) [72] or glycerine [106] can be used for this purpose.

Yakubovsky *et al.* investigated the morphological and optical properties of gold layers ranging in thickness from 20nm to 200nm [107]. The team showed that the physical characteristics of the gold layer, such as film thickness, have an effect on the dielectric constant and therefore on the refractive index [107]. The gold layers were deposited on silicon substrate with E-Beam Evaporation (EBE). The team characterised the thickness of the gold layer as well as the surface roughness using AFM. Further the team employed X-Ray Diffraction (XRD) to investigate the polycrystalline structure of the gold films. The average grain size D was estimated by the Debye-Scherrer equation. The grain size increases as the thickness of the film increases. The team showed that an increase in the grain size improves the SPR results [107].

The effect of the gold surface roughness was investigated by Hoffmann *et al.* The team deposited 50nm of gold on substrates that have previously been coated with ranging thicknesses of LiF. The LiF layer effected the roughness of the gold surface [106]. A semi-cylindrical BK-7 prism was employed. Shifts in the resonance angle as well as an increase in the width of the dip are an indication of the scattering of plasmons [106]. The surface roughness effects the scattering which in turn affects the surface plasmons. The team concluded that the dielectric constant of the gold substrate changes with the roughness amplitude [106].

Agarwal *et al.* investigated surface roughness of silver on SPR chips [108]. The team found

that the thicker the substrate layer the smoother it becomes. The team also showed that using a titanium adhesion layer results in a smoother surface. They achieved an average roughness of 0.651 nm at an average silver layer thickness of 50.85 nm [108].

One way to verify the thickness of the gold layer is Atomic Force Microscopy (AFM). The working principle of an AFM is fairly simple. A sharp tip, which is connected to a cantilever, is dragged the across a sample. The deflection of the tip, due to the forces acting on it, is determined by measuring the deflection of the cantilever [109]. A repulsive force between the sample and the tip exists, with the force increasing as the distance between the tip and the sample decreases. AFMs often have two modes, namely: static and dynamic modes [109]. When an AFM operates in static mode, the deflection of the cantilever, due to the repulsive force, is determined with a laser beam. In dynamic mode, the cantilever vibrates as it moves across the sample. The cantilever is excited to oscillate at a frequency near the free resonance frequency of the cantilever [109]. When the repulsive force acts on the tip it will increase the resonance frequency of the cantilever. This, in turn, alters the amplitude of the oscillation on the cantilever. As with static mode, a laser beam is used to detect the deflection of the cantilever [109]. A schematic representation of the working principle of an Atomic Force Microscope can be seen in Figure 3.7.

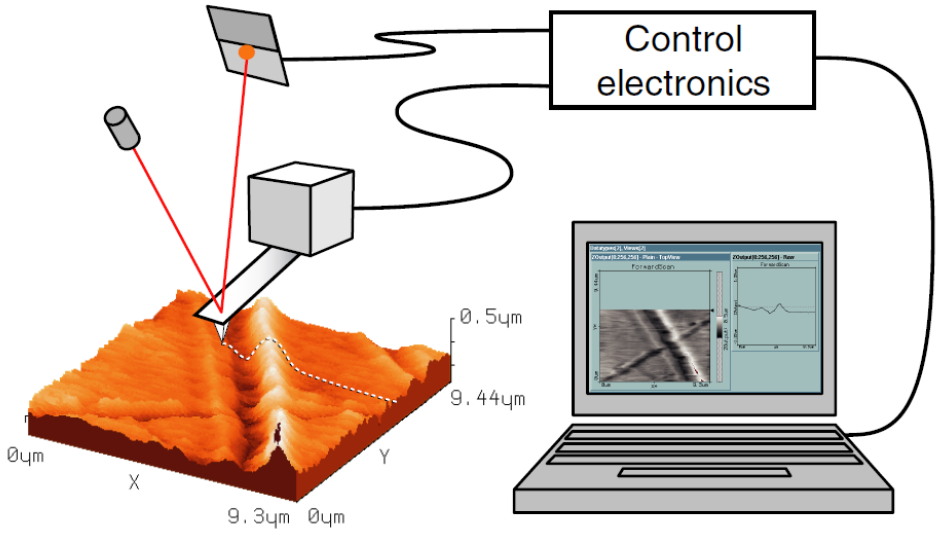

Figure 3.7: Schematic representation of an atomic force microscope (from [109])

The information obtained from the laser beam is then entered into a feedback loop. This is done to keep the tip-sample interaction constant by adjusting the tip sample distance [109]. The output of the feedback loop is thus the sample height. An AFM can create a three-dimensional image of a sample. The scanning takes place across the x and y-axis and the height of the sample, the z-value, is documented as a function of x and y [109].

LSPR is dependent on the size and shape of the nanoparticles, therefore it is important that the nanoparticles be manufactured in a repeatable manner. Electron Beam Lithography (EBL) is a method that can be implemented to pattern the substrate with gold nanoshapes in the desired manner [102]. This method, however, is costly. A cheaper

method is annealing a deposited thin gold layer [102]. The heating of the film results in the agglomeration of the gold. However, due to the poor adhesion of the gold to glass, this method is not favoured. Another method often implemented is the chemical binding of gold colloids [102].

3.2.2 Immobilisation Methods

When considering various options of immobilisation for SPR techniques it is important to keep in mind that the method is based on changes to the dielectric constant at the sensor surface. Hence it is important to ensure that little to no unspecific binding can take place on the gold surface [110]. Another important aspect to keep in mind is the length of the cross-linker. It is best kept as short as possible to ensure close proximity to the gold surface.

In the literature, Self-Assembled Monolayers (SAMs) are often applied in the development of SPR sensors. As discussed in Chapter 2 the advantages of SAMs are that the capture antibodies are immobilised such that the active binding site faces the sample and this method has high surface coverage. These advantages come at the cost of extra production steps.

SAMs form tightly packed robust chains which create a thin interface, in the nanometre range. The interface makes it possible for the proteins to bind to the substrate with a higher surface density [111].

SAMs on gold substrates are often formed by submerging the metallic substrate in a thiolic solution. The substrate is submerged for different times, ranging from minutes to hours [112]. By using mixtures of modified alkanethiols, several different SAM surfaces can be created. The alkanethiol consists of three main sections, that can be seen in Figure 3.8; the thiol head group, that adsorbs onto the gold layer, the hydrophobic body, and the terminal functional group [113]. From the functional group, the capture antibody can be covalently immobilised with the assistance of cross-linkers.

3-Mercaptopropionic acid (3MPA) is a short chain alkanethiol that can be employed to create a SAM [114]. The terminal group of 3MPA is carboxyl, this will result in a hydrophilic SAM [113]. Cysteamine can also be used, it has a amine termial group and also results in a hydrophilic SAM. Other thiols include alkanethiols, arenethiol and alkanedithiol, which can also be implemented to form a SAM [113].

In many cases, non-cross-linked carboxymethylated dextran is bound to the SAM layer. Dextran has the advantage that it allows very little non-specific adsorption of biomolecules. The dextran can be modified with carboxyl groups, which in turn act as the starting point for the covalent binding of ligands [72].

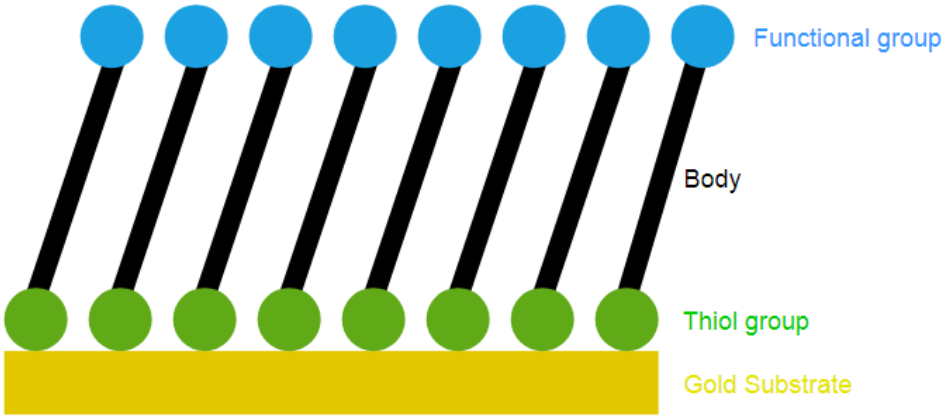

Figure 3.8: Schematic representation of a self-assembled monolayer

There are a number of cross-linkers that can be implemented to covalently attach the antibody to the terminal group of the alkanethiol. 1-Ethyl-3-(3-dimethylaminopropyl)carbodiimide (EDC) in combination with N-Hydroxysuccinimide (NHS) is often implemented to bind an amine group to a carboxyl group [71]. Proteins that have been covalently bound to the SAMs cannot easily be removed. It may be considered to wash the protein and SAM coated substrate with surfactant solutions, such as Tween 20, to re-use them.

In other cases, biotinylated alkyl thiol (BAT) is implemented. In this instance a SAM is formed and a biotin molecule is attached to the functional end group [115]. This is a very popular approach due to the aforementioned affinity between biotin and streptavidin. Streptavidin is then used as an intermediate molecule as it has four binding sites for biotin [115]. The streptavidin thus binds to the biotinylated SAM, while also providing binding sites to the biotinylated capture antibody.

As mentioned in the Chapter 2, it is important to verify the immobilisation steps. There are various methods to do this. Ellman's and Bradford assays can be considered for this [116]. Ellman's solution, which is 5,5'-dithio-bis-(2-nitrobenzoic acid), can be used as a direct colorimetric assay to determine the amount of thiol in a solution, as it reacts to thiol groups. The reaction that takes place between Ellman's reagent and thiol groups induces a colour change, which can be measured using a spectrophotometer. The higher the optical density reading, the more thiol is in the solution. This method can be implemented to determine how much thiol is in the alkanethiol mixture into which the substrate is submerged before and after incubation. If there is less thiol in the solution after the incubation period, it can be assumed that thiol adsorption onto the substrate occurred [117].

The Bradford protein assay works similarly to Ellman's except it is used to detect the amount of protein in the solution instead of thiol groups. This can be used to determine if the capture antibody binds to the SAM. The amount of protein in the solution is measured before and after incubation. Once again if less protein is in the solution after incubation, it can be assumed that the protein has bound to the SAM [118].

Atomic Force Microscopy (AFM) has been implemented for the imaging of biological molecules. Wadu-Mesthrige *et al.* investigated the immobilisation of proteins on SAMs with AFM [73]. The team considered BSA, lysozyme (LYZ), and normal rabbit IgG, for

their investigation. The team concluded that AFM has been shown to be a viable tool for the imaging on individual proteins, as well as their orientation, after the immobilisation process [73].

3.2.3 Results and Interpretation

In this section the signal outputs, data processing and imaging methods used in connection with SPR will be discussed. SPR results are generally given in the form of two graphs, namely, the reflectance curve (Figure 3.9) and a sensorgram (Figure 3.10).

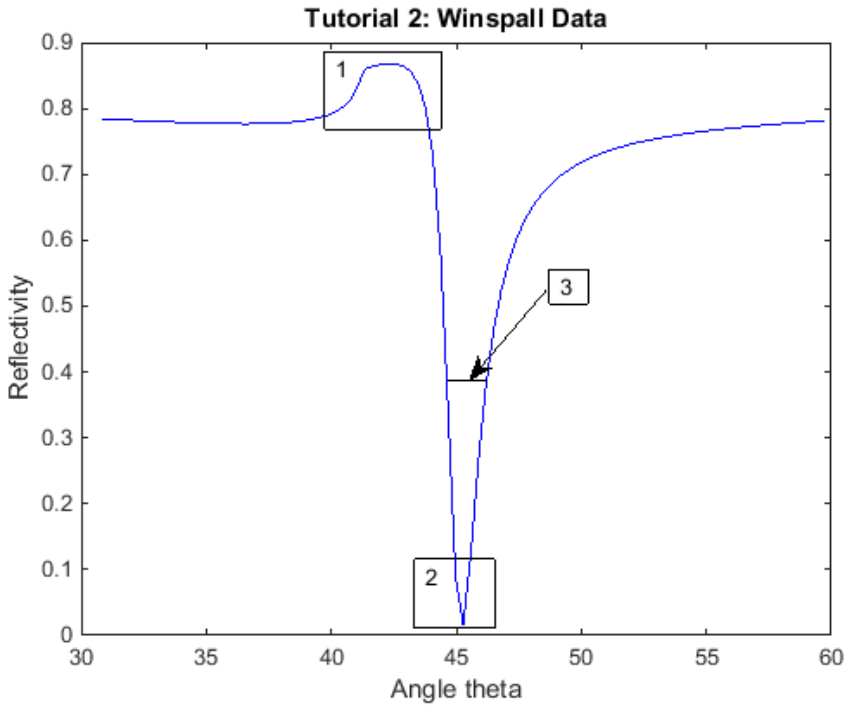

Figure 3.9: Surface Plasmon Resonance reflection curve (adapted from [119])

As previously discussed, the excitation of the plasmons results in an intensity minimum in the reflected light. The reflectance curve shows at which angle the dip in the light intensity occurs. The y-axis indicates the light intensity and the x-axis the angle of reflectance. If a binding action takes place on the surface of the SPR chip, there will be a shift in the reflectance angle. The change in the shift is directly proportional to the mass of the binding that takes place [25]. In this reflectance curve, there are three features to pay attention to when analysing SPR data. The first feature (numbered 1 in Figure 3.9) is known as the edge of total internal reflection and plays an important role in the validation of the SPR measurement [119]. The angle at this point is dependent on the dielectric constants of the prism and the sample and is therefore fixed for the system [119]. The resonance angle is numbered 2 in Figure 3.9 and indicates the angular position of the intensity minimum. The minimum is not necessarily at zero. Lastly, feature 3 on Figure 3.9 is referred to as the Full Width Half Maximum (FWHM) [119]. Figure 3.10 makes use of data obtained from Winspall based on the Resonant Technologies GmbH *"Surface Plasmon Resonance Simulate your reflectivity curve with WinSpall"* tutorial [120].

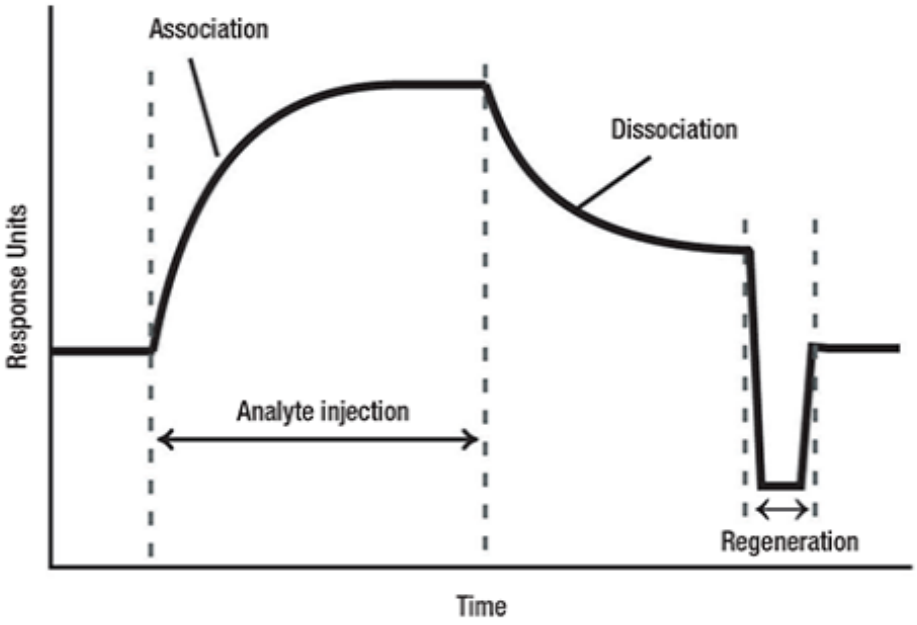

Figure 3.10: Schematic representation of SPR sensorgram (from [121])

The sensorgram depicts the kinetic behaviour of binding action. Sensorgrams are acquired by plotting reflectivity, angle or wavelength (y-axis) against time (x-axis). The graph consists of four phases known as association, equilibrium, dissociation, and regeneration [121]. From the sensorgram, the association and dissociation constants can be determined. The ratio of these values is known as the binding constant. The sensorgram can also be used to determine the concentration of the analyte in the sample [122]. At the equilibrium, the response is directly proportional to the concentration of the analyte [122].

3.2.3.1 Imaging Methods

Wong and Olivo describe different types of SPR imaging methods [123]. SPR imaging can be dependent on a number of variables, namely: intensity, angle, wavelength, phase, and polarisation.

Intensity SPR imaging is based on the measurement of the shift in the intensity minimum. This method is applied to the Kretschmann configuration. The resonance angle is fixed and the absorption profile of the reflected light is analysed [123]

One method of SPR imaging is spectral imaging; this makes use of a polychromatic light source [123]. Instead of making use of the reflected light intensity, this method uses the resonance wavelength to make two-dimensional images [124].

Wong and Olivo also describe the Phase and Polarization Contrast-Based SPR Imaging. When SPR is achieved, the phase of the light is changed, due to the energy transfer that takes place [123]. A common method for the phase detection in SPR is known as Heterodyne Detection [125].

3.2.4 Simulation

Ji *et al.* consider different methods of simulating SPR curves. These methods include MATLAB, Winspall, TFCalc, COMSOL, and Ansoft HFSS [126].

Winspall is a free software that was developed by Juergen Worm from the Max-Planck-Institute for Polymer Research in Mainz, Germany. This software makes use of the Fresnel equation and matrix formalism to predict the SPR curve [126]. It allows the user to enter some of the variables in SPR such as light polarisation and wavelength, the prism type and the various layers and their properties.

Figure 3.11 shows an example of the results from Winspall. The data used for this example was acquired from [126].

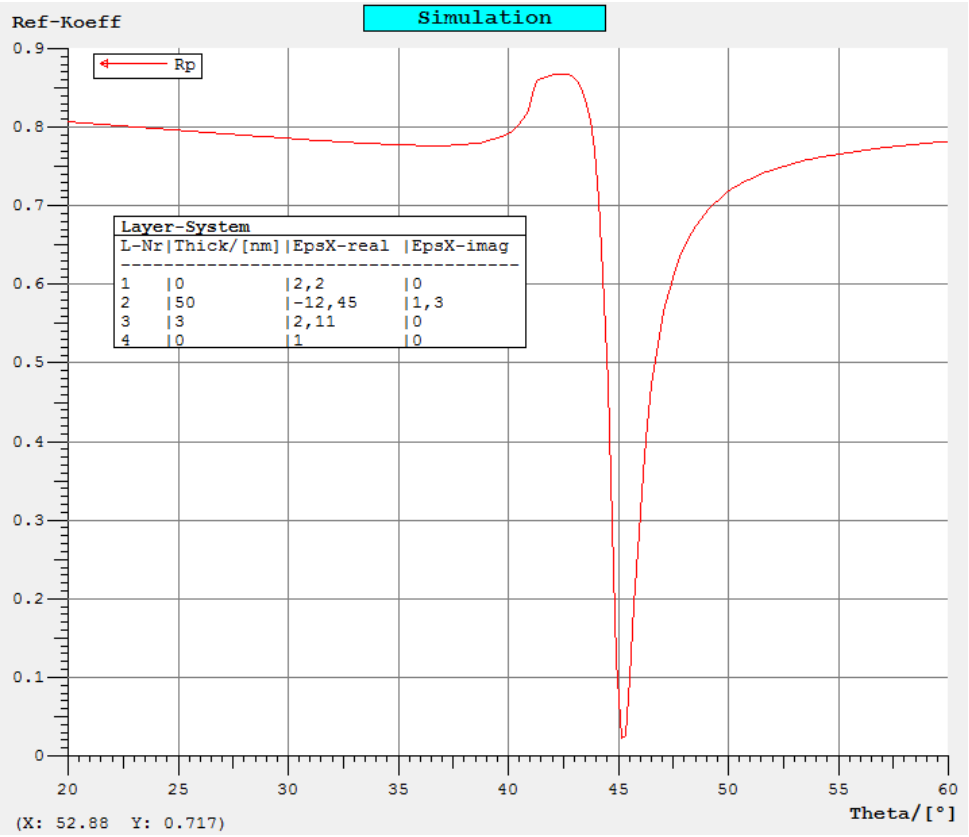

Figure 3.11: Winspall results (from [127])

According to Ji *et al.*, the software is limited to smooth metal layer surfaces [126] and is, therefore, not suitable for patterned chips or chips coated with nano-islands/rods/particles.

COMSOL Multiphysics modelling software was developed by COMSOL Inc and uses finite element analysis to predict the SPR curve. The software requires a simulation model, defined material properties, as well as meshing and boundary conditions, to determine results [126].

Ji *et al.* compared the FEM and Winspall simulations to experimental results, Table 3.1 shows their results [126]. From this table, it can be seen that the COMSOL simulation

outcome correlated more closely to the experimental results than the Winspall simulation. However, Winspall results were within a 15 % error margin [126].

Table 3.1: Results of the SPR simulations vs the experimental results

	Winspall	COMSOL	Experiment
Water	67.1°	62.6°	62.7°
50% ethanol	71.7°	65.0°	65.1°
100% ethanol	72.5°	65.3°	65.3°

An SPR Calculator can be downloaded from the MathWorks website. The calculator is MATLAB code written by Luigi Cristofolini [128]. The calculator is user-friendly and allows the user to alter variables using sliders. The calculator assumes a 90° angle prism and is limited to three layers.

In August 2018, Bipradip Chakraborty from Gauhati University wrote MATLAB code that allows the plotting of experimentally gained data against the predicted curve [129].

3.2.5 Existing SPR Devices

SPR sensors have been found useful for gas monitoring, clinical diagnostics, environmental analysis and food safety tests [25], [130]. However, the existing devices reviewed here will focus on SPR devices used for clinical tests.

3.2.5.1 Commercial SPR sensors

Many companies such as Bruker [131], Nicoya [57], BioNavis [132] and Plasmetrix [133] have commercialised SPR sensors. These SPR machines convert the signals, such as the angle shift, into easily understandable results that are displayed in such a way that they are easy to interpret [81].

The Sierra SPR-32 is an analytical instrument by the company Bruker. This state-of-the-art machine is a high-performance, real-time and label-free analysis device based on SPR in the Kretschmann configuration. The device makes use of Hydrodynamic Isolation technology to deliver high throughput. The device has 8 flow channels with 4 detection spots, which leads to a total of 32 individual sensors [134]. This device has low noise and high sensitivity detection. It further has a robust microfluidic sample delivery system. A different assay can be performed at each flow channel. The continuous-flow microfluidic system allows for the kinetic analysis of the sample. The machine is further capable of parallel processing. The software allows for a user-friendly interface with fully automated assay templates, as well as single or grouped sensorgram viewing and data analysis [131].

Plasmetrix is a company that specialises in compact and portable plasmonic devices. The device, which is depicted in Figure 3.12, is based on the Kretschmann configuration. The company describes their product as “an affordable and versatile system for education and research.” The device is adaptable with accessible and interchangeable fluidics. The device is also relatively small ($150 \times 50 \times 32$ mm) and can easily be partially disassembled for cleaning. The device can reach a SPR resolution of up to 1×10^{-6} RIU [133].

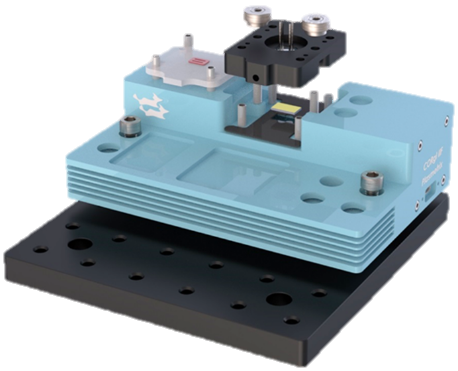

Figure 3.12: Plasmetrix Corgi (from [133])

3.2.5.2 SPR sensor for the detection of TB

Prabowo *et al.* tested portable organic light-emitting diode- (OLED-) based surface plasmon resonance for the detection of TB [135]. The team detected IS6110 DNA which is present in the Mycobacterium tuberculosis. The DNA was labelled with DIG. A SAM was used to functionalise the gold surface. Anti-DIG was immobilised to the SAM using EDC and NHS [135]. The DIG labelled DNA samples bound to the anti-DIG on the gold substrate. 600 clinical sputum samples were tested with the device, a sensitivity of 96.6% and specificity 98.46% was obtained. The team concluded that the SPR biosensor could be considered as a suitable device for the detection of TB [135].

3.2.5.3 SPR detection of cytokines

In the past SPR has been successfully implemented for the detection of cytokines [136]. However, since cytokines are low in mass and SPR is dependent on the mass change in the dielectric sensing medium. Therefore, methods to enhance the signal are required. The non-specific binding on the sensor substrate surface needs to be illuminated. Additionally, the addition of mass increasing labels and tags can increase the detection ability of the sensor. Examples are secondary antibodies or gold nanoparticles [136]. The purification of the sample prior to introducing it to the sensor also improves these results [136].

Battaglia *et al.* developed a fibre-optic SPR sensor for the detection of 3 cytokines linked to wound healing (IL-1, IL-6, and TNF-α) [137]. The team implemented a N-hydroxysuccinimide ester of 16-mercaptohexadecanoic acid (NHS-MHA) SAM and immobilised anti-IL-1, anti-IL-6, or anti-TNF-α onto the SAM layer. The SPR sensor was equilibrated for 20min, then it was introduced to a sample containing the target analyte for 20min. the sensor was then placed back into the equilibration medium. The limits of detection for IL-1, IL-6 and TNF-α were 0.29 ng·ml^{-1}, 0.45 ng·ml^{-1} and 1.3 ng·ml^{-1} in saline solution [137].

3.3 Conclusion

In this chapter SPR was investigated in detail. It started with a brief history of the phenomenon and then continued by describing the theory behind it. SPR in biosensors was

explored. Different configurations were considered and various parts of an SPR system were discussed. The Kretschmann configuration was selected for this project due to its simplicity and its popularity in literature. The SPR chip for grating coupled devices is difficult to produce, since a pattern on the surface is required. Due to the rounded surface of the fibre, both gold coating the fibre and immobilising on this surface will potentially pose challenges. With the Kretschmann configuration the coating is a simple flat layer. Also, since the chip is a separate part in the Kretschmann configuration, it can easily be replaced between sample tests or if it should get damaged. Further, a fibre configuration as well as the waveguide systems require additional equipment, such as spectrophotometers and interferometers respectively. SAMs, as an immobilisation method, were further investigated as they have high density surface coverage and low non-specific binding. 3MPA in combination with EDC/NHS was selected for this project. 3MPA is a short chain and EDC/NHS is a zero length cross-linker. Using a BAT would require extra steps, such as adding streptavidin, which will also add to the length of the immobilisation layer. Further, biotin is more expensive than 3MPA. The chapter continuous to discuss the results and how to interpret them. Additionally, simulation methods and existing devices were looked at.

Chapter 4

Methodology

This chapter is a discussion of the chosen methodology. It briefly touches on the main design choices made, discusses these and justifies them with information from literature. The chapter is broken into various subsections, which will cover the decisions regarding the different biosensor elements. The first section that is discussed is the hardware, which touches on the experimental setup that was implemented to verify the photonic section of the sensor and further states the design decisions for other hardware elements. It moves on to describe the used immobilisation method. Later, the planned software is briefly described and lastly simulations with the chosen parameters are included.

4.1 Hardware

The hardware of this project consists of various complex subsections. This section breaks the hardware into smaller sections, namely experimental setup, sensor chip, electronics,fluidic system and prototype frame. The Kretschmann configuration has been selected for this biosensor as this configuration is commonly implemented and has shown promising results as demonstrated by Zhou *et al.* [101].

4.1.1 Experimental Setup

Once the parameters of the SPR system have been selected, it is important to confirm that the photonic section of the sensor works. This is done using a laser, a prism and a gold chip, and testing it to see if the SPR phenomenon can be observed. The setup is as follows:

- Place a prism on to a turn table, such that the gold surface of the glass chip is in line with the turn table's centre of rotation.
- Position the laser so that it is at a 90° angle to the gold substrate.
- Aim the laser onto the gold, while observing both the transmitted and reflected light from the prism.
- Slowly rotate the turntable while observing the transmitted and reflected light.

If the SPR phenomenon is achieved, there will be no light transmitted and a dark band will be visible in the reflected light. Using this method, the resonance angle can be

determined experimentally. Figure 4.1 shows a schematic of the experimental setup. This experimental setup is adapted from [138] and [139].

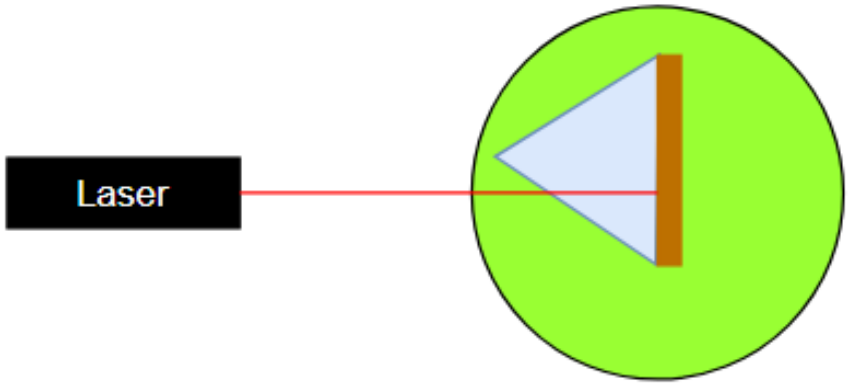

(a) Initial position

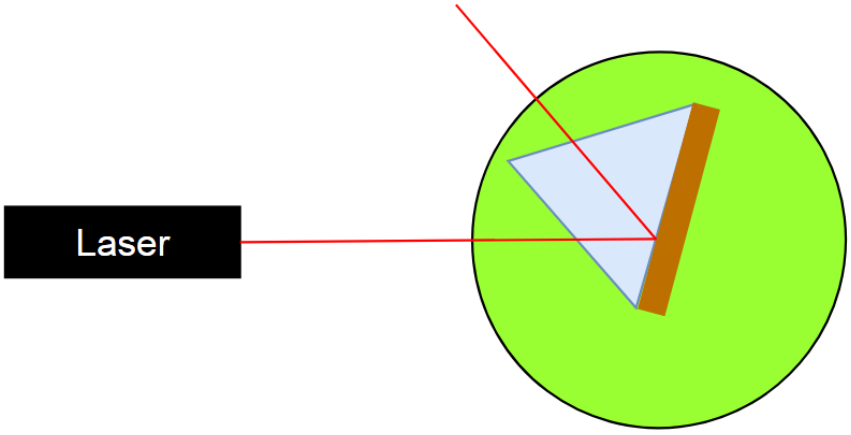

(b) Position after rotation

Figure 4.1: Schematic representation of the experimental setup

Coulter used a 632.8 nm He-Ne laser [139] and Mustafeez used a 633 nm He-Ne laser [138]. Pluchery *et al.* created intensity curves of the SPR using 3 different wavelengths, namely, red (633 nm), yellow (589 nm) and green (546 nm). This experiment showed the deepest intensity dip using the red laser [140]. Therefore, a He-Ne laser with a wavelength of roughly 633 nm was implemented. Further, the laser's output should be as constant as possible, if the laser output is not constant a feedback system will need to be implemented. since He-Ne lasers are too big to be easily implemented in point of care devices two other lasers were tested and compared. A digital handheld optical power and energy meter console, the PM100D from Thorlabs was used to measure the power output from the two lasers that were investigated for this project.

4.1.2 Sensor Chip

The glass chosen for the sensor chip is soda lime glass with a refraction index of 1.5207. Gold is chosen because, as previously mentioned, it is inert and yields a deep reflectance dip as shown by Mukhtar *et al.* [104]. Silver is not chosen because it oxidises. The Central Analytical Facilities (CAF) has a gold coater, the LEICA EM ACE200. The thickness chosen is 50 nm, and again this choice is based on the research done by Mukhtar *et al.*

[104]. The gold has a refractive index of 0.13967 and an extinction coefficient of 3.7105, at 661 nm wavelength. AFM analysis was done to confirm the thickness and smoothness of gold on the glass surface. The main requirement for these chips is that the SPR phenomenon can be created with them. Ideally the gold chips would be reusable.

4.1.3 Electronics

A suitable laser was determined for the prototype. The light wavelength, as well as the laser's ability to deliver a constant output intensity, were considered. Further, a laser power supply circuit to ensure the correct operation conditions for the laser was designed. This design aimed to be portable, so that the system can be used in the field.

4.1.4 Microfluidic System

The following dimensions for the system are proposed: 1 mm width, 10 mm length and 150 µm depth. These values were chosen from Cappi *et al.* [100]. The depth of the channel is so shallow so that the sample is brought into close proximity with the capture antibodies on the chip. Figure 4.2 shows a modified design. This design includes a well, to increase the surface area, and thus making the positioning of the laser easier. It is proposed that the channel will be manufactured with the SAND laser cutter.

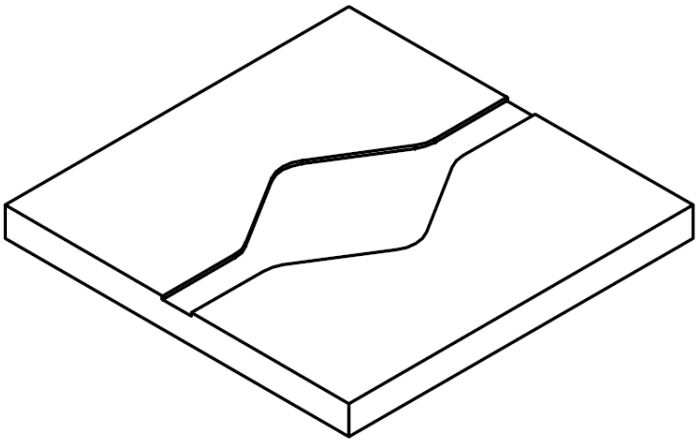

Figure 4.2: Microfluidic channel design

The material chosen is acetal, as it is strong, mechanically stable, has a low friction coefficient and a low water absorption [141]. Double-sided tape is proposed to stick the channel to the chip, as done by Cappi *et al.* [100]. It is required that the microfluidic system brings the sample into close contact to the gold substrate without leaking.

4.2 Prototype Frame

The prototype frame acts as a holder for all the components, allowing them to be setup in the Kretschmann configuration. The design aims to be adjustable so that the parts can easily moved and aligned.

4.3 Immobilisation

In previous chapters, various methods of immobilisation were discussed and a SAM was chosen as the best option for the project. The antibodies for this project are supplied from the animal TB research group. The immobilisation represented in Figure 4.3. The gold chips were submerged in a high concentration of 3MPA (5-10 mmol) overnight. In this time the thiol head of the polymer will adsorb into to the gold. To activate the carboxyl group on the EDC and NHS will be mixed in a ratio of 2 to 3 and introduced to the SAM layer on the gold chip for 15min at room temperature. The desired concentration of the protein was prepared in PBS. The carboxyl on the other end of the 3MPA polymer will be activated with EDC and NHS to bind with the protein.

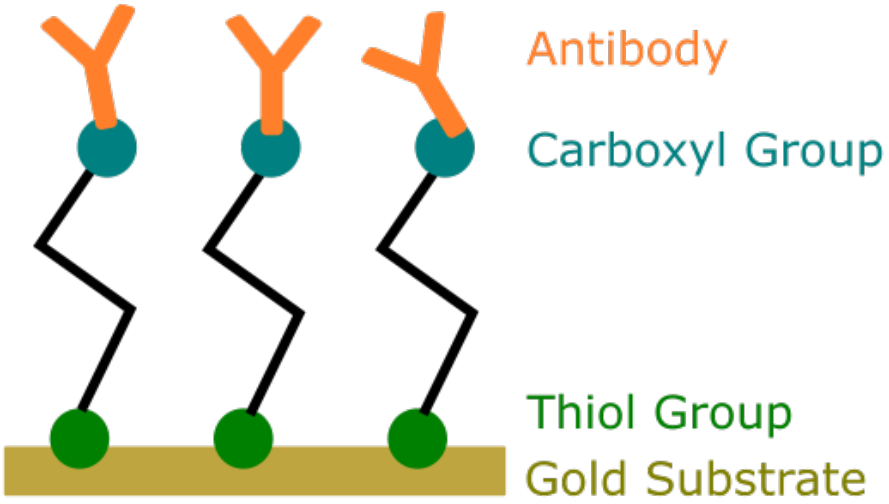

Figure 4.3: Schematic of proposed immobilisation

To confirm the binding between the thiol and the gold surface, Ellman's method will be implemented. Ellman's reagent was prepared in the reaction buffer. A standard curve was created using the known concentration. For the confirmation of the binding of the protein, Bradford assays were performed. Protocols for these verification methods and the immobilisation method are given in Appendix E.

4.4 Proposed sensing mechanism

Once the biorecognition element has been immobilised to the SAM on the sensor surface a baseline can be established. Then the sample is introduced to the sensor surface and thereby to the recognition element. The binding of the analyte to the recognition element antigen will change the mass of the biological elements connected to the gold chip. This will affect the dielectric properties of the medium, which in turn affects the properties of the reflected light. Figure 4.4 shows the expected binding of the antigen. For this project the Antigen is IP-10/INF-γ and antibodies are anti-IP-10/anti-INF-γ.

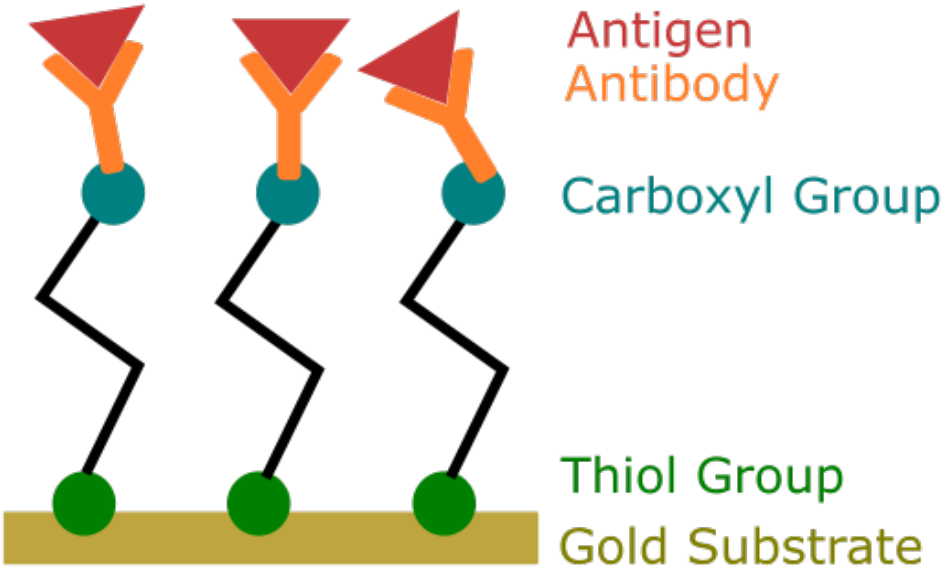

Figure 4.4: A schematic representation of the sensing mechanism

4.5 Software

The proposed software requires a processor and a camera. The camera is to be positioned such that the reflected laser light is seen. OpenCV in combination with Python will be used to create an algorithm to analyse the images attained from the camera. OpenCV is an open source library that has a large number of optimised algorithms that are often implemented in computer vision applications [142]. Python is a programming language that is chosen because of its simplicity and because it easily interfaces with OpenCV. The software will have to be able to depict the intensity curve of the SPR signal. A Raspberry Pi 4 was chosen for this project, It has a 4GB RAM, which is large in comparison to other single-board computers. A large amount of RAM is required when processing a large number of images in a small amount of time. Further, it can be easily connect to a monitor and other devices via USB or Bluetooth, which is practical in the development phase of the project.

4.6 Simulation of Proposed System

As described in Chapter 3, there are various simulation methods available. Due to the complexity of COMSOL and the required computing power, Winspall and various MATLAB simulations were conducted. The parameters entered into the programs can be seen in Table 4.1. The chosen wavelength is 661 nm and the refractive indexes and extinction coefficients were obtained from a refractive index database created by Polyanskiy [143].

Table 4.1: Parameters for simulations

Layer	Refractive index (n)	Extinction coefficient (k)
Prism	1.5137	0
Gold	0.13967	3.7105
Air	1	0

The results from the Winspall simulation [127] are depicted in Figure 4.5. A 90° triangular prism was selected for the simulation. As can be seen, the intensity minimum is expected to be at 42.61°.

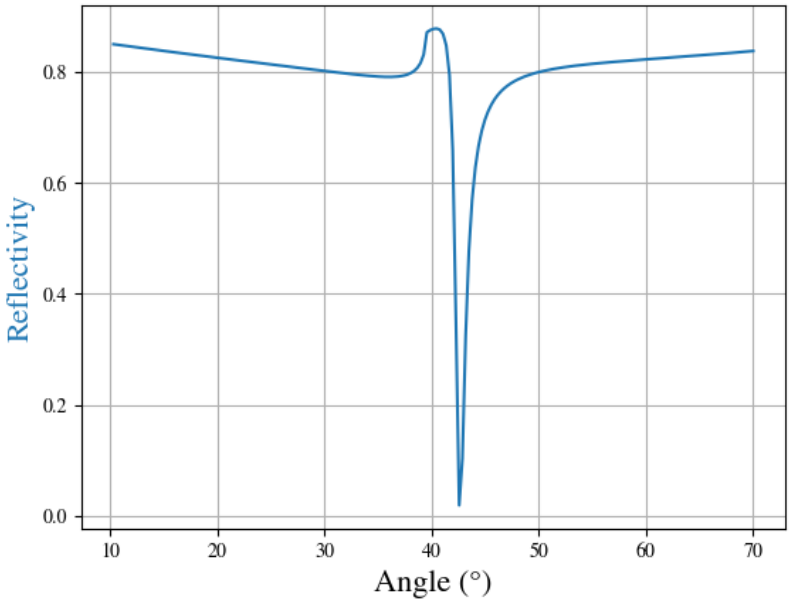

Figure 4.5: Results from the Winspall simulation

The Surface Plasmon Resonance Calculator, written by Luigi Cristofolini [128], yields the result shown in Figure 4.6. The angle at which the minimum is reached is 42.5°.

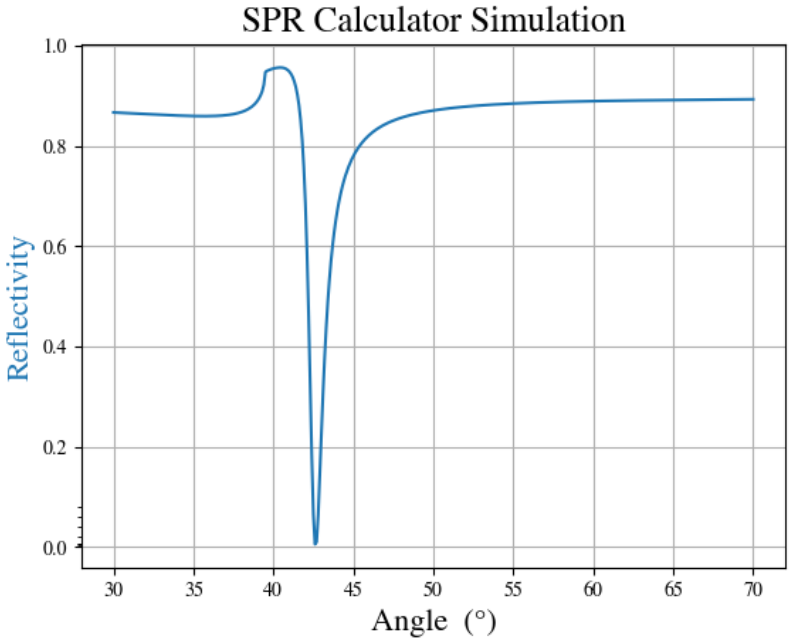

Figure 4.6: Results from the SPR calculator

The MATLAB code, written by Bipradip Chakraborty, showed the results depicted in Figure 4.7. The expected minimum is at 43.39°.

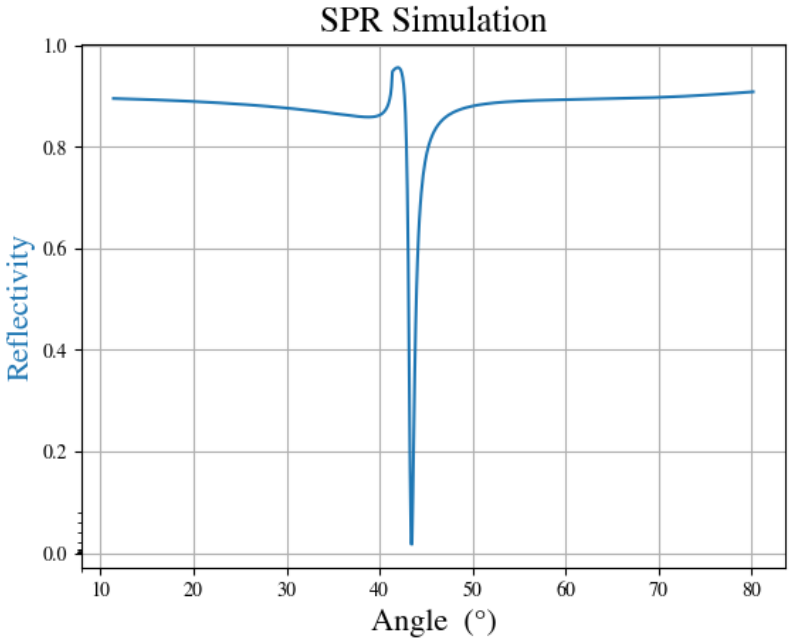

Figure 4.7: Results from the Bipradip Chakraborty simulation

The results from the MATLAB code written for this project, using the equations discussed in Section 3.1, yielded the following results. The intensity minimum is expected to be at 43.54°.

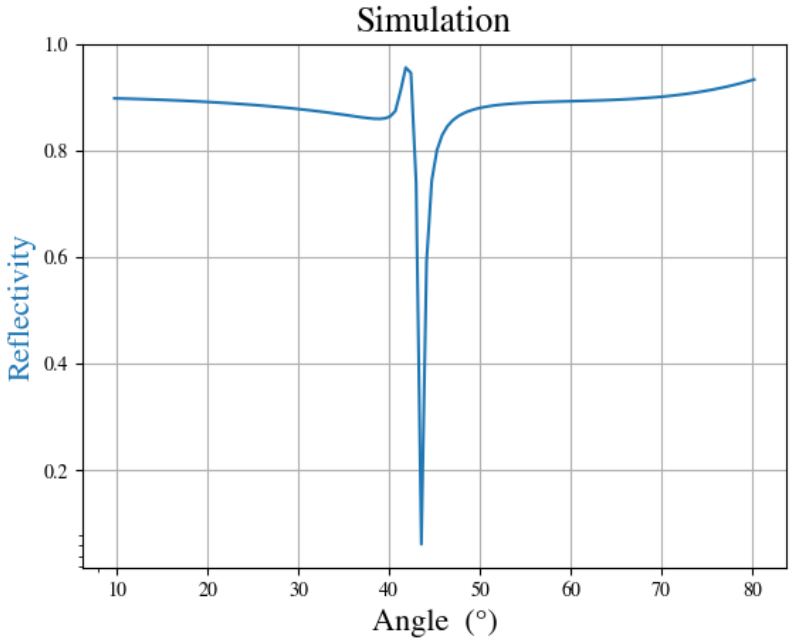

Figure 4.8: Results from MATLAB code

Table 4.2 shows a summary of the results from the various simulations. It only shows the angle and value of the expected intensity minimum.

Table 4.2: Summary of the simulations

Simulation Method	Angle of intensity minimum	Reflective units
Winspall	42.61°	0.015
SPR calculator	42.50°	0
Bipradip Chakraborty Simulation	43.39°	0.01821
MATLAB code	43.54°	0.06167

Figure 4.9 shows the results of all simulations on the same set of axes.

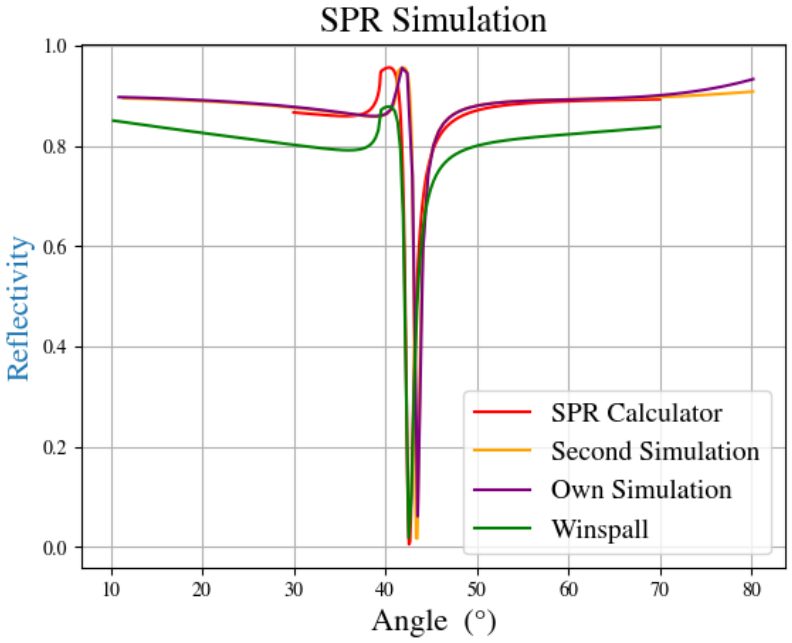

Figure 4.9: Combined simulation results

From these simulations it can be seen that, in theory, the chosen parameters should show the SPR phenomenon at about 42° to 44°.

4.7 Proposed Testing Method of the Complete System

The following testing method is proposed; initially the system will be primed with BSA, to minimise the amount of non-specific binding that takes place. This will be followed by a buffer solution. Lastly, the antigen solution with a known concentration in PBS will be introduced to the system, starting with a high and then a low concentration. Once it has been established which concentrations the system can detect, the tests will be randomised.

4.8 Summary

Figure 4.10 shows the proposed configuration. The selected immobilisation method is a SAM made with 3MPA. The gold layer will be 50 nm thick and the glass chip will be about 1 mm thick. The matching fluid will be glycerine; to couple the two glass surfaces. The refraction index of the liquid should be as close to that of the glass as possible to avoid refraction of the laser beam. The refraction index of glycerine is 1.473. Ideally, this layer should be as thin as possible, but is dependent on the roughness of the glass surfaces. Various prisms were investigated.

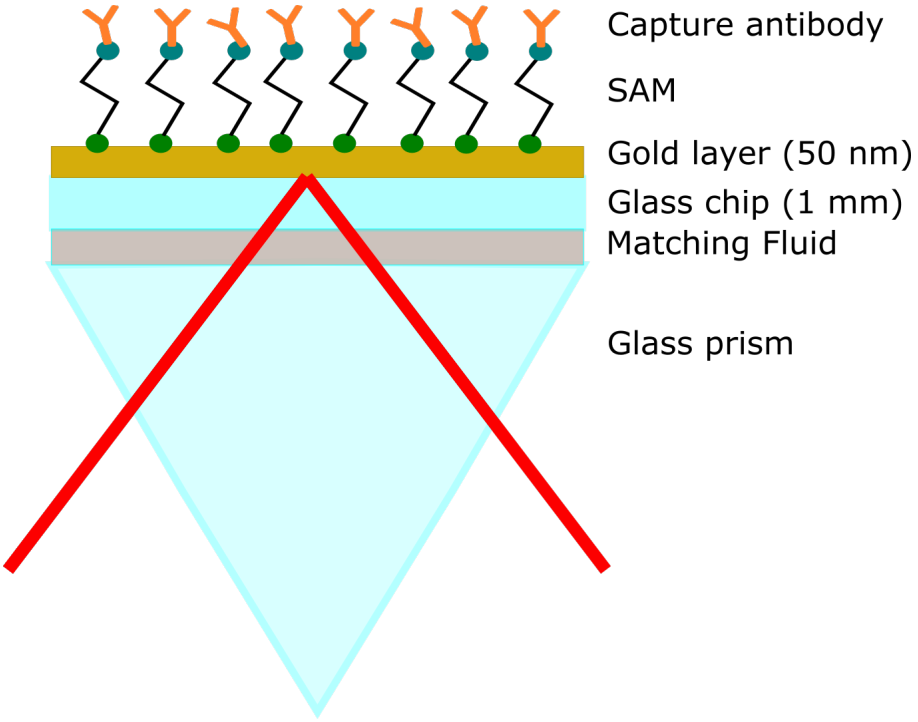

Figure 4.10: A schematic representation of the proposed configuration

Chapter 5

Design, Manufacturing and Prototyping

This chapter discusses the implementation of the design decisions discussed in Chapter 4. It details modifications to the designs, the manufacturing processes and testing of the various sections.

5.1 Hardware

The hardware of this project underwent numerous alterations during the development process. This subsection starts with a discussion on the manufacturing of the SPR sensor chip and moves on to discuss the experimental setup for the testing of the photonic aspect of the project. Further, both the electronic and microfluidic system design is discussed. Lastly, the prototype is described.

5.1.1 Sensor Chip

To manufacture the SPR chips, 1 mm thick microscope slides made of soda lime glass were cut into 15 $\times$ 15 mm squares by the Department of Chemistry and Polymer Science. Soda lime glass has a refractive index of 1.526 at a wavelength of 632.8 nm [143]. These chips were then taken to the CAF unit at the Department of Geology, where they were cleaned with ethanol before coating. They were placed into a LEICA EM ACE200 coater with a gold target. The sputter coating process was broken into four runs, 10.7, 10.6, 10.6, 10.6 nm, respectively adding to a total gold thickness of of 43.5 nm of gold. This was considered to be sufficient as previously mentioned studies recommended a gold thickness between 40 and 50 nm and Moreina *et al.*, stated that the thickness of the noble metal should be less than the wavelength of the light from the energy source [86]. Unfortunately it was not possible to add the recommended 2 nm layer of chromium or titanium for better adhesion between the gold and glass, as the CAF facilities do not offer these services. It is also important to note that titanium oxidises and hence the titanium and gold layers need to be applied directly after each other while maintaining a vacuum.

After the first batch was manufactured it was decided that, in future, the chips will be made smaller, 10 $\times$ 10 mm, to reduce the amount of chemicals required for the immobilisation process. It was also be observed that ethanol was not sufficient to clean the glass

thoroughly enough before the coating, dark marks could be seen on the chips. Therefore the second batch of chips were cut into 10 × 10 mm pieces and cleaned with a UV-O cleaner before being coated with 50 nm of gold. Figure 5.1 shows photographs of the chips that were manufactured. Figure 5.1 (a) shows unused gold chips and Figure 5.1 (b) shows some chips that were coated in gold and had gone through the immobilisation process. These chips were then cleaned with the UV-O cleaner and washed with both DI water and ethanol. It can be seen that, due to the lack of sufficient adhesion between the gold and the glass, general handling and cleaning have damaged the gold on the chips. Therefore, these chips cannot be reused.

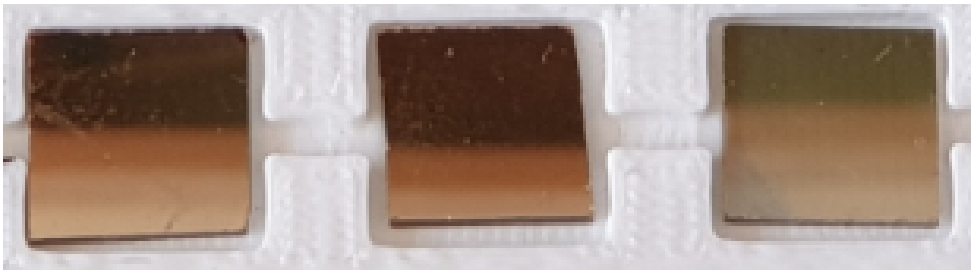

(a) Unused gold chips

(b) Used and cleaned gold chips

Figure 5.1: Gold chips before and after cleaning

Surface scans of the gold substrate were made with a Nanosurf Easyscan 2 Atomic Force Microscope. The operating mode of the AFM was set to static force mode. Figure 5.2(a) shows the results from the analysis of a clean, i.e. unused gold surface on a glass chip. The big white spots are assumed to be dust particles. An intial scan of a larger section was done, Figure 5.2(a) and 5.2(c), then a larger magnification of a selected area was done 5.2(b) and 5.2(d). The line analysis, (Figures 5.2(c) and 5.2(d)), show a cross-section of the area analysed on a specific line, indicated with the black triangle on Figures 5.2(a) and 5.2(b) respectively.

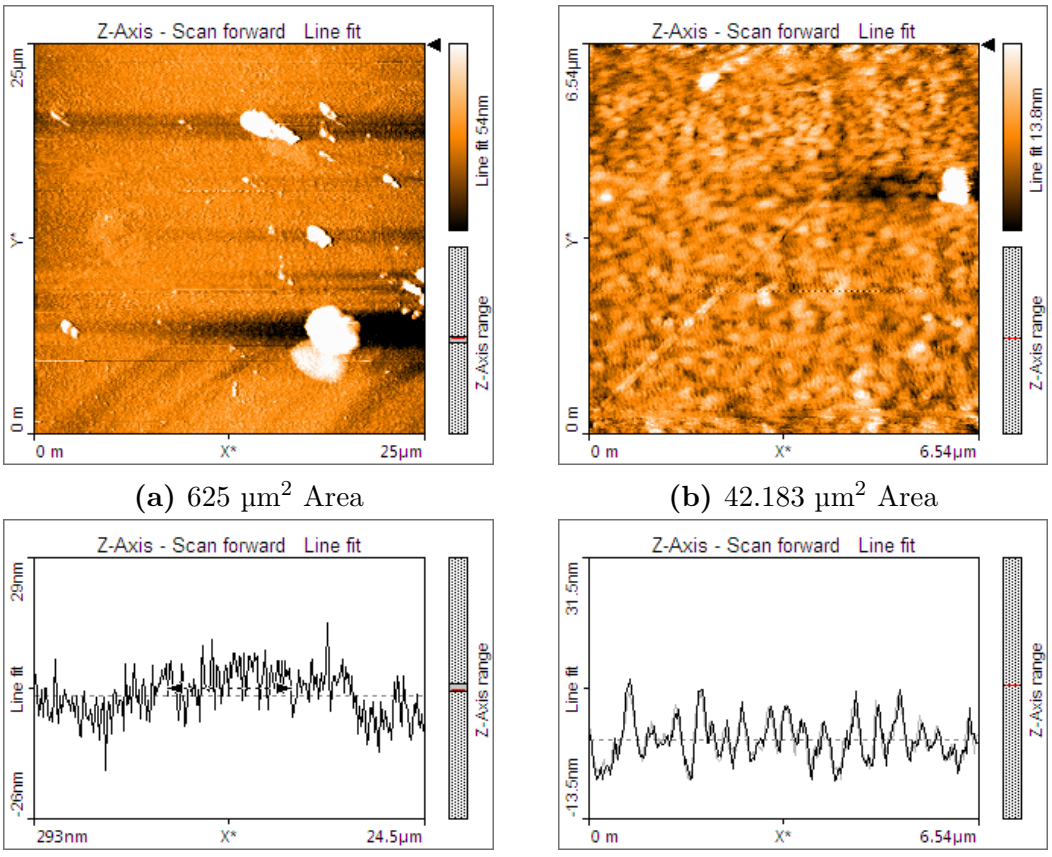

(a) 625 µm^2 Area **(b)** 42.183 µm^2 Area

(c) Cross-section of (a) **(d)** Cross-section of (b)

Figure 5.2: Atomic Force Microscope Images of Unused Gold

The average surface roughness of a 30.13 pm^2 area was found to be 1554.4 pm. Table 5.1 shows the area roughness parameters obtained from the aforementioned AFM analyses.

Table 5.1: Results of the Atomic Force Microscope of unused gold chips

Parameter	Symbol	Value	Unit
The Roughness Average	S_a	1554.400	pm
The Mean Value	S_m	-8.869	pm
The Root Mean Square	S_q	1986.100	pm
The Valley depth	S_v	-9.922	nm
The Peak Height	S_p	12.494	nm
The Peak-Valley Height	S_y	22.416	nm

Further AFM analysis was done on a damaged chip, to determine the gold substrate thickness, and the obtained image can be seen in Figure 5.3. The dark line shows the edge of a scratch. Here it can be seen that the gold layer thickness is roughly 50 nm.

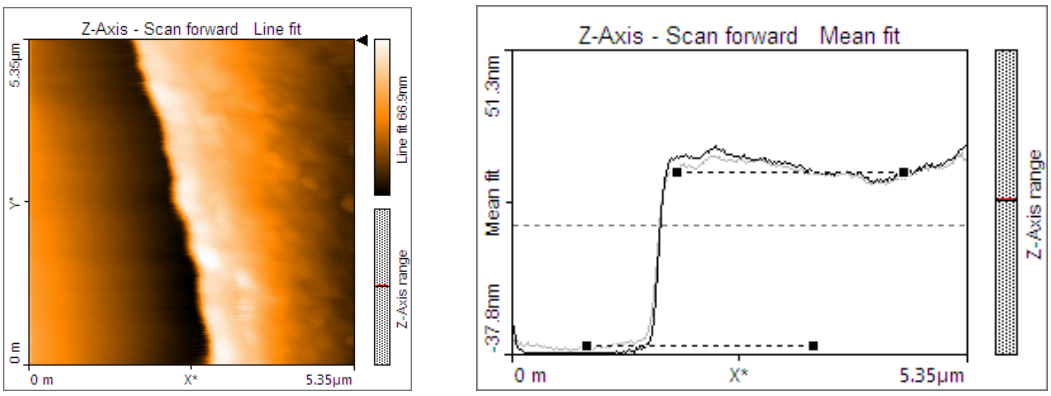

(a) Top view of edge **(b)** Cross section of edge

Figure 5.3: Atomic Force Microscope Image of a damaged gold surface

Since the chips cannot be reused, new batches of the chips had to be manufactured. The third batch, however, failed to show the SPR phenomenon that was observed with the previous batch, during the experimental setup, see Section 5.1.3 for more on the experimental setup. It was decided to do Energy Dispersive X-Ray (EDX) analysis on the gold layer on the chip. The report from CAF can be seen in Appendix B. It was seen that a sample from the second batch of chips, which showed the SPR phenomenon, was on average 99,29% gold and 0,71% copper. A sample from the third batch was, on average, only 57,16% gold and 42,84% palladium. The third batch of chips was coated at the CAF unit in Tygerberg, as the coater at the Stellenbosch unit was out of order. It was later determined that the coater at Tygerberg uses a different target, which in this case contained palladium and less gold than required.

A Winspall simulation was done using a wavelength of 635 nm and a triangular prism as inputs. At a wavelength of 635 nm, palladium has a refractive index of $n = 1.7714$ and an extinction coefficient of $k = 4.3$, which were used as parameters for the simulation. The curve obtained is shown in Figure 5.4. From this it can be seen that no clear intensity minimum can be achieved with palladium, in this configuration. Hence, it was decided that these chips are not suited for the project.

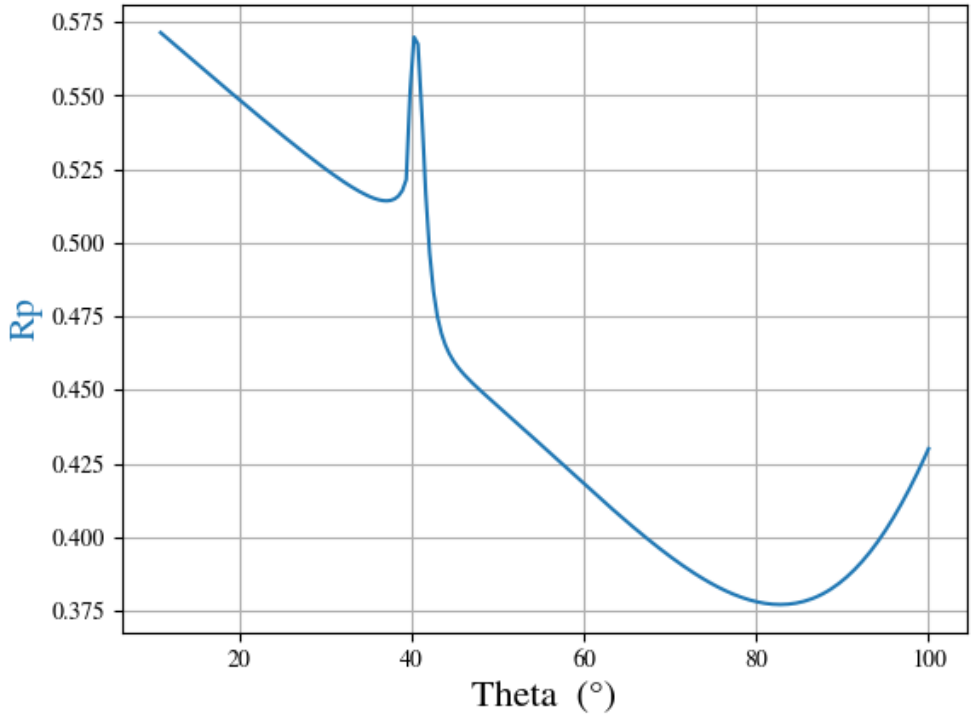

Figure 5.4: Winspall simulation of palladium substrate

A new batch of chips was manufactured. The glass was cleaned in a ultrasonic bath and, again, coated with gold at CAF using the coater at the Stellenbosch CAF unit with the gold target, which had been repaired. Once again EDX analysis on this, fourth, batch was done by CAF, and the metal film was 100% gold. These EDX results from CAF can be seen in Appendix B.

5.1.2 Laser Selection

The He-Ne laser is too big to be employed in the prototype, two other lasers were considered for the prototype. According to Masson, SPR instrumentation is down-scalable since the optical measurements depend on wavelength and angle, and not on intensity [82]. The LNCQ28MS01WW from Panasonic and the VLM-635-03 from Infiniter, the data sheets for these lasers can be seen in Appendix C, were considered. The Infiniter laser is an economical red dot laser, its light focused and collimated onto a small point. The Panasonic is a laser diode that requires additional lenses to focus the light and a heat sink. In order to test the Panasonic laser, a heat sink for the diode was designed in line with the specification in the Panasonic Application Note for RED and/or IR TO-CAN Laser Diodes [144]. A digital handheld optical power and energy meter console, the PM100D from Thorlabs was used to measure the power output from the two lasers. Three tests were run per laser and the results can be seen in Figure 5.5. The aim was to see how long the lasers take to stabilise and how their power is effected when the device is switched on or off. With the Panasonic sensor data sets one and three show that upon switching on the power output takes a while to stabilise and data set two and three show that it overshoots when it is switched off. The Infiniter laser shows a more constant out put and

from data set one it can be seen that it stabilises fast and does not overshoot when being switched on and off.

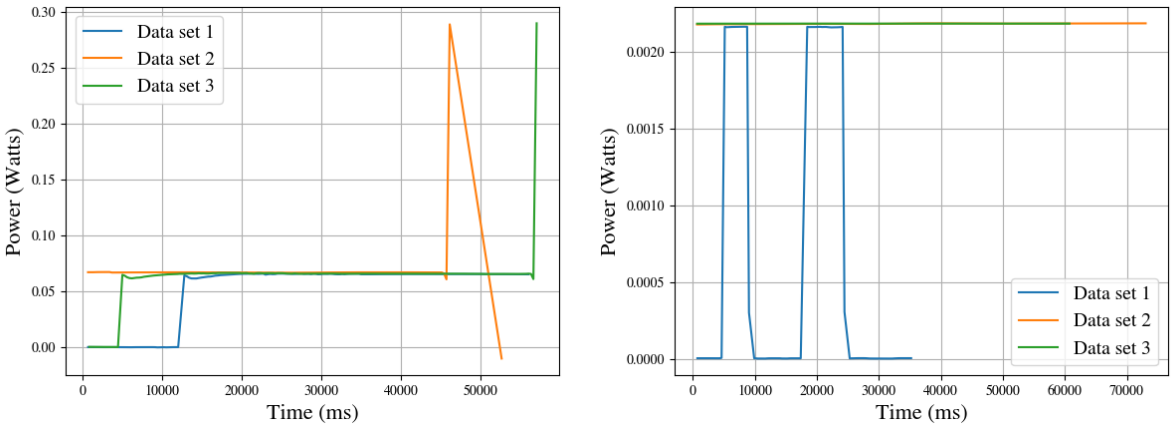

(a) Panasonic laser **(b)** Infiniter laser

Figure 5.5: Laser power test results

The properties of the lasers are summarised in Table 5.2. Both lasers wavelength lies between 600 and 700 nm, which is desired. Both lasers are partially linearly polarised. This was tested by using a linear polariser. If a linearly polarised light source goes thorough a linear polariser at a specific angle no light will exit the polariser. It can be seen from Figure 5.5(a) that the Panasonic laser overshoots when being switched off. It also takes a while for it to stabilise after being switched on. This and the fact that additional hardware is required to collimate the Panasonic laser beam, led to the Infiniter being chosen to be the prototype. Since the Infiniter laser power output is fairly stable, as seen from Figure 5.5(b), it was decided that no laser power feedback system would be required. The power supply circuit design for the laser can be seen in Section 5.1.4. Additionally the Infiniter laser is cheaper than the Panasonic laser.

Table 5.2: Comparison of lasers

Property	Panasonic laser	Infiniter laser
Wavelength	661 nm	635 nm
Polarisation	Linear	Linear
Power	0,0669 W	0,0021 W
Beam type	Divergent	Collimated
Stability	Overshoots	Constant output
Cost	R 740.80	R 341.84

5.1.3 Experimental Setup

The experimental set up, that was described in Section 4.1.1 was built at the Department of Physics at Stellenbosch University. The laser employed for this setup was a Siemens LGK 7653 helium-neon (He-Ne) laser with an emission wavelength of 632.8 nm. A photograph of the setup can be seen in Figure 5.6. A beam expander was implemented to

enlarge the light beam. This was done to make the light signal bigger, and therefore easier to see with the human eye. Glycerine was used as the coupling fluid between the glass chips and the prism. For this setup, a 30 mm equilateral triangular K9 glass prism with a refractive index of 1.5146 at 632.8 nm was used [143]. A rotation stage, to secure the prism in position, was designed and 3D printed. It was designed such that the gold layer was the centre of rotation, which was done to ensure that the laser hits the gold layer. Linear polarisers were added to polarise the light to the desired state. The p-polarisation of the light was confirmed by using an optical phenomenon known as the Brewster's angle. When p-polarized light moves from one dielectric medium to another at the Brewster angle it will undergo complete transmission. Therefore, by implementing a glass plate it is expected that a minimum in the reflected light is seen if the incident ray is p-polarised [145].

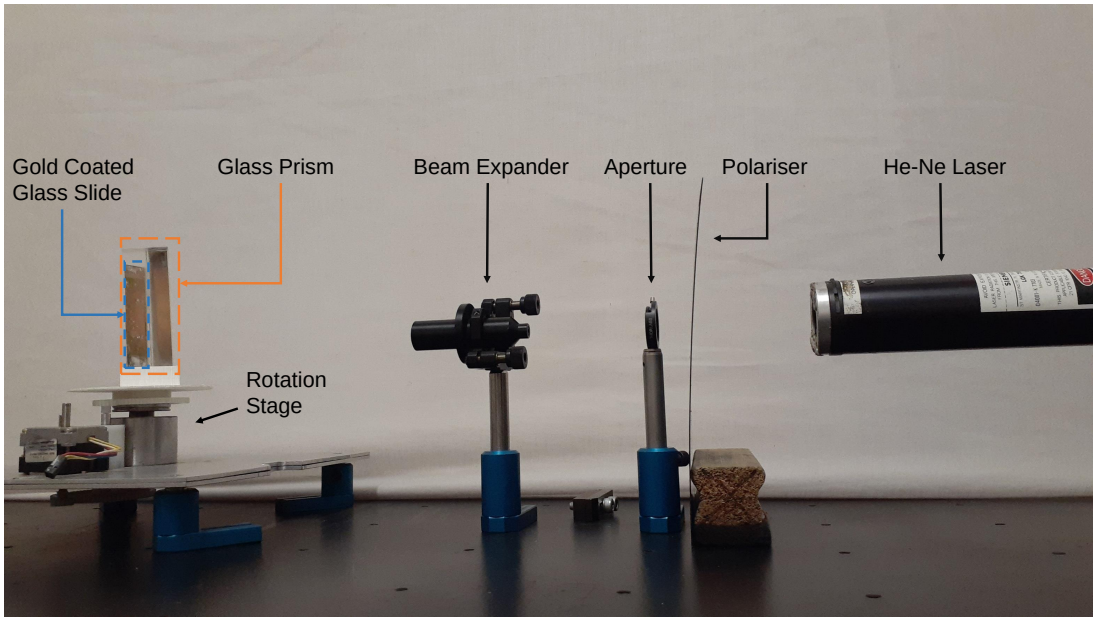

Figure 5.6: Photograph of the prototype experimental setup of SPR

This setup yielded promising results. A dip in the reflected light intensity was observed when p-polarised light hit the prism at an angle of approximately 45°. To confirm that the dip observed was indeed SPR the polariser was flipped 90° so that the light source was s-polarised, in this configuration the dip was not observed, hence it is concluded that the SPR phenomenon occurred. Figure 5.7 shows the brightness of the reflected laser light at different prism angles. This image was created by taking snap shots from a video that was taken as the prism was rotated. These snap shots were then combined into one image. It shows the initially full signal as it is reflected off the gold surface as the signal gradually dims to the SPR effect and then back as the full size. This is in line with what is expected, when looking at a SPR curve. The scattering of light is possibly due to the surface roughness of the gold layer.

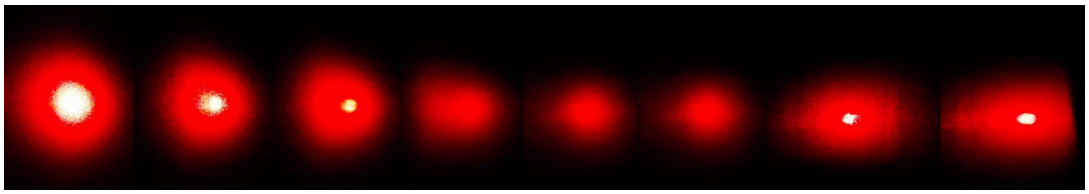

Figure 5.7: SPR phenomenon observed with the triangular prism and the He-Ne laser

The SPR experiment was repeated implementing the Infiniter laser, in place of the He-Ne laser. The dip in the reflected light was observed, however it was less defined and not as dark as with the helium-neon laser.

The experiment was repeated once again with the helium-neon laser and a different prism. The prism used was a half cylinder prism made of an unknown transparent plastic-like material. The light reflected dispersed in the desired manner and the SPR phenomenon was observed. However, the dip was not as dark as with the K9 optical glass prism, and it may be due to the material lacking clarity and light not scattering as anticipated. Another half cylinder prism of unknown material was acquired, but it showed no visible dip in the light intensity.

An additional prism was ordered from Thorlabs. This prism is a uncoated plano-convex cylindrical lens made from N-BK7 with a D-like shape. A CAD image of the prism, from Thorlabs, can be seen in Appendix C. The refractive index of N-BK7 material is 1.5151 at 632.8 nm wavelength [143]. A new rotation stage adapter was designed and 3D printed for this prism. It was initially tested in the same configuration as in Figure 5.6, with the He-Ne laser. The expected bifurcation of the light could be seen. However, the result was unclear and additional unexpected reflections were observed. The beam expander was removed to decrease the beam size and screw locations, on the 3D printed adapter, were altered to eliminate them as possible sources of additional reflections. This led to a clearer result. A photograph of the reflected light from this setup is shown in Figure 5.8. The test was repeated using the Infiniter laser, to confirm if this D-shaped prism and the chosen laser show the desired result. The SPR phenomenon could be clearly observed. Further, the polariser that was initially used was a fairly large plastic sheet polariser, this made it difficult adjust and align. Therefore, a better quality glass lens polariser and turntable frame were purchased.

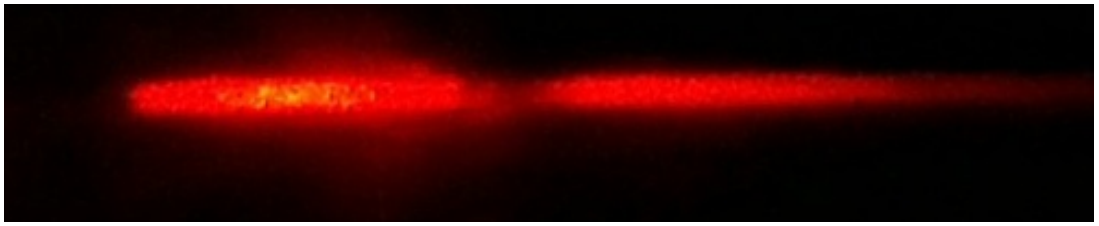

Figure 5.8: SPR phenomenon observed with the D-shaped prism and the He-Ne laser

A summary of the various tested setups and their results can be seen in Table 5.3. From this table it was decided to employ the Infiniter laser, no polariser and the D-shaped prism form Thorlabs for the development of the prototype.

Table 5.3: Summary of experimental setups

No.	Setup					Result
1	He-Ne laser	Polariser 1	Beam expander	Triangular prism	Gold chip	A dip was observed in the reflected light was observed, as the prism was rotated. The lowest intensity was achieved at roughly 45°
2	He-Ne laser	Polariser 1		Triangular prism	Gold chip	Similar to Experiment 1 the SPR phenomenon was observed. However, as expect, due to the lack of the beam expander, the resultant signal was smaller.
3	He-Ne laser	Polariser 1	Beam expander	Semicircular prism 1	Gold chip	The light dispersed in the desired manner, and the SPR phenomenon could be observed. However it was very unclear and not as clean as expected.
4	He-Ne laser	Polariser 1	Beam expander	Semicircular prism 2	Gold chip	As with experiment 3 the light dispersed. However the SPR phenomenon was not observed.
5	He-Ne laser	Polariser 2		Triangular prism	Gold chip	This setup was done to establish the best orientation for the new polariser. It was found that the darkest dip in the light was obtained when the polariser was set to 70°.

6	He-Ne laser	Polariser 2	Beam expander	D-shaped prism	Gold chip	The signal obtained was very messy. A lot of unexpected light scattering influenced the signal. SPR was observed.
7	He-Ne laser	Polariser 2		D-shaped prism	Gold chip	The removing of the beam expander cleared the signal. SPR was observed.
8	Infiniter laser	Polariser 1	Beam expander	Triangular prism	Gold chip	As in experiment 1 a dip in the reflection was observed, the darkest point was achieved at roughly 45°. However, the dip was not a dark as in experiment 1.
9	Infiniter laser	Polariser 1		Triangular prism	Gold chip	In this setup the SPR dip was observed. A smaller less prominent dip than experiment 1 was achieved.
10	Infiniter laser	Polariser 2		Triangular prism	Gold chip	The polariser was set to 70°. The SPR dip could be observed.

11	Infiniter laser 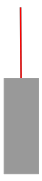	Polariser 2 		D-shaped prism 	Gold chip 	A clear SPR signal was observed.
12	Infiniter laser 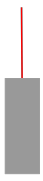			D-shaped prism 	Gold chip 	The SPR phenomenon was observed.

The setup lacked good repeatability. The SPR results were not always obtained, it was assumed that misalignment and dust may be the cause of the problem. The set up was cleaned and realigned. There were still issues with achieving the SPR signal with the D-shaped prism. It was considered that the focal point of the D-shaped prism might be the cause of the problem [146]. The focal point lies outside of the lens. Figure 5.9 shows an image from the ThorLabs website [147].

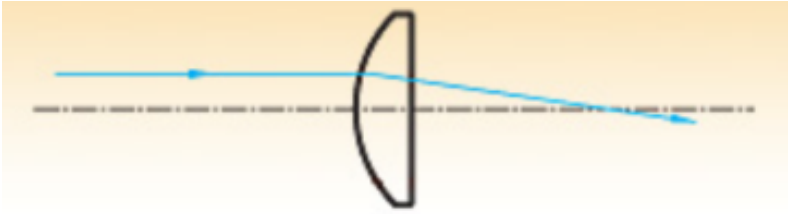

Figure 5.9: Schematic presentation of the focal point of a lens (from [147])

It was considered implementing a system of lenses with different focal lengths, to adjust the focal point to fall exactly on the gold layer, may help [146]. Venteon vWaistwatcher computes the propagation of laser beams among other functions. Using a free version of Venteon vWaistwatcher software the laser beam's propagation and behaviour through lenses was simulated [148]. Figure 5.10 depicts the results from the simulation. It was decided to place a lens with a radius of curvature of 51 mm, 10 cm away from the D-shaped prism. According to the simulation this will force the focal point to be on the gold substrate.

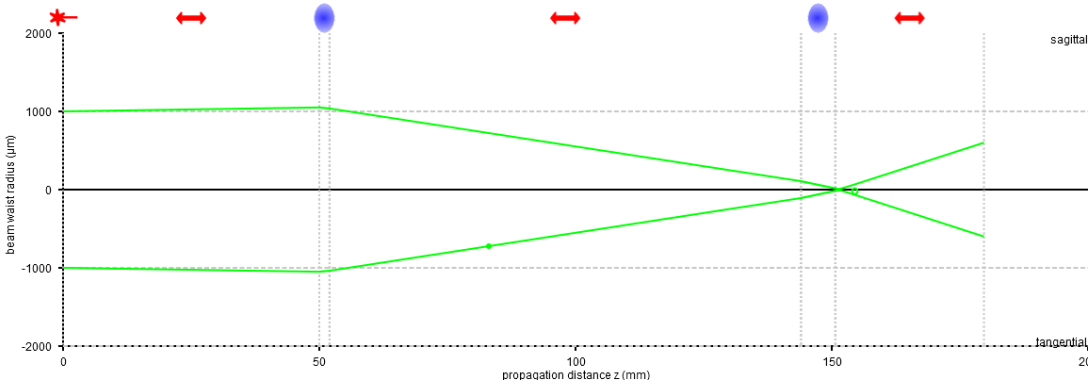

Figure 5.10: Results from the vWaistwatcher simulation

Additional lenses were applied to shift the focal point. Unfortunately, the SPR phenomenon could not be observed. It is suspected that the shape of the D-shaped prism is an issue. Figure 5.11, shows the possible behaviour of the light inside of the D-shaped prism. It is possible, because the sides of the prism (indicated in green) are sand blasted and that the light cannot escape the prism. From the image it can seen that as moving the beam relative to the prism, and ensuring that the light enters the prism at the correct angle and location may solve the problem. This may also explain why the setup worked previously.

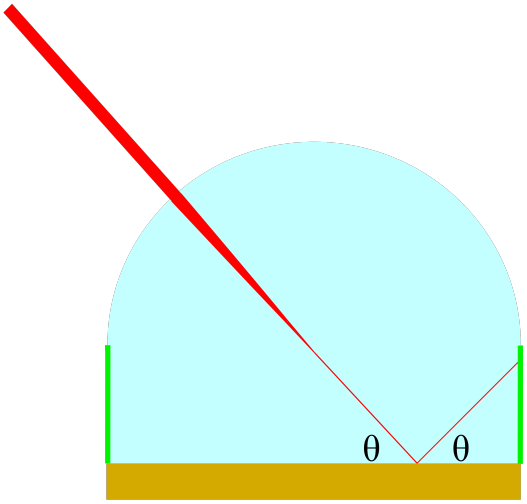

Figure 5.11: Schematic representation of light refraction in the D-shaped prism.

Various other setups using different prisms, matching fluids and beam splitters were tried, however these also did not yield a clear SPR phenomenon with the D-shaped prism [149]. A triangular prism, which had a layer of silver directly coated on one plane did produce a clear resonance. Hence the prism and the gold layer could be the reason for the poor results. More tests were done using the same triangular prism and a gold coated slide as with previous tests. Here a decrease in the contrast could be observed, however these results were not as distinct as those previously obtained. A setup such as this is very sensitive and hence good quality optics are important in these experiments. Further, all these tests were done using the naked eye, there may have be instances were SPR was achieved, but not seen, as the human eye is not ideal for intensity sensing. SPR was seen previously and with more investigation a reproducible set up could be produced.

5.1.4 Electronics

A power supply circuit was designed for the Infiniter laser consisting of a 9 volt battery, a 5 volt voltage regulator and a 33 Ω, 2 Watt resistor. The circuit can be seen in Figure 5.12. The 9 V battery allows the circuit, along with the laser, to be mobile. The voltage regulator ensures that the voltage across the resistor and and laser does not exceed 5 V and the resistor controls the current entering the laser. From Ohm's law the current entering the laser is less than 50 mA and the voltage across it is is less than 5 V. This is in line with the values specified on the components data sheet. A Printed Circuit Board (PCB) was designed, created and tested. This was done to ensure that the circuit is stable and that the connections can tolerate repeated movement. Additionally, a box to hold the PCB and the battery was designed and 3D printed. This allowed the circuit board to be transported while minimising the wear on the components and wires.

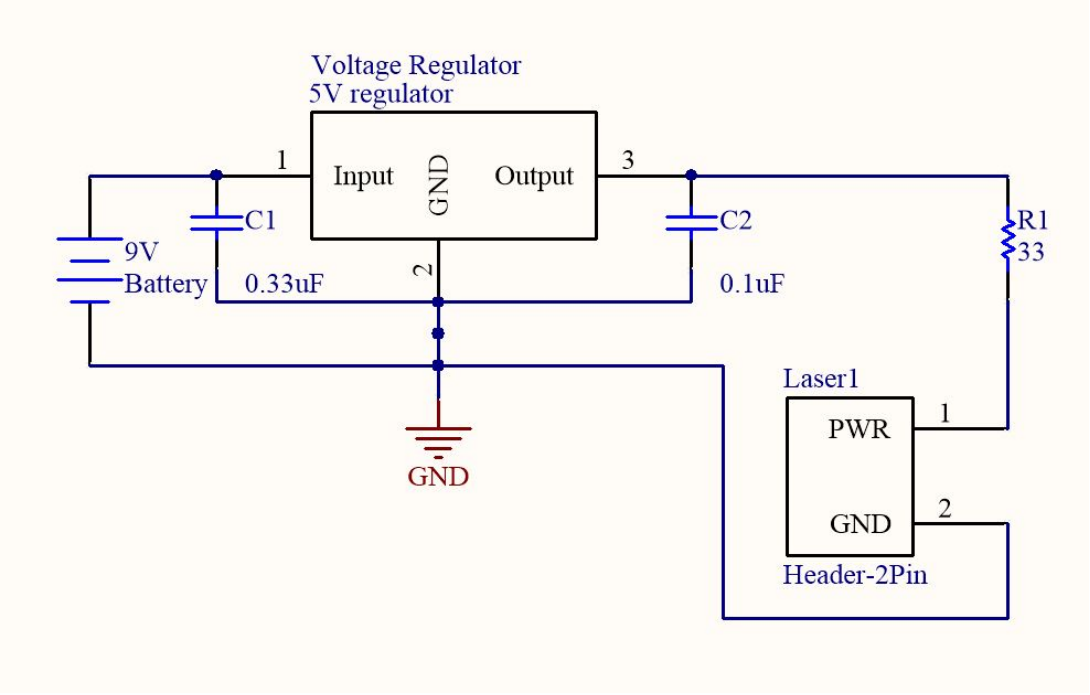

Figure 5.12: Schematic presentation of electronic circuit

5.1.5 Microfluidic system

The design for the microfluidic system was repeatedly adjusted and edited, due to manufacturing issues in the form of the unexpected breakdown of the SAND group laser cutter, as well as other factors. The revised design can be seen in Figure 5.13. The fluid flow direction is as indicated with the arrows on the assembly drawing, Figure 5.13(a). The components width is 14 mm and the length is 20 mm. The channel is 9 mm long. This dimension is based on the chip size, since the chip is 10 mm wide the channel need to be shorter. The width at the inlet and outlet is 1 mm making it slightly bigger than the inlet and outlet holes, which is based on [100] allowing for standard needle connections. The channel is 4 mm wide at its widest point, making a well so that more sample comes into contact with the surface of the chip. The diamond shape with rounded edges was designed to promote laminar flow, as opposed to a round well.

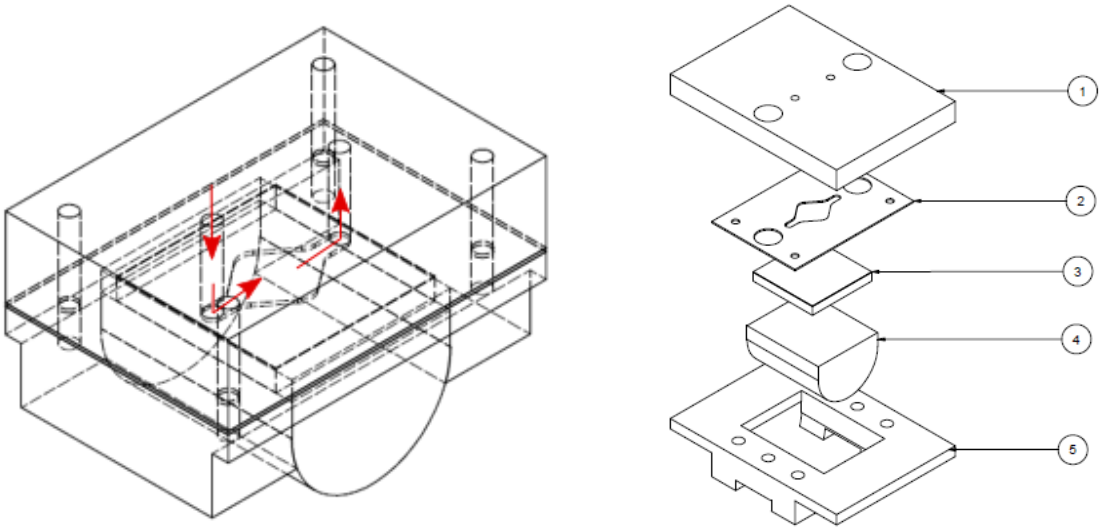

(a) Assembled part **(b)** Exploded view of part

Figure 5.13: Schematic representation of the microfluidic system

Figure 5.13(b) shows an exploded view of the assembly. Part one is the top, which is also seen in 5.16(c). Part two is the gasket, which is also seen in 5.16(b). Part three is the gold coated glass chip and part four is the glass prism, the CAD image of the prism can be seen in Appendix C. Part five is the prism holder that secures the prism in place.

COMSOL simulations of the designed microfluidic channel were done [150]. The simulations were done at an inflow rate of 1 ml·s^{-1}. Figure 5.14 and Figure 5.15 show the shear rate and velocity respectively. Figure 5.14(a) shows the shear rate at the bottom of the flow channel, where the shear rate is the greatest. The flow inlet is at the bottom and the outlet at the top. It can be seen that the largest shear rate is reached at the inlet. Figure 5.14(b) is a cross section through the width of the flow channel. Here it can be seen that the greatest shear rate is reached at the top and bottom of the channel. The shear rate at the bottom of the channel is on the left side. Since the shear rate is high in this area the gold layer may be damaged.

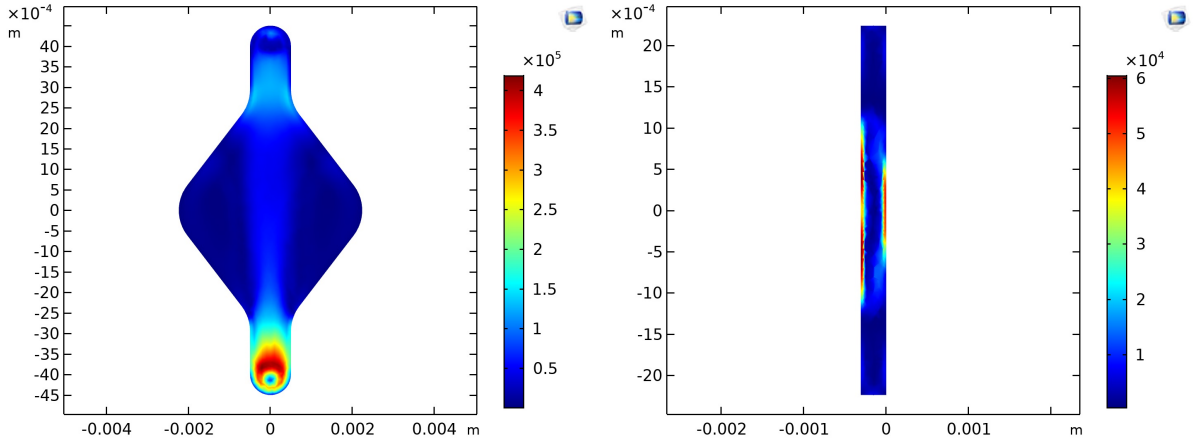

(a) Shear rate at bottom of microfluidic channel

(b) Cross section of shear rate

Figure 5.14: Shear rate in the microfluidic channel

Figure 5.15(a) shows the velocity profile at mid-height of the microfluidic channel. The liquid reaches a velocity of 6 $m \cdot s^{-1}$ at the inlet. A steady velocity of approximately 2.5 $m \cdot s^{-1}$ is reached at the centre of the channel. Since both the shear rate and the velocity are high, but not usual for flow channels, it was decided that a inflow rate of less than 1 $ml \cdot s^{-1}$ would be used.

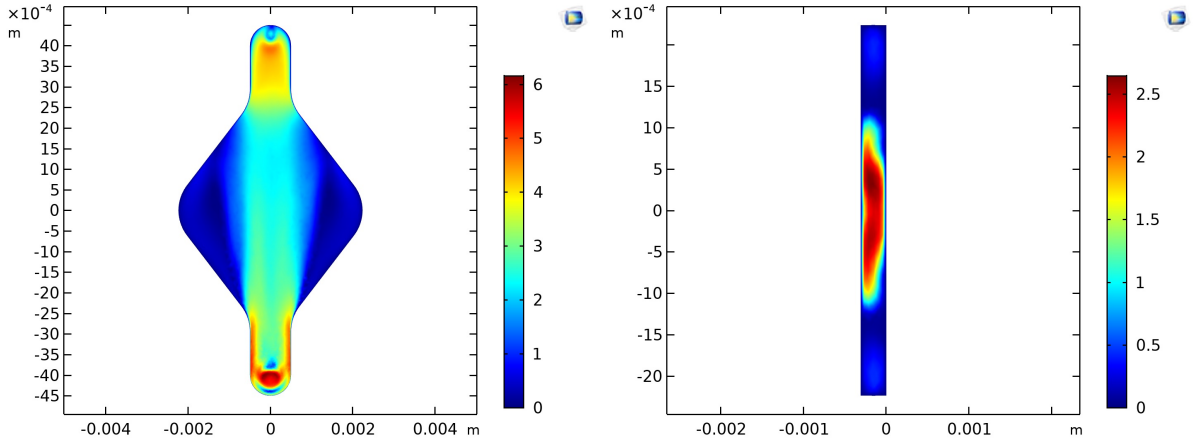

(a) Velocity in microfluidic channel

(b) Cross section of velocity in microfluidic channel

Figure 5.15: Velocity in microfluidic channel

Figure 5.16, shows the manufactured components of the flow channel. Initially the parts were 3D printed, however, the material was difficult to work with and since the resolution was not good enough, these parts were not sufficient. The gasket, Figure 5.16(b), was laser cut from latex. The prism holder, Figure 5.16(a), as well as, the top 5.16(c) were machined out of acetal. Hypodermic needles were shortened and inserted to the inlet and outlet (found on the top) of the microfluidic system and glued in place. This allowed the syringes to be easily connected to the needle hub, eliminating leakages and allowing the flow system to be easily connected to a syringe pump.

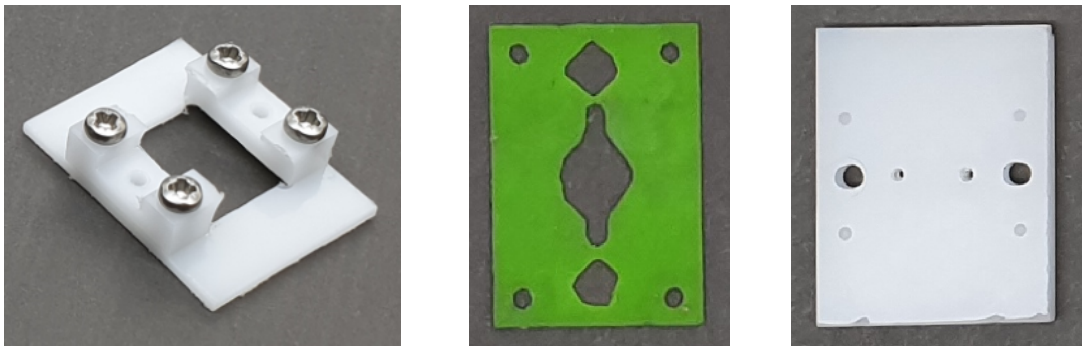

(a) Prism holder, bottom part of fluidic system

(b) Gasket

(c) Top part of fluidic system.

Figure 5.16: Parts of the microfluidic system

The system was designed and manufactured so that there is an overlap between the gasket, the gold chip, the prism holder and the top. This was done so that when the screws are tightened, pressure is exerted on the gasket and the system seals tightly. The system was tested with DI water and it was found that no leakage occurs.

5.1.6 Prototype Frame

The prototype frame was designed to be as flexible as possible. The laser's position as well as it's angle can be adjusted. The camera and the prism holder are in slots that allow for the x-position to be adjusted. However, the parts are all kept in alignment in the y-axis. This ensures that the laser light hits the prism at the correct angle and the reflection then falls where the camera is able to see it. The height of the assembly can also be adjusted, allowing the distance between the laser and the prism to be altered as required.

The original prototype frame design is depicted in Figure 5.17. The parts of the prototype frame are as follows:

1. Bracket
2. Camera holder
3. Laser
4. Screws
5. Microfluidic channel system
6. Laser holder
7. Threaded rods

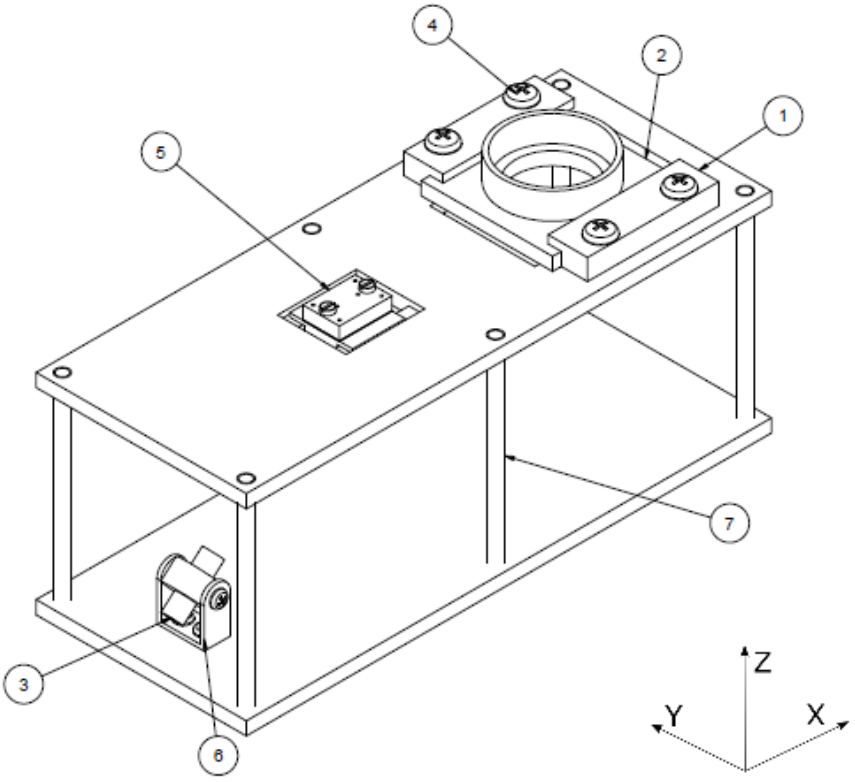

Figure 5.17: Original prototype frame design

The brackets act as rails for the camera holder, into which the AUSDOM AW615 1080P PC WebCam fits securely. The screws secure the brackets in place. The laser can rotate in the laser holder, so that the angle at which the light hits the prism can be adjusted. The threaded legs allow the height of the prototype to be adjusted. Further, a box enclosure that slides over the assembly was manufactured and painted with Black 2.0, to minimise the light entering and scattering within the prototype.

The drawing files of selected parts can be seen in Appendix D

5.2 Immobilisation

An immobilisation tray was designed, to reduce the amount of chemicals required for the immobilisation process, when compared to using individual cuvettes for each chip. The tray is reusable and can be seen in Figure 5.18. The tray has enough space for 50 SPR chips and is machined out of acetal (Delrin). This material was chosen due to its inert nature. It should not take part in chemical reactions, thus it will not effect the immobilisation process. This also makes it reusable. The tray has tweezer slots to allow for the sensor chips to be easily handled with tweezers. Further, the tray fits into a air tight container which protects the samples from the environment and allows them to be transported easily. The tray was machined at the workshop of Department of Electrical and Electronic Engineering at Stellenbosch University. Figure 5.18(a) shows the initial design of the tray and Figure 5.18(b) shows a photograph of the tray. The initial well depth was 3 mm. However, it was found that this is not deep enough and the depth was

adjusted to 4 mm, allowing for the required immobilisation volume to be added without spilling. The white acetal can easily be labelled with a black marker, to keep track of the samples and can then be easily removed using ethanol. The tweezer slots worked well and allowed for easy handling of the chips.

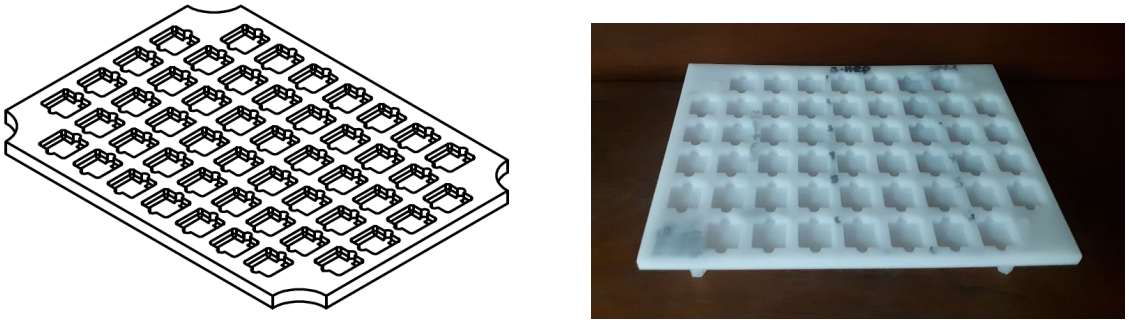

(a) Immobilisation tray design **(b)** Photograph of immobilisation tray

Figure 5.18: Immobilisation Tray

Immobilisation took place at the Department of Physiology at Stellenbosch University.

5.2.1 SAM formation

During the first iteration of the immobilisation process 18 chips were used and the protocols described in section E.1 were used. For this first iteration 10 mmol concentration of 3MPA was used in a 70% ethanol solution. BSA was used as a protein instead of the capture antibody, to reduce cost of the experiment and verify the immobilisation method. BSA is a protein, that like antibodies, has amine groups on its surface, hence the immobilisation process will be the same. Should the immobilisation of the BSA be successful the following experiments can be done using antibodies.

The Ellman's assay results show that in 15 of the 18 gold chips there were lower amounts of thiols in the remaining solution. Hence, one can assume that in those 15 cases some of the thiols were adsorbed onto the gold. However, these amounts were very low and the results were inconsistent. As can be seen from the standard curve in Figure 5.19(a) for the Ellman's solution, the optical density values for the high percentages (80 - 100%) are in very close proximity to each other, which could indicate that the Ellman's assay saturates. Figure 5.19(b) shows a scatter plot of the sample data, the red line indicates the optical density of the 100% from the standard curve. These results may indicate that either very little binding took place since so much thiol remained in solution, or that the gold was saturated since a high concentration of 3MPA was used.

The sample labelled *four (4)* in Figure 5.19(b) has a significantly lower optical density value than the other samples. This is likely due to human error during the sample collection process. It is also important to note that since the sampling is done by hand, it takes time to add the Ellman's solution to the samples, hence not the same amount of time has elapsed between the all the samples.

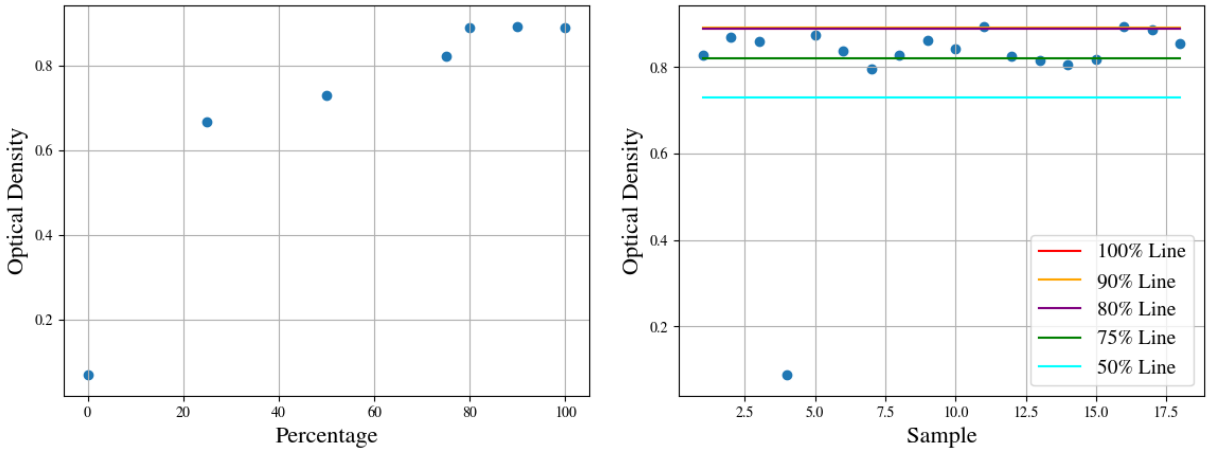

(a) Ellman's assay standard curve **(b)** Ellman's assay sample results

Figure 5.19: Ellman's assay test one results

In the Bradford scatter, shown in Figure 5.20(b), three of the results lie above the 100% line, which implies that those samples contained more protein than the control. The remaining 15 samples are between the 100% and 75% lines. Since some samples contained a higher concentration of the protein than the control, it can be assumed that either a measurement mistake was made or non-specific adsorption may have taken place in the Eppendorf Tubes (Eppis) and the tray. Another reason for these results may be that the carboxyl activation with the ECD/NHS linker may not have been successful.

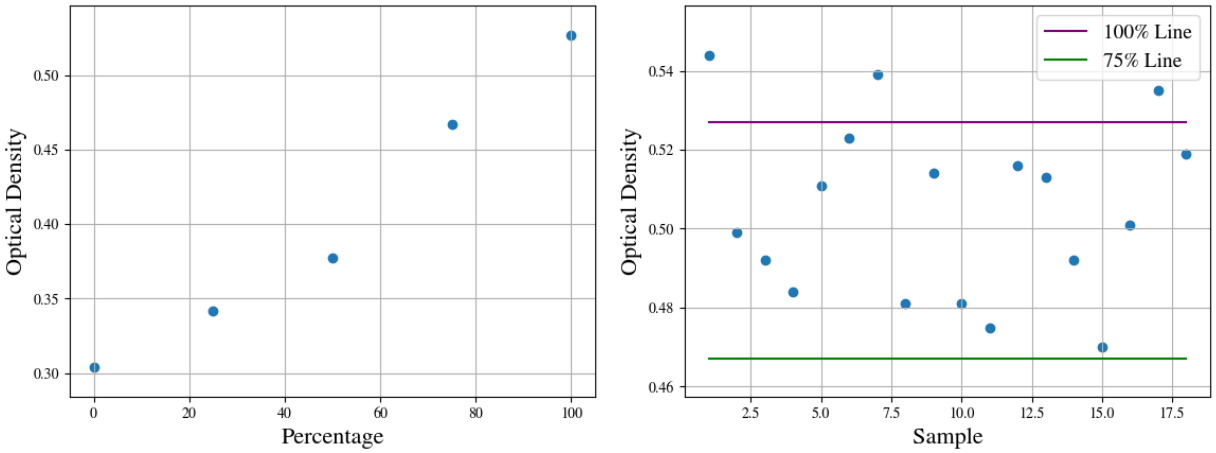

(a) Bradford assay standard curve **(b)** Bradford's assay sample results

Figure 5.20: Bradford assay test one results

Since the Ellman's assay saturated the experiment was repeated using a 5 mmol concentration of 3MPA in 100% ethanol. Five chips were prepared in the immobilisation tray and placed on the shaker overnight. The Ellman's assay standard curve can be seen in Figure 5.21(a) The Ellman's essay results Figure 5.21(b) showed that the samples lie

between the 50 and 100% lines. This indicates that less thiols remained in the solution than in the control, therefore one can assume that thiols adsorbed onto the gold layer.

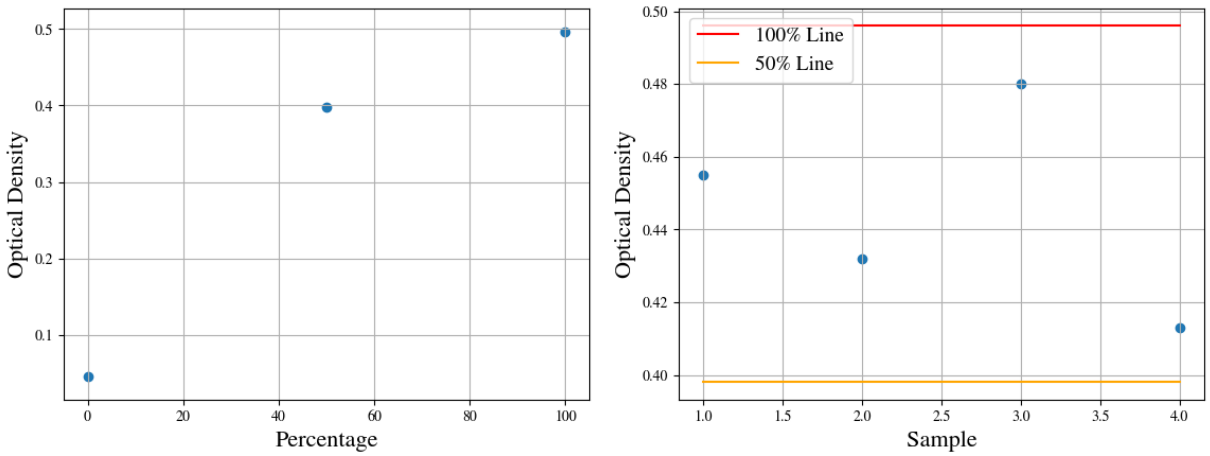

(a) Ellman's assay standard curve **(b)** Ellman's assay sample results

Figure 5.21: Ellman's assay test two results

The Bradford standard curve can be seen in Figure 5.22(a), however this standard curve's 100% optical density value seems out of place. This may again be due to human error during the making of the standard curve samples. The Bradford solution formed bubbles when introduced to the sample, these bubbles may have led to errors during the well plate reading process in the spectrophotometer. The results from this test lie between the 25% and 75% line, hence it is assumed the protein binding to the 3MPA SAM took place.

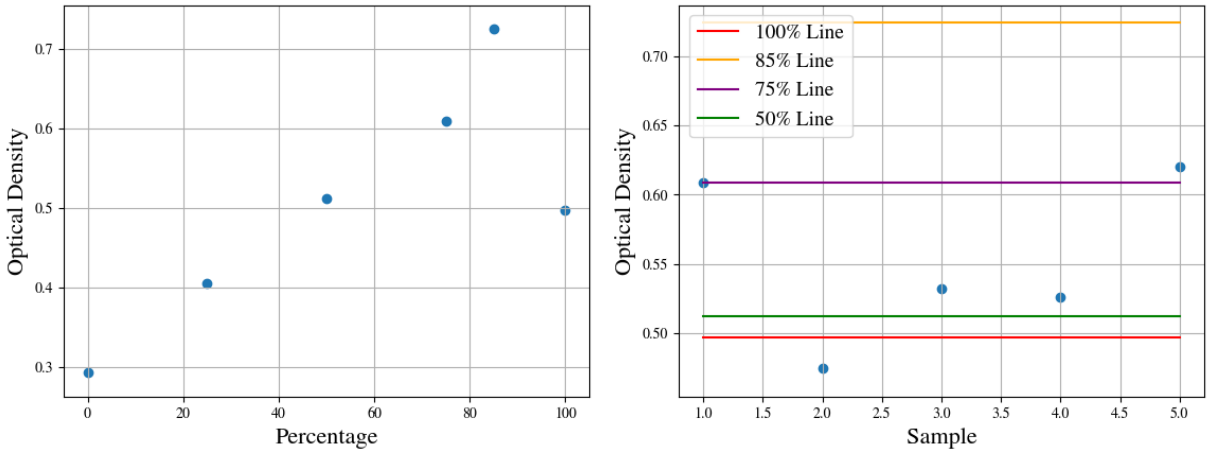

(a) Bradford assay standard curve **(b)** Bradford assay sample results

Figure 5.22: Bradford assay test two results

It was during this point of the project that it was brought to the attention of the SAND research group that a fault in the EDC suppliers shipping method may lead to problems

in the immobilisation process [151]. EDC forms by-products when stored or shipped at too high temperatures. These by-products may interfere with the immobilisation process, leading to a decrease in immobilisation efficiency [151]. New EDC from a different supplier was ordered for further experiments.

Additionally, sulfo-NHS was purchased by the SAND research group. Sulfo-NHS is water soluble and since MES buffer is prepared in DI water, it is thus water based and therefore one can expect that the sulfo-NHS dissolves better in the MES buffer than the NHS, which may lead to better results.

The immobilisation procedure was repeated once again, this time 5 previously unused and 5 previously used gold chips where used. The used gold chips were from previous immobilisation tests and were cleaned in the UV-O cleaner and washed with ethanol. The gold layer was partially visibly damaged after this process, refer to Figure 5.1. This is likely due to the lack of the chromium or titanium adhesion layer.

Figure 5.23 shows the results from this test. The samples labelled *'N'* refer to the previously unused chips and the samples labelled *'C'* refer to the previously used chips. The Ellman's and Bradford assay standard curves, Figures 5.23(a) and 5.24(a) respectively, are satisfactory. Figure 5.23(b) shows that more 3MPA was adsorbed onto the previously used chips as opposed to the previously unused chips. This result is unexpected as the gold layer was damaged and therefore less gold surface area was available for the absorption to take place.

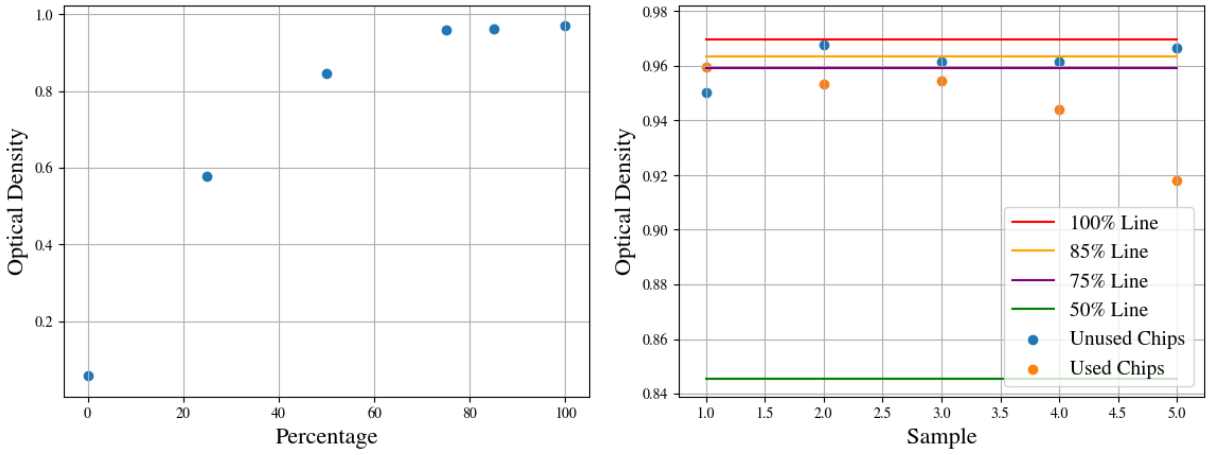

(a) Ellman's assay standard curve **(b)** Ellman's assay sample results

Figure 5.23: Ellman's assay test three results

The Bradford standard curve, as well as the results, can be seen in Figure 5.24(a) and Figure 5.24(b), respectively. All of the Bradford sample results lie above the 100% control value, which is unexpected and not what is desired. Again, this may be due to human error in the immobilisation process, non-specific adsorption or the EDC/sulfo-NHS not working as expected.

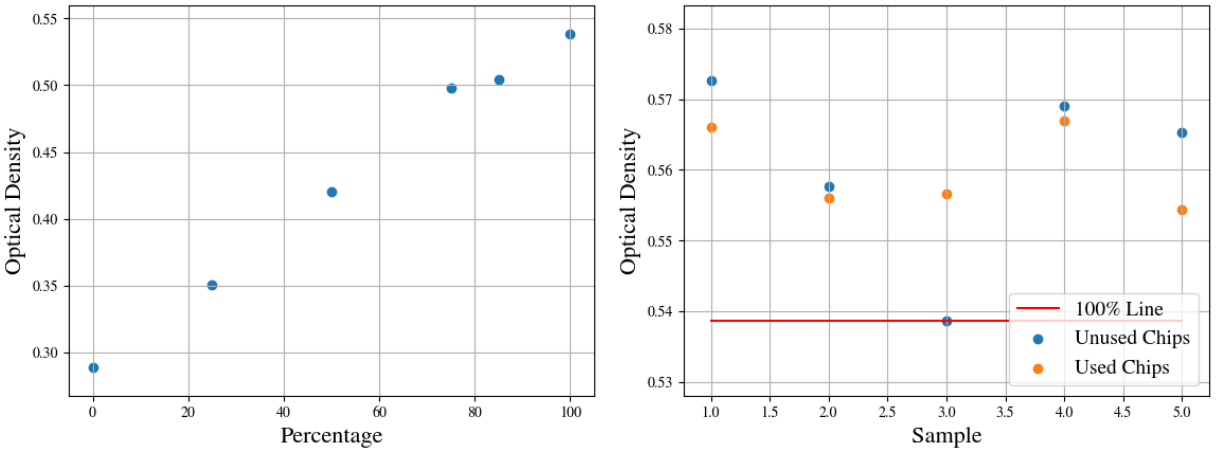

(a) Bradford assay standard curve **(b)** Bradford assay sample results

Figure 5.24: Bradford assay test three results

A Thermo Scientific NanoDrop Lite spectrophotometer was used to analyse the EDC/NHS samples. NHS is an autofluorescing chemical and the NanoDrop sensor exposes the sample to a specific wavelength and measures the optical density of the sample. The higher the reading, the more NHS within the sample, i.e. the less NHS has bound onto the chip. Figure 5.25 shows the results obtained from the NanoDrop Spectrophotometer. The control sample is depicted in red, the previously unused chips in green, and the previously used chips in blue. It can be seen from the graph that blue dots, i.e. the previously used chips, all attained higher optical density readings than the previously unused chips (seen as green dots). This means that more NHS was in the samples of the previously used chips, i.e. more NHS has bound to the previously unused chips than to the used chips.

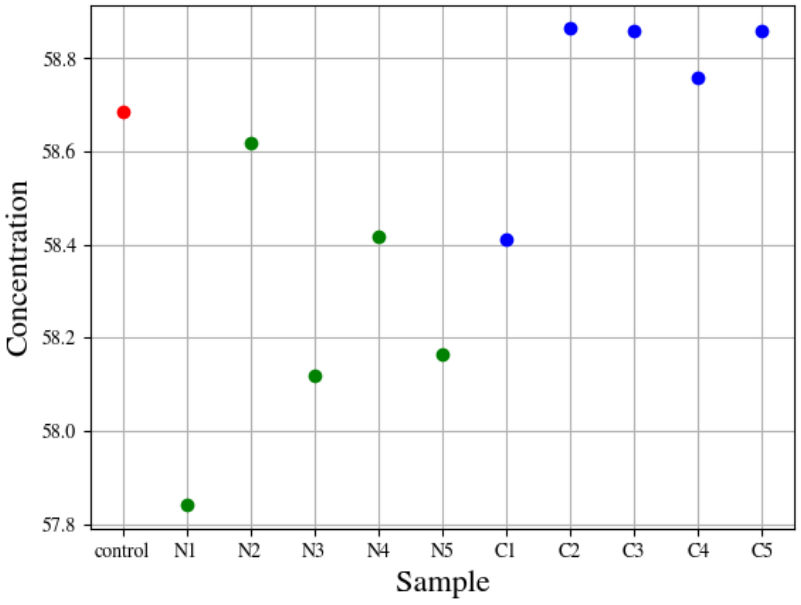

Figure 5.25: NHS results from the NanoDrop spectrophotometer

5.2.2 Streptavidin Adsorption

The simple adsorption of streptavidin onto a gold surface was considered as an alternative method of immobilisation, due to the previously mentioned bioaffinity between biotin and streptavidin (refer to Section 2.3.2.1). The anti-IP-10 and anti-IFN-γ proteins received from the animal TB research group are biotinylated and should hence easily bind to the streptavidin. This method was initially not considered, as the adsorption of the streptavidin onto gold does not result in a bond as strong as covalent bonding. This may effect the re-usability of the gold chip. Further, the surface density of this immobilisation method may differ to that of the SAM. The immobilisation method affects the system's baseline and not the SPR effect. Should the antibodies bind as expected, then a shift in the SPR minimum should still occur when the sample is introduced.

The protocol described in Appendix E.2 was followed. Here streptavidin with HRP label is immobilised. Tetramethylbenzidine (TMB) is then added with the HRP to induce a colour effect. This colour effect will then indicate if binding occurred. Figure 5.26, shows the results of the adsorption of different concentrations of streptavidin into gold chips. The dilutions tested were 1:1000, 1:800 and 1:500. The Standard curves of the tests all look good. It appears that no saturation takes place. Here all the results lie between the 75% and 100% line. This may mean that either very little streptavidin bound to the gold or that the concentrations were so high that the gold surface was saturated.

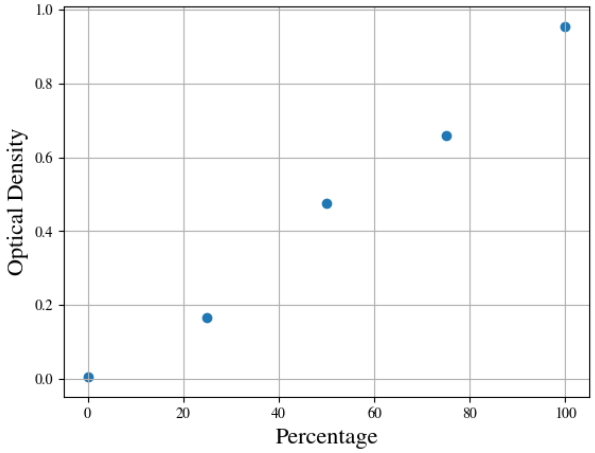

(a) Standard curve

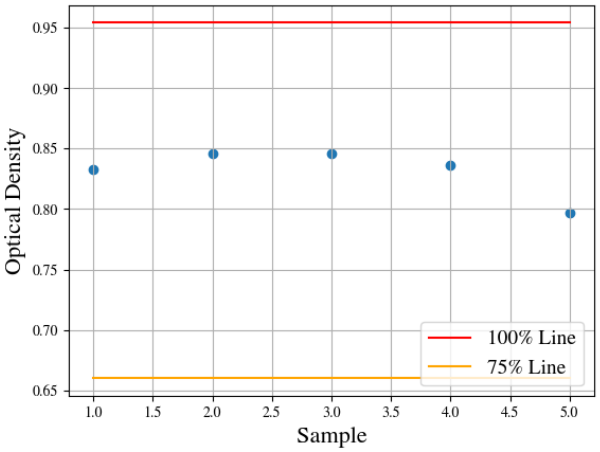

(b) Sample results

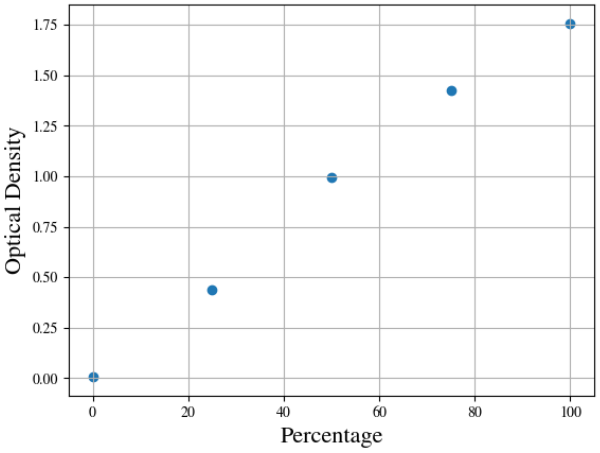

(c) Standard curve

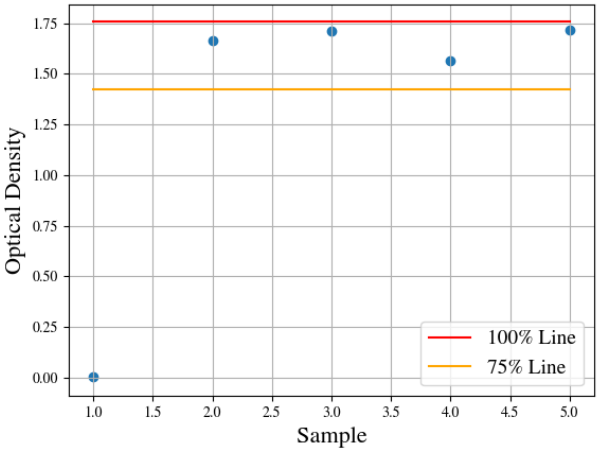

(d) Sample results

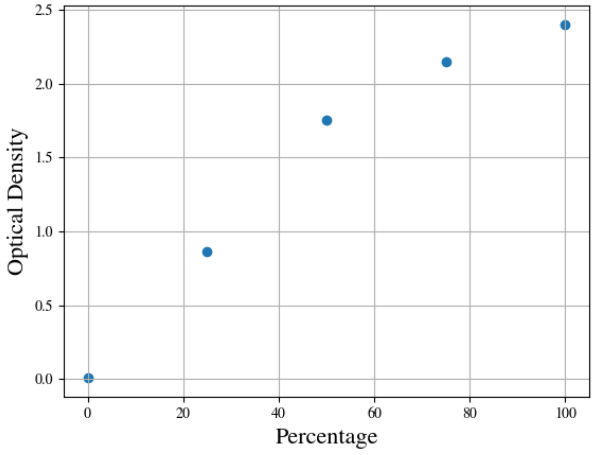

(e) Standard curve

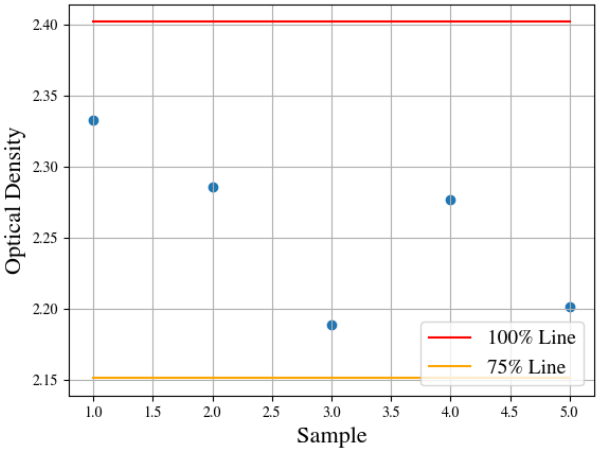

(f) Sample results

Figure 5.26: Streptavidin adsorption results

Ellman's and Bradford assays are time sensitive and some of the sample proteins can

adsorb into container walls, which may lead to inaccurate readings. Hence, a new confirmation method was considered. Fluorescein isothiocyanate (FITC) is a fluorescent marker that binds to the amine groups. As mentioned in Chapter 2, amine groups can be found all over antibodies. The principle is that FITC is allowed to bind to the antibodies that have immobilised on the substrate, and these substrates are then analysed using a fluorescence microscope. If the sample fluoresces it can be assumed that antibody binding occurred.

For the initial test using this method 10 mg·ml^{-1} of cysteamine was used. Cysteamine is a chemical compound that has two functional groups, namely thiol and amine. The principle here is that the thiol group adsorbs onto the gold substrate and the FITC then binds to the amine group. Figure 5.27 shows the sandwich formed. The aim of this test was to see if the thiol adsorption takes place as expected. The protocol can be seen in Appendix E.

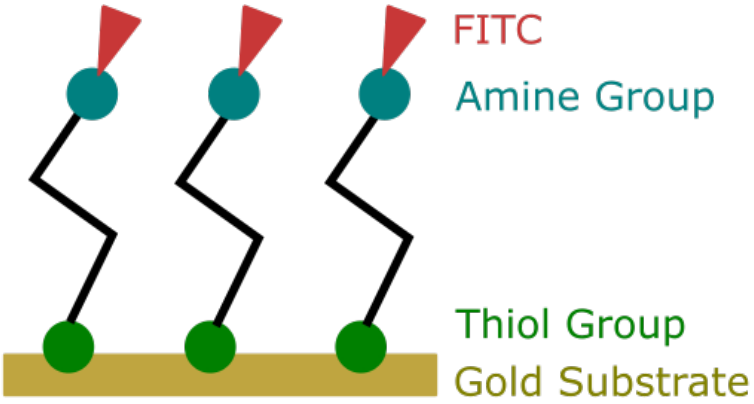

Figure 5.27: Schematic representation of cysteamine immobilisation

All the FITC samples were then analysed with a Zeiss Axio Observer wide field fluorescence microscope. The cysteamine and FITC sample batch showed little to no fluorescence. Later, tests from colleagues led us to believe that the cysteamine did not behave as expected. It is assumed that due to the storage conditions the substance may have denatured.

A new sample batch was created. This batch is based on the proposed antibody immobilisation strategy discussed in Chapter 4. A schematic representation of this method can be seen in Figure 5.28. The thiol group of the 3MPA adsorbs onto the gold substrate, EDC and NHS activates the carboxyl terminal group, the amine groups on the antibody then bind to carboxyl group. The FITC then binds to the antibody. For this sample set, 5 mmol concentration of 3MPA, 4 µg·ml^{-1} of IP-10 capture antibody (Anti-IP-10) and 5 mg·ml^{-1} of FITC in ethanol were used. The FITC preperation protocol can be seen in Appendix E.

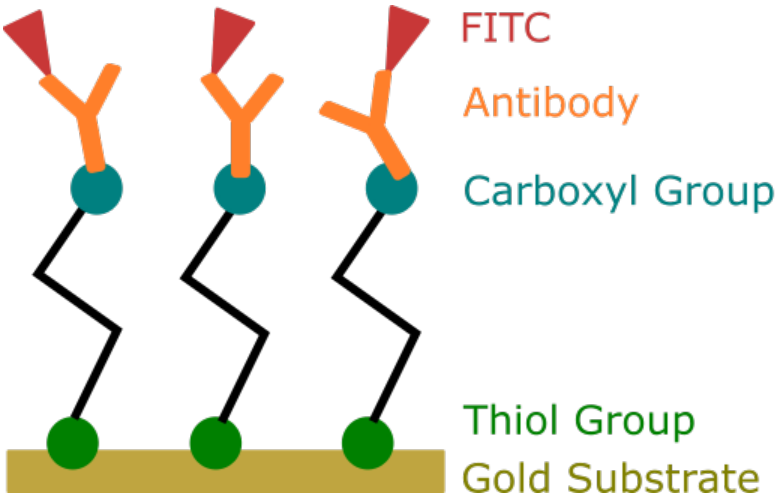

Figure 5.28: Schematic representation of FITC binding to a SAM

Figure 5.29 shows the images obtained from the fluorescence microscope. All the images were processed at the same brightness and contrast. The bright spots are assumed to be due to variation in the substrate properties or noise that may arise from not rinsing the FITC off properly after the incubation step. The control image is obtained from a blank gold chip. Five of the self-manufactured gold chips and one gold IDE were used. IDEs are, as mentioned in Section 2.2.2.5, substrates that can be implemented in electrochemical sensors. Metrohm 10 µm gold IDEs were used to determine if the substrate may be the cause of the problems. If immobilisation on the IDE occurs it is possible that the gold substrate on the SPR chip may be the cause of the immobilisation problems. Samples 1 through 5 were the chips and sample 6 the IDE. The brighter splotches on Sample 5 are assumed to be scratches on the gold surface of the chip. From these images it can be seen that the samples are a brighter shade of green, compared to the control. This means that some FITC bound to the samples. However, the IDE images show no change in fluoresce between the control and the FITC image.

(a) Control image

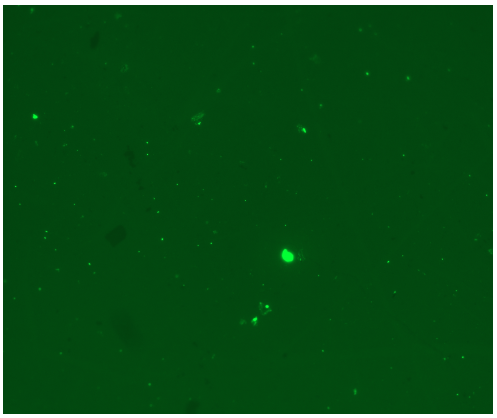

(b) SAM sample one image

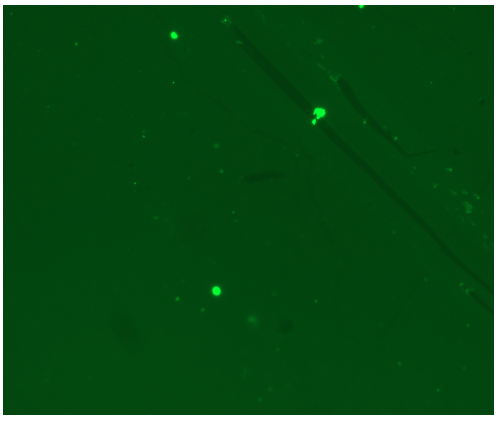

(c) SAM sample two image

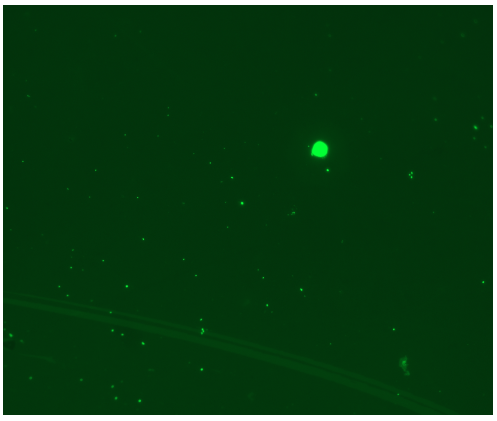

(d) SAM sample three image

(e) SAM sample four image

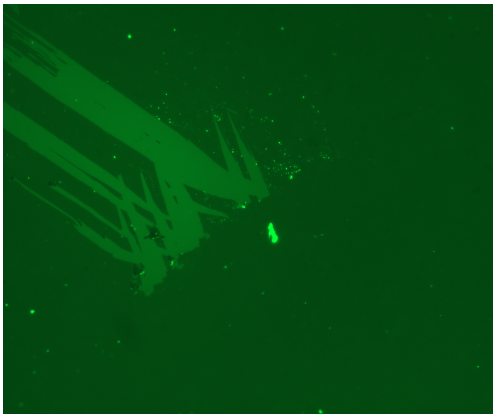

(f) SAM sample five image

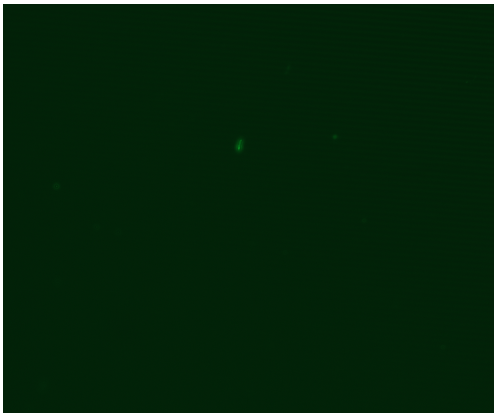

(g) IDE control image

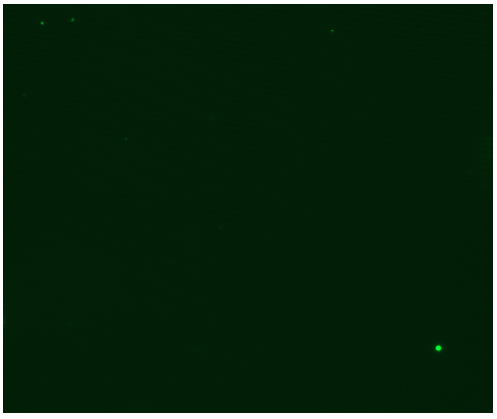

(h) SAM sample six (IDE) image

Figure 5.29: Fluorescent imaging of SAM antibody binding with FITC

NanoDrop tests were done on the samples as well. Figure 5.30 shows the results. Figure 5.30(a) depicts the results of the 3MPA adsorption, *M1-M5* are the SPR chips, *Mc* is the control and *Me* the IDE. Two of the gold chip samples lie above the control. Three of the gold chip samples, as well as the IDE sample lie below the control. The IDE sample had the lowest concentration of 3MPA, which implies that the most adsorption of 3MPA was on the IDE. Figure 5.30(b) shows the results of the antibody binding to the SAM, here most of the values lie above the control, *AbMc*, which means that either the Eppendorf tube adsorbed the antibodies or the EDC/NHS activation was not successful.

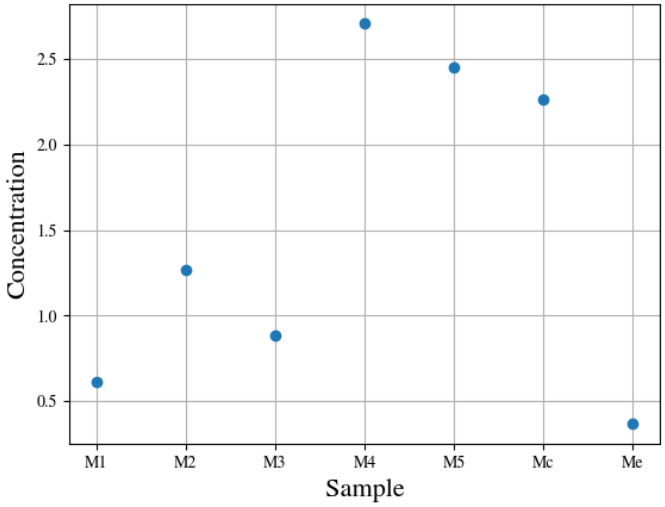

(a) 3MPA adsorption

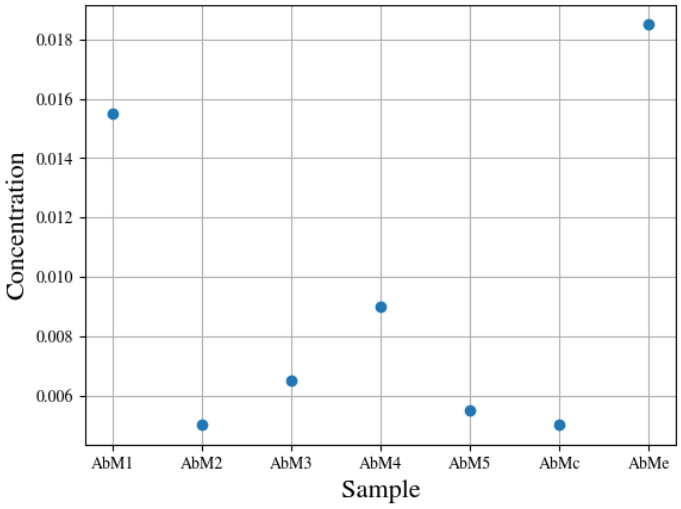

(b) Antibody binding

Figure 5.30: SAM NanoDrop results

An additional batch of chips using the streptavidin/biotin method was made. However, it is unclear if FITC binds to the lysine, i.e. amine groups on the streptavidin. This may interfere with the signal. A schematic representation of the binding is shown in

Figure 5.31. Streptavidin was diluted 1:1000 and 4 µg·ml^{-1} of anti-Ip-10 antibody were used.

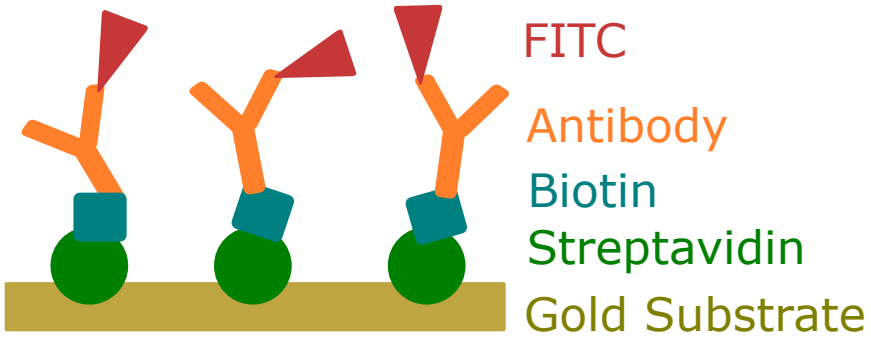

Figure 5.31: Schematic Representation of FITC binding to a Antibody Immobilised via Affinity Immobilisation

Figure 5.32 shows the images obtained from the fluorescence microscope. Once again, all the images were processed at the same brightness and contrast. Here too, the bright spots are assumed to be due to variation of the substrate properties or noise that may arise from not rinsing the FITC off properly after the incubation step. The control image is obtained from a blank gold chip. From these images it can be seen that the samples are a brighter shade of green, compared to the control. This means that some FITC bound to the chips.

(a) Control image

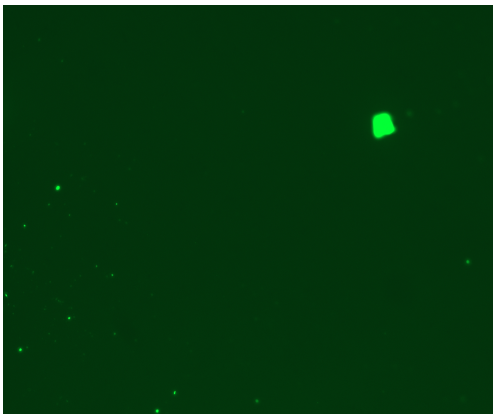

(b) Affinity sample one image

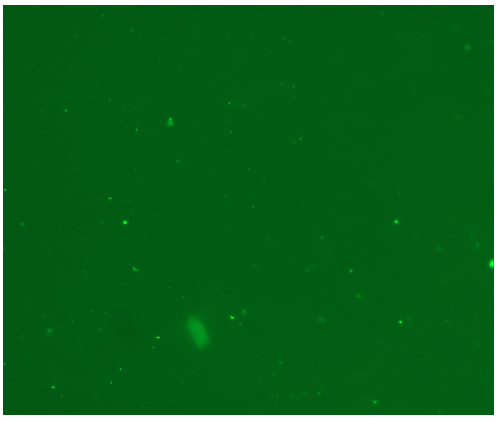

(c) Affinity sample two image

(d) Affinity sample three image

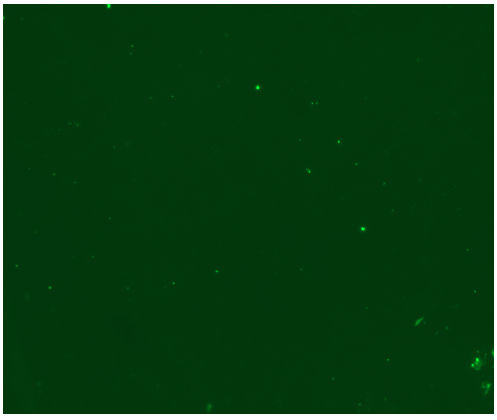

(e) Affinity sample two image

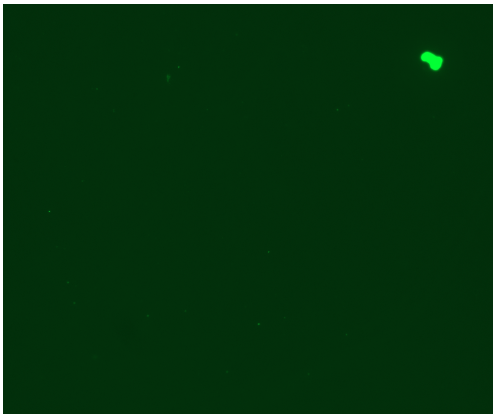

(f) Affinity sample three image

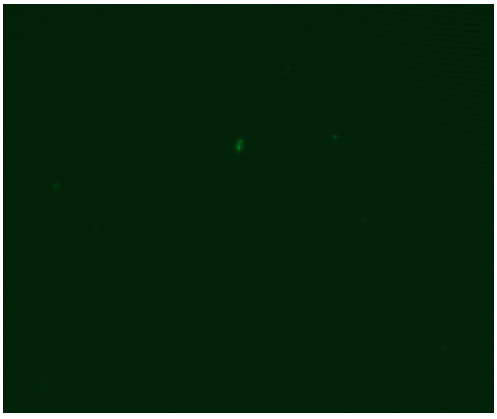

(g) IDE control image

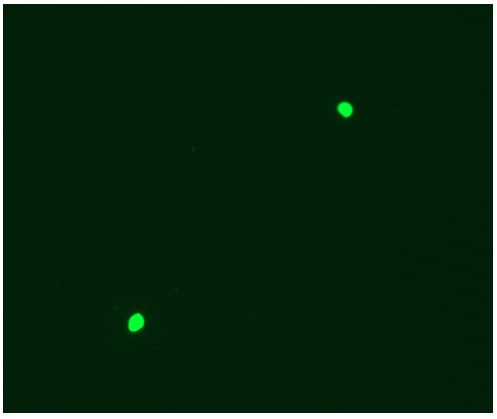

(h) Affinity sample six (IDE) image

Figure 5.32: Fluorescent imaging of affinity antibody binding with FITC

NanoDrop tests were done on these samples too, and the results can be seen in Figure 5.33. Figure 5.33(a) shows that, four of the five gold chip samples have a higher concentration of streptavidin than the control. Again, this result is unexpected as the control should have the highest value. The gold IDE sample has the lowest concentration of streptavidin, which means the highest amount of streptavidin adsorbed onto the gold. Figure 5.33(b) shows similar results, the gold chip showing higher concentrations than the control and the gold IDE showed a concentration lower than the control.

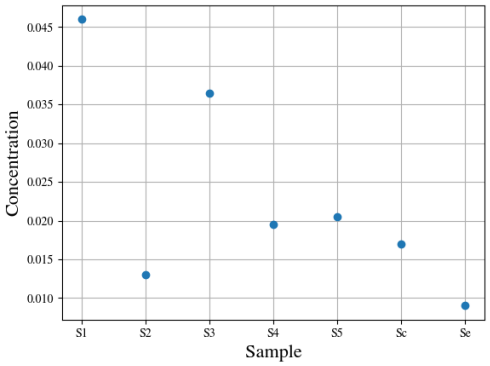

(a) Streptavidin Adsorbtion

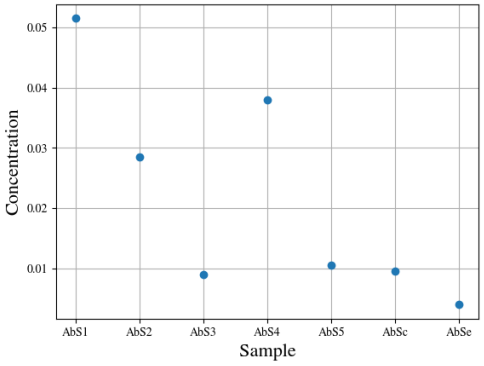

(b) Antibody Binding

Figure 5.33: Affinity binding NanoDrop results

Another set using the SAM method of immobilisation was made (Figure 5.28). For this sample set, 10 mmol concentration of 3MPA, 10 µg·ml^{-1} of antibody and 5 mg·ml^{-1} of FITC in ethanol were used. Figure 5.34 shows the images obtained from the fluorescence microscope. All the images were processed at the same brightness and contrast. The bright spots are assumed to be due to variation of the substrate properties or noise that may arise from not rinsing the FITC off properly after the incubation step. For this set two control images were obtained; one from a blank gold chip and another form a plain gold control incubated with FITC. From these images it can be seen that FITC adsorbs onto the gold substrate, which may indicate that the fluorescence seen is due to the FITC adsorbing directly onto the gold and not due to if binding to the amine groups on the antibody.

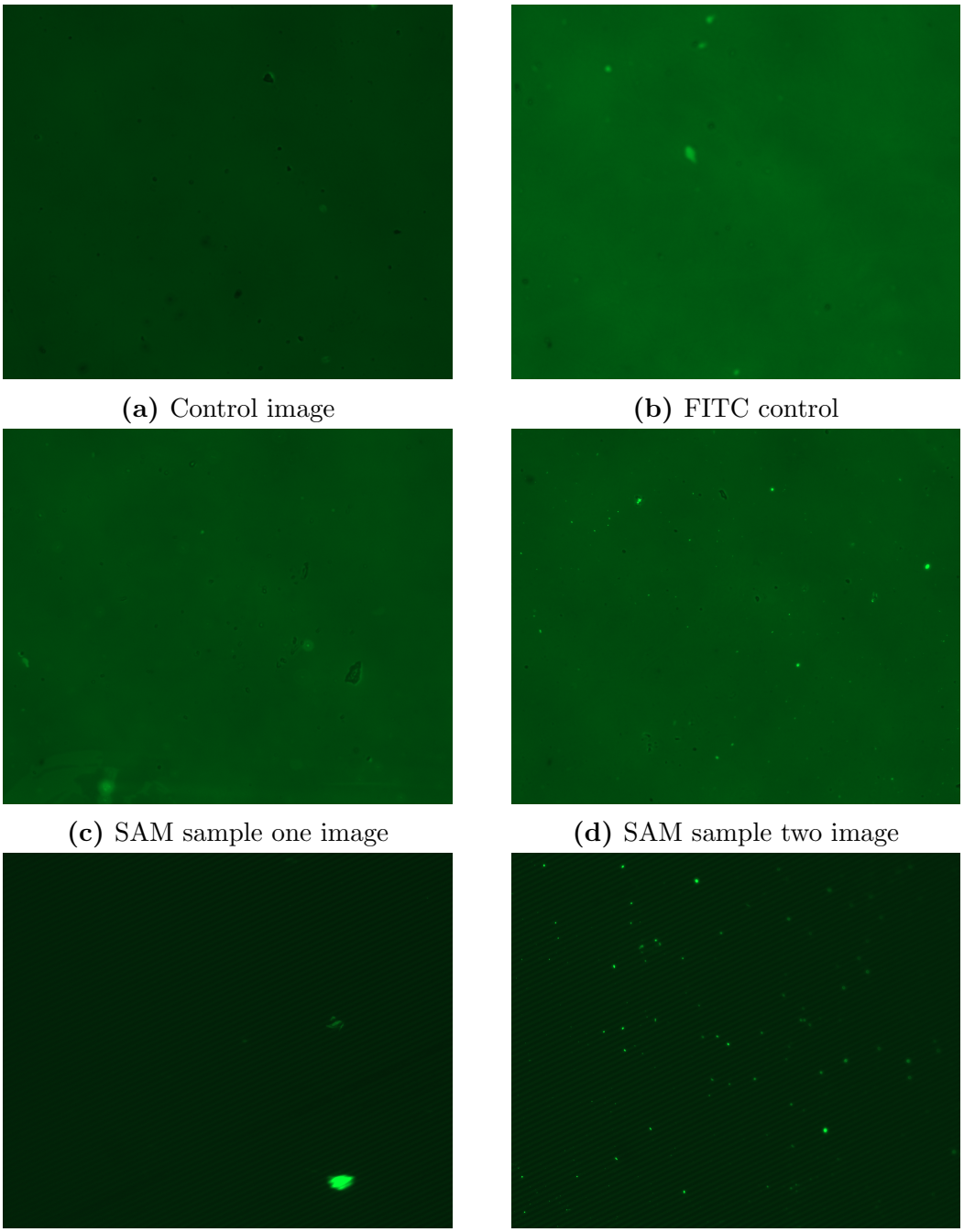

(a) Control image

(b) FITC control

(c) SAM sample one image

(d) SAM sample two image

(e) IDE control image

(f) SAM sample 6 (IDE) image

Figure 5.34: Fluorescent imaging of SAM antibody binding with FITC

Another batch of affinity based chips was also created. For this set streptavidin was diluted 1:1000 and 10 µg·ml^{-1} of antibody was used.

Figure 5.35 shows the images obtained from the fluorescence microscope. Once again, all the images were processed at the same brightness and contrast. The control image is obtained from a blank gold chip. From these images it can also be seen that FITC adsorbs into the gold substrate, which may indicate that the fluorescence seen is due to the FITC adsorbing directly into the gold and not due to it binding to the amine groups on the antibody.

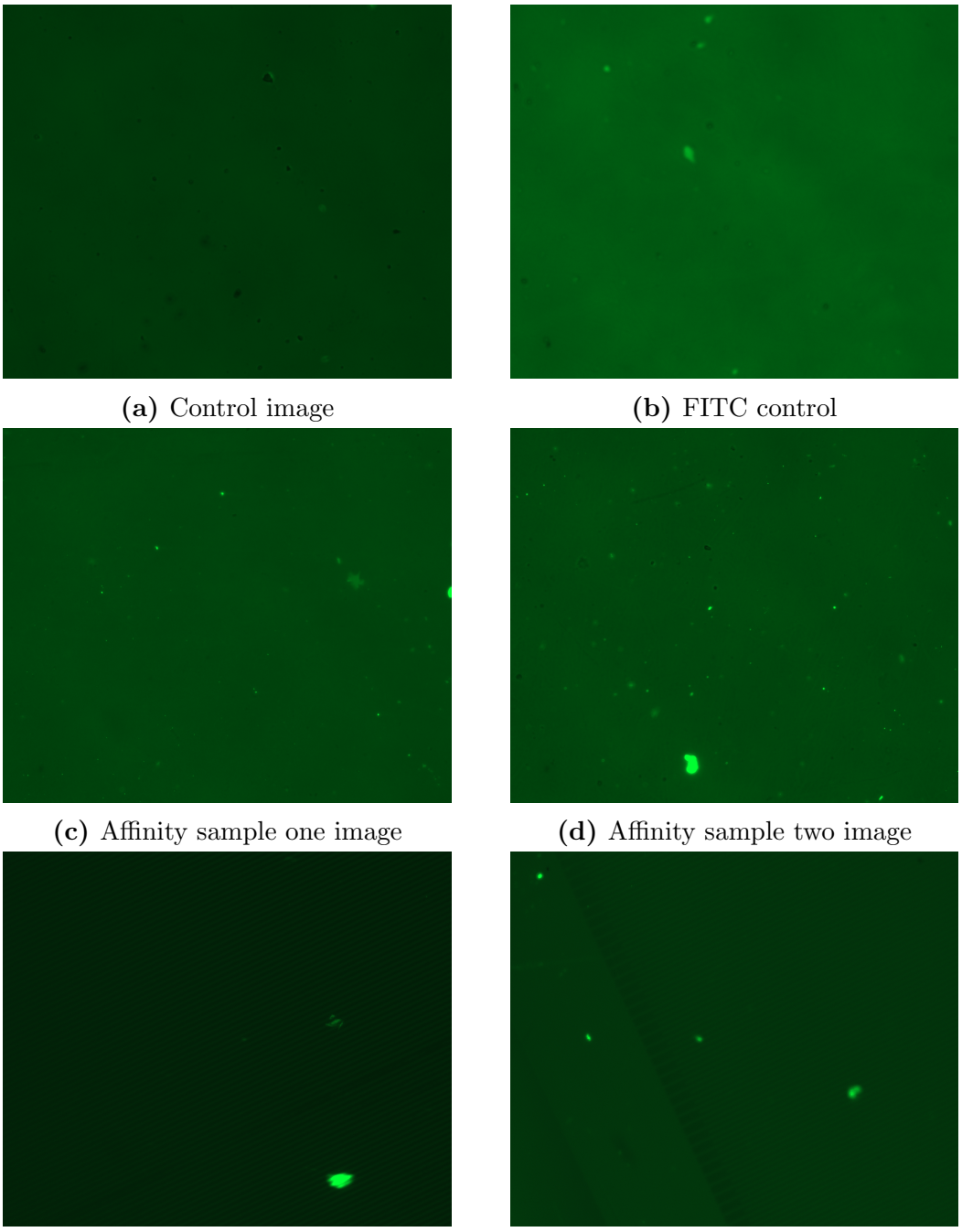

(a) Control image

(b) FITC control

(c) Affinity sample one image

(d) Affinity sample two image

(e) IDE control image

(f) Affinity sample 6 (IDE) image

Figure 5.35: Fluorescent imaging of affinity antibody binding with FITC

NanoDrop test were done to determine the antibody adsorption. Figure 5.36(a) shows the antibody binding to the SAM and Figure 5.36(b) shows the antibody binding to the streptavidin. It can be seen that the values for the chips lie above the value of the control and that the value for IDE is lower than the control value. Hence, there may be the issue with the gold substrate of the gold chip.

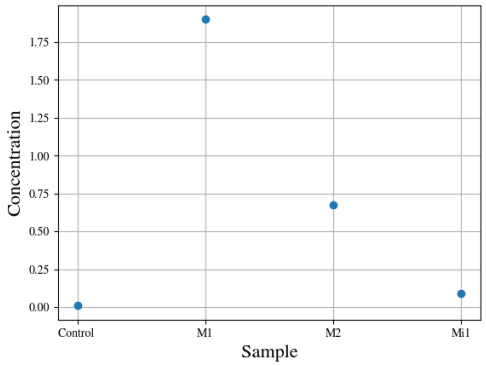

(a) Antibody binding to SAM

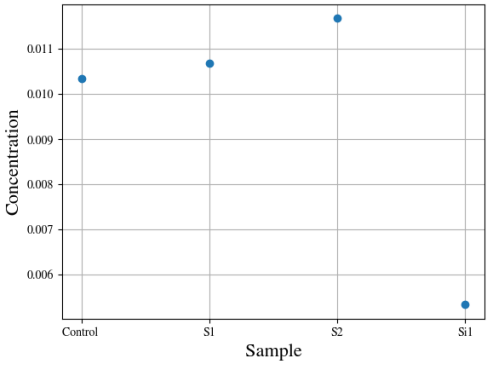

(b) Antibody binding to streptavidin

Figure 5.36: Antibody binding NanoDrop results

5.2.3 Immobilisation Summary

After the first experiment, where the Ellman's assay saturated, the experiment was redone using a lower concentration of 3MPA. During this run better results were obtained and protein binding took place. However, supply issues may have caused problems with the EDC. New EDC was bought and the tests were repeated again. During this third test water soluble sulfo-NHS was used in place of NHS. Here it seemed as if no binding of the protein occurred. Therefore, sulfo-NHS was deemed inadequate and not used again.

These tests yielded a low concentration of binding, therefore Streptavidin adsorption was done to determine if this method would lead to better results, since there may be problems with the 3MPA, EDC or NHS. Streptavidin adsorption results were considered to be good as sample values all were below the 100% line and the standard curves did not saturate. Even though only between 75% and 100% bound, it may be that since the concentration used was so high that the substrate may have saturated.

The high concentration of chemicals were employed to ensure good surface coverage, this may have been excessive and could have led to the standard curve to saturate. This may mean that, even though only a small percentage of the substance bound, enough was adsorbed into the gold to lead to good surface coverage. This was another reason why FITC and the microscope imaging was considered: to see how well and uniform the surface was covered.

Steps were taken to determine the potential problems with the SAM immobilisation method. FITC and cysteamine were employed. The aim of this test was to determine if the thiol adsorption on the gold took place as expected. If the cysteamine immobilisation had been successful, the problem could be the 3MPA. Perhaps the 3MPA does not adsorb because it was faulty.

The test showed little to no fluorescence, hence it was considered that the gold substrate might have been the reason for the experiments giving the expected results. The IDEs were implemented as an alternative to validate the immobilization method. If immobilisation occurred on the IDE and not on the gold substrate, the gold might have been the cause of the problems. However, it was later discovered, by colleagues, that the cysteamine used might have been the issue.

The results obtained from the microscope and the NanoDrop were contradictory. The 3MPA NanoDrop results showed that more 3MPA adsorbed into the IDE than into the chips and the results for the chips were inconsistent. The NanoDrop test for the antibody showed that the IDE sample had a very high concentration of the antibody, which means that little antibody bound to the SAM on the IDE. Perhaps, non-specific binding of the antibody directly into the gold occurred, which may explain the lower antibody concentration in the NanoDrop tests of the chips and the bright fluorescence in the images.

Since these results were inconclusive, the streptavidin adsorption, which had previously shown promise, was repeated with antibody and FITC. Later, it was discovered that the FITC can adsorb directly into the gold and hence the test seemed invalid, since it was unclear if the fluorescent effect that occurred were due to the immobilisation taking place as desired or if non-specific adsorption of the FITC into the gold was taking place.

As mentioned, the unnecessarily high concentrations of the substances may have been excessive and made it seem that insufficient binding occurred, even though in reality it may have been enough to sufficiently cover the substrate surface. The fact that the Ellman's assay standard curve saturates made the results difficult to interpret. The issues may not necessarily lie with the immobilisation method but verification methods. Anti-rabbit or other anti-anti-IP-10 with dye markers can be implemented. This may solve the problem with non-specific binding of the FITC.

No more immobilisation attempts were made as there were too many variables that influence the process. In order to obtain better results it is recommended that all samples be stored in the same type of holders, since Eppendorf tube and acetal may have different chemical reactivity to the samples and the walls of the Eppis as well as, the acetal tray may adsorb chemicals which, in turn may affect the results.

Even though attention was paid to correct laboratory methodology and the pipettes were calibrated, laboratory work errors such as pipetting errors, dilution mistakes, and incorrect incubation times, may have occurred. Many of the chemicals are light sensitive and may accidentally have been exposed to light. The 3MPA is prone to aerobic degradation [152] and may have accidentally been exposed to air. During the aliquoting process the 3PMA was handled under inert gas conditions, perhaps one can do the dilution and immobilisation under similar conditions, to avoid the oxidation of the substance. The cleaning/washing steps may not have been done adequately. In this section there were many unexpected results and the experiments seemed to have a poor reproducibility.

It was found that the gold adsorbs the FITC too, which affects the fluorescents of the microscopy results. The gold chips do not behave as expected. Other possible reasons for poor results is that the laboratory space is not humidity or temperature controlled. Further analysis will have to be done to address these issues and the immobilisation methods will have to be optimised.

In future, the experiment should be repeated using a lower concentration of 3MPA that is fresh and was handled under inert gas conditions. Further, the implementation of anti-antibodies for the verification process should be considered.

5.3 Software

The software for this system was developed with Python and OpenCV. The Raspbian operating system was flashed onto a SD card and inserted into a Raspberry Pi 4 with 4GB RAM.

For the initial development of the system, images from articles were analysed and the results from the software were compared to the results in the article. The block diagram of the intensity plotting algorithm can be seen in Figure 5.37. The images are read by *cv.imread*. The y-values are chosen depending on the height of the image. The pixels along these lines are then analysed. The RGB value for each selected pixel is determined, the values at the x position is then averaged and plotted on a graph.

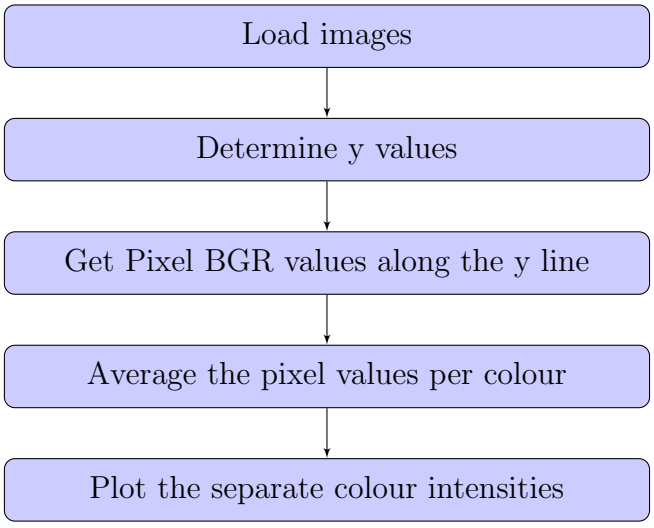

Figure 5.37: Block diagram of algorithm to plot the intensity curve of the SPR signal

Figure 5.38 shows the image obtained from Pluchery *et al.* [140].

Figure 5.39 shows the analysis of the original image, Figure 5.39 (a). Figures 5.39 (b) and (c) show the data of the image after it has been split. The colours in (b) are unclear, hence the viridis colours are shown in (c). Viridis is a colour map that ranges from blue to yellow, and its purpose is to facilitate visualising the intensity variation of the different channels. Here it can be seen that the main colour in the image is red. Figures 5.39 (d) and (e) show the pixel intensity, where (d) shows the intensity of the grey scale image and (e) of the Red, Green and Blue (RGB) colours. From both these images the intensity

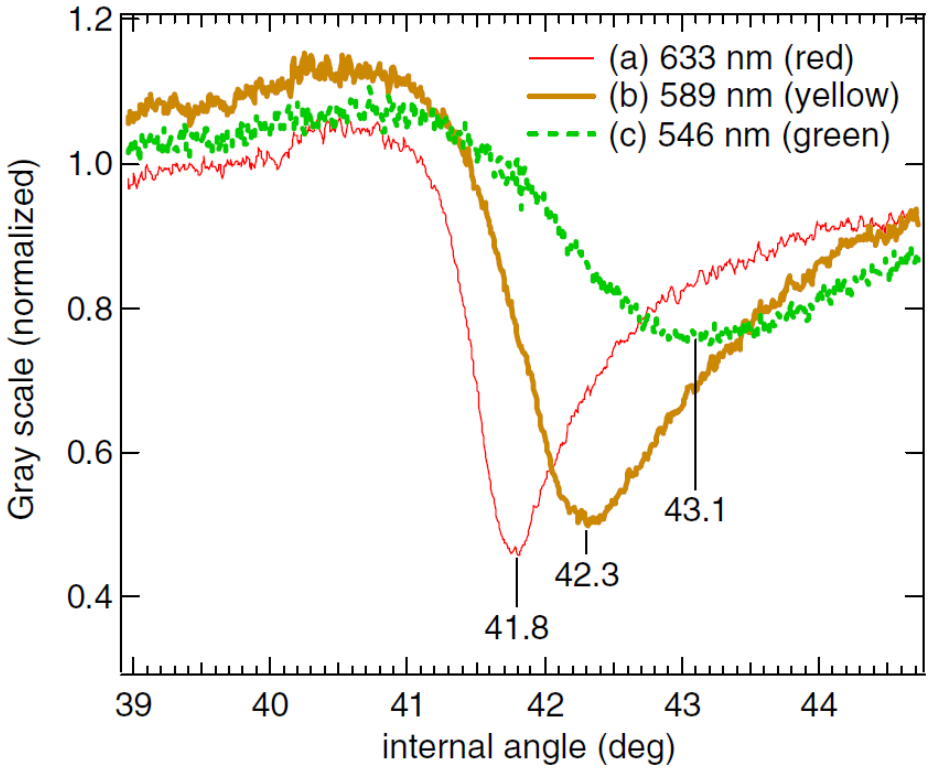

Figure 5.38: Colour intensity curve from [[140]]

dip can be seen. The red curve's shape is similar to that from Pluchery *et al.* [140]. The code for the channel splitting, of both RGB and viridis, was adapted from Innat [153].

(a) Original SPR image from [[140]]

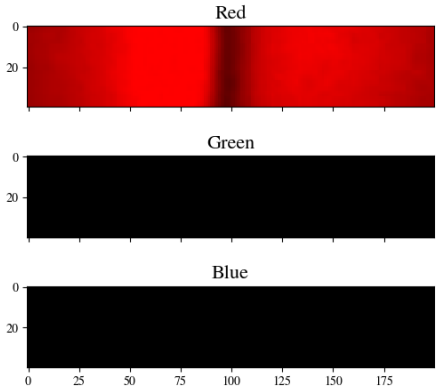

(b) Image split into RGB channels

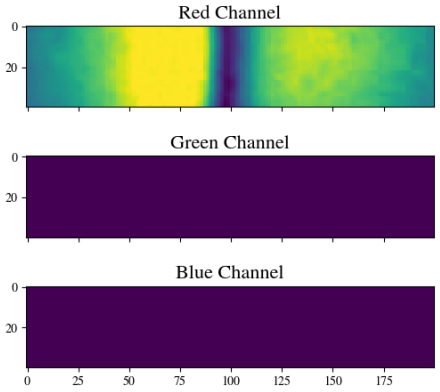

(c) Image split into RGB channels displayed in viridis

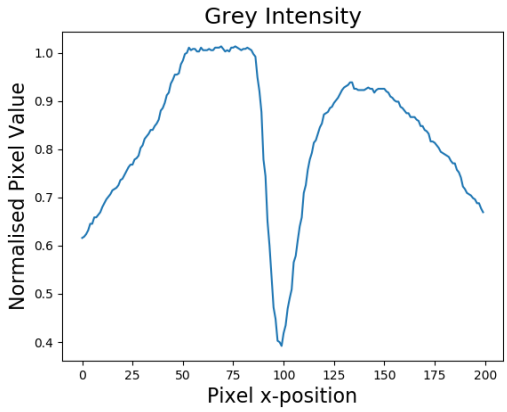

(d) Grey intensity curve

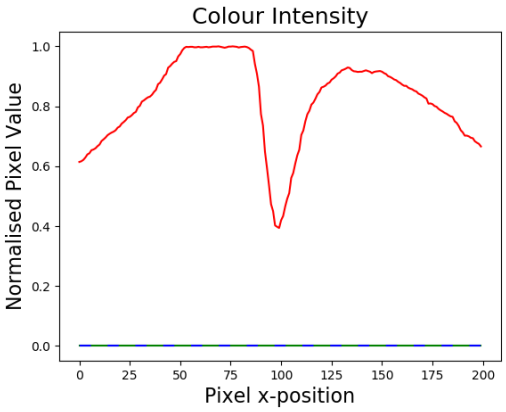

(e) RGB intensity curves

Figure 5.39: Analysis of image obtained from literature [Adapted from [140]]

The previous manipulations were applied to the image shown in Figure 5.40(a) which was obtained by taking a single frame capture from a video taken of the working experimental setup, described in Section 5.1.3. From Figure 5.40 (b) and (c) it can be seen that the main signal is red. However, there are some signals from the green and blue spectrum. Due to the influence of the green signal the greyscale intensity, Figure 5.40 (d), showed an unexpected peak before the dip. The red intensity seen (in red) on Figure 5.40 (e) shows the expected curve shape.

(a) SPR image from experimental setup

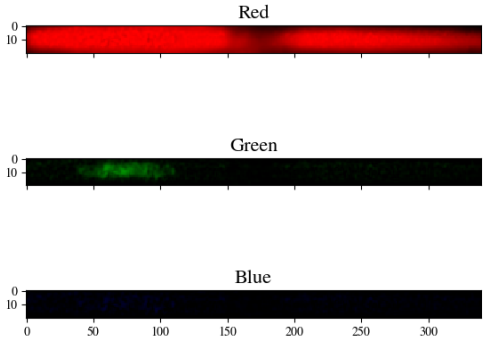

(b) Image split into RGB channels

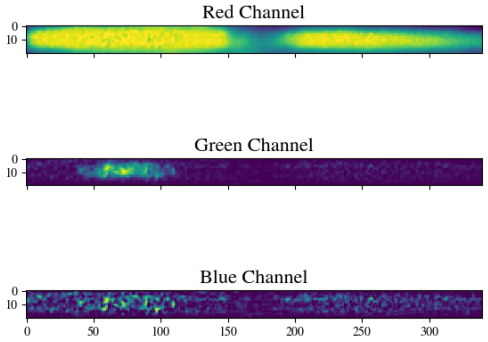

(c) Image split into RGB channels displayed in viridis

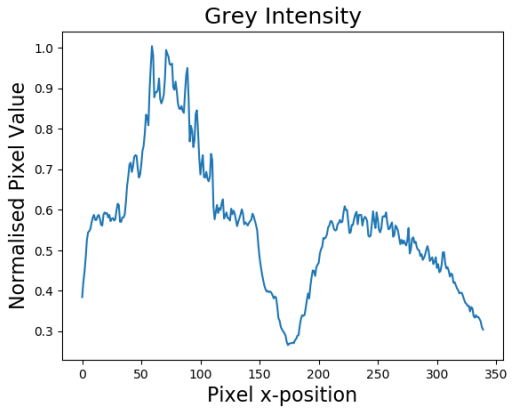

(d) Grey intensity curve

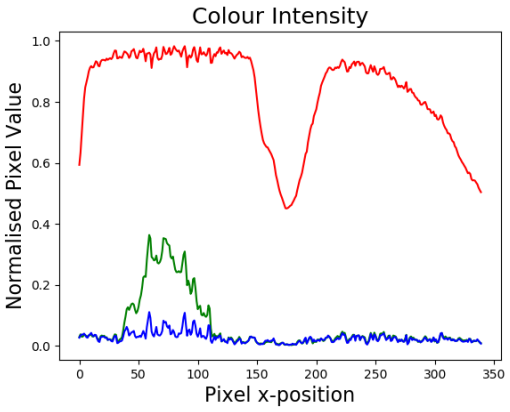

(e) RGB intensity curves

Figure 5.40: Analysis of image obtained form the experimental setup

Other algorithms were created. Figure 5.41, shows the block diagram of the basic algorithm used to capture frames from a video. This is done so that the video can be analysed one image at a time. OpenCV's *cv.imread* and *cv.imwrite* functions were used in this algorithm.

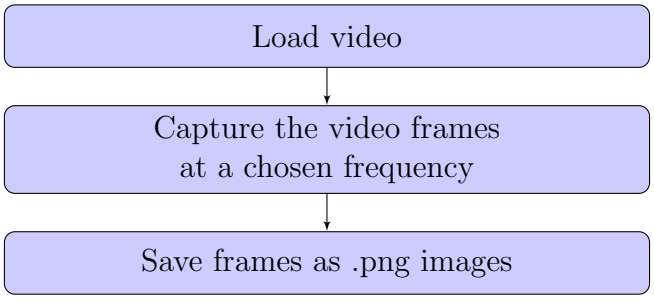

Figure 5.41: Block diagram of the frame capturing algorithm

The following section describes the algorithm used to rotate and crop the images. The code used was adapted from the ProgrammerSought website [154]. Figure 5.42 shows the block diagram of the main image processing algorithm. The algorithm loops though a set of images. In the case depicted, it loops though a folder of images captured from a video, which showed the SPR phenomenon. The images are loaded using the OpenCV *cv.imread* function. OpenCV's *cv.cvtColor* and *cv.COLOR2GRAY* commands are used to convert the images to grey scale. The function *cv.threshold* is used to create a binary image. To locate the contours, *cv.findContours* uses the binary image, then the function *cv.contourArea* is used to determine the area of the contour, a simple *if* statement is used to ensure that only contours with a surface area greater than 1500 px are considered. This is done so that reflected light and other noise signals are ignored. The *getOrientation* function is called and this algorithm is depicted in Green. Principal Component Analysis (PCA) is performed on the data in the image, Opencv's *cv.PCACompute* returns the mean, the eigenvectors as well as the eigenvalues of the data. The eigenvectors are then used to determine the angle between the light stripe and the x-axis. Using this angle, the image is rotated by that magnitude and saved for later analysis.

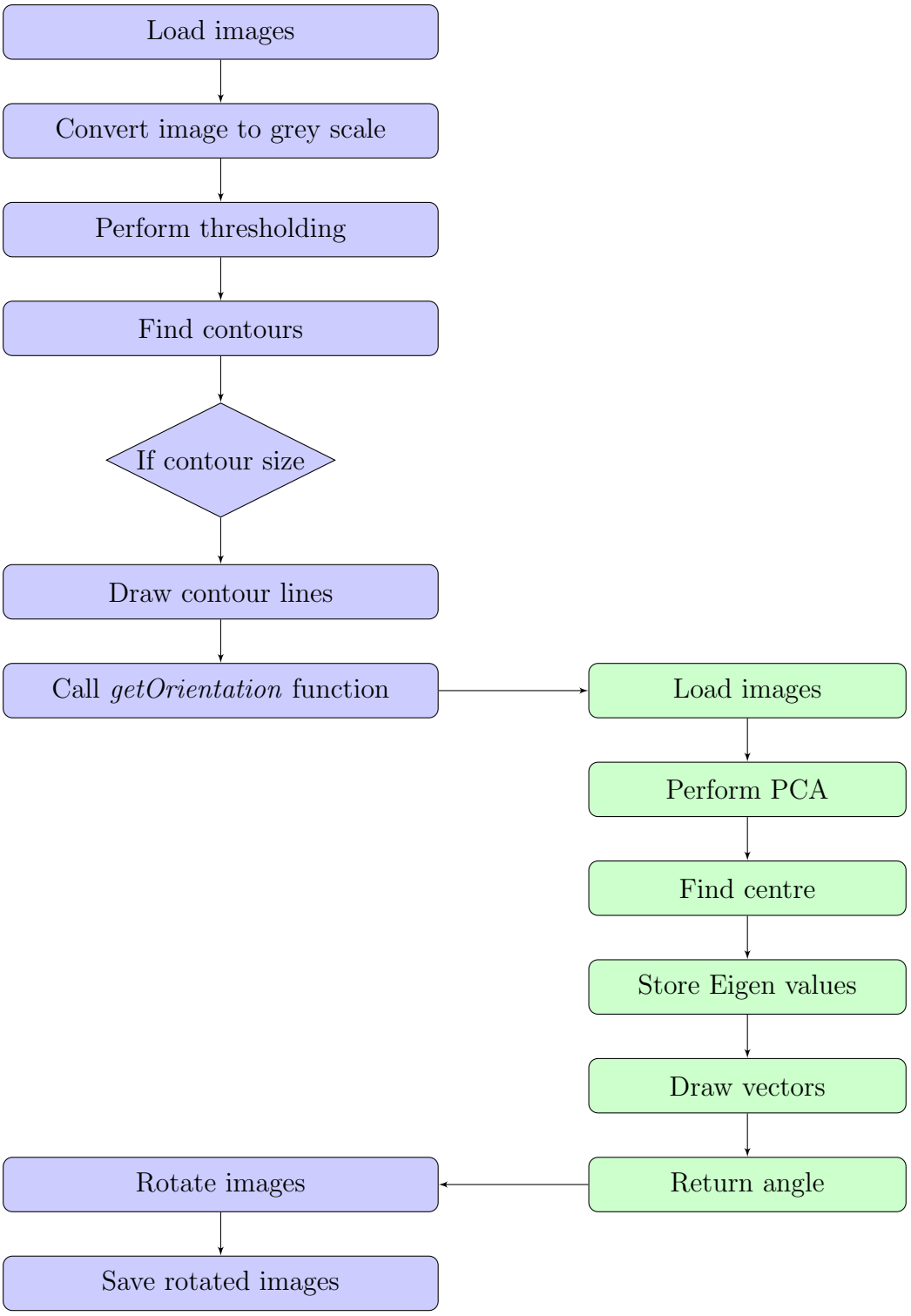

Figure 5.42: Block diagram of the image processing algorithm

Figures 5.43 through to Figures 5.45, show the various manipulations described in the block diagram Figure 5.42 one step at a time. Figure 5.43(a) shows the original image which was captured from a video. The grey scale image can be seen in Figure 5.43(b) and the black and white binary image can be seen in Figure 5.43(c).

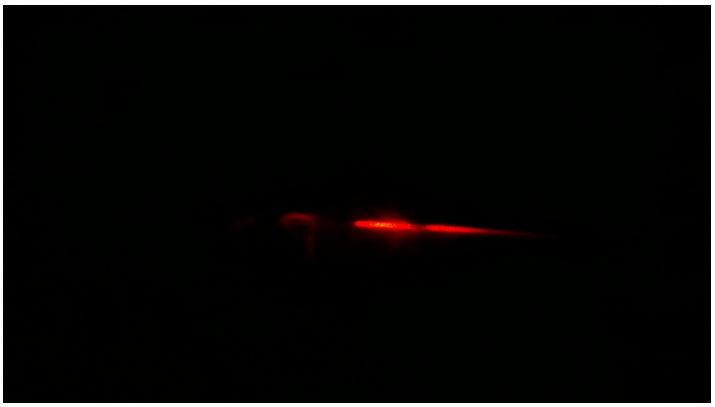

(a) Original image

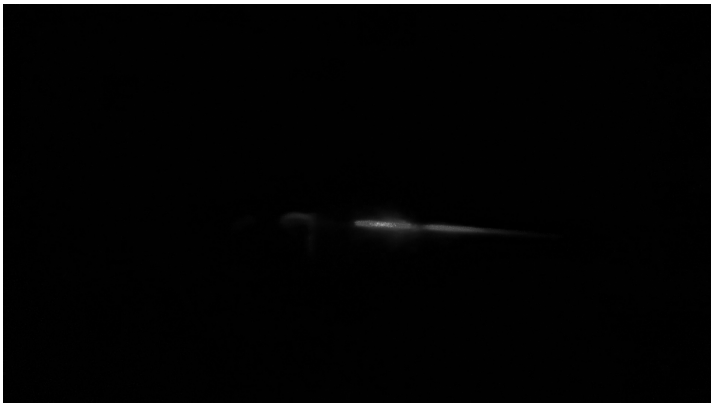

(b) Greyscale image

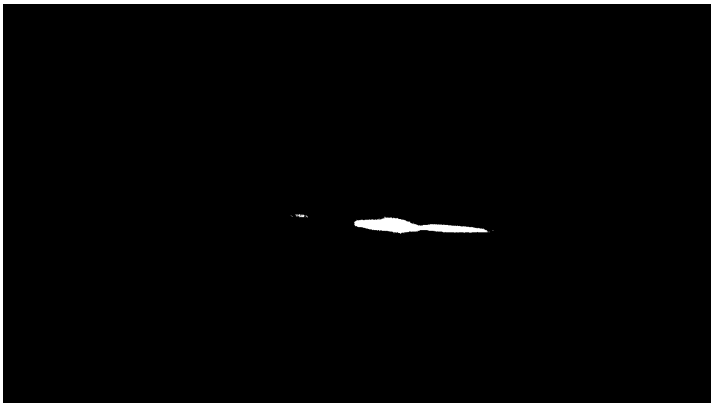

(c) Binary image

Figure 5.43: Image manipulations

Figure 5.44 shows the contour lines of the reflected light. Figure 5.44(a) shows all the contours, where as Figure 5.44(b) only shows the contours with a big enough area to ignore the noise and random light scattering.

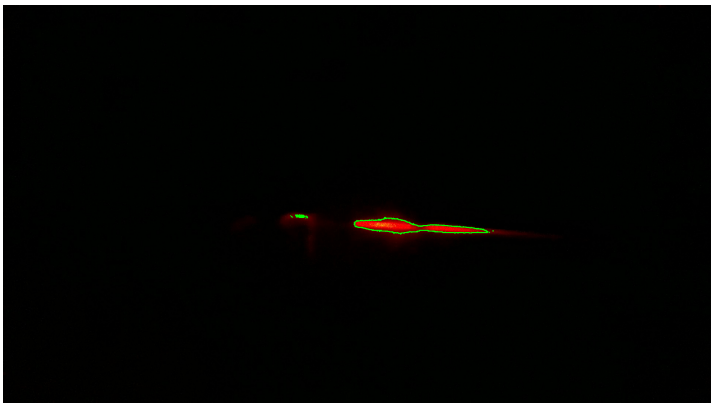

(a) Contour

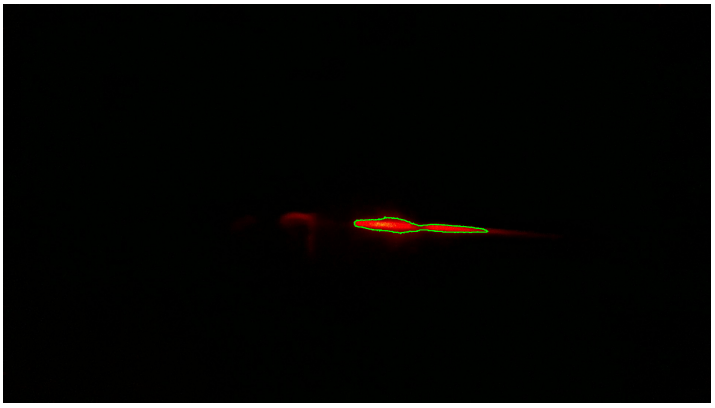

(b) Contour after *if* statement

Figure 5.44: Application of the contours

After the contours have been determined the image is cropped to make it smaller. The eigenvalues and eigenvectors are determined using PCA; these vectors are shown in Figure 5.45(b). Vector one is the white arrow. Vector two, the cyan vector, is scaled up to be 5 times its original size to make it easier to see. Finally, Figure 5.45(c) is the rotated final image that gets saved for later analysis.

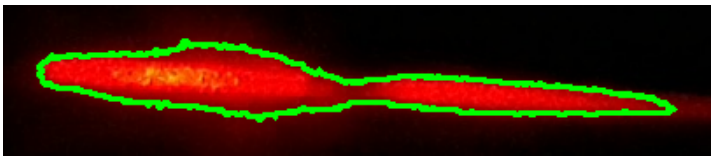

(a) Cropped Image

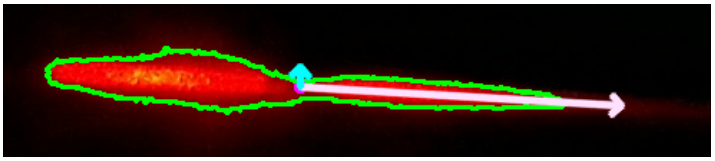

(b) Image with eigenvectors

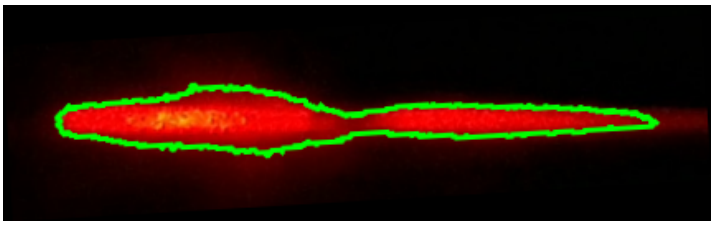

(c) Rotated Image

Figure 5.45: Cropped and rotated images

Figure 5.46 shows the intensity analysis of 3 consecutive images captured from a video, during which the prism was rotated. This was done to mimic the expected results from a protein binding, i.e. when the binding takes place successfully the dip is expected to shift. In this case the dip stays in place when the prism is rotated, so that there is shift in the position of the dip relative to the whole signal. Figures 5.46(a) to (c) show the original image, Figures 5.46(d) to (f) show the cropped and rotated images, and Figures 5.46(g) to (i) show the RGB intensity results for the images. From these images it can be seen that an intensity curve from the images can be obtained. It can also be seen that the green portion of the signal is not constant. It can be seen in Figure 5.46(d), to the right of the dip, that the signal appears almost yellow, which can also be seen in the peak of the green intensity on Figure 5.46(g). With more data the software can be better tested and optimized.

It is important to note that the x-axis depicts the pixels' x-position and not the angle as is common with SPR intensity graphs. This is because the SPR angle and prism position in the system are not finalised. Currently the design is flexible to allow for the adjustment of these components in order to find the location where SPR occurs manually. However, when these components are fixed, reference points can be established that, along with the software, can be used to document the intensity dip relative to the angle of incidence.

(a) Original image (b) Original image (c) Original image

(d) Cropped and rotated image (e) Cropped and rotated image (f) Cropped and rotated image

(g) RGB intensity of the image (h) RGB intensity of the image (i) RGB intensity of the image

Figure 5.46: Red test image

5.4 Prototype Testing

All the parts were combined to form the SPR system. This section will discuss the testing process of the system. Figure 5.47 shows a photograph of the combined parts. The camera is secured inside the camera holder, which can easily be moved forwards and backwards. A 1 ml syringe is inserted into the syringe hub. The microfluidic assembly is in a slot on the top part of the prototype assembly, where its position can be adjusted to achieve SPR conveniently within in the camera's view. The blue box, labelled *Power supply*, contains the PCB with the laser power supply electronics. The Infiniter laser is held in the laser holder. The enclosure is not depicted, so that the various components are visible.

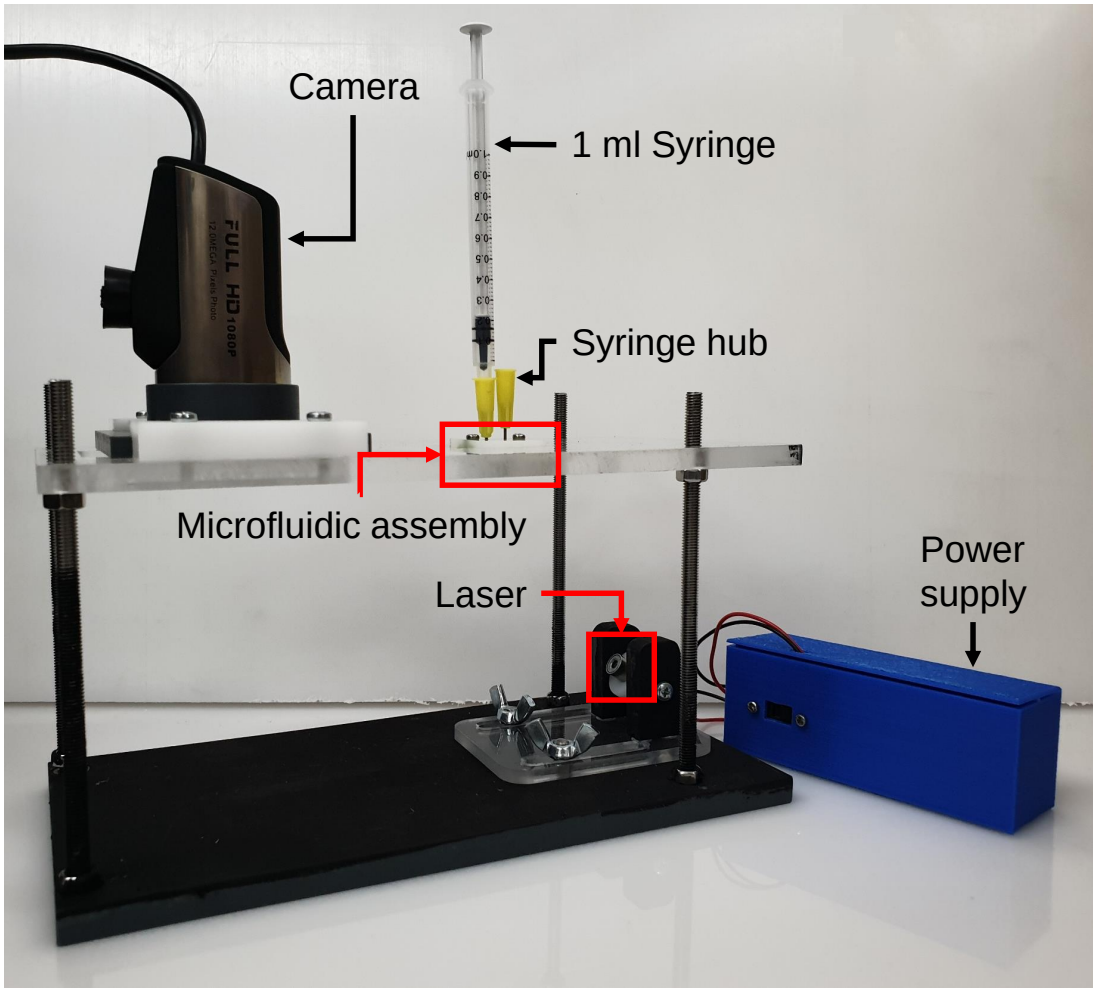

Figure 5.47: Labelled complete prototype

Figure 5.48(a) shows a photograph of the system with the laser switched on and Figure 5.48(b) shows an image taken by the camera in the prototype. The SPR phenomenon was observed in the prototype. This was confirmed by rotating the laser 90°, the dip was not observed in the new laser orientation. When the laser was rotated 90° back, the dip was observed again.

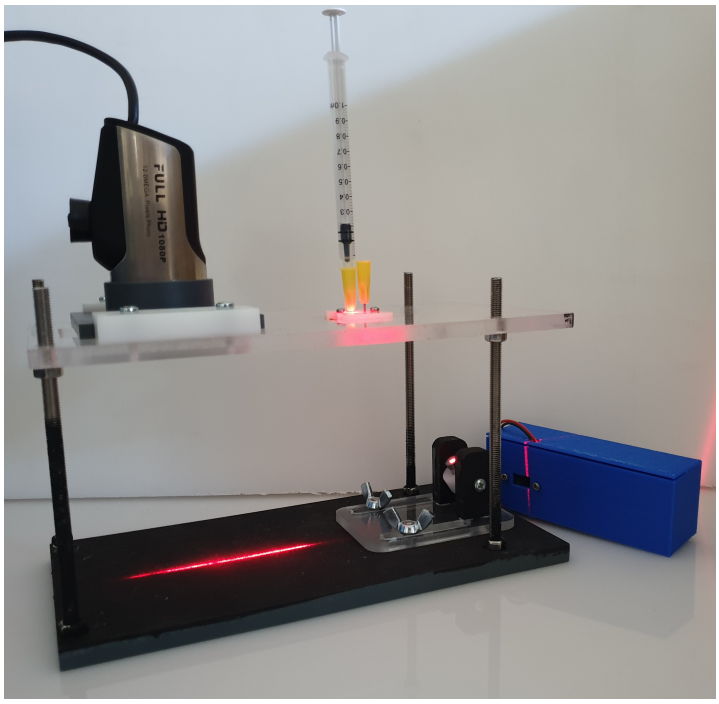

(a) Prototype with laser turned on

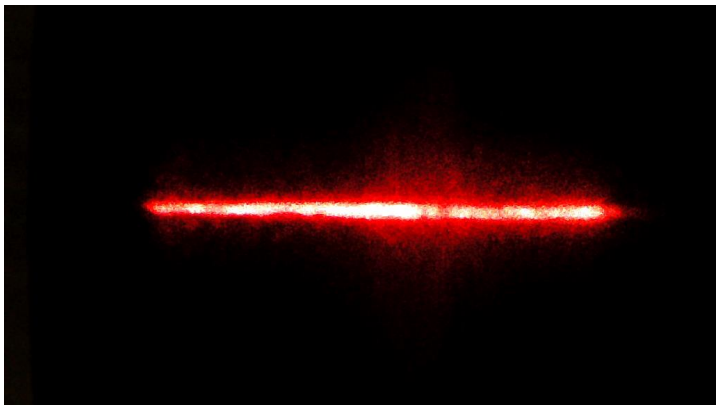

(b) Image captured from the camera in the prototype

Figure 5.48: SPR in the prototype

A number of tests were done to determine whether a shift in the intensity minimum takes place, with a mass addition to the gold surface. The tests were done with cysteamine and BSA, as both these chemicals adsorb onto the gold and should therefore induce a shift in the intensity minimum band. The cysteamine was prepared in DI water and the BSA was prepared in PBS. The concentrations that were analysed are given in Table 5.4. Both the association and dissociation were tested. Moreira *et al.* used 10% BSA in water, to test their autosampler system and were able to determine the mutual diffusion coefficient [86].

Table 5.4: Substance concentrations

Substance	Concentration ($mg \cdot ml^{-1}$)
Cysteamine	8
	5
	3
BSA	10
	8
	5
	3
	1

The tests were done as described in Appendix E.

It was observed that the microfluidic system leaked when the gold chips were too small and/or too much pressure was applied to the syringe plunger during sample introduction. It was also observed that, since sample introduction was done manually, the entire signal shifts, i.e. the whole the optical image relative to the camera, as pressure is applied to the syringe plunger. When the microfluidic system was taken apart after the test, it was seen that the gold adheres to the gasket and hence damages the gold chip. The flow rate of the sample into the channel was kept well below 1 $ml \cdot s^{-1}$. This was ensured by slowly depressing the plunger of the 1 ml syringe.

Figure 5.49 shows photographs of the signal during the tests. Figure 5.49(b), Figure 5.49(e) and Figure 5.49(g) show multiple dips in the intensity. This is unexpected and it is unclear if the dips are due to SPR or are caused by something else, such as dirt or other light signal interference. Further, from Figure 5.49(a), Figure 5.49(b) and Figure 5.49(h) it can be seen that there is a lot of light dispersion. This may be caused by liquid or dirt on the curvature of the prism.

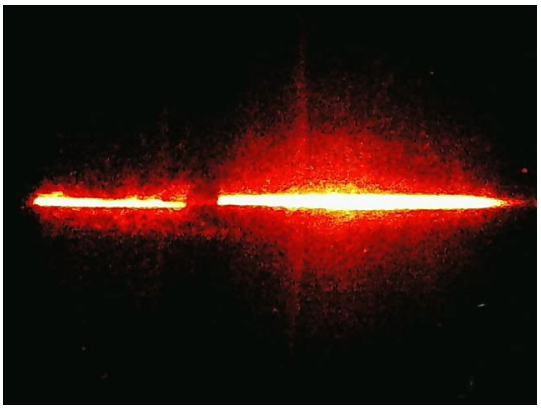

(a) 3 mg·ml^{-1} Cysteamine

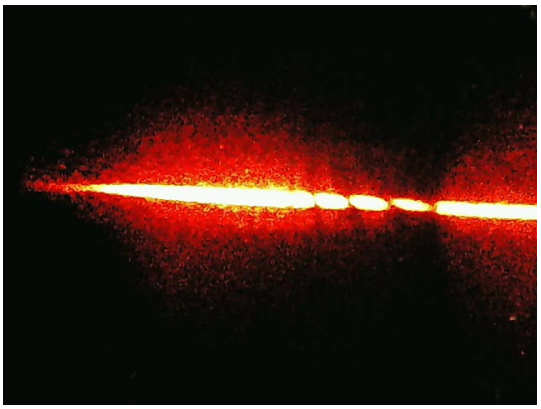

(b) 5 mg·ml^{-1} Cysteamine

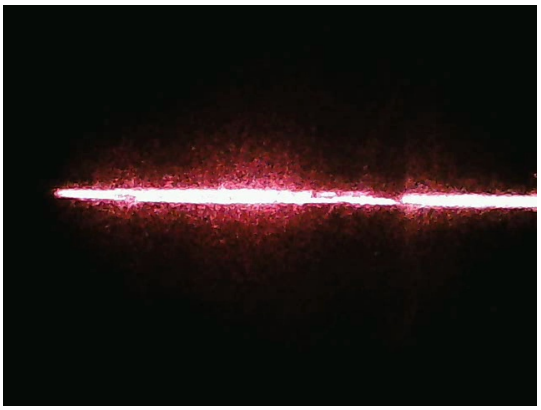

(c) 8 mg·ml^{-1} Cysteamine

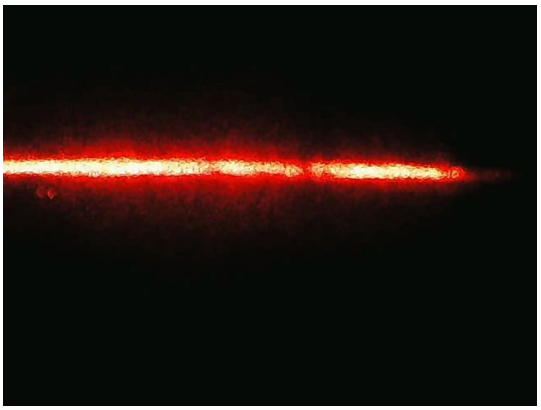

(d) 1 mg·ml^{-1} BSA

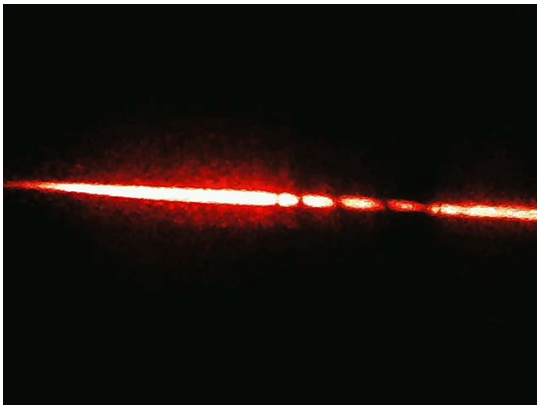

(e) 3 mg·ml^{-1} BSA

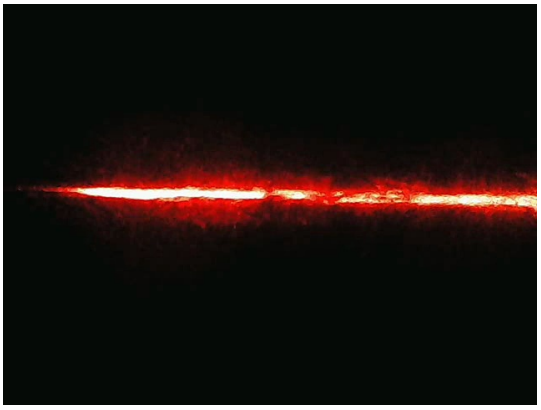

(f) 5 mg·ml^{-1} BSA

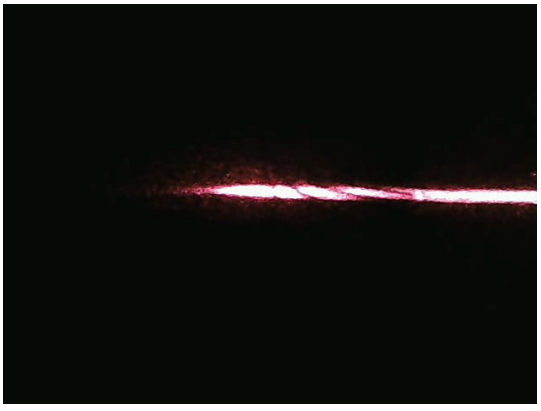

(g) 8 mg·ml^{-1} BSA

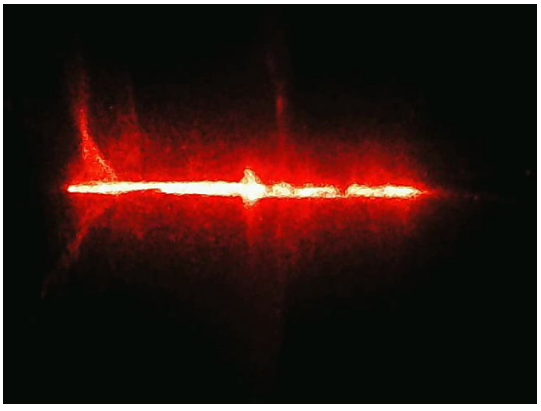

(h) 10 mg·ml^{-1} BSA

Figure 5.49: Images from various tests

During the tests no shifts in the intensity minima were observed with the naked eye, with the exception of the 10 mg·ml^{-1} concentration of BSA, where periodic shifting was observed. It is thought that this may be because BSA is a large molecule and the concentration is so high that the molecules continuously bind and unbind to the gold layer. When PBS was introduced to this test the periodic shift was no longer observed.

The various steps of the data analysis can be seen in Figure 5.50. The original images are from the 2nd second and the 70th second of the video.

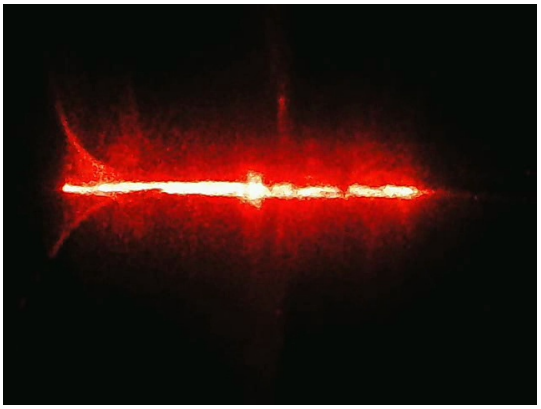

(a) Original image at 2 seconds

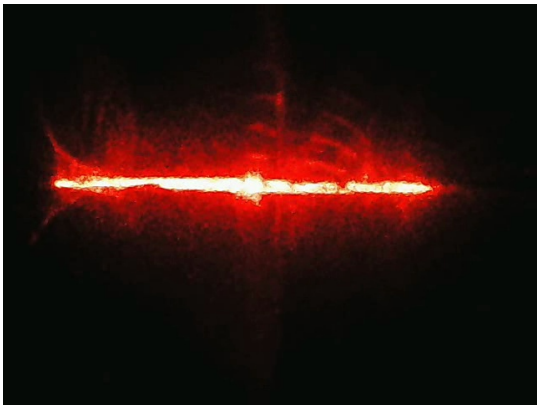

(b) Original image at 70 seconds

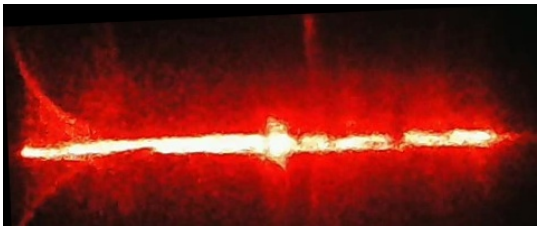

(c) Cropped and rotated image at 2 seconds

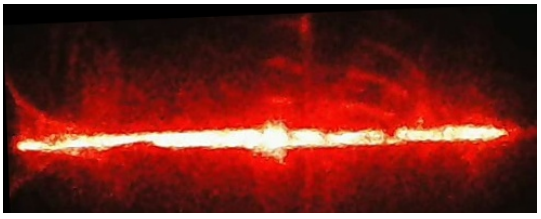

(d) Cropped and rotated image at 70 seconds

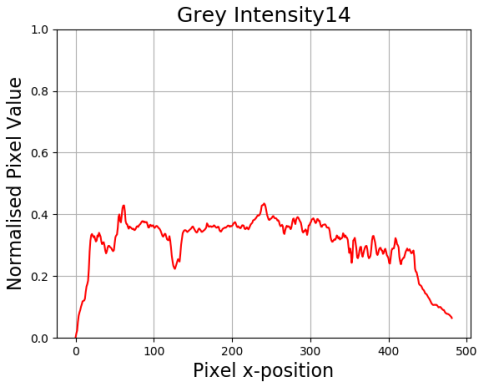

(e) Intensity graph at 2 seconds

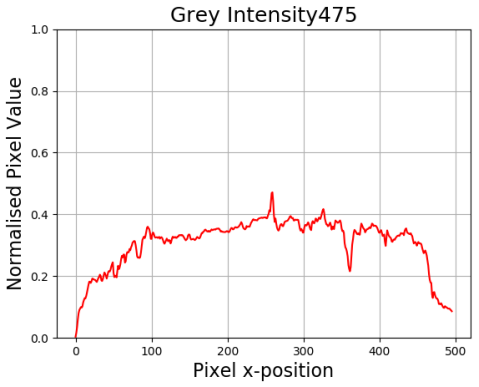

(f) Intensity graph at 70 seconds

Figure 5.50: The first analysis of the 10 mg·ml^{-1} concentration of BSA results

During the data analysis process it was observed that the signal obtained from the camera is more white than red. This may indicate that there was more light than the camera could handle i.e the signal was too bright. This means that the signal was saturated and that high intensity data may be lost. A possible solution to this problem would be to adjust the exposure settings of the camera. However, the grey scale intensity algorithm was used to analyse the images, instead of the red intensity. It was also observed that

the signal intensity within the same data set was not constant. It may have been that environmental light may have interfered, or that the laser intensity was not as constant as expected.

From the results it can be seen that the thresholding needs adjustment. Due to the light scattering, the signal is not just a line. When the signal is not a clear straight line and the scattering is asymmetric, the vectors determined by the PCA are no longer correct. This affects the PCA, which in turn affects the image rotation, as well as the image cropping. It was therefore decided to crop the images without using the PCA and rotation algorithm, since the signal is already well aligned to the x-axis.

Figure 5.51 shows the analysis of 3 images from the data set. Cropping the images smaller yielded better intensity curves. The blue square on the original image shows where the image was cropped. However, it was observed that the resulting curve is not very smooth and it appears that the average intensity value of the curve is inconsistent from frame to frame, even in the regions of the signal where the intensity is expected to remain constant. A change in the width of the dip can be seen, even though no clear shift in the minimum can be observed.

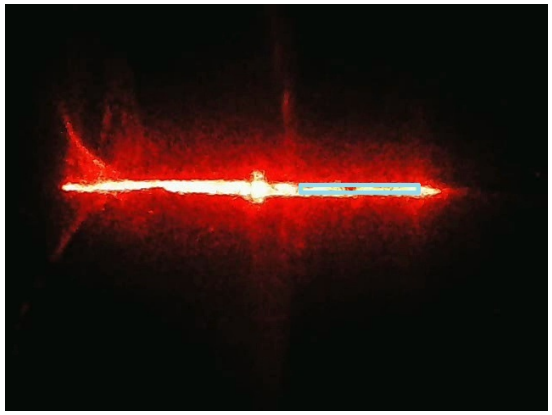

(a) Original image at 16 seconds

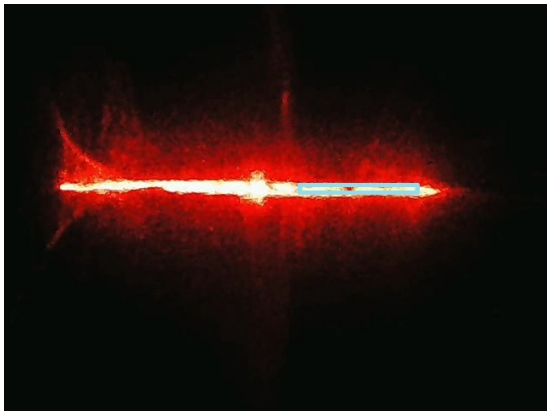

(b) Original image at 49 seconds

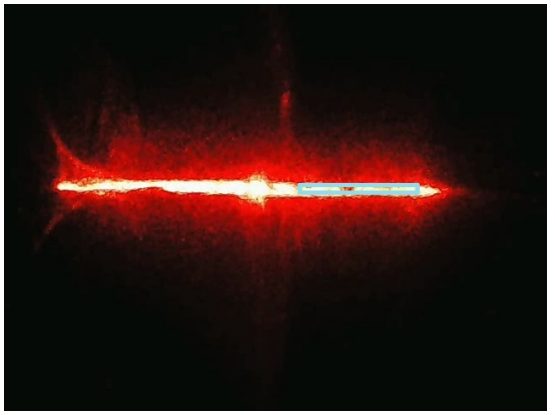

(c) Original image at 149 seconds

(d) Cropped image at 16 seconds

(e) Cropped image at 49 seconds

(f) Cropped image at 149 seconds

(g) Intensity graph at 16 seconds

(h) Intensity graph at 49 seconds

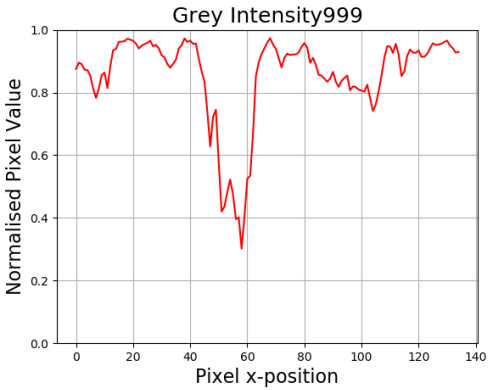

(i) Intensity graph 149 seconds

Figure 5.51: The second analysis of the 10 mg·ml^{-1} concentration of BSA results

5.5 Summary

In this chapter the design, manufacturing, and testing of various components of an SPR biosensor are discussed.

The first component that is described is the gold chip. These chips were hand-cut and gold coated. The adhesion between the gold and the glass was not sufficient and therefore the gold substrate is easily damaged, and hence the chips could not be reused. The gold substrate was roughly 50 nm thick, which was desired, and with these chips the SPR phenomenon was observed.

In the photonic experimental section, two different lasers were tested and compared, leading to the selection of the Infiniter laser, due to its low cost, good stability and beam type. Various optical configurations and prisms were tested. The SPR phenomenon was observed in some of these configurations. However, the results could not always be repeated. Despite this, the Infiniter laser with the D-shaped prism was selected as the configuration to be implemented in the prototype, as it showed the desired signal with a clear SPR dip.

The electronics system implemented is a basic power supply that powers the laser. The system is easy to use and portable.

The microfluidic channel had to be redesigned due to manufacturing constraints. The new design underwent various iterations during the manufacturing process. However, the final design is satisfactory. When the glass chip is big enough and only a low pressure is applied when the liquid is introduced to the system, no leaking occurs.

The prototype is adjustable and sturdy. All components fit into the prototype securely. The position of various parts of the system is adjustable, making it easier to adapt the system. The enclosure, painted with Black 2.0, eliminates a large amount of ambient light.

The immobilisation process yielded a lot of issues. Both SAM formation and streptavidin adsorption were considered and tested. Various concentrations and incubation times were applied. Numerous verification methods were implemented. The results are often unexpected and inconsistent, and therefore inconclusive. Unfortunately, no further investigations were done on immobilisation.

Using Python and OpenCV, various algorithms to manipulate the obtained data were developed. The algorithms were applied to an image obtained in literature, as well as an image obtained from the photonic experimental setup. The PCA algorithm, that is used to rotate the images, does not work as desired when the signal is not clear i.e., scatters. However, in the prototype, when the camera is aligned correctly, no image rotation is required. Once the image is cropped, the SPR curves can be obtained.

Chapter 6

Discussion

This section serves a summary of the designing and manufacturing process, and discusses the results.

6.1 Gold chip

The gold chip compares with what is in literature in terms of size and gold layer thickness. The hand cut glass chips were 10×10 mm is size which is in line with the sizes offered by existing manufacturers, further the gold layer was the desired $\sim$50 nm thick. However, both the adhesion and surface roughness are not ideal. A titanium or chromium layer should be added to improve adhesion, this layer may also improve the surface roughness as shown by Agarwal *et al.* [108].

6.2 Prism

The photonic experiment suffered from a lack of repeatability. The set up was in line with numerous experiments in literature. Different configurations and prisms were tested. The results for the triangular prism were good, as the SPR signal was observed. However, there was visible scattering, which is likely due to the surface roughness of the gold layer. The experiments with the D-shaped prism were good, yet not repeatable. Both prisms are made of BK7 material which is commonly implemented in literature. The D-shaped prism was not ideal, due to its shape. In literature most sensors use a semi-circular or triangular prisms. The implementation of a larger semi-circular shaped prism would possibly have been better, as it will be easier to align. Additionally, ray tracing could have been beneficial, as this would aid in the prediction of the laser beam's behaviour and locations within the experimental setup.

6.3 Fluidic channel

Unfortunately, the microfluidic system was not tested with a syringe pump. This would have allowed for the evaluation of the microfluidics under operational conditions. However, when 10×10 mm SPR chip was employed and the inlet speed was below 1 ml$\cdot$s^{-1}, no leaking occurred.

6.4 Prototype

The prototype is adjustable and sturdy, as was intended with the design. The prototype is larger than the Plamonix SPR sensor and a reduction in both weight and size will improve the design.

6.5 Immobilisation

The immobilisation process yielded a lot of issues. Various steps were taken to determine where the problems occurred. The immobilisation summary in Chapter 5 details the issues faced and the steps taken to solve them. The high concentrations of the thiols that were used to ensure good surface coverage may have been excessive and made it seem as if too little binding took place, since the standard curves saturated. More tests employing greater variety of concentrations may have led to more conclusive results. Additionally, as it was discovered that the FITC adsorbs into the gold layer, a different verification method would have been beneficial. The use of fluorescently tagged anti-anti-bodies may have yielded better results, as these would only bind to the antibodies and not to the substrate.

Upon further research, a 3MPA SAM may not have been ideal for this application. A NHS-MHA SAM would have been a better match. NHS-MHA SAMs minimise non-specific binding and therefore increase SPR sensitivity, which is necessary when using cytokines as biomarkers [136].

6.6 Software

Various algorithms to manipulate the obtained data were developed. The PCA algorithm, that is used to rotate the images, does not work as desired when the signal showed light scattering. However, images from the prototype required no image rotation, as everything aligned well. Once the image was cropped, the SPR curves can be obtained. The data was analysed after the test and not in real time, as the system was too slow. The programming language *C++* would improve the speed as it has less overhead and can handle larger volumes of data faster.

6.7 System testing

Since the immobilisation was unsuccessful, the system as a whole could not be tested as planned with the antigens. However, tests were done using cysteamine and BSA. Unfortunately, these tests could not be repeated as the sensor signal did not produce a SPR band upon further testing. The lack of reproducibility in these tests makes it difficult to draw conclusions or make comparisons with what is found in literature. However, at a high concentration of BSA a change in the SPR band's width was observed.

Chapter 7

Recommendations

The testing of the various parts of the system revealed that many of them need refinement. This section will discuss recommendations for the various hardware parts, as well as the software of the project.

The gold layer on the chips is easily damaged, therefore a titanium or chromium adhesion layer should be added. The surface roughness of the gold layer plays a significant role in the SPR signal, it is assumed that the light scattering in the signal may be due to the roughness of the layer. It is recommended that techniques to improve the surface roughness are investigated. Further, purchasing SPR chips from companies that specialise in SPR products should be considered.

The experimental setup will have to be improved, to deliver repeatable results. Different prism shapes and sizes, as well as different prism and lens combinations will need to be investigated. A larger semicircular prism may be beneficial in the development stage, as it would be easier to handle and align. Further, a prism with a coating could be considered. These coatings can effect the optical properties of the optics, i.e. the way the light is polarised and transmitted. Additionally, they can reduce reflections and act as a filter for unwanted wavelengths [155].

The leaking of the microfluidic system may be eliminated if the SPR chips all have the same size i.e. are big enough to seal the system correctly. Further the pressure that may lead to the leaking can be reduced by implementing a syringe pump. Not only will this reduce the pressure, but it will also allow for control over the speed at which the sample is introduced to the SPR chip. A syringe pump can also be used to generate dynamic results, which in combination with software tracking the displacement of the location of the intensity dip, will allow for the creation of sensorgrams. These can aid in the analysis of the obtained data.

The prototype can be made more compact, by reducing the size of the various components, making it easier to transport and use in the field. Further, different material types can be investigated to make the prototype lighter. The entire prototype can be painted with Black 2.0 to block out more of the environmental light, minimising noise signals. The cameras exposure settings should be investigated. Aspects such as shutter speed and aperture should be considered. Further, filters can be implemented to filter out unwanted wavelengths, such as infrared, green and blue light, this should reduce the noise in the signal.

The immobilisation method needs to be investigated and refined. The unknowns should be eliminated and various different chemical concentrations, incubation times and temperatures will need to be investigated systematically. The effects of external factors, such as environmental temperature and humidity, will need to be minimised. Other confirmation methods should be researched. 3MPA immobilisation could be done under inert gas conditions, to minimise the chances of oxidation. Once the BSA immobilisation is successful the antibody immobilisation can done and then be further optimised. Anti-rabbit or other anti-anti-IP-10 proteins with dye labels can be considered to confirm if immobilisation takes place. Here again, considering to purchase chips from SPR chip companies may help overcome this problem. SPR chip companies offer gold chips with various functionalised surfaces [105]. Further, since the identified biomarkers are cytokines, mass increasing labels for the tagging of the target in the field before introducing it to the sensor could be investigated.

The software algorithms can be optimised. *C++* can be considered as a coding language. *C++* has less overhead, can handle larger volumes of data faster and can easily be compiled into an executable file. Further, the software can be modified so that it has a user friendly interface, in an app-like style, allowing the user to access the data and results with a smart phone. Once the correct prism position and laser angle have been established, reference angles can be determined on the output signal and with the aid of software the intensity graph can be created so that the angle is displayed on the x-axis and not the pixel position. Additionally, the system can be modified to use the phone camera, instead of an additional external camera, for data acquisition.

Moreira *et al.* created an autosampler for an SPR system [86]. This would be a beneficial addition to an SPR system, as it allows for the easy handling of multiple samples.

Chapter 8

Conclusion

This thesis set out to reach a number of goals. This chapter will revisit the previous chapters and highlight how these goals were achieved.

The first goal was to establish a basic understanding of bTB and its effects on society. This was done in Chapters 1 and 2. Bovine Tuberculosis is a contagious disease that can affect a wide range of mammals and if left untreated, can result in death. As discussed in Chapter 1, due to the disease impact on food safety, public health and other socioeconomic sectors, it must thus be surveilled and controlled. Since current diagnostic methods have drawbacks, a biosensor was proposed as a possible aid in the detection of the disease and thus an aid in the surveillance of it's spread. Chapter 2 discussed the current diagnostic methods and their drawbacks. ELISAs detect cell-mediated immune responses, such as the production of IP-10 and IFN-γ. These two biomarkers were concluded to be the biomarkers for the project.

The following goals was to investigate biosensors and methods implemented to detect diseases, to gain an outline of existing diagnostics methods as well as to determine a biosensor type based on the findings in the aforementioned review. Chapter 2 satisfies both these goals. A literature review of existing biosensor types and immobilisation methods was done and was followed by the selection of the biosensor type. The review discusses the critical elements that make up a biosensor and describes various biosensor types, such as piezoelectric, electrochemical and optical. It further investigates immobilisation techniques. From the findings in this literature review it was decided that an SPR sensor will be used for this project.

It was further required that an understanding of SPR be established. Chapter 3, is a detailed investigation of SPR. The theory behind the phenomenon is discussed and different configurations were considered. Further, existing devices were explored. From this chapter the Kretschmann configuration and SAM immobilisation method were chosen for this thesis.

The next goals were to design and develop the parts of the biosensor based on the findings in literature and test these parts, to verify their functionality. Chapter 4 briefly discusses the initial plan for the design and development, justifying these decisions with examples from literature. Chapter 5 discusses the design and development of various parts of the biosensor in detail. It further describes the next goal, the evaluation of these components, reporting on the challenges faced, the methods implemented to investigate the problems

and steps taken to solve these issues. The manufacturing of the gold chips was considered satisfactory, as the SPR phenomenon could be observed using these, despite the scattering. Even though the results from the photonic section were not repeatable, they proved that the SPR phenomenon could be achieved using the proposed configuration. The designed power supply powered the laser successfully. The implementation of the microfluidic channel showed promise. The testing of the immobilisation method was demanding. Two different methods and verification techniques were applied, and unfortunately no conclusive results were obtained. The software achieved what was required when the desired signal was analysed, i.e. when no scattering occurred.

Further, the prototype was constructed and evaluated. Unfortunately, not all the parts of the system worked as desired separately, hence the system as a whole could not be validated. However, the prototype was tested using BSA and cysteamine. A periodic change in the intensity dip's width was observed in the SPR signal when the 10 $mg{\cdot}ml^{-1}$ concentration of BSA was used.

The last goal was to recommend improvements for the system. Many of the components require further refinement, for which recommendations are given in Chapter 6. Even though not all the components met their requirements, steps toward the development of a feasible SPR device have been made. It showed that a portable laser, power supply and an optically simple configuration can be implemented to create the SPR phenomenon. Furthermore, when high concentrations of BSA were introduced to the gold surface, periodic changes in the signal were observed with the naked eye. With better component refinement it should be possible to create an SPR biosensor for the detection of bTB in the field.

Appendices

Appendix A

A.1 Kingfisher Protocol

UNIVERSITEIT STELLENBOSCH UNIVERSITY

SU ANIMAL TB RESEARCH GROUP
Division Molecular Biology and Human Genetics
Laboratory Standard Operating Procedures

KINGFISHER BOVINE IP-10 ELISA – IN HOUSE			
SOP#: LP_007	**Version #:** 2.0	**Effective Date:** 12.02.2018	Page **1** of **7**
Prepared by:	**Reviewed by:**	**Approved by Principal Investigator:**	
(Signature & Date) 09.02.2018	(Signature & Date) 09.02.2018	(Signature & Date) 09.02.2018	
Netanya Bernitz PhD student SU-Animal TB	Wynand Goosen Post-Doctoral Fellow SU-Animal TB	Prof Michele Miller Principal Investigator SU-Animal TB	

TABLE OF CONTENTS

1. SCOPE

The aim of this standard operating procedure is to describe how to perform the in-house Kingfisher Bovine IP-10 ELISA.

2. RESPONSIBILITIES

It is the responsibility of the laboratory personnel to:

- Follow this SOP as written, and
- To take the necessary safety precautions when handling biological specimens during this process.

It is the responsibility of laboratory management to ensure that this procedure is appropriate for its intended use and that all personnel involved in this process are appropriately trained before processing any samples.

The in-house Kingfisher Bovine IP-10 ELISA formulation method needs to be completed when performing this ELISA. Keep a record of the formulation method with the sample report.

3. BACKGROUND

None.

4. PROCEDURE

4.1. CONSUMABLES AND EQUIPMENT

- 0.5µg/ml anti-bovine IP-10 capture antibody (cAb) (Kingfisher, #PB0385B-100)
- 0.2µg/ml biotinylated anti-bovine IP-10 detection antibody (dAb) (Kingfisher, #PBB0393B-050)
- 10µg/ml bovine IP-10 recombinant protein (Kingfisher, #RP0079B-005)
- Blocking Buffer
- Wash Buffer
- *Streptavidin*-HRP (R&D Systems, #DY998)
- 3,3',5,5'-tetramethylbenzidine (TMB) Substrate Reagent Kit (BD Biosciences, #BD/555214
- 2M H_2SO_4
- Flat-bottom, 96-well, Maxisorp clear plates (Nunc, #442404)
- Plate sealer for 96-well plate (Greiner, #A5596)
- ELISA plate reader

- 37°C incubator
- 24°C incubator
- 4°C fridge
- P10 pipette
- P20 pipette
- P200 pipette
- P1000 pipette
- P10 tips
- P20 tips
- P200 tips
- P1000 tips

4.2. METHODS

Day 1:

1. Prepare cAb. Dilute stock 2000x (1mg/ml) to working concentration 0.5µg/ml in 1x PBS.
2. Add 100µl of cAb solution to each well and cover with a plate sealer. Incubate overnight (O/N) at 4°C.

Day 2:

3. Decant cAb solution from plate and wash wells 4x with 300µl Wash Buffer.
4. Add 200µl of Blocking Buffer per well and cover with plate sealer. Block for 1 hour at 24°C.
   Note: Incubate samples in an incubator at 24°C and not on the bench. Always place ELISA plates on a layer of paper towel as surfaces may influence the temperature of the ELISA.
5. Decant Blocking Buffer and wash wells 4x with 300µl Wash Buffer.
6. Prepare standards in Blocking Buffer as follows:

   Make up the first standard (10 000pg/ml) by diluting 10µl of the Bovine IP-10 recombinant protein in 10ml Blocking Buffer. Thereafter, do 2-fold serial dilutions by diluting 500µl of the previous dilution in 500µl Blocking Buffer (Figure 1 and Table 1)

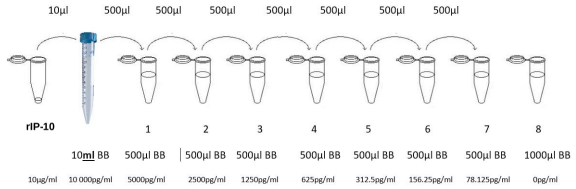

Figure 1: An illustration of the dilution series required to make up concentrations 5000pg/ml-78.125pg/ml from a 1µg/ml stock solution of rIP-10

Table 1: Standards 1-8 and the amounts required to make up 5000pg/ml to 0pg/ml using a serial dilution from a starting concentration of 10000pg/ml

Standard	Blocking Buffer (µl)	Previous standard (µl)	Final concentration (pg/ml)
1	500	500	5000
2	500	500	2500
3	500	500	1250
4	500	500	625
5	500	500	312.5
6	500	500	156.25
7	500	500	78.125
8	500	0	0

7. Dilute samples (1:4) in Blocking Buffer:
   a) Aliquot 90µl of Blocking Buffer to wells of a deep-well/ round bottomed 96 well culture plate.
   b) Add 30µl of your sample to the wells of a deep-well/round bottomed 96 well culture plate.
8. Add 100µl of each standard in duplicate to the appropriate wells.
9. Add 100 µl of diluted samples to the appropriate wells.
10. Cover the plate with a plate sealer and incubate standards and samples for two hours at 24°C.
11. Decant standards and samples and wash wells 4x with 300µl Wash buffer.
12. Prepare dAb in Blocking Buffer. Dilute stock (1mg/ml) 5000x in Blocking Buffer (0.2µg/ml).
13. Add 100µl of dAb solution to each well, cover the plate with a plate sealer and incubate for 1 hour at 24°C.
14. Decant dAb solution and wash wells 4x with 300µl Wash buffer.
15. Prepare *Streptavidin*-HRP (200x) in Blocking Buffer.

16. Add 100µl of *Streptavidin*-HRP solution to each well, cover plate with a plate sealer and incubate for 1 hour at 24°C.
17. Decant *Streptavidin*-HRP solution and wash plate 4x with 300µl Wash buffer.
18. Prepare TMB by mixing equal volumes of substrate A and B.
19. Add 100µl of TMB solution (use within 15 minutes of mixed) to each well and incubate for 20 min at 24°C in the dark without plate sealer. Start timing when TMB is added to the first well.
20. Add 50µl of 2 M H_2SO_4 in the same order as the TMB was added.
21. Read absorbance at 450nm and 630nm.
22. Calculate $OD_{final} = OD_{450nm} - OD_{630nm}$
23. Determine the concentration of samples from the linear standard curve and correct for the dilution factor (x4).

How to log transform data when standard curve is not linear:

1. Open Prism.
2. Under 'New table and graph' select 'XY'.
3. Under 'Y' select 'Enter and plot a single Y value for each point' and select 'Create'
4. In the x column add the known concentrations from the standard curve and in the y column add the corresponding OD's from the plate reader.
5. Also, add unknown ODs in the y column under standard curve OD's
   Note: to transform (log-log) STD curve and OD values.
6. Select 'Analyze'.
7. Under 'Transform, Normalise..' select 'Transform'.
8. Under 'Function list' select 'Pharmacology and biochemistry transform'.
9. Select 'Log-Log'.
   Note: Now STD curve concentrations and ODs have all been log transformed and the STD curve can be generated and data be interpolated.
10. Select 'Analyze'.
11. Under 'XY Analyses' select 'Non-linear regression (curve fit)'.
12. Under 'Polynomial' select 'Second Order Polynomial (quadratic)'.
13. Under 'Interpolate' select 'Interpolate unknowns from standard curve'
    Note: Then a table of results will pop up with an r^2 value for your standard curve and a sheet for 'Interpolated X values' will be available.
14. These interpolated values need to be changed back.
15. Select 'Analyze'.
16. Under 'Transform, Normalize..' select 'Transform'.
17. Under the function list select Standard functions.
18. Select 'Transform X values using $X=10^X$'.
19. Select 'Transform Y values using $Y=10^Y$'.
    Note: Final 'Interpolated X values' will appear, these are the final concentrations (the ODs should revert to what initially were inserted into prism)

Reporting:

Complete the Animal TB research report form available on google drive (link and SOP version 2.0).

4.3. REAGENT PREPARATION

- **Capture antibody (cAb):** Anti-bovine IP-10 polyclonal Ab (pAb) (Kingfisher, #PB0385B-100). Stored at 4°C. Stock solution: 1mg/ml. Working solution: 0.5µg/ml
- **Detection antibody (dAb):** Biotinylated Anti-bovine IP-10 pAb (Kingfisher, #PBB0393B-050). Stored at 4°C. Stock solution: 1mg/ml. Working solution: 0.2µg/ml
- **Recombinant Bovine IP-10 protein** (Kingfisher, #RP0079B-005), 5µg of lyophilized protein to be reconstituted with 500µl of 1% BSA and stored at -80°C (Tower 36 Row 6) in 12µl aliquots. No freeze- thawing so throw away aliquot when finished. Stock solution: 10µg/ml. Working solution: 5000pg/ml
- 1g BSA crystals (Roche, #10735086001) + 100ml 1x PBS. Mix with magnetic stirrer bar and filter sterilize with 0.22µm filter.
- **Blocking Buffer:** 50ml 1% BSA + 450ml Wash Buffer.
- **1x PBS:** 100ml 10x PBS (Lonza, #BE17-517Q) + 900ml dH20
- **Wash Buffer (PBS-Tween-20):** 500µl Tween-20 (Sigma Aldrich, #P5927) + 1 L 1x PBS

5. DEFINITIONS

- cAb- capture antibody
- dAb- detection antibody
- HRP- horse radish peroxidase
- OD- optical density
- STD- standard
- TMB- 3,3',5,5'-tetramethylbenzidine
- r- recombinant
- IP-10- Interferon-gamma induced protein 10

6. REFERENCES

7. SUPPORTING DOCUMENTS

- In-house Kingfisher Bovine IP-10 ELISA formulation method.
- Reporting

8. AVAILABILITY

The original signed version of this document is kept by the Quality Assurance Officer. Training documents available in personnel folders. A copy of the document can be found on the document management system ALFRESCO/SU Animal TB google drive.

9. DOCUMENT HISTORY

Version No.	Date	Location of Change History	Author/ Reviewer	Approving Official	Date Approved	Next Review Date
1.0	06.02.018	Throughout document	Animal TB Group	Prof M Miller	07.02.2018	12.01.2019

Appendix B

EDX

These analyses were done at Electron Microscopy unit of Stellenbosch University's Central Analytical Facilities by Dr Alicia Botes.

B.1 EDX Analysis of Batch Two

Ronja Hess **12/2/2020**

Au_Cu

Electron Image 1

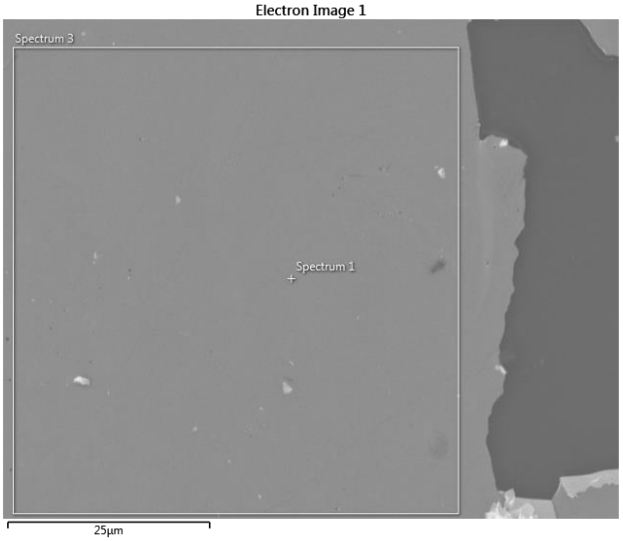

OXFORD INSTRUMENTS
The Business of Science®

Ronja Hess **12/2/2020**

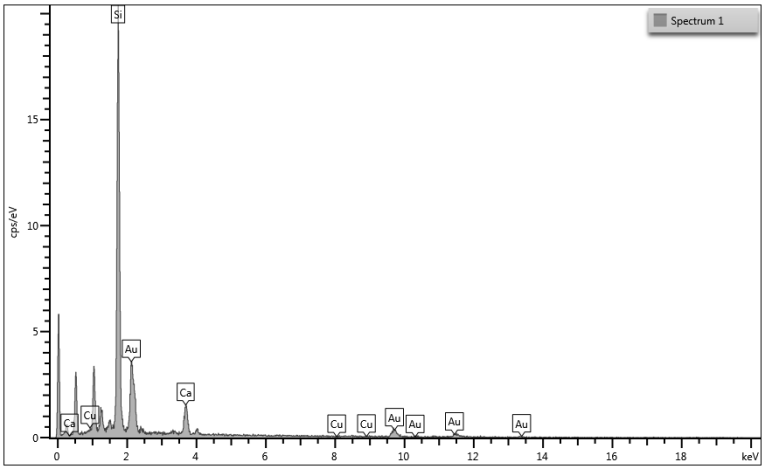

Ronja Hess **12/2/2020**

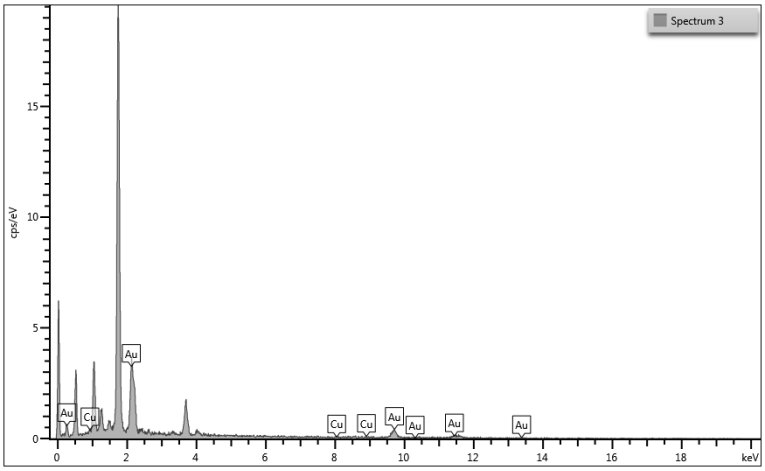

Ronja Hess **12/2/2020**

Result Type	Weight %

Spectrum Label	Spectrum 1	Spectrum 3
Cu	0.00	1.41
Pd	0.00	0.00
Au	100.00	98.59
Total	100.00	100.00

Statistics	Cu	Pd	Au
Max	1.41	0.00	100.00
Min	0.00	0.00	98.59
Average	0.71	0.00	99.29
Standard Deviation	1.00	0.00	1.00

OXFORD INSTRUMENTS
The Business of Science®

B.2 EDX Analysis of Batch Three

Ronja Hess **12/2/2020**

Au_Pd

Electron Image 2

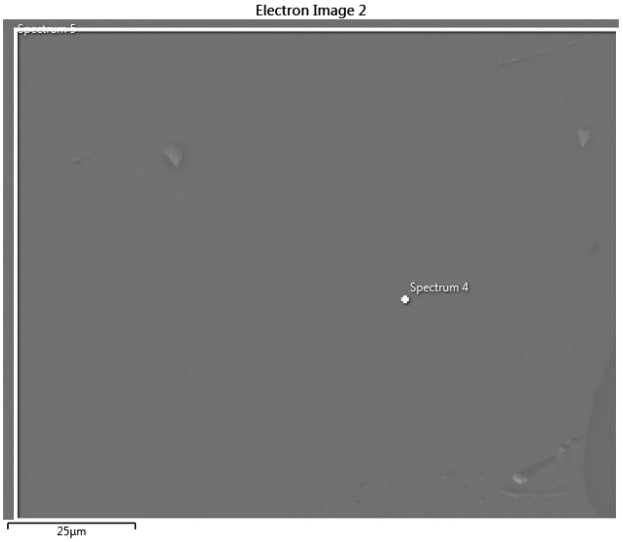

OXFORD INSTRUMENTS
The Business of Science®

Ronja Hess **12/2/2020**

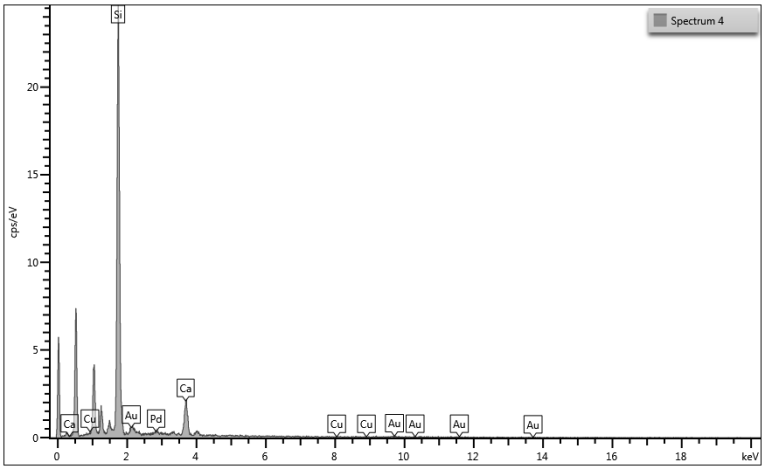

Ronja Hess **12/2/2020**

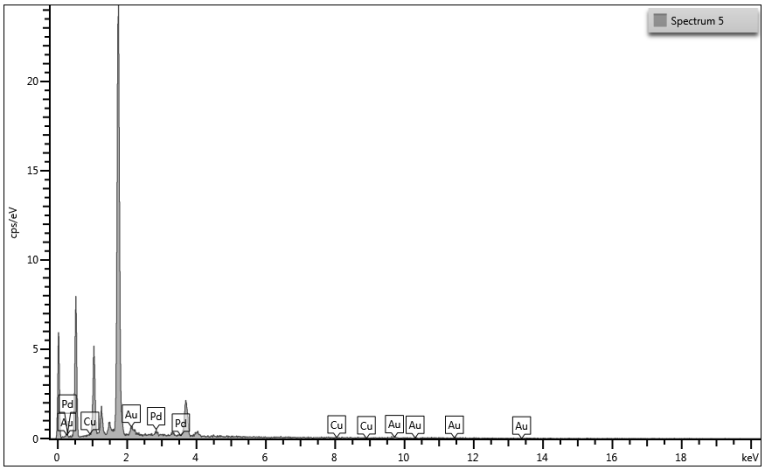

Ronja Hess **12/2/2020**

Result Type	Weight %

Spectrum Label	Spectrum 4	Spectrum 5
Pd	40.81	44.88
Au	59.19	55.12
Total	100.00	100.00

Statistics	Pd	Au
Max	44.88	59.19
Min	40.81	55.12
Average	42.84	57.16
Standard Deviation	2.88	2.88

OXFORD INSTRUMENTS
The Business of Science®

B.3 EDX Analysis of Batch Four

B.3.1 Sample 1

Aluminum Slides **1/12/2021**

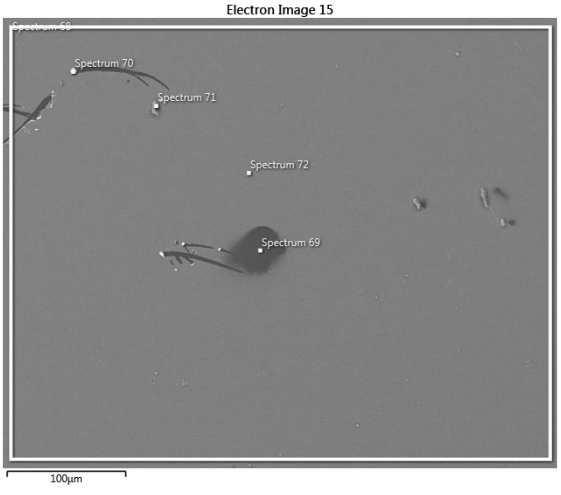

OXFORD INSTRUMENTS
The Business of Science®

Aluminum Slides **1/12/2021**

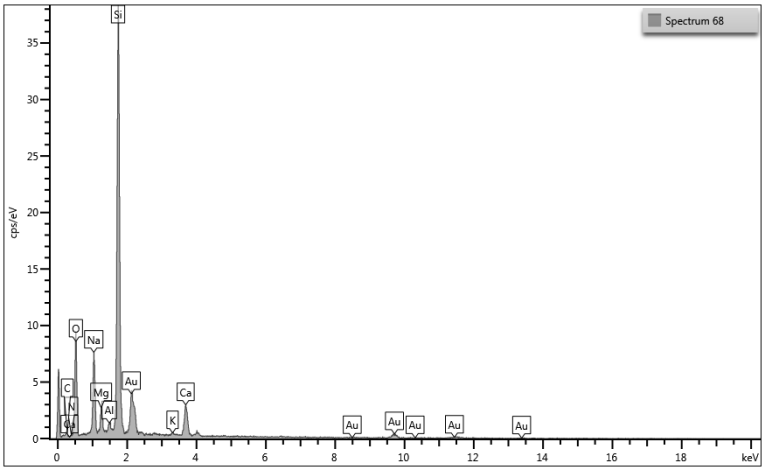

OXFORD INSTRUMENTS
The Business of Science®

Aluminum Slides **1/12/2021**

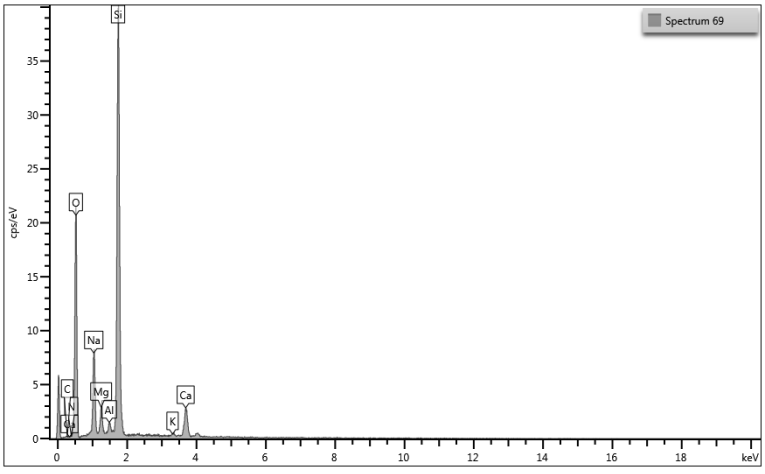

OXFORD INSTRUMENTS
The Business of Science®

Aluminum Slides **1/12/2021**

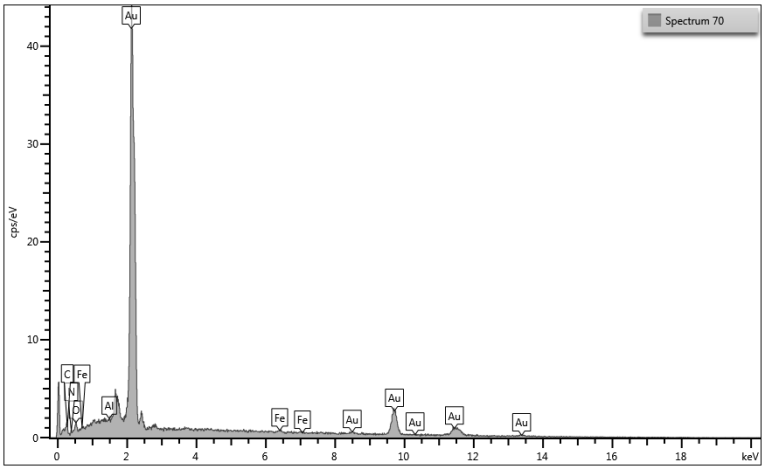

OXFORD INSTRUMENTS
The Business of Science®

Aluminum Slides **1/12/2021**

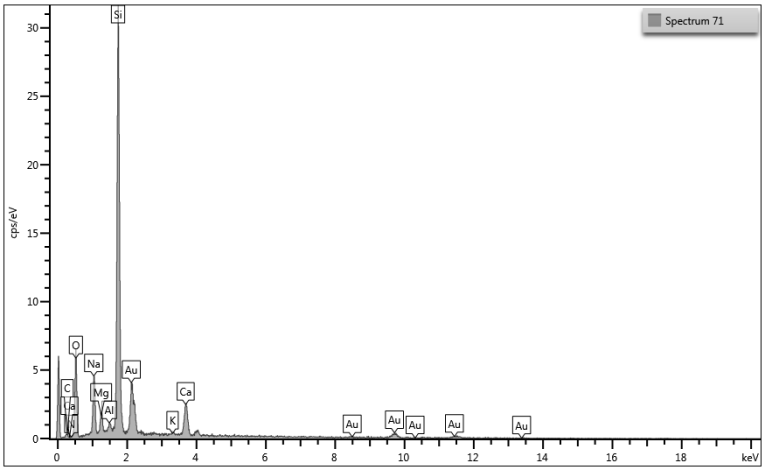

OXFORD INSTRUMENTS
The Business of Science®

Aluminum Slides **1/12/2021**

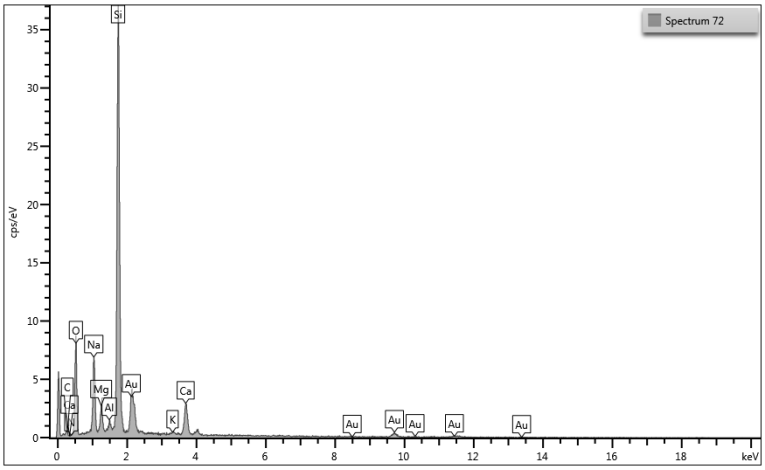

OXFORD INSTRUMENTS
The Business of Science®

Aluminum Slides **1/12/2021**

Result Type	Weight %

Spectrum Label	Spectrum 68	Spectrum 69	Spectrum 70	Spectrum 71	Spectrum 72
Au	100.00	0.00	100.00	100.00	100.00
Total	100.00	0.00	100.00	100.00	100.00

Statistics	Au
Max	100.00
Min	0.00
Average	80.00
Standard Deviation	44.72

OXFORD INSTRUMENTS
The Business of Science®

B.3.2 Sample 2

Aluminum Slides **1/12/2021**

Electron Image 16

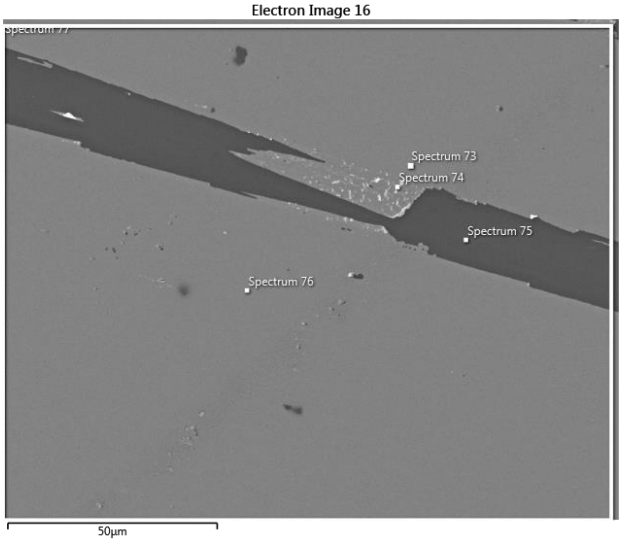

OXFORD INSTRUMENTS
The Business of Science®

Aluminum Slides **1/12/2021**

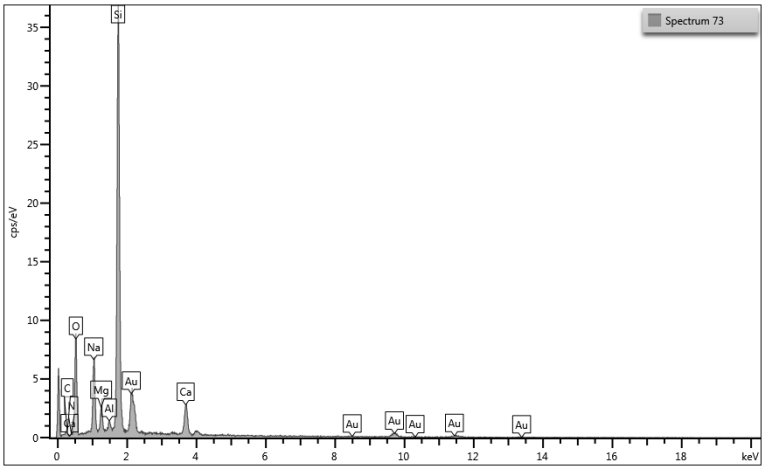

OXFORD INSTRUMENTS
The Business of Science®

Aluminum Slides **1/12/2021**

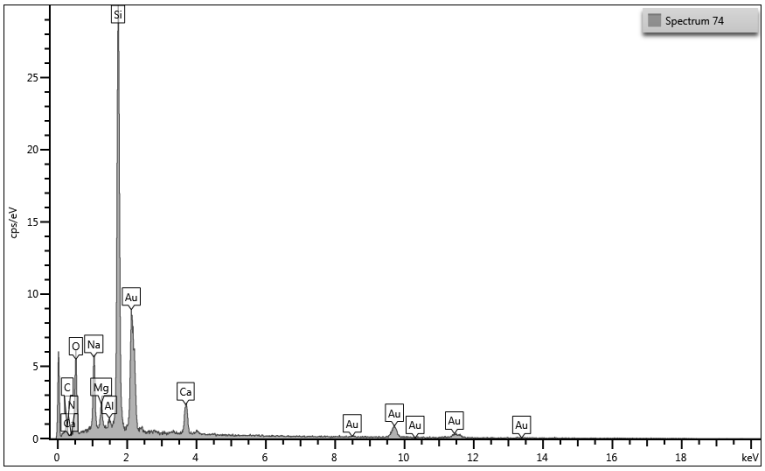

OXFORD INSTRUMENTS
The Business of Science®

Aluminum Slides **1/12/2021**

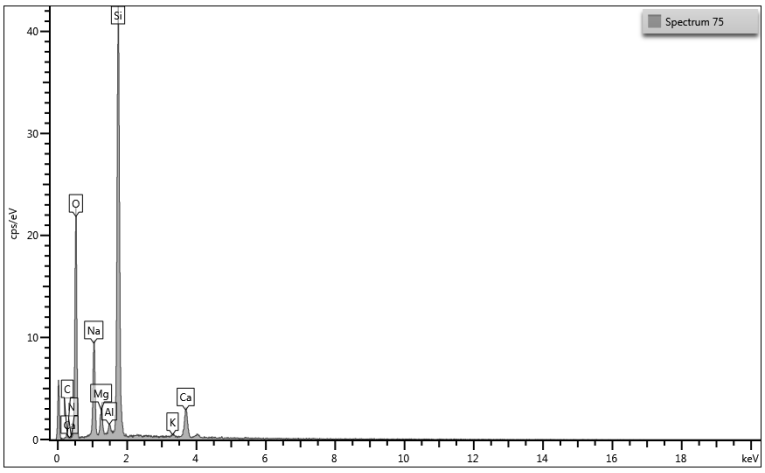

OXFORD INSTRUMENTS
The Business of Science®

Aluminum Slides **1/12/2021**

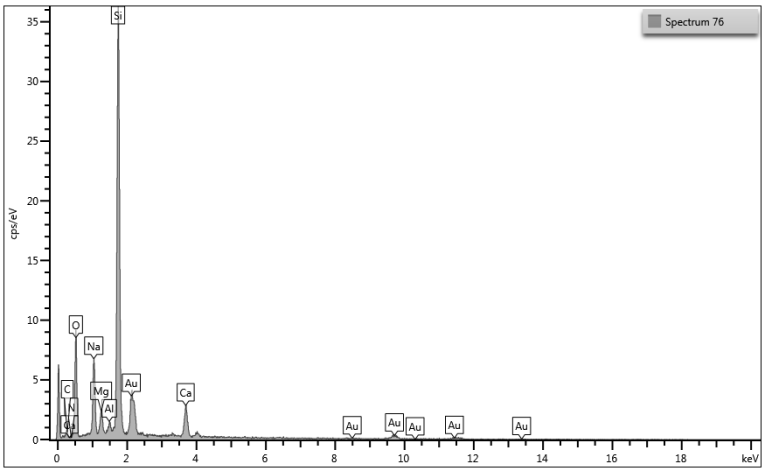

OXFORD INSTRUMENTS
The Business of Science®

Aluminum Slides **1/12/2021**

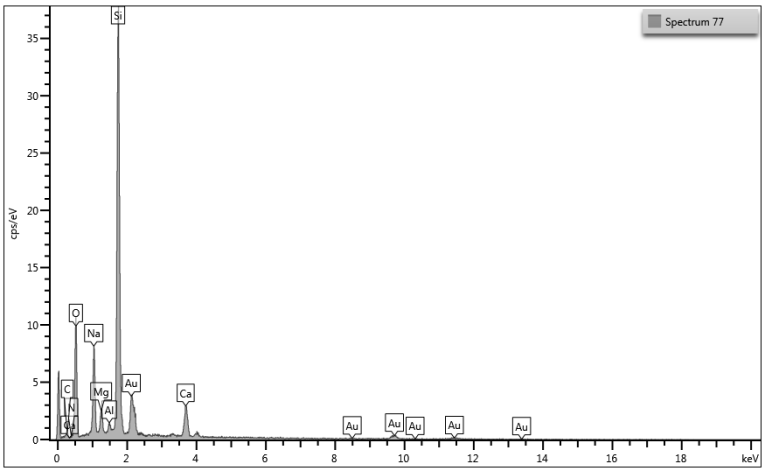

OXFORD INSTRUMENTS
The Business of Science®

Aluminum Slides **1/12/2021**

Result Type	Weight %

Spectrum Label	Spectrum 73	Spectrum 74	Spectrum 75	Spectrum 76	Spectrum 77
Au	100.00	100.00	0.00	100.00	100.00
Total	100.00	100.00	0.00	100.00	100.00

Statistics	Au
Max	100.00
Min	0.00
Average	80.00
Standard Deviation	44.72

OXFORD INSTRUMENTS
The Business of Science®

Appendix C

Data sheets and Technical Information

C.1 Panasonic Laser

The data sheet for the Panasonic laser [156].

Panasonic

LNCQ28MS01WW

Description

LNCQ28MS01WW is a MOCVD fabricated 660nm band wavelength laser diode with multi quantum well structure, using TO-56 CAN package to ensure versatile use.

Features

- Wavelength: 661 nm (typ.)
- High output power and temperature: 100 mW, Max+85°C (CW)
  300 mW, Max+85°C (pulse)
  350 mW, Max+75°C (pulse)
- Package: TO-56 CAN
- With photo diode(PD)

Package

Applications

- Optical disk drive
- Sensing
- Analysis
- Measurement
- Agriculture
- Other industrial use

Absolute Maximum Ratings

Item		Symbol	Value	Unit	Condition
Output power		Po	100	mW	CW
			300	mW	pulse[1)]
			350	mW	pulse[2)]
Reverse voltage	LD	Vr_LD	1.5	V	CW
	PD	Vr_PD	5	V	CW
Operating case temperature		Tc	–10 to +85	°C	CW
			–10 to +85	°C	pulse[1)]
Storage temperature		Tstg	–40 to +85	°C	

Note) 1) Pulse width≦40ns, duty≦33%
2) Pulse width≦40ns, duty≦33% Operating case temperature condition: -10～+75°C

Electrical and Optical Characteristics

T=25°C, CW, Po=90 mW

Item		Symbol	Min.	Typ.	Max.	Unit	Condition
Threshold current		Ith	35	50	70	mA	
Operating current		Iop	110	128	165	mA	
Operating voltage		Vop	2.0	2.4	3.0	V	
Monitoring Current		Im	0.1	0.4	1.0	mA	
Wavelength		λ	656	661	665	nm	
Beam Divergence	Parallel	θh	7.5	9.0	13.0	deg	FWHM
	Perpendicular	θv	13.0	15.0	19.5	deg	FWHM

FWHM: Full width at half maximum

Typical Characteristics

Output Power vs Current (CW)

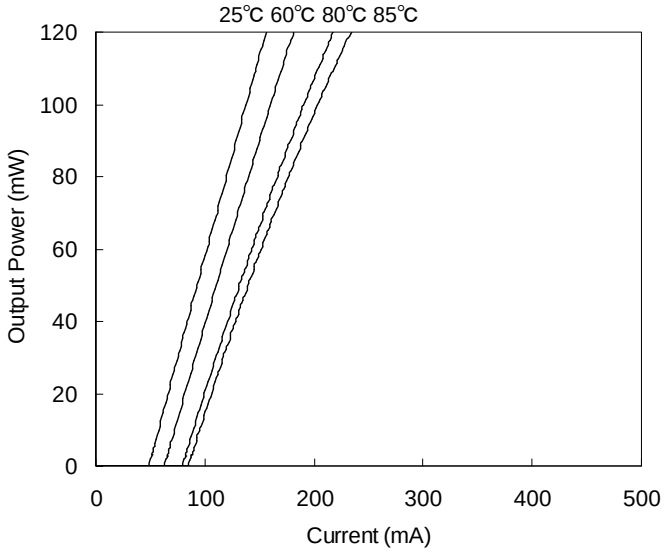

Voltage vs Current (CW)

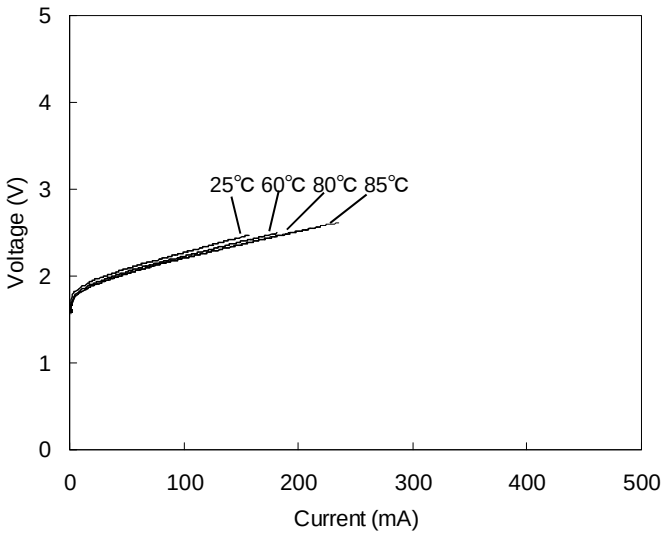

Output Power vs Current (Pulse)

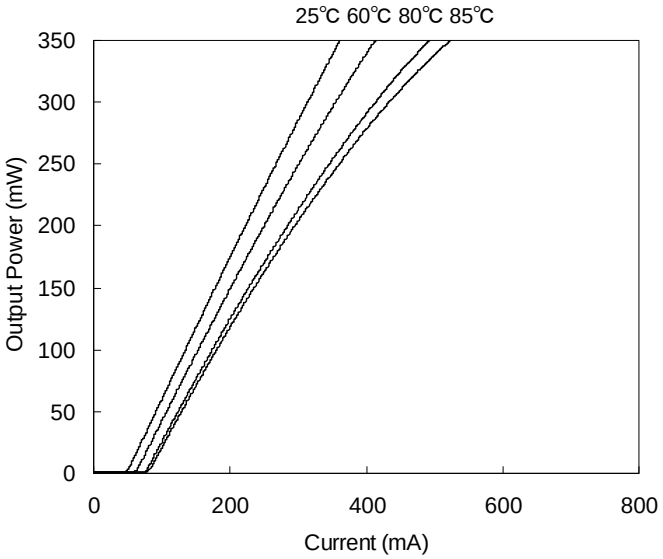

Voltage vs Current (Pulse)

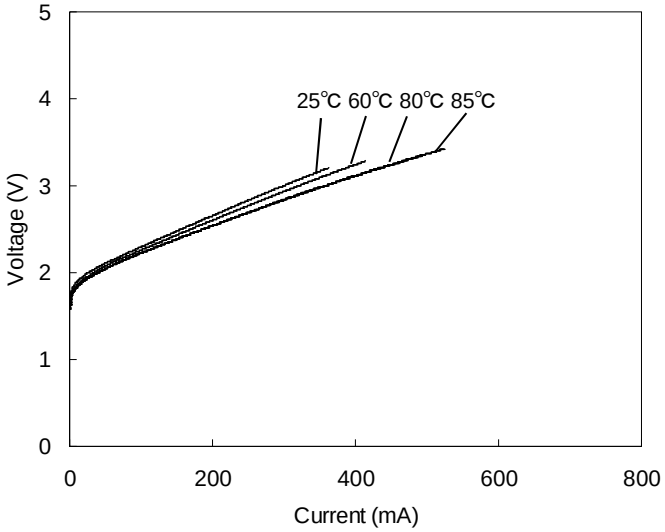

Typical Characteristics

Beam Divergence
Parallel to the Junction (CW)

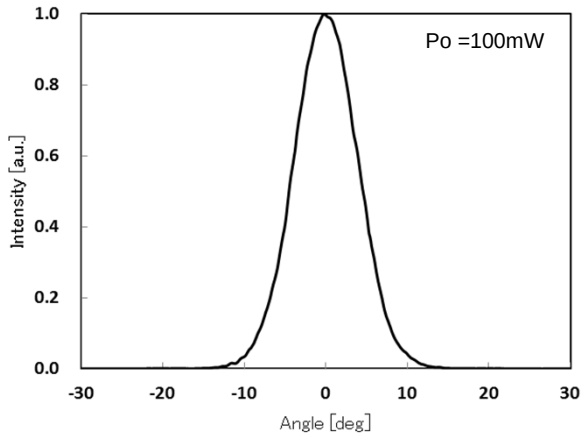

Beam Divergence
Perpendicular to the Junction (CW)

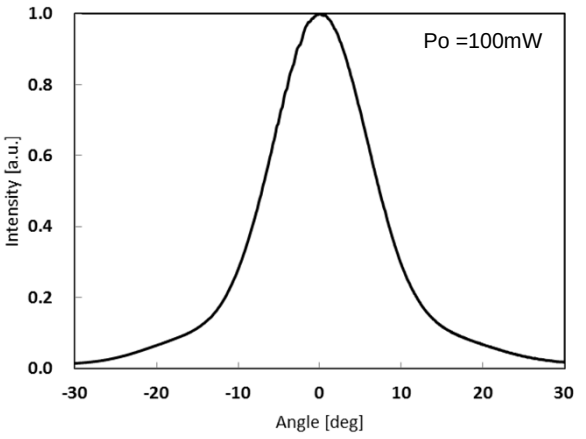

Beam Divergence of Parallel
to the Junction vs Output Power (CW)

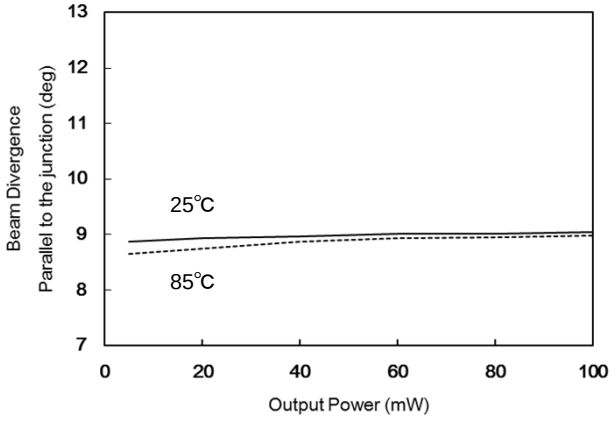

Beam Divergence of Perpendicular
to the Junction vs Output Power (CW)

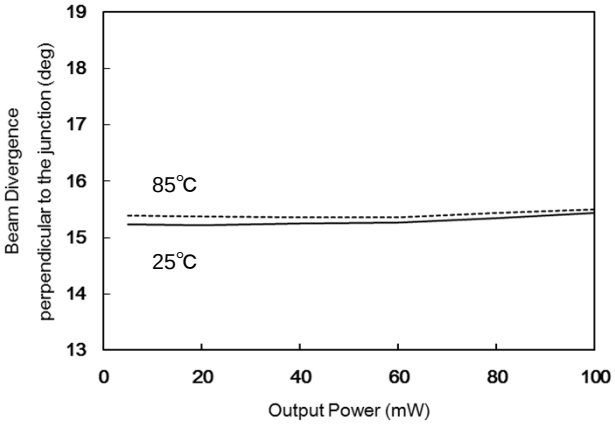

Wavelength vs Temperature (CW)

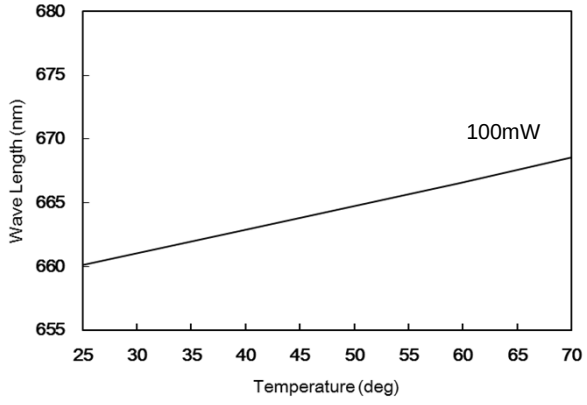

Monitoring Current vs Output Power (CW)

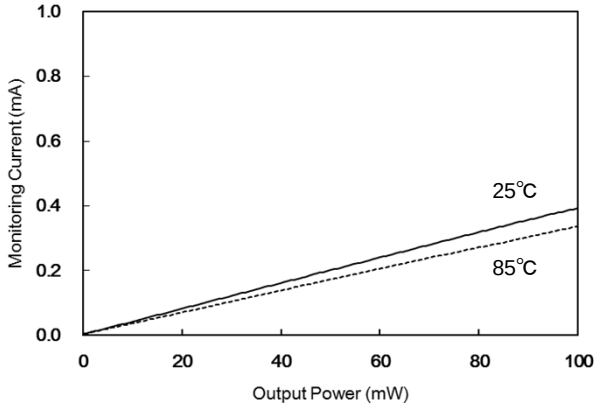

Package Dimensions

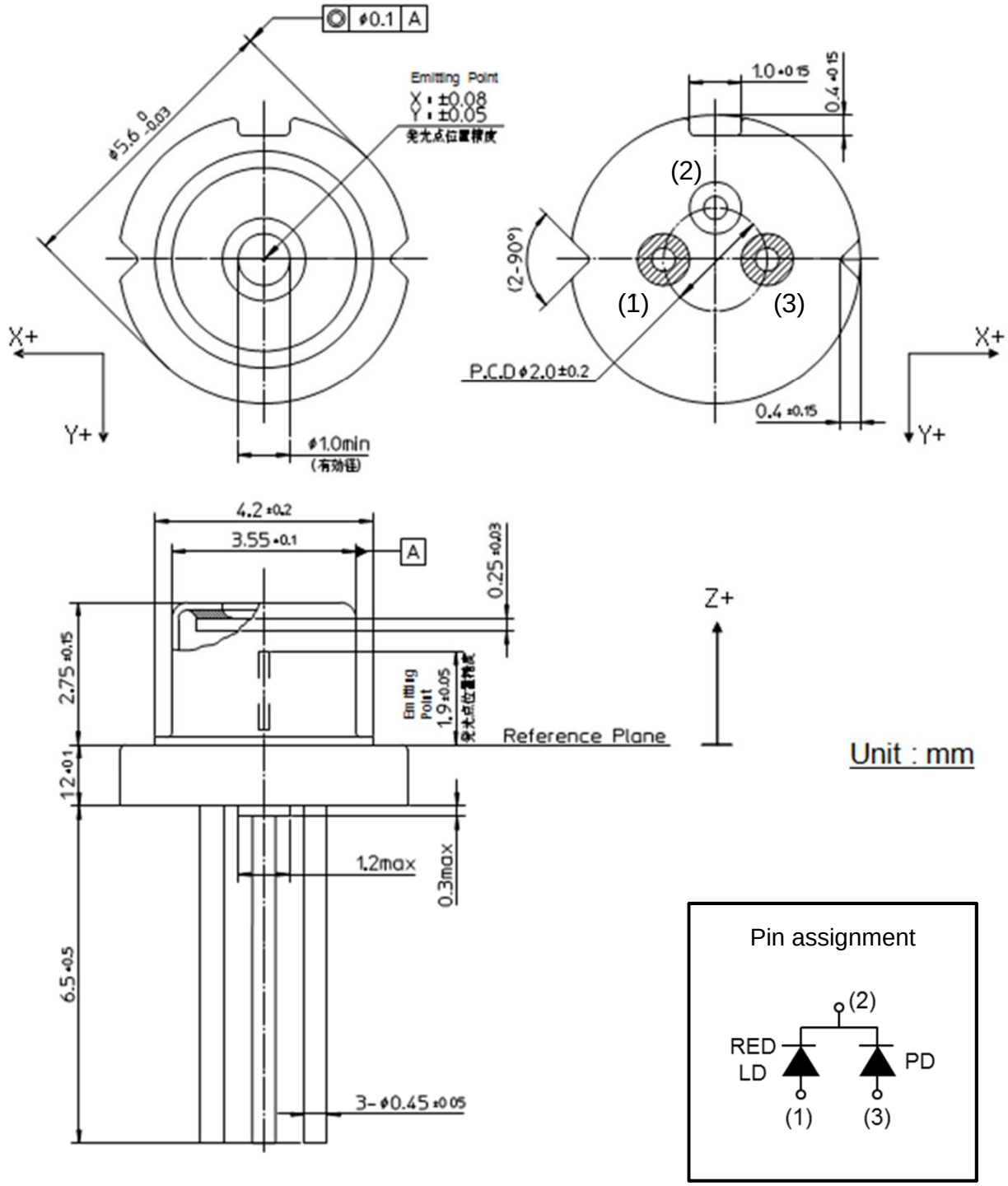

Note)
1. X-Y tolerance of lead is specified on the package bottom plane.

Packing Specifications

1 Packing Material

1.1 Tray

Material: PS Conductive (Black)

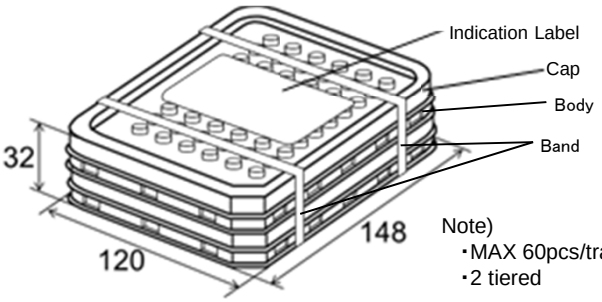

Note)
・MAX 60pcs/tray
・2 tiered

1.2 Laminated Aluminum Pack

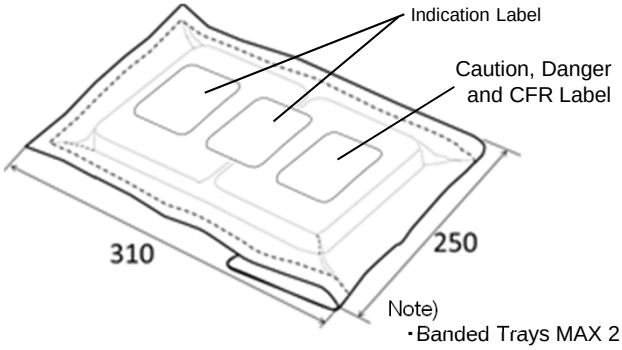

Note)
・Banded Trays MAX 2 sets

1.3 Packing Case

Material: Corrugated fiber board

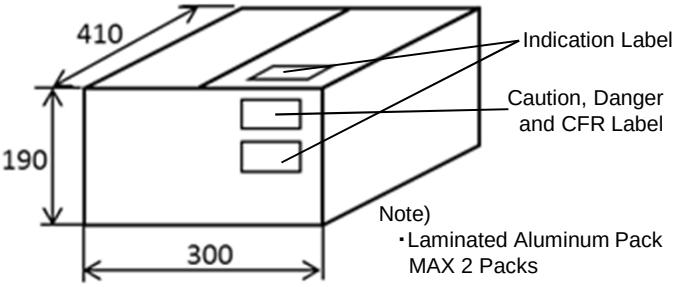

Note)
・Laminated Aluminum Pack
MAX 2 Packs

※As for label indication except ①(Order person part number), ②(Order person part number and Quantity), ③(Serial number and Corporate code), and ④(Quantity), the information only for our process control. Therefore, revision might be done for improvement without notice.

1) Indication on Top Tray

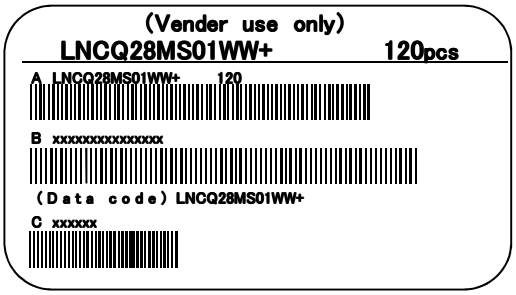

2) Indication on Laminated Pack

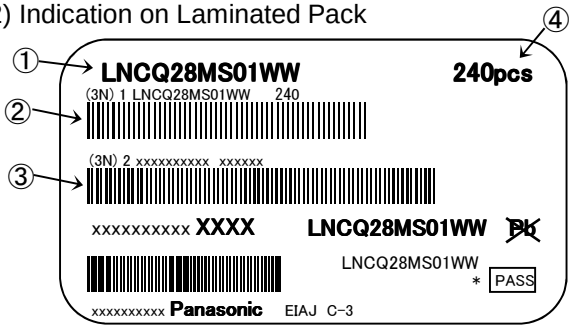

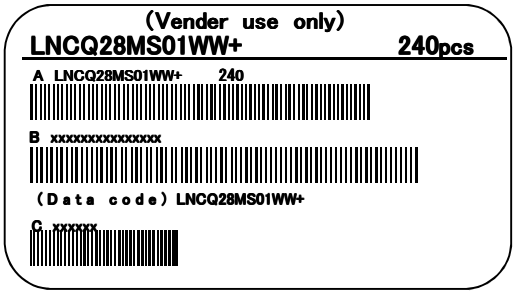

3) Indication on packing case

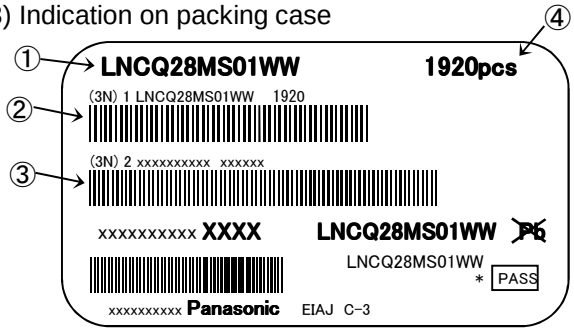

2 Packaging Quantity

Form	Quantity	Contents
Tray	n=60	--
Laminated Aluminum Pack	n=240	Tray: 4
Packing Case	n=240 to 1920	Aluminum Pack:1 to 8

Warning

■ Laser class
This product is ranked “Class IIIb laser” according to IEC60825-1 and JIS standard 6802 “Laser Product Emission Safety Standards,” so that safety protection is necessary when laser beam is radiated.

Cautions

■ TO-56 CAN packaged laser diode
This product uses a TO-56 CAN package to ensure versatile use.

■ Prevention of Electrostatic discharge (ESD) and surge stress
Semiconductor laser diode is a device sensitive to ESD and surge, so that sufficient cautions are needed. If electrostatic discharge is applied to a laser diode, intensive light emission may occur instantaneously, leading to the potential for catastrophic damage in the laser diode or degradation of the laser diode in a short time.
Therefore, taking all possible measures against ESD and surge for usage of CAN packaged laser diode is strongly requested.

■ Heat sink design
As case temperature becomes higher, the life of semiconductor laser diode becomes shorter. So appropriate heat dissipation design is required. Especially it is effective to make a thermal connection to the highly thermally conductive heat sink at the base plate of a TO56 package.

■ Precautions for soldering
Excess heating to laser diode package during soldering may affect eutectic solder and/or laser diode itself. Soldering must be done as quickly as possible with controlling the heating temperature. Lead(terminal) soldering with appropriate cooling time is strongly recommended. Also, soldering position of lead(terminal) is recommended to be more than 2mm away from the package body.

・Soldering temperature: below 350℃
・Heating period: within 3 s
・Soldering position: 2mm away from the package body

⚠ Caution for Safety

⚠DANGER	Do not touch or look into the laser beam directly. The laser beam may cause injury to the eye or skin, or loss of eyesight.

Request for your special attention and precautions in using the technical information and semiconductors described in this book

(1) If any of the products or technical information described in this book is to be exported or provided to non-residents, the laws and regulations of the exporting country, especially, those with regard to security export control, must be observed.

(2) The technical information described in this book is intended only to show the main characteristics and application circuit examples of the products. No license is granted in and to any intellectual property right or other right owned by Panasonic Corporation or any other company. Therefore, no responsibility is assumed by our company as to the infringement upon any such right owned by any other company which may arise as a result of the use of technical information de-scribed in this book.

(3) The products described in this book are intended to be used for general applications (such as office equipment, communications equipment, measuring instruments and household appliances), or for specific applications as expressly stated in this book.
Please consult with our sales staff in advance for information on the following applications, moreover please exchange documents separately on terms of use etc.: Special applications (such as for in-vehicle equipment, airplanes, aerospace, automotive equipment, traffic signaling equipment, combustion equipment, medical equipment and safety devices) in which exceptional quality and reliability are required, or if the failure or malfunction of the products may directly jeopardize life or harm the human body.
Unless exchanging documents on terms of use etc. in advance, it is to be understood that our company shall not be held responsible for any damage incurred as a result of or in connection with your using the products described in this book for any special application.

(4) The products and product specifications described in this book are subject to change without notice for modification and/or improvement. At the final stage of your design, purchasing, or use of the products, therefore, ask for the most up-to-date Product Standards in advance to make sure that the latest specifications satisfy your requirements.

(5) When designing your equipment, comply with the range of absolute maximum rating and the guaranteed operating conditions (operating power supply voltage and operating environment etc.). Especially, please be careful not to exceed the range of absolute maximum rating on the transient state, such as power-on, power-off and mode-switching. Otherwise, we will not be liable for any defect which may arise later in your equipment.
Even when the products are used within the guaranteed values, take into the consideration of incidence of break down and failure mode, possible to occur to semiconductor products. Measures on the systems such as redundant design, arresting the spread of fire or preventing glitch are recommended in order to prevent physical injury, fire, social damages, for example, by using the products.

(6) Comply with the instructions for use in order to prevent breakdown and characteristics change due to external factors (ESD, EOS, thermal stress and mechanical stress) at the time of handling, mounting or at customer's process. We do not guarantee quality for disassembled products or the product re-mounted after removing from the mounting board.
When using products for which damp-proof packing is required, satisfy the conditions, such as shelf life and the elapsed time since first opening the packages.

(7) When reselling products described in this book to other companies without our permission and receiving any claim of request from the resale destination, please understand that customers will bear the burden.

(8) This book may be not reprinted or reproduced whether wholly or partially, without the prior written permission of our company.

No.010618

C.2 Infiniter Laser

The data sheet for the Infiniter laser [157].

INFINITER®

Economical Laser

VLM-635/650-03 Series

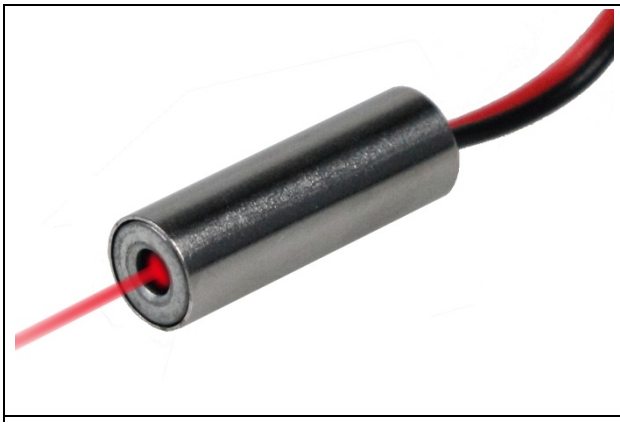	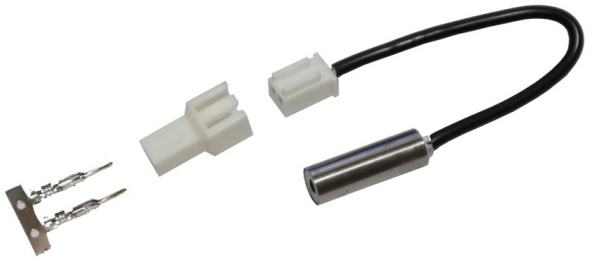
Lead Wire type	Connector type

FEATURES:

- Economical Red Dot Laser.
- Ideal for economical Laser Pointer solution.
- This module has integrated optic, laser diode, and APC driver circuit.
- APC Driver Circuit enables the Laser output power safe and constant.
- Aspherical plastic lens provides Dot Laser.
- Dimensions: Φ7 x 21 mm (Φ0.276" x 0.827")
- Wavelength : 635 / 650 nm
- Output power: Class II – less than 1mW / Class IIIa – less than 5mW.
- Beam Divergence (Half Angle) : 0.6 mRad
- 2.6~5 VDC operation.
- Connection type: Lead wire / Connector.

APPLICATIONS:

- Economical Red Dot Laser - Low cost solution for consumer grade positioning, measuring, pointing and laser sighting device.
- Wood processing.
- Metal processing.
- Stone processing.
- Textile industry.
- Food industry.
- Automotive industry.
- Medical science

INFINITER®

VLM-635/650-03 Series

OUTLINE DIMENSIONS (UNITS: mm)

Outline (Lead Wire type)

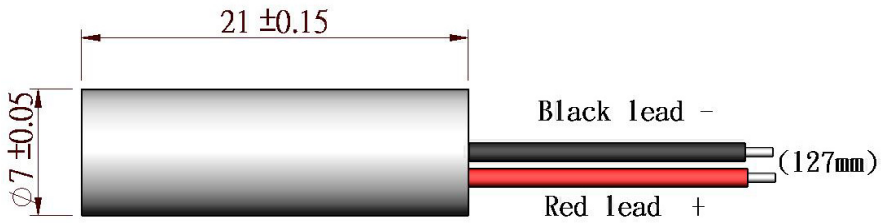

Outline (Connector type)

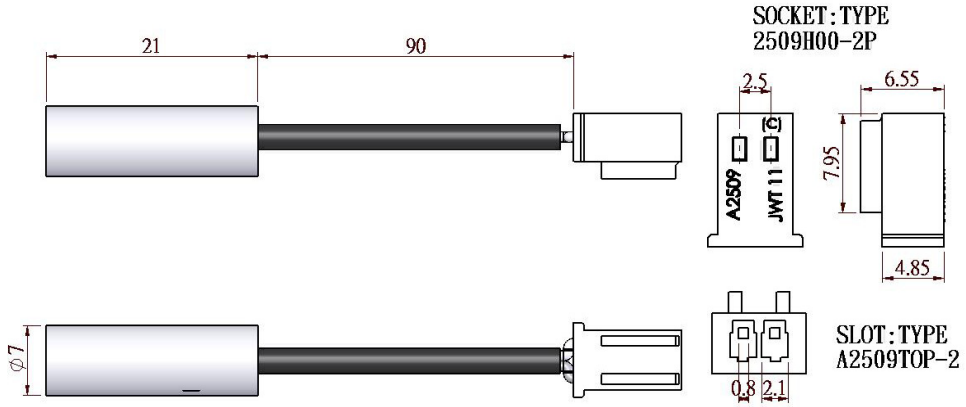

SPECIFICATIONS

SPECIFICATIONS		635-03	650-03
1	Dimensions	Φ7 x 21 mm (Φ0.276" x 0.827")	
2	Operating voltage (Vop)	2.6~5 VDC	
3	Operating current (Iop)	< 50mA	< 35mA
4	Continuous wave output power (Po)	LPT<1mW / LPA≦2.5mW	
5	Wavelength at peak emission (λp)	630~645nm	645~665nm
6	Collimating lens	Aspherical plastic lens(ø5)	
7	Spot size at 5M	6±1 mm	
8	Divergence (Half Angle)	0.6 mRad	
9	Operating temp. range	+15°C ~ +30°C (Room Temperature)	
10	Storage temp. range	-20°C ~+65°C	
11	Housing	Steel	
12	Mean time to failure (MTTF) 25℃	5000hrs	10000hrs

Note : Laser module housing is an electrical positive surface, it is imperative that contact between the laser module and the machine be avoided. This is to prevent damage from the machine electrical leakage. Surge protected power supply to the laser module is strongly recommended.

INFINITER®

VLM-635/650-03 Series

ORDER CODE

Order Code	Wavelength	Output Power	Connection Type
VLM-635-03 LPA	635 nm	≦2.5mW	Lead Wire
VLM-635-03 LPT	635 nm	＜1mW	Lead Wire
VLM-635-03 CPA	635 nm	≦2.5mW	Connector
VLM-635-03 CPT	635 nm	＜1mW	Connector
VLM-650-03 LPA	650 nm	≦2.5mW	Lead Wire
VLM-650-03 LPT	650 nm	＜1mW	Lead Wire
VLM-650-03 CPA	650 nm	≦2.5mW	Connector
VLM-650-03 CPT	650 nm	＜1mW	Connector

SAFETY LABEL

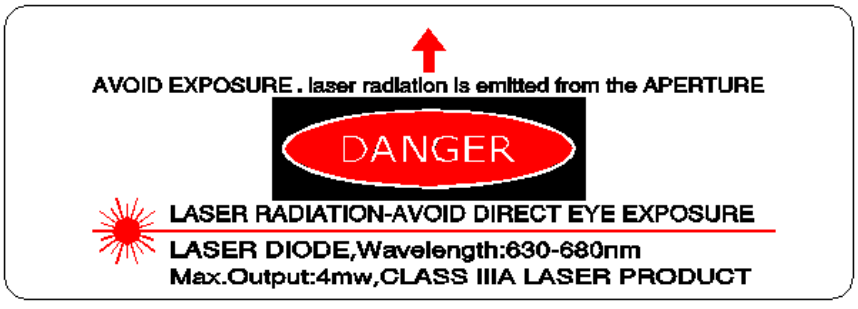

C.3 Prism

The CAD drawing of the [158].

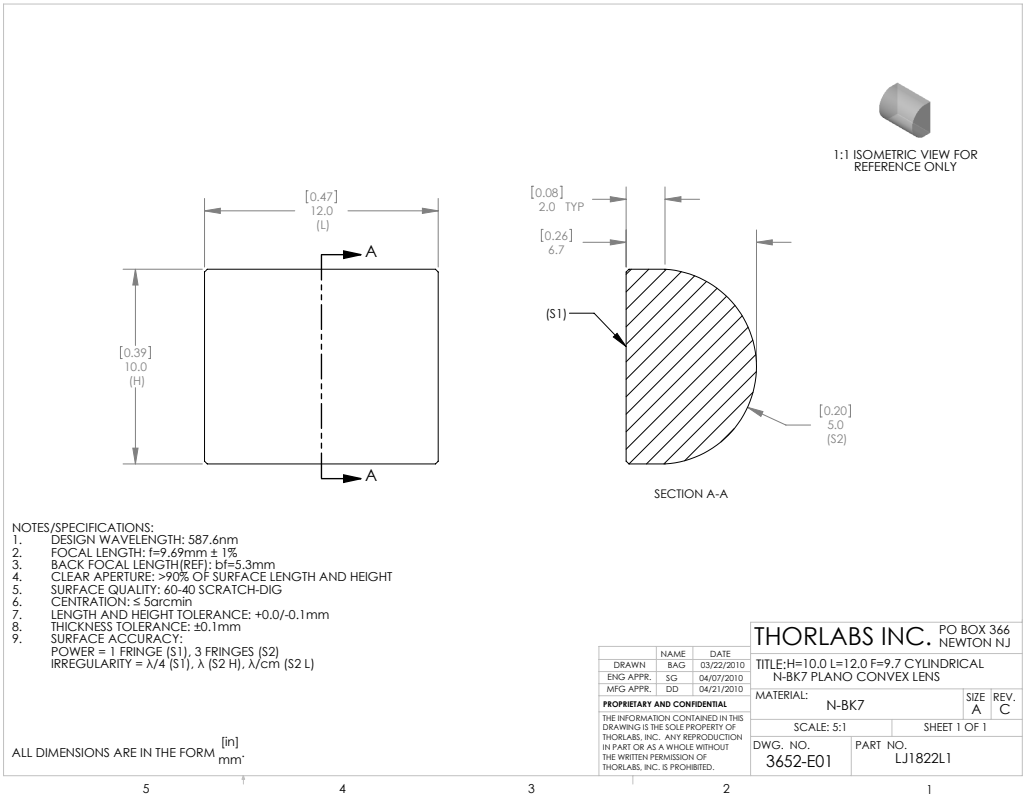

Appendix D

CAD drawings

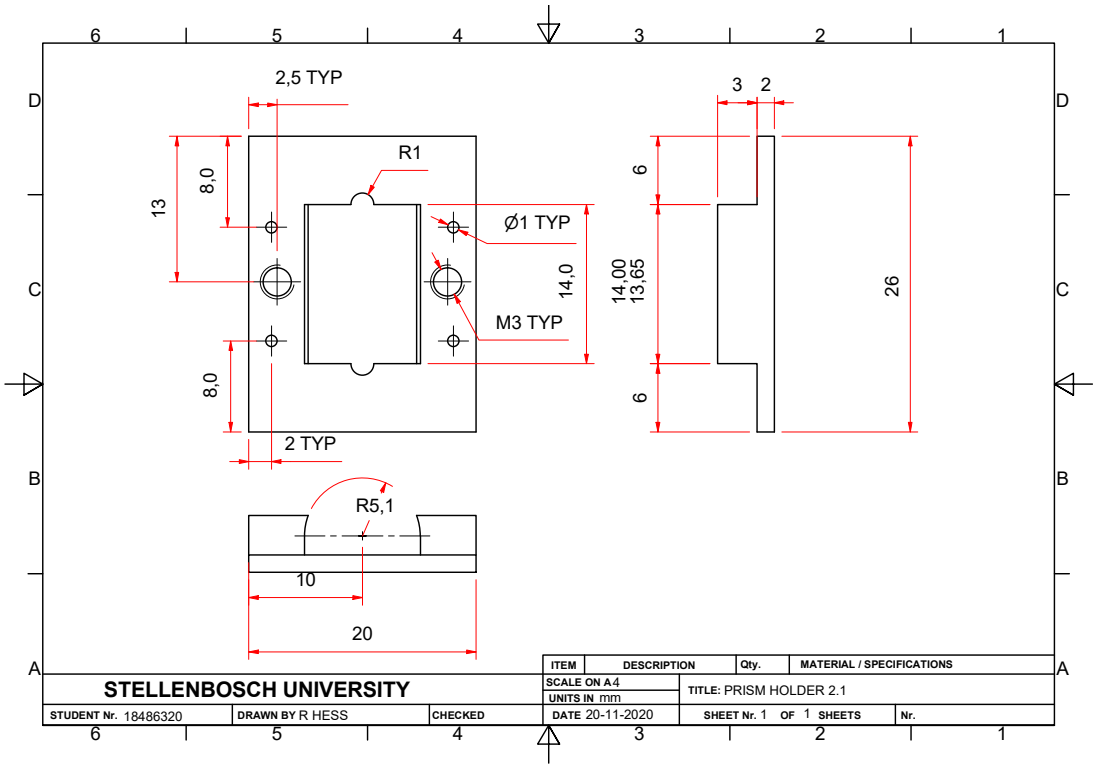

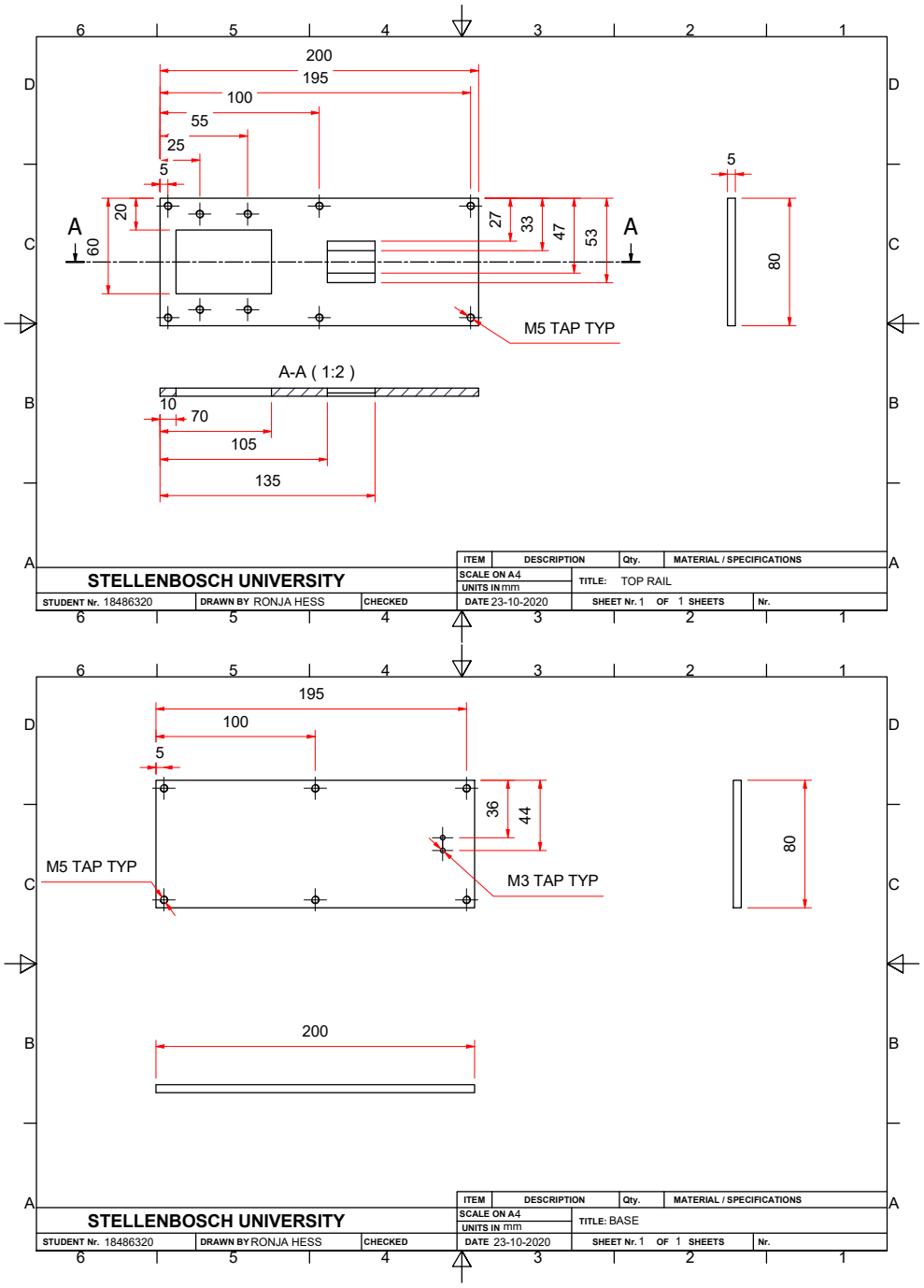

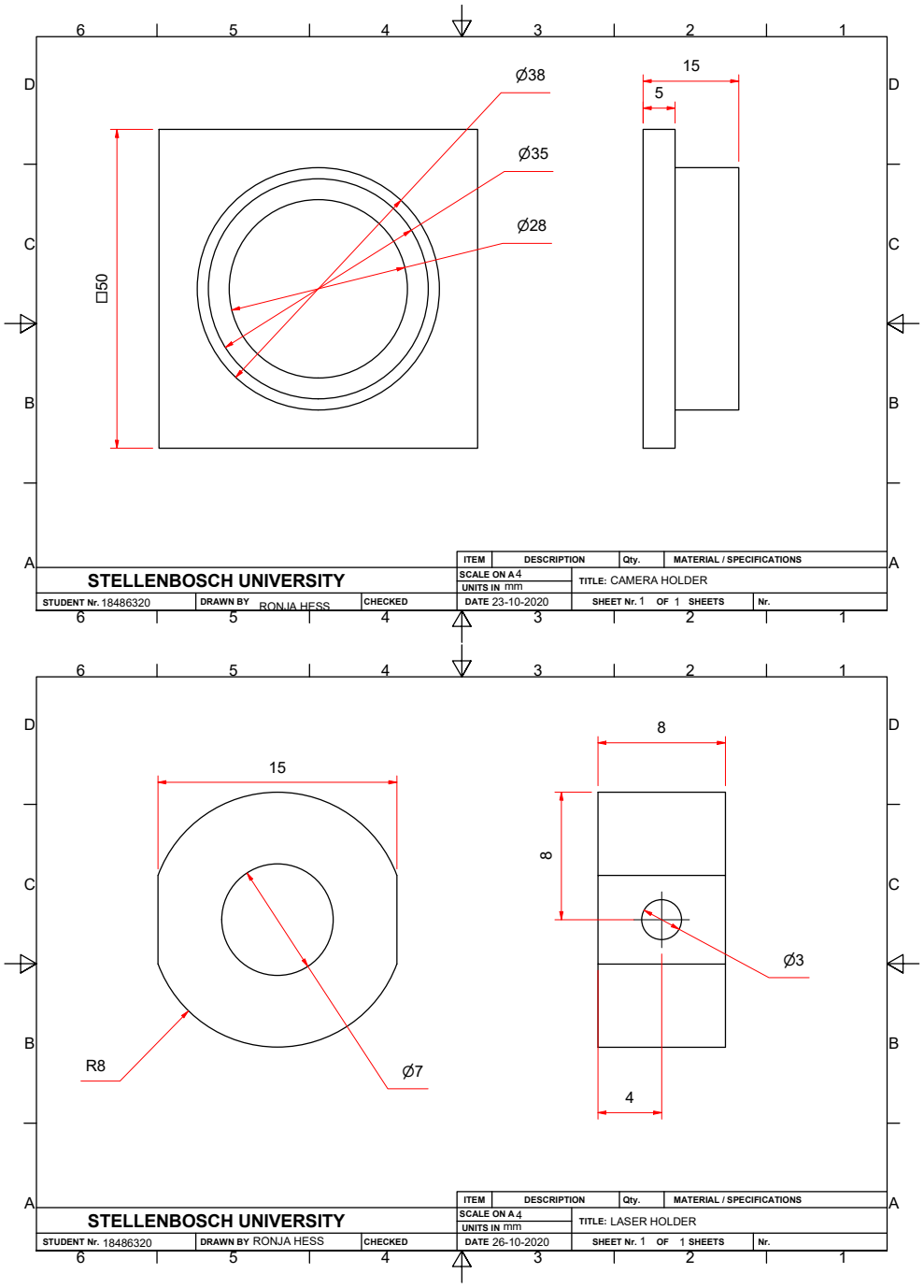

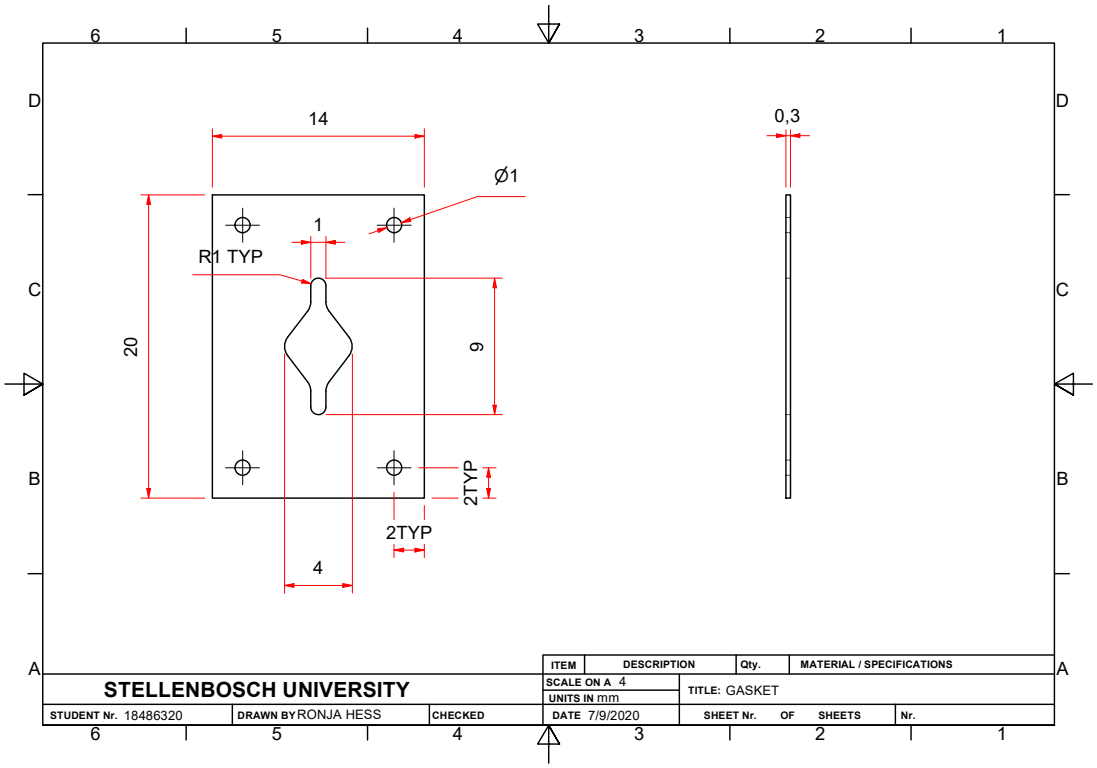

Appendix E

Protocols

This appendix discusses the procedures for both of the tested immobilisation protocols namely: SAM formation and Streptavidin adsorption. It also discusses the protocols for the confirmation methods implemented to confirm the immobilisation steps namely: Ellman's and Bradford Assay. Lastly, it shows the calculations required for concentration and volume determination.

E.1 SAM Formation and Confirmation

The SAM formation was adapted from *Self-Assembled Monolayers Related Reagents* **Dojindo2010** The cross-liking procedure was adapted from [159], Section *Procedure for EDC/NHS Crosslinking of Carboxylates with Primary Amines*. The Bradford assay procedure was adapted from [118]. The Ellman's Procedure was adapted from [117], *Section Quantitating Sulfhydryl Groups Based on Molar Absorptivity*.

E.1.1 Reagents

- Phosphate-Buffered Saline (PBS)
- Ethanol
- 3 Mercaptopropionic acid (3MPA)
- 2-(N-morpholino)ethanesulfonic acid (MES)
- 1-Ethyl-3-(3-dimethylaminopropyl)carbodiimide (EDC)
- N-Hydroxysuccinimide (NHS)
- Ellman's reagent
- Ellman's reagent reaction buffer (0.1M sodium phosphate, pH 8.0, containing 1mM EDTA)
- Bradford reagent
- Deionised DI water

E.1.2 Consumables

- Eppendorf Tubes
- Paper towels
- Gloves
- Face masks
- Pipette tips
- 96 Well plate

E.1.3 Equipment

- 4°C Fridge
- Pipettes
- 96 Well plate reader
- Shaker

E.1.4 Thiol adsorption 3MPA

1. Dilute 3MPA in ethanol to reach desired concentration. Use equations E.1 and E.2 in section E.5 for the calculations.
2. Add 300 µl 3MPA dilution to gold chips and make sure to leave a control volume. Incubate at room temperature overnight.

E.1.5 Ellman's protocol

1. Fill 25 µl samples, taken from the liquid in which the chip incubated, and Ethanol into a 96 well plate.
2. Use the control volume make a standard curve.
3. Prepare Ellman's reagent, in the dark.
4. Incubate for 15 min.
5. Add 225 µl of Ellman's reagent to each well in the dark.
6. Using a plate reader, read the absorbance at 412 nm
7. Create the standard curve.
8. Determine the concentration in each sample using the standard curve.

E.1.6 Ellman's protocol control samples for standard curve

Table E.1 shows an example of the creation of the samples for the Ellman's assay control curve [160]. All the volumes are in microlitres.

Table E.1: Example of Ellman's Standard curve volumes

Percentage	Control volume	Ethanol volume	Total volume
100	25	0	25
75	18.75	6.25	25
50	12.5	12.5	25
25	6.25	18.75	25
0	0	25	25

E.1.7 Cross-linker and Protein Immobilisation

1. Wash gold chips with MES buffer.
2. Prepare desired amount of EDC in MES buffer, 4 mg·ml^{-1}.
3. Prepare desired amount of NHS in MES buffer, 6 mg·ml^{-1}.
4. Combine EDC and NHS mixtures with a 2 to 3 ratio.
5. Add 300 µl of EDC\NHS mixture to the gold chips and incubate at room temperature for 15min.
6. Prepare the desired and concentration of the protein in PBS.
7. Wash gold chips with PBS buffer.
8. Add 300 µl of BSA dilution to the gold chips and incubate in a 4°C fridge for at least 4 hours.

E.1.8 Bradford Assay

1. Add 2 µl sample to each well.
2. Add 23 µl of PBS to each well
3. Use the control to create the standard curve samples.
4. Prepare Bradford reagent.
5. Add 225 µl Bradford reagent to wells.
6. Incubate for 15 min.
7. Using a plate reader, read the absorbance at 595 nm.
8. Create the standard curve.
9. Determine the concentration in each sample using the standard curve.

E.1.9 Bradford protocol control samples for standard curve

Table E.2 shows an example of the creation of the samples for the Bradford assay control curve[160]. All the volumes are in microlitres.

Table E.2: Example of Bradford standard curve volumes

Percentage	Control volume	PBS	Total volume
100	2	23	25
75	1.5	23.5	25
50	1	24	25
25	0.5	24.5	25
0	0	25	25

E.2 Streptavidin Adsorption and Confirmation

The following is based on a protocol developed at the SU ANIMAL TB RESEARCH GROUP Division Molecular Biology and Human Genetics [9].

E.2.1 Reagents

- PBS
- Steptavidin-HRP
- 3,3', 5,5'-tetramethylbenzidine (TMB)
- 2M Sulphuric acid (H_2SO_4)

E.2.2 Consumables

- Gloves
- Pipette tips
- 96 Well plate

E.2.3 Equipment

- 37°C Incubator
- 4°C Fridge
- Pipettes
- 96 Well plate reader

E.2.4 Procedure

1. Dilute the streptavidin-HRP in PBS to the desired concentration.
2. Add 300 µl of diluted-HRP to the gold chips and incubate at 37°C for 1 (one) hour.
3. Fill samples and PBS into a 96 well plate. Using the control make a standard curve.
4. Prepare TMB by mixing reagent A and B together.
5. Add 50 µl of mixed TMB (using within 15min of mixing) incubate for 20 min at 24°C in the dark. Start timing when the TMB is added to the first well.
6. Add 25 µl of H_2SO_4 to each well, after the 20min incubation period. (This is done to stop the reaction from continuing). Add H_2SO_4 in the same order as the TMB.
7. Using a plate reader, read the absorbance at 450 nm and 620 nm.
8. Calculate the final optical density of each well. $OD_{final} = OD_{450}$ - OD_{620}
9. Create the standard curve.
10. Determine the concentration in each sample using the standard curve.

E.2.5 Cysteamine adsorption

1. Dilute cysteamine in ethanol to reach desired concentration 10mg·ml^{-1}.
2. Add 300 µl cysteamine dilution to gold chips
3. Incubate at room temperature 3 hours.

E.3 FITC

The following is adapted from [161]

E.3.1 Reagents

- $NaHCO_3$ powder
- DI water
- NaOH
- FITC powder
- Ethanol
- PBS
- PBST (PBS with tween)

E.3.2 Consumables

- Gloves
- Pipette tips

E.3.3 Equipment

- Pipettes

E.3.4 Procedure

Note: Work with FITC is done in the dark.

1. Mix fresh sodium bicarbonate ($NaHCO_3$) at a pH of 9 and a concentration of 10 $mg{\cdot}ml^{-1}$.
2. Weigh off the desired amount of FITC powder
3. Mix the powder with 100% ethanol to make a stock solution.
4. Add 50 µl of the stock solution to 2.45 ml of sodium bicarbonate until the desired concentration is reached.
5. Incubate for 3 hours
6. Rinse with PBS
7. Rinse with PBST
8. Do fluorescence imaging

E.4 System Testing procedure

This section details the testing procedure of the prototype.

1. Prepare the samples.
2. Draw sample into a 1 ml syringe.
3. Turn on the laser,
4. Start the video recording.
5. Gradually depress the syringe plunger forcing the sample into the microfluidic channel.
6. Wait for 10 minutes.
7. Stop the recording.
8. Switch off the laser.
9. Remove the syringe.

E.5 Calculations

$$m = C \cdot V_n \cdot M \tag{E.1}$$

where m is the required mass in gram, C is the concentration desired in moles per litre, V is the volume of mixture needed in litre and M is the molar mass of the component.

$$V_s = \frac{m}{\rho} \tag{E.2}$$

where V_s is the volume of the substance, m the mass and ρ is the relative density of the substance.

Reference list

[1] A. S. Hassan *et al.*, "Dynamics of mycobacterium and bovine tuberculosis in a human-buffalo population", *Computational and Mathematical Methods in Medicine*, vol. 2014, 2014, ISSN: 17486718. DOI: 10.1155/2014/912306.

[2] W. J. Goosen *et al.*, "IP-10 is a sensitive biomarker of antigen recognition in whole-blood stimulation assays used for the diagnosis of Mycobacterium bovis infection in African buffaloes (Syncerus caffer)", *Clinical and Vaccine Immunology*, vol. 22, no. 8, pp. 974–978, 2015, ISSN: 1556679X. DOI: 10.1128/CVI.00324-15.

[3] A. Rinaldi, "Tackling animal diseases to protect human health: As veterinary science celebrates cattle plague eradication, the inextricable link between human, animal and ecosystem health is increasingly appreciated", *EMBO Reports*, vol. 14, no. 1, pp. 31–35, 2013, ISSN: 1469221X. DOI: 10.1038/embor.2012.201.

[4] W. J. Goosen *et al.*, "The stability of plasma IP-10 enhances its utility for the diagnosis of Mycobacterium bovis infection in African buffaloes (Syncerus caffer)", *Veterinary Immunology and Immunopathology*, vol. 173, pp. 17–20, 2016, ISSN: 18732534. DOI: 10.1016/j.vetimm.2016.03.013.

[5] W. Y. Ayele *et al.*, "Bovine tuberculosis: an old disease but a new threat to Africa", vol. 8, no. 8, pp. 924–937, 2004.

[6] M. Domingo *et al.*, "Pathology of bovine tuberculosis", *Research in Veterinary Science*, vol. 97, no. S, S20–S29, 2014, ISSN: 15322661. DOI: 10.1016/j.rvsc.2014.03.017.

[7] W. Goosen, *Current diagnostic methods*, personal communication, Feb. 2019.

[8] abcam. "Sandwich elisa protocol", abcam, [Online]. Available: https://www.abcam.com/protocols/sandwich-elisa-protocol-1#:~:text=A%20sandwich%20ELISA%20measures%20antigen,antibodies%20in%20sandwich%20ELISA%20systems. (visited on 02/23/2021).

[9] SU ANIMAL TB RESEARCH GROUP, *Kingfisher bovine ip-10 elisa, in house*, Stellenbosch University, 2018.

[10] N. J. Ronkainen *et al.*, "Electrochemical biosensors", *Chemical Society Reviews*, vol. 39, no. 5, pp. 1747–1763, Apr. 2010, ISSN: 14604744. DOI: 10.1039/b714449k.

[11] P. Mehrotra, "Biosensors and their applications - A review", *Journal of Oral Biology and Craniofacial Research*, vol. 6, no. 2, pp. 153–159, 2016, ISSN: 22124268. DOI: 10.1016/j.jobcr.2015.12.002.

[12] C. K. O'Sullivan *et al.*, *Piezoelectric immunosensors - Theory and applications*, 1999. DOI: 10.1080/00032719908542975.

[13] P. Skládal, "Piezoelectric biosensors", *TrAC - Trends in Analytical Chemistry*, vol. 79, pp. 127–133, 2016, ISSN: 18793142. DOI: 10.1016/j.trac.2015.12.009.

[14] M. Mascini *et al.*, "Piezoelectric sensors for dioxins : a biomimetic approach", vol. 20, pp. 1203–1210, 2004. DOI: 10.1016/j.bios.2004.06.048.

[15] S. P. Mohanty and E. Koucianos, "Biosensors: A tutorial review", *IEEE Potentials*, vol. 25, no. 2, pp. 35–40, 2006, ISSN: 02786648. DOI: 10.1109/MP.2006.1649009.

[16] S. P. Schoeman, "Development of a biosensor for the early detection of tuberculosis", M.S. thesis, Stellenbosch University, Mar. 2019.

[17] S. Zhang *et al.*, "Materials and techniques for electrochemical biosensor design and construction", vol. 15, 2000.

[18] L. Wang *et al.*, "A label-free electrochemical biosensor for ultra-sensitively detecting telomerase activity based on the enhanced catalytic currents of acetaminophen catalyzed by Au nanorods", *Biosensors and Bioelectronics*, vol. 124-125, pp. 53–58, Jan. 2019, ISSN: 18734235. DOI: 10.1016/j.bios.2018.09.098.

[19] J. Janssen *et al.*, "Carbon nanotube-based electrochemical biosensor for label-free protein detection", *Biosensors*, vol. 9, no. 4, 2019, ISSN: 20796374. DOI: 10.3390/bios9040144.

[20] A. Matsumoto and Y. Miyahara, *Current and emerging challenges of field effect transistor based bio-sensing*, Nov. 2013. DOI: 10.1039/c3nr02703a.

[21] K. S. Kim *et al.*, "The fabrication, characterization and application of aptamer-functionalized Si-nanowire FET biosensors", *Nanotechnology*, vol. 20, no. 23, 2009, ISSN: 09574484. DOI: 10.1088/0957-4484/20/23/235501.

[22] K. V. Singh *et al.*, "3D nanogap interdigitated electrode array biosensors", *Analytical and Bioanalytical Chemistry*, vol. 397, no. 4, pp. 1493–1502, Jun. 2010, ISSN: 16182642. DOI: 10.1007/s00216-010-3682-z.

[23] S. S. Yee and G. nter Gauglitz, "Surface plasmon resonance sensors: review", vol. 54, pp. 3–15, 1999.

[24] W. M. Mukhtar *et al.*, "Optimization of SPR signals: Monitoring the physical structures and refractive indices of prisms", *EPJ Web of Conferences*, vol. 162, 2017, ISSN: 2100014X. DOI: 10.1051/epjconf/201716201001.

[25] P. Damborský *et al.*, "Optical biosensors", *Essays in Biochemistry*, vol. 60, no. 1, pp. 91–100, Jun. 2016, ISSN: 00711365. DOI: 10.1042/EBC20150010.

[26] M. Li *et al.*, "Plasmon-enhanced optical sensors: A review", vol. 140, no. 2, pp. 386–406, Jan. 2015, ISSN: 13645528. DOI: 10.1039/c4an01079e.

[27] G. Ertürk *et al.*, "Microcontact imprinting based surface plasmon resonance (SPR) biosensor for real-time and ultrasensitive detection of prostate specific antigen (PSA) from clinical samples", *Sensors and Actuators, B: Chemical*, vol. 224, pp. 823–832, 2016, ISSN: 09254005. DOI: 10.1016/j.snb.2015.10.093.

[28] S. Qu *et al.*, "A rapid and highly sensitive portable chemiluminescent immunosensor of carcinoembryonic antigen based on immunomagnetic separation in human serum", *Analytica Chimica Acta*, vol. 766, pp. 94–99, Mar. 2013, ISSN: 00032670. DOI: 10.1016/j.aca.2012.12.043.

[29] M. Yao and J. C. Wolfe, "A laser-induced fluorescence biosensor by using ellipsoidal reflector", *Optics and Laser Technology*, vol. 39, no. 5, pp. 1040–1045, Jul. 2007, ISSN: 00303992. DOI: 10.1016/j.optlastec.2006.05.002.

[30] F. Ma *et al.*, "Fluorescent Biosensors Based on Single-Molecule Counting", *Accounts of Chemical Research*, vol. 49, no. 9, pp. 1722–1730, Sep. 2016, ISSN: 15204898. DOI: 10.1021/acs.accounts.6b00237.

[31] F. Sizaire *et al.*, "Automated screening of AURKA activity based on a genetically encoded FRET biosensor using fluorescence lifetime imaging microscopy", *Methods and Applications in Fluorescence*, vol. 8, no. 2, 2020, ISSN: 20506120. DOI: 10.1088/2050-6120/ab73f5.

[32] S. Padilla-Parra and M. Tramier, "FRET microscopy in the living cell: Different approaches, strengths and weaknesses", *BioEssays*, vol. 34, no. 5, pp. 369–376, May 2012, ISSN: 02659247. DOI: 10.1002/bies.201100086.

[33] V. X. T. Zhao *et al.*, "Colorimetric biosensors for point-of-care virus detections", *Materials Science for Energy Technologies*, vol. 3, pp. 237–249, 2020, ISSN: 25892991. DOI: 10.1016/j.mset.2019.10.002.

[34] K. M. Koczula and A. Gallotta, "Lateral flow assays", *Essays in Biochemistry*, vol. 60, no. 1, pp. 111–120, Jun. 2016, ISSN: 00711365. DOI: 10.1042/EBC20150012.

[35] Abingdon Health. (2019). "See how a lateral flow immunoassay works", [Online]. Available: https://www.youtube.com/watch?v=z07CK-4JoFo.

[36] D. Van Noort and C.-F. Mandenius, "Porous gold surfaces for biosensor applications", vol. 15, pp. 203–209, 2000.

[37] G. Jin *et al.*, "Development of biosensor based on imaging ellipsometry and biomedical applications", *Thin Solid Films*, vol. 519, no. 9, pp. 2750–2757, 2011, ISSN: 00406090. DOI: 10.1016/j.tsf.2010.12.175.

[38] J. L. Stehle *et al.*, "Multi-pass spectroscopic ellipsometry", *Thin Solid Films*, vol. 555, pp. 143–147, 2014, ISSN: 00406090. DOI: 10.1016/j.tsf.2013.05.148.

[39] C. Negara, "Thickness Measurement of Thin Films on Curved Surfaces with Ellipsometry", Jan. 2015. DOI: 10.5445/KSP/1000047712.

[40] X. Fan *et al.*, "Sensitive optical biosensors for unlabeled targets: A review", *Analytica Chimica Acta*, vol. 620, no. 1-2, pp. 8–26, Jul. 2008, ISSN: 00032670. DOI: 10.1016/j.aca.2008.05.022.

[41] S. H. Hsu and Y. T. Huang, "A novel Mach-Zehnder interferometer based on dual-ARROW structures for sensing applications", *Journal of Lightwave Technology*, vol. 23, no. 12, pp. 4200–4206, 2005, ISSN: 07338724. DOI: 10.1109/JLT.2005.859435.

[42] Practical Ninjas. (Feb. 2018). "Basics and principle of raman spectroscopy — learn under 5 min — stokes and anti-stokes — ai 09", [Online]. Available: https://www.youtube.com/watch?v=SsIYDEma_cU.

[43] I. Notingher, "Raman Spectroscopy Cell-based Biosensors", *Sensors*, vol. 7, pp. 1343–1358, 2007, ISSN: 1424-8220.

[44] P. P. Freitas *et al.*, "Magnetoresistive sensors", *Journal of Physics Condensed Matter*, vol. 19, no. 16, Apr. 2007, ISSN: 09538984. DOI: 10.1088/0953-8984/19/16/165221.

[45] J. Llandro *et al.*, "Magnetic biosensor technologies for medical applications: A review", *Medical and Biological Engineering and Computing*, vol. 48, no. 10, pp. 977–998, Oct. 2010, ISSN: 01400118. DOI: 10.1007/s11517-010-0649-3.

[46] V. Nabaei *et al.*, "Biosensors and Bioelectronics Magnetic biosensors : Modelling and simulation", vol. 103, no. November 2017, pp. 69–86, 2018. DOI: 10.1016/j.bios.2017.12.023.

[47] V. D. Krishna *et al.*, "Giant magnetoresistance-based biosensor for detection of influenza A virus", *Frontiers in Microbiology*, vol. 7, no. MAR, Mar. 2016, ISSN: 1664302X. DOI: 10.3389/fmicb.2016.00400.

[48] K. Ramanathan and B. Danielsson, "Principles and applications of thermal biosensors", vol. 16, pp. 417–423, 2001.

[49] Abbott. "DETERMINE™ TB LAM Ag", [Online]. Available: https://www.globalpointofcare.abbott/en/product-details/determine-tb-lam.html#:~:text=Support%20Tech%20Support-,The%20Determine%E2%84%A2%20TB%20LAM%20Ag%20test%20empowers%20you%2C%20at,detecting%20sputum%20smear%20negative%20patients..

[50] A. Zewude *et al.*, "Evaluation of Mycobacterium tuberculosis lipoarabinomannan antigen assay and rapid serology blood test for the diagnosis of bovine tuberculosis in Ethiopia", *BMC Veterinary Research*, vol. 15, no. 1, pp. 1–9, 2019, ISSN: 17466148. DOI: 10.1186/s12917-019-2114-3.

[51] H. V. Kelley *et al.*, "Accuracy of Two Point-of-Care Tests for Rapid Diagnosis of Bovine Tuberculosis at Animal Level using Non-Invasive Specimens", *Scientific Reports*, vol. 10, no. 1, pp. 1–10, 2020, ISSN: 20452322. DOI: 10.1038/s41598-020-62314-2.

[52] H. R. Bermúdez *et al.*, "Evaluation of a lateral flow assay for the diagnosis of mycobacterium bovis infection in dairy cattle", *Journal of Immunoassay and Immunochemistry*, vol. 33, no. 1, pp. 59–65, 2012, ISSN: 15321819. DOI: 10.1080/15321819.2011.594473.

[53] A. Fresco-Taboada *et al.*, "A lateral flow assay for the rapid diagnosis of Mycobacterium bovis infection in wild boar", *Transboundary and Emerging Diseases*, vol. 66, no. 5, pp. 2175–2179, 2019, ISSN: 18651682. DOI: 10.1111/tbed.13260.

[54] K. P. Lyashchenko *et al.*, "Rapid detection of serum antibody by dual-path platform VetTB assay in white-tailed deer infected with Mycobacterium bovis", *Clinical and Vaccine Immunology*, vol. 20, no. 6, pp. 945–953, 2013, ISSN: 1556679X. DOI: 10.1128/CVI.00120-13.

[55] M. Boadella *et al.*, "Serologic tests for detecting antibodies against Mycobacterium bovis and Mycobacterium avium subspecies paratuberculosis in Eurasian wild boar (Sus scrofa scrofa)", *Journal of Veterinary Diagnostic Investigation*, vol. 23, no. 1, pp. 77–83, 2011, ISSN: 10406387. DOI: 10.1177/104063871102300111.

[56] T. J. Kerr *et al.*, "Diagnosis of Mycobacterium bovis infection in free-ranging common hippopotamus (Hippopotamus amphibius)", *Transboundary and Emerging Diseases*, no. September 2020, pp. 1–7, 2021, ISSN: 18651682. DOI: 10.1111/tbed.13989.

[57] "6 Advantages of Surface Plasmon Resonance Technology", Nicoya, [Online]. Available: https://nicoyalife.com/blog/6-advantages-of-spr-technology/ (visited on 06/27/2020).

[58] D. Bélanger and J. Pinson, "Electrografting: A powerful method for surface modification", *Chemical Society Reviews*, vol. 40, no. 7, pp. 3995–4048, Jun. 2011, ISSN: 14604744. DOI: 10.1039/c0cs00149j.

[59] K. Syslová *et al.*, "Dopamine analysis in neuroscience research", *Dopamine: Functions, Regulation and Health Effects*, no. January, pp. 81–111, 2012.

[60] Wikimedia Commons. (2016). "File:Immunoglobulin basic unit.svg", Wikimedia Commons, [Online]. Available: https://commons.wikimedia.org/wiki/File:Immunoglobulin_basic_unit.svg (visited on 05/16/2021).

[61] Q. Yu *et al.*, "Technological Development of Antibody Immobilization for Optical Immunoassays: Progress and Prospects", vol. 45, no. 1, pp. 62–75, Jan. 2015, ISSN: 15476510. DOI: 10.1080/10408347.2014.881249.

[62] S. Liébana and G. A. Drago, "Bioconjugation and stabilisation of biomolecules in biosensors", *Essays in Biochemistry*, vol. 60, no. 1, pp. 59–68, Jun. 2016, ISSN: 00711365. DOI: 10.1042/EBC20150007.

[63] Reichert Technologies. (2017). "Explained: Sensor Chips for Surface Plasmon Resonance and Other Applications", [Online]. Available: https://bitesizebio.com/34644/biosensor-chips-surface-plasmon-resonance/ (visited on 06/17/2020).

[64] L. Ahrens *et al.*, "Biotin-Avidin-Mediated Capture of Microspheres on Polymer Fibers", *Molecules*, vol. 24, no. 11, pp. 1–15, 2019. DOI: 10.3390/molecules24112036.

[65] Y. Jung *et al.*, "Recent advances in immobilization methods of antibodies on solid supports", *Analyst*, vol. 133, no. 6, pp. 697–701, 2008, ISSN: 00032654. DOI: 10.1039/b800014j.

[66] P. Dennler *et al.*, "Antibody conjugates: From heterogeneous populations to defined reagents", *Antibodies*, vol. 4, no. 3, pp. 197–224, 2015, ISSN: 20734468. DOI: 10.3390/antib4030197.

[67] E. Pensa *et al.*, "The chemistry of the sulfur-gold interface: In search of a unified model", *Accounts of Chemical Research*, vol. 45, no. 8, pp. 1183–1192, Aug. 2012, ISSN: 00014842. DOI: 10.1021/ar200260p.

[68] J. Ljungblad, "Antibody-conjugated Gold Nanoparticles integrated in a Fluorescence based Biochip", M.S. thesis, Linköpings University, Linköping, Sweden, Jun. 2009.

[69] C. K. Dixit and A. Kaushik, "Nano-structured arrays for multiplex analyses and Lab-on-a-Chip applications", *Biochemical and Biophysical Research Communications*, vol. 419, no. 2, pp. 316–320, Mar. 2012, ISSN: 0006291X. DOI: 10.1016/j.bbrc.2012.02.018.

[70] ThermoFisher Scientific. "Chemistry of Crosslinking", ThermoFisher Scientific, [Online]. Available: https://www.thermofisher.com/za/en/home/life-science/protein-biology/protein-biology-learning-center/protein-biology-resource-library/pierce-protein-methods/chemistry-crosslinking.html (visited on 06/17/2020).

[71] ThermoFisher. "Crosslinker Selection Tool", ThermoFisher Scientific, [Online]. Available: https://www.thermofisher.com/za/en/home/life-science/protein-biology/protein-labeling-crosslinking/protein-crosslinking/crosslinker-selection-tool.html (visited on 06/17/2020).

[72] SPR pages. "Sensor Surface", SPR pages, [Online]. Available: https://www.sprpages.nl/spr-overview/sensor-chips (visited on 06/17/2020).

[73] K. Wadu-Mesthrige *et al.*, "Immobilization of Proteins on Self-Assembled Monolayers", Tech. Rep., 2000, pp. 380–388.

[74] D. A. Tomalia *et al.*, "A New Class of Polymers: Starburst-Dendritic Macromolecules", vol. 17, no. I, pp. 117–132, 1985.

[75] E. Abbasi *et al.*, "Dendrimers: Synthesis, applications, and properties", vol. 9, no. 1, pp. 1–10, 2014, ISSN: 1556276X. DOI: 10.1186/1556-276X-9-247.

[76] R. Vinicius *et al.*, "New Advances in General Biomedical Applications of", no. 27, pp. 1–27, 2018. DOI: 10.3390/molecules23112849.

[77] X. Yu *et al.*, "A novel surface plasmon resonance imaging interferometry for protein array detection", *Sensors and Actuators, B: Chemical*, vol. 130, no. 1, pp. 52–58, Mar. 2008, ISSN: 09254005. DOI: 10.1016/j.snb.2007.07.106.

[78] P. Vermette *et al.*, "Immobilization and surface characterization of NeutrAvidin biotin-binding protein on different hydrogel interlayers", *Journal of Colloid and Interface Science*, vol. 259, no. 1, pp. 13–26, 2003, ISSN: 00219797. DOI: 10.1016/S0021-9797(02)00185-6.

[79] R. W. Wood, "On a remarkable case of uneven distribution of light in a diffraction grating spectrum", *Proceedings of the Physical Society of London*, vol. 18, no. 1, pp. 269–275, 1901, ISSN: 14787814. DOI: 10.1088/1478-7814/18/1/325.

[80] Y. Hong *et al.*, "Nanobiosensors based on localized surface plasmon resonance for biomarker detection", vol. 2012, 2012, ISSN: 16874110. DOI: 10.1155/2012/759830.

[81] SPR pages. "Surface Plasmon Resonance", SPR pages, [Online]. Available: https://www.sprpages.nl/spr-overview/spr-theory (visited on 06/21/2020).

[82] J. F. Masson, "Portable and field-deployed surface plasmon resonance and plasmonic sensors", *Analyst*, vol. 145, no. 11, pp. 3776–3800, 2020, ISSN: 13645528. DOI: 10.1039/d0an00316f.

[83] G. A. Lopez *et al.*, "Recent advances in nanoplasmonic biosensors: Applications and lab-on-a-chip integration", *Nanophotonics*, vol. 6, no. 1, pp. 123–136, 2017, ISSN: 21928614. DOI: 10.1515/nanoph-2016-0101.

[84] Khan Academy. (Jul. 2014). "Polarization of light, linear and circular light waves physics khan academy", [Online]. Available: youtube.com/watch?v=HH58VmUbOKM&t=305s (visited on 06/15/2020).

[85] Edmund optics. "Introduction to polarization", Edmund optics, [Online]. Available: https://www.edmundoptics.com/knowledge-center/application-notes/optics/introduction-to-polarization/ (visited on 02/25/2021).

[86] C. Silva Moreira *et al.*, "Features and application of a microcontroller-driven autosampler applied to a surface plasmon resonance biosensor platform", Tech. Rep., 2014.

[87] I. Pockrand, "Surface plasma oscillations at silver surfaces with thin transparent and absorbing coatings", Tech. Rep., 1978, pp. 577–588.

[88] K. Kurihara *et al.*, "Asymmetric SPR sensor response curve-fitting equation for the accurate determination of SPR resonance angle", Tech. Rep.

[89] S. Singh *et al.*, "SPR based fibre optic biosensor for phenolic compounds using immobilization of tyrosinase in polyacrylamide gel", *Sensors and Actuators, B: Chemical*, vol. 186, pp. 388–395, 2013, ISSN: 09254005. DOI: 10.1016/j.snb.2013.06.034.

[90] SPR pages. "SPR Instrument Design", SPR pages, [Online]. Available: https://www.sprpages.nl/spr-overview/configurations (visited on 06/21/2020).

[91] M. Moreno-Sereno *et al.*, "Laser Interferometry for Broad Area SPR-Grating Couplers in Chemical Applications", *Proceedings*, vol. 1, no. 4, p. 323, Aug. 2017, ISSN: 2504-3900. DOI: 10.3390/proceedings1040323.

[92] I. Koudela and S. S. Yee, "Surface plasmon resonance sensors based on diffraction gratings and prism couplers: sensitivity comparison", Tech. Rep., 1999, pp. 16–24.

[93] A. Nabok *et al.*, "Development of planar waveguide-based immunosensor for detection of low molecular weight molecules such as mycotoxins", *Sensors and Actuators, B: Chemical*, vol. 247, pp. 975–980, Aug. 2017, ISSN: 09254005. DOI: 10.1016/j.snb.2017.01.197.

[94] A. Suzuki *et al.*, "Development of novel optical waveguide surface plasmon resonance (SPR) sensor with dual light emitting diodes", *Sensors and Actuators, B: Chemical*, vol. 106, no. 1 SPEC. ISS. Pp. 383–387, 2005, ISSN: 09254005. DOI: 10.1016/j.snb.2004.08.021.

[95] C. R. Lavers *et al.*, "Planar optical waveguides for sensing applications", Tech. Rep., 2000, pp. 85–95.

[96] B. Sepúlveda *et al.*, "LSPR-based nanobiosensors", vol. 4, no. 3, pp. 244–251, Jun. 2009, ISSN: 17480132. DOI: 10.1016/j.nantod.2009.04.001.

[97] SPR pages. "LSPR", SPR pages, [Online]. Available: https://www.sprpages.nl/15-weblinks/154-nicoya-lifesciences?highlight=WyJsc3ByIiwibHNwcidzIl0= (visited on 06/21/2020).

[98] M.-h. Chiu *et al.* "Fast surface defect measurement using a SPR sensor and a CCD camera", [Online]. Available: http://citeseerx.ist.psu.edu/viewdoc/download?doi=10.1.1.483.4126&rep=rep1&type=pdf.

[99] A. R. Wheeler *et al.*, "Poly(dimethylsiloxane) microfluidic flow cells for surface plasmon resonance spectroscopy", *Sensors and Actuators, B: Chemical*, vol. 98, no. 2-3, pp. 208–214, 2004, ISSN: 09254005. DOI: 10.1016/j.snb.2003.06.004.

[100] G. Cappi *et al.*, "Label-Free detection of tobramycin in serum by transmission-localized surface plasmon resonance", *Analytical Chemistry*, vol. 87, no. 10, pp. 5278–5285, May 2015, ISSN: 15206882. DOI: 10.1021/acs.analchem.5b00389.

[101] J. Zhou *et al.*, "Quantification of shellfish major allergen tropomyosin by SPR biosensor with gold patterned Biochips", *Food Control*, vol. 107, Jan. 2019, ISSN: 09567135. DOI: 10.1016/j.foodcont.2019.02.041.

[102] A. Bonyar *et al.*, "Development of a localised surface plasmon resonance sensor based on gold nanoparticles", in *Proceedings of the 2014 37th International Spring Seminar on Electronics Technology, ISSE 2014*, Institute of Electrical and Electronics Engineers Inc., 2014, pp. 369–374, ISBN: 9781479944552. DOI: 10.1109/ISSE.2014.6887627.

[103] R. Bakhtiar, "Surface plasmon resonance spectroscopy: A versatile technique in a biochemist's toolbox", *Journal of Chemical Education*, vol. 90, no. 2, pp. 203–209, 2013, ISSN: 00219584. DOI: 10.1021/ed200549g.

[104] W. M. Mukhtar *et al.*, "Effect of Noble Metal Thin Film Thicknesses on Surface Plasmon Resonance (SPR) Signal Amplification", *Journal of Advanced Research in Materials Science*, vol. 49, no. 1, pp. 1–9, 2018. DOI: www.akademiabaru.com/arms.html.

[105] Sofchip. (2018). "Surface plasmon resonance sensor chips", Sofchip, [Online]. Available: https://sofchip.com/j1001.jsp (visited on 02/19/2021).

[106] A. Hoffmann *et al.*, "Effect of roughness on surface plasmon scattering in gold films", *Journal of Physics Condensed Matter*, vol. 10, no. 24, pp. 5503–5513, 1998, ISSN: 09538984. DOI: 10.1088/0953-8984/10/24/025.

[107] D. I. Yakubovsky *et al.*, "Optical constants and structural properties of thin gold films", *Optics Express*, vol. 25, no. 21, p. 25 574, 2017, ISSN: 1094-4087. DOI: 10.1364/oe.25.025574.

[108] S. Agarwal *et al.*, "Effect of Surface Roughness on the Performance of Optical SPR Sensor for Sucrose Detection: Fabrication, Characterization, and Simulation Study", *IEEE Sensors Journal*, vol. 16, no. 24, pp. 8865–8873, 2016, ISSN: 1530437X. DOI: 10.1109/JSEN.2016.2615110.

[109] Nanosurf AG, *Operating instruction easyscan 2 afm*, English, version Version 1.6, Nanosurf AG, 164 pp.

[110] S. Löfås and B. Johnsson, "A novel hydrogel matrix on gold surfaces in surface plasmon resonance sensors for fast and efficient covalent immobilization of ligands", *J. Chem. Soc., Chem. Commun.*, pp. 1526–1528, 21 1990. DOI: 10.1039/C39900001526.

[111] S. Asiaei *et al.*, "Fast kinetics of thiolic self-assembled monolayer adsorption on gold: Modeling and confirmation by protein binding", *Journal of Physical Chemistry B*, vol. 118, no. 47, pp. 13 697–13 703, 2014, ISSN: 15205207. DOI: 10.1021/jp509986s.

[112] Dojindo. "Self-Assembled Monolayers Related Reagents", Dojindo, [Online]. Available: https://www.dojindo.eu.com/Protocol/SAM_Protocol.pdf.

[113] C. Vericat *et al.*, "Self-assembled monolayers of thiols and dithiols on gold: new challenges for a well-known system", *Chemical Society Reviews*, vol. 39, no. 5, pp. 1805–1834, 2010, ISSN: 14604744. DOI: 10.1039/b907301a.

[114] R. Karimi Shervedani *et al.*, "Selective Detection of Dopamine in the Presence of Ascorbic and Uric Acids through its Covalent Immobilization on Gold Mercaptopropionic Acid Self-assembled Monolayer", *Electroanalysis*, vol. 29, no. 1, pp. 272–279, 2017, ISSN: 15214109. DOI: 10.1002/elan.201600220.

[115] M. Seifert *et al.*, "Characterization of streptavidin binding to biotinylated, binary self-assembled thiol monolayers - Influence of component ratio and solvent", *Langmuir*, vol. 26, no. 9, pp. 6386–6393, 2010, ISSN: 07437463. DOI: 10.1021/la904087s.

[116] A. Du Toit, "Optimization of protein immobilization on gold surfaces", unpublished, 2020.

[117] ThermoScientific. "Ellman's Reagent", ThermoScientific, [Online]. Available: https://assets.thermofisher.com/TFS-Assets/LSG/manuals/MAN0011216_Ellmans_Reag_UG.pdf.

[118] Sigma aldrich. "Bradford Reagent", Sigma aldrich, [Online]. Available: https://www.sigmaaldrich.com/content/dam/sigma-aldrich/docs/Sigma/Bulletin/b6916bul.pdf.

[119] Resonant Technologies Gmbh. "Features of a SPR reflectivity curve", Resonant Technologies Gmbh, [Online]. Available: http://www.res-tec.de/tutorials/res-tec-tutorial-01.pdf.

[120] Resonant Technologies. "Simulate your reflectivity curve with WinSpall", Resonant Technologies Gmbh, [Online]. Available: http://www.res-tec.de/tutorials/res-tec-tutorial-02.pdf.

[121] K. Thoren, "The Role of Surface Plasmon Resonance in Clinical Laboratories — AACC.org", *Clinical Laboratory News*, pp. 1–7, 2019.

[122] SPR pages. "A curve", SPR pages, [Online]. Available: https://www.sprpages.nl/sensorgram-tutorial/a-curve?highlight=WyJzZW5zb3JncmFtIiwic2Vuc29yZ3JhbXMi= (visited on 07/03/2021).

[123] C. L. Wong and M. Olivo, "Surface Plasmon Resonance Imaging Sensors: A Review", *Plasmonics*, vol. 9, no. 4, pp. 809–824, Aug. 2014, ISSN: 1557-1955. DOI: 10.1007/s11468-013-9662-3.

[124] J. S. Yuk *et al.*, "Application of spectral SPR imaging for the surface analysis of C-reactive protein binding", *Sensors and Actuators, B: Chemical*, vol. 119, no. 2, pp. 673–675, 2006, ISSN: 09254005. DOI: 10.1016/j.snb.2006.01.031.

[125] S. Deng *et al.*, "Phase-sensitive surface plasmon resonance sensors: Recent progress and future prospects", *Sensors (Switzerland)*, vol. 17, no. 12, 2017, ISSN: 14248220. DOI: 10.3390/s17122819.

[126] L. Ji *et al.*, "Investigation of surface plasmon resonance phenomena by finite element analysis and Fresnel calculation", *Sensors and Actuators, B: Chemical*, vol. 198, pp. 82–86, 2014, ISSN: 09254005. DOI: 10.1016/j.snb.2014.02.105.

[127] Jürgen Worm, *Winspall*, version 3.02 Release:0.1, Germany: Max Planck Institute for Polymer Research, 2009.

[128] L. Cristofolin. (2020). "Surface Plasmon Resonance Calculator ", [Online]. Available: https://www.mathworks.com/matlabcentral/fileexchange/13700-surface-plasmon-resonance-calculator (visited on 06/15/2020).

[129] B. Chakraborty, *Is there any method to calculate spr using matlab?*, Aug. 2018.

[130] K. Ichihashi and T. Iwata, "Numerical simulation of a metal diffraction grating-based SPR sensor with a water-immersion lens", *Optical Review*, vol. 24, no. 6, pp. 668–676, 2017, ISSN: 13499432. DOI: 10.1007/s10043-017-0361-8.

[131] Bruker. "Unlocking the Analytical Power of Surface Plasmon Resonance", [Online]. Available: https://www.bruker.com/products/surface-plasmon-resonance.html (visited on 06/22/2020).

[132] BioNavis. "Discover the world of MP-SPR and find a solution to your research needs!", BioNavis, [Online]. Available: https://www.bionavis.com/ (visited on 06/22/2020).

[133] Plasmetrix. "Plasmetrix Surface Plasmon Resonance devices", Plasmetrix, [Online]. Available: https://plasmetrix.com/products/ (visited on 06/22/2020).

[134] SPR pages. "SPR Instruments", SPR pages, [Online]. Available: https://www.sprpages.nl/instruments (visited on 06/22/2020).

[135] B. A. Prabowo *et al.*, "Rapid screening of Mycobacterium tuberculosis complex (MTBC) in clinical samples by a modular portable biosensor", *Sensors and Actuators, B: Chemical*, vol. 254, pp. 742–748, 2018, ISSN: 09254005. DOI: 10.1016/j.snb.2017.07.102.

[136] M. Singh *et al.*, "Emerging cytokine biosensors with optical detection modalities and nanomaterial-enabled signal enhancement", *Sensors (Switzerland)*, vol. 17, no. 2, 2017, ISSN: 14248220. DOI: 10.3390/s17020428.

[137] T. M. Battaglia *et al.*, "Quantification of cytokines involved in wound healing using surface plasmon resonance", *Analytical Chemistry*, vol. 77, no. 21, pp. 7016–7023, 2005, ISSN: 00032700. DOI: 10.1021/ac050568w.

[138] W. Mustafeez. (2011). "Surface plasmon resonance demo", [Online]. Available: https://physlab.lums.edu.pk/images/c/c8/SPR.pdf.

[139] D. Coulter. (2014). "Surface plasmon resonance", [Online]. Available: https://www.youtube.com/watch?v=RO6Rq6-cqsY (visited on 10/01/2020).

[140] O. Pluchery *et al.*, "Laboratory experiments for exploring the surface plasmon resonance", *European Journal of Physics*, vol. 32, no. 2, pp. 585–599, 2011, ISSN: 01430807. DOI: 10.1088/0143-0807/32/2/028.

[141] Dielectric Manufacturing. "Acetal Characteristics", Dielectric Manufacturing, [Online]. Available: https://dielectricmfg.com/knowledge-base/acetal/ (visited on 01/18/2021).

[142] OpenCV. "OpenCV About", OpenCV, [Online]. Available: https://opencv.org/about/ (visited on 02/21/2020).

[143] M. Polyanskiy. "Refractive Index database", [Online]. Available: https://refractiveindex.info/ (visited on 12/23/2020).

[144] Panasonic, *RED and/or IR TO-CAN Laser Diodes Application Note*, Panasonic, 2018.

[145] G. Bosman, *Brewster angle*, personal communication, Feb. 2021.

[146] ——, *Setup*, personal communication, Feb. 2021.

[147] ThorLabs. "Plano-convex cylindrical lenses, n-bk7, uncoated", ThorLabs, [Online]. Available: https://www.thorlabs.com/newgrouppage9.cfm?objectgroup_id=2803&pn=LJ1822L1 (visited on 02/09/2021).

[148] Daniel Steingrube, *Venteon vwaistwatcher*, version 1.3.4.0.

[149] G. Bosman and M. Tame, *Setup*, personal communication, Feb. 2021.

[150] R. Daniel, *Comsol*, personal communication, Feb. 2021.

[151] BioNovis Team. (2020). "Warning about EDC", BioNovis Team, [Online]. Available: `http://www.bionavis.com/en/news/warning-about-edc/` (visited on 09/09/2020).

[152] *Safety data sheet 3-mercaptopropionic acid*, Sigma-Aldrich.

[153] M. Innat. (2018). "Basic image processing in python - part 1", Codementor community, [Online]. Available: `https://www.codementor.io/@innat_2k14/image-data-analysis-using-numpy-opencv-part-1-kfadbafx6` (visited on 01/08/2021).

[154] ProgrammerSought. "Using opencv to calculate PCA for image orientation correction", [Online]. Available: `https://www.programmersought.com/article/9534136088/` (visited on 02/02/2020).

[155] Edmund optics. "An introduction to optical coatings", Edmund optics, [Online]. Available: `https://www.edmundoptics.com/knowledge-center/application-notes/lasers/an-introduction-to-optical-coatings/` (visited on 02/19/2021).

[156] *Laser diode lncq28ms01ww*, Panasonic, Apr. 2018.

[157] *Economical laser vlm-635/650-03 series*, Infiniter, 2014.

[158] ThorLabs. "Auto cad pdf", ThorLabs, [Online]. Available: `https://www.thorlabs.com/thorproduct.cfm?partnumber=LJ1822L1`.

[159] ThermoScientific. "NHS and Sulfo-NHS", ThermoScientific, [Online]. Available: `http://tools.thermofisher.com/content/sfs/manuals/MAN0011309_NHS_SulfoNHS_UG.pdf`.

[160] A. Pretorius, *Standard curve*, personal communication, Sep. 2020.

[161] Sigma aldrich. "Fluorescein isothiocyanate", Sigma aldrich, [Online]. Available: `https://www.sigmaaldrich.com/content/dam/sigma-aldrich/docs/Sigma/Product_Information_Sheet/f7250pis.pdf`.